UNIVERSIDADE FEDERAL DO CEARÁ
CENTRO DE TECNOLOGIA
DEPARTAMENTO DE ENGENHARIA ESTRUTURAL E CONSTRUÇÃO CIVIL
PROGRAMA DE PÓS-GRADUAÇÃO EM ENGENHARIA CIVIL

ELIAS FERREIRA LIMA

INVESTIGATION OF THE HARDENING KINETICS OF ALKALI-ACTIVATED BINDERS USING MACHINE LEARNING, MECHANICAL WAVES AND RHEOLOGY

FORTALEZA
2025

ELIAS FERREIRA LIMA

INVESTIGATION OF THE HARDENING KINETICS OF ALKALI-ACTIVATED BINDERS USING MACHINE LEARNING, MECHANICAL WAVES AND RHEOLOGY

M.Sc. thesis presented to the Post-Graduate Program in Structures and Civil Construction, as a partial fulfillment of the requirements for the Master's degree in Civil Engineering at Federal University of Ceará.

Area within the Graduate Program: Civil Construction

Advisor: Prof. Dr. Lucas Feitosa de Albuquerque Lima Babadopulos.

FORTALEZA

2025

Dados Internacionais de Catalogação na Publicação
Universidade Federal do Ceará
Sistema de Bibliotecas
Gerada automaticamente pelo módulo Catalog, mediante os dados fornecidos pelo(a) autor(a)

L697i Lima, Elias Ferreira.
Investigation of the hardening kinetics of alkali-activated binders using machine learning, mechanical waves and rheology / Elias Ferreira Lima. – 2025.
171 f. : il. color.

Dissertação (mestrado) – Universidade Federal do Ceará, Centro de Tecnologia, Programa de Pós-Graduação em Engenharia Civil: Estruturas e Construção Civil, Fortaleza, 2025.
Orientação: Prof. Dr. Lucas Feitosa de Albuquerque Lima Babadopulos.
Coorientação: Prof. Dr. Antonin Fabbri.

1. Alkali-activated binders (AABs). 2. Hardening kinetics. 3. Machine learning. 4. Impact resonance test. 5. Rheology. I. Título.

CDD 624.1

ELIAS FERREIRA LIMA

INVESTIGATION OF THE HARDENING KINETICS OF ALKALI-ACTIVATED BINDERS USING MACHINE LEARNING, MECHANICAL WAVES AND RHEOLOGY

M.Sc. thesis presented to the Post-Graduate Program in Structures and Civil Construction, as a partial fulfillment of the requirements for the Master's degree in Civil Engineering at Federal University of Ceará.

Area within the Graduate Program: Civil Construction

Advisor: Prof. Dr. Lucas Feitosa de Albuquerque Lima Babadopulos.

Approved in: 15/12/2025.

COMMITTEE

Prof. Dr. Lucas Feitosa de Albuquerque Lima Babadopulos (Advisor)
Federal University of Ceará (UFC)

Prof. Dr. Antonin Frabbri (Co-advisor)
École Nationale des Travaux Publics de l'État (ENTPE)

Prof. Dra. Heloina Nogueira da Costa
Universidade Federal do Ceará (UFC)

Prof. Dr. Cédric Sauzéat
École Nationale des Travaux Publics de l'État (ENTPE)

ACKNOWLEDGEMENTS

Dedico esse trabalho a todos que me ajudaram, primeiramente a Deus que guiou meus passos até aqui. A minha mãe Sueli, meu pai Raimundo e meus irmãos Patrícia e Raimison, por todo o apoio dado desde sempre. Em especial aos meus pais, que se sacrificaram de maneiras que talvez eu nunca compreenda totalmente, para que eu tivesse a educação formal que lhes foi negada.

Aos meus amigos da pós-graduação Madson, Abcael, Flávio, Sombra, Otávio, Eulália, Karol, Benício, Andressa, Halana, Caio, Iuri, Thayná, Jéssica e Marcelo, que me proporcionaram tantos momentos felizes, fazendo toda a diferença na jornada. Aos meus amigos da graduação, Werleson, Leonildo, Bruna, Yara e Daniel, que estão comigo a anos, e foram força quando eu não acreditava em mim mesmo. As minhas amigas da vida, Naiane e Emile, que embora longe fisicamente, sempre estão presentes.

Ao meu orientador, Prof. Dr. Lucas Babadopulos, que impactou positivamente minha trajetória desde o momento que o conheci. Fez-me acreditar em sonhos que pareciam inalcançáveis, ajudou-me a torná-los realidade e despertou em mim o impulso de querer sempre mais. Seus conselhos, elogios e principalmente as críticas me abriram portas e transformaram meu crescimento acadêmico e pessoal.

Ao Prof. Dr. Antonin Fabbri, pela excelente coorientação e pela forma acolhedora com que me recebeu na França, possibilitando uma experiência transformadora em minha trajetória acadêmica e pessoal. À professora Dra. Heloina Costa e professor Dr. Cédric Sauzéat pelas contribuições importantíssimas ao trabalho, e pela disponibilidade para compor a banca.

À Fundação Cearense de Apoio ao Desenvolvimento Científico e Tecnológico (FUNCAP), expresso minha gratidão pelo apoio financeiro. Esse suporte foi fundamental para a execução deste trabalho, permitindo dedicação integral às atividades acadêmicas.

A Leonia, Wesley, Johnny, Rômulo e Assis, do Laboratório de Mecânica dos Pavimentos (LMP), manifesto meu sincero agradecimento pelo apoio técnico e pelas trocas de conhecimento que enriqueceram este trabalho. Ao Helano, Paulo Vitor e Manoel, do Laboratório de Materiais e Construção Civil (LMCC), agradeço pela colaboração e pela assistência durante as etapas experimentais. Registro ainda minha gratidão a Annie e Iolanda, cuja dedicação, paciência e atenção fizeram toda a diferença nessa jornada.

“Once you learn to read, you will be forever free”

Frederick Douglass

ABSTRACT

The urgent need to reduce CO_2 emissions in the construction industry has driven the search for sustainable alternatives to conventional binders. Alkali-activated binders (AABs) have emerged as a promising solution due to their lower environmental impact and capacity to incorporate industrial wastes. Although extensive research has examined the mechanical performance of AABs, their fresh-state behavior and hardening mechanisms remain insufficiently understood. This gap hinders the optimization of their rheological and microstructural development, which are essential for reliable performance. In parallel, the growing use of machine learning in materials science has opened new perspectives for predicting binder properties; however, its application to AABs remains in its early stages. Existing studies employing non-destructive test (NDT) techniques, particularly ultrasonic pulse velocity, have provided valuable insights into early-age transitions but are limited in capturing the complex viscoelastic behavior of these materials. Impact resonance, in contrast, has demonstrated strong potential for evaluating dynamic properties in hardened cementitious and asphalt materials, yet it has not been adapted for fresh-state analysis. In this context, the main objective of this research is to investigate the hardening mechanisms of AABs through the combined use of machine learning, impact resonance, and microstructural characterization. The methodology is organized into three stages. First, machine learning algorithms will be developed to estimate fresh and hardened properties based on chemical composition. Second, a novel impact resonance test apparatus will be designed and optimized through FEM (Finite Element Method) simulations to enable accurate monitoring of AABs in the fresh state. Finally, the hardening kinetics of AABs will be assessed through impact resonance and rheological time-sweep tests, coupled with thermal and chemical analyses such as Fourier Transform Infrared Spectroscopy (FTIR), Thermogravimetric Analysis (TGA), and isothermal calorimetry. The integration of these experimental and computational approaches is expected to advance the understanding of hardening mechanisms in AABs and provide a foundation for improved predictive and monitoring tools. The main findings of this research reveal that artificial neural networks (ANN), random forest (RF), and bagging regression (BR) demonstrated the highest predictive performance for estimating setting time and compressive strength of AABs from chemical composition. In parallel, the impact resonance test proved to be a highly effective nondestructive tool for monitoring early-age hardening, showing strong correlations with rheological parameters and calorimetric evolution over time. Integrating impact resonance test with rheology, calorimetry, FTIR, and TGA provides a coherent, multi-scale understanding of

early-age hardening in AABs and reveals calcium availability as the dominant factor governing their mechanical and microstructural evolution. This work is carried out in collaboration between the Federal University of Ceará (UFC), Brazil, and ENTPE, France.

Keywords: alkali-activated binders (AABs); hardening kinetics; machine learning; impact resonance test; rheology.

RESUMO

A necessidade urgente de reduzir as emissões de CO_2 na indústria da construção civil tem impulsionado a busca por alternativas sustentáveis aos ligantes convencionais. Os ligantes álcali-ativados (AABs, do inglês) surgem como uma solução promissora devido ao seu menor impacto ambiental e à capacidade de incorporar resíduos industriais. Embora pesquisas extensas tenham examinado o desempenho mecânico dos AABs, o comportamento no estado fresco e os mecanismos de endurecimento permanecem insuficientemente compreendidos. Essa lacuna dificulta a otimização do desenvolvimento reológico e microestrutural, aspectos essenciais para o desempenho confiável do material. Paralelamente, o uso crescente de técnicas de *machine learning* na ciência dos materiais tem aberto novas perspectivas para a predição das propriedades dos ligantes, contudo, sua aplicação em AABs ainda se encontra em estágios iniciais. Estudos existentes que empregam técnicas não destrutivas (NDTs, *Non-destructive tests),* particularmente a velocidade de pulso ultrassônico, forneceram contribuições valiosas sobre as transições em idades iniciais, mas apresentam limitações quanto à captura do comportamento viscoelástico complexo desses materiais. Em contraste, o método de ressonância por impacto (*Impact Resonance Test*) tem demonstrado forte potencial na avaliação de propriedades dinâmicas em materiais cimentícios e asfálticos no estado endurecido, embora ainda não tenha sido adaptado para análises no estado fresco. Nesse contexto, o principal objetivo desta pesquisa é investigar os mecanismos de endurecimento de ligantes ativados por álcali por meio do uso combinado de aprendizado de máquina, ressonância por impacto e caracterização microestrutural. A metodologia está organizada em três etapas. Primeiramente, algoritmos de *machine learning* serão desenvolvidos para estimar propriedades no estado fresco e endurecido com base na composição química. Em seguida, um novo aparato de ensaio de ressonância por impacto será projetado e otimizado por meio de simulações em Método dos Elementos Finitos (FEM, do inglês), visando permitir o monitoramento preciso dos AABs no estado fresco. Por fim, a cinética de endurecimento dos AABs será avaliada por meio de ensaios de ressonância por impacto e varreduras reológicas no tempo (time sweep), associadas a análises térmicas e químicas, como Espectroscopia no Infravermelho por Transformada de Fourier (FTIR), Análise Termogravimétrica (TGA) e calorimetria isotérmica. A integração dessas abordagens experimentais e computacionais é esperada para avançar a compreensão dos mecanismos de endurecimento em AABs e fornece uma base para o desenvolvimento de ferramentas aprimoradas de predição e monitoramento. Os principais resultados desta pesquisa evidenciam que as redes neurais artificiais (ANN), o *random forest* (RF) e o *bagging regression*

(BR) apresentaram o desempenho preditivo mais robusto para estimar o tempo de pega e a resistência à compressão de ligantes álcali-ativados a partir de parâmetros químicos. Em paralelo, o ensaio de ressonância por impacto demonstrou elevada eficácia como técnica não destrutiva para o monitoramento do endurecimento em idades iniciais, exibindo correlações expressivas com a evolução reológica e calorimétrica. A integração da ressonância por impacto com reologia, calorimetria, FTIR e TGA possibilitou uma interpretação multiescalar e coerente da cinética de endurecimento, permitindo identificar a disponibilidade de cálcio como o fator preponderante na evolução mecânica e microestrutural dos sistemas estudados. Este trabalho é desenvolvido em colaboração entre a Universidade Federal do Ceará (UFC), Brasil, e a ENTPE, França.

Palavras-chave: ligantes álcali-ativados; cinética de endurecimento; *machine learning*; ressonância por impacto; reologia.

LIST OF FIGURES

LIST OF TABLES

LIST OF ABBREVIATIONS AND ACRONYMS

AABs	Alkali-activated binders
ABNT	Associação Brasileira de Normas Técnicas (Brazilian Association of Technical Standards)
AB	AdaBoost
ANN	Artificial Neural Network
ASTM	American Society for Testing and Materials
BR	Bagging Regression
C-A-S-H	Gel composed of CaO-Al_2O_3-SiO_2-H_2O
C-(N)-A-S-H	Gel composed of CaO-(Na_2O)-SiO_2-H_2O
C-S-H	Gel composed of CaO-SiO_2-H_2O
DSR	Dynamic Shear Rheometer
DT	Decision Tree
FA-BR	Fly ash from Brazil
FA	Fly ash from France
FEM	Finite Element Method
FFT	Fast fourier transform
FTIR	Fourier transform infrared
|G*|	Complex Modulus
G’	Storage Modulus
G”	Loss Modulus
GGBS	Ground Granulated Blast Furnace Slag
IC	Isothermal Calorimetry
IRT	Impact Resonance Test
IWV	Impact Wave Velocity
N/B	Alkali content
NBR	Norma Brasileira (Brazilian Standard)
NaOH	Sodium Hydroxide
Na_2SiO_3	Sodium Silicate
N-A-S-H	Gel composed of Na_2O-Al_2O_3-SiO_2-H_2O
MAE	Mean Absolute Error
ML	Machine Learning
MPR	Multivariate Polynomial Regression

MSE	Mean Squared Error
PCB	Portland cement binder
PLA	Polylactic Acid
PU	Polyurethane
R^2	Coefficient of Determination
RF	Random Forest
S/N	Silica modulus
TGA	Thermogravimetric Analysis
UPV	Ultrasonic Pulse Velocity
W/B	Water-to-Binder ratio

TABLE OF CONTENTS

1 INTRODUCTION

The growing need to reduce CO_2 emissions from the construction industry has driven the development of alternatives to Portland cement. Among them, alkali-activated binders (AABs) have emerged as a promising option due to their lower environmental impact. These materials are produced by activating aluminosilicate-rich precursors, such as fly ash, steel slag, and metakaolin, with alkaline solutions, typically sodium silicate (Na_2SiO_3) and sodium hydroxide (NaOH) (Xie *et al.*, 2020; Zhang *et al.*, 2020).

Most existing studies on alkali-activated systems focus on mechanical performance, with limited attention to the fresh state behavior (Tekle; Hertwig; Holschemacher, 2021). The main factors influencing the setting development of AABs include binder content, the alkali-to-binder ratio, the concentration and proportions of the activating solution, and the water content (Nagajothi; Elavenil, 2018). The nature of the gels formed (N-A-S-H, C-A-S-H, or hybrid structures) depends largely on calcium availability (Provis; Bernal, 2014), which also affects the kinetics of gel formation. This has been object of studies from the Federal University of Ceará (UFC) over the past 8 years (Costa, 2022; Carvalho, I. C. *et al.*, 2024; Souza, 2024; Araújo *et al.*, 2025).

In light of this, it is essential to deepen the understanding of those processes and improve prediction, using more advanced tools. Some authors have successfully employed machine learning to predict AAB properties based on key compositional and curing parameters (Nguyen *et al.*, 2020; Ahmad *et al.*, 2022; Tang *et al.*, 2022). However, the specific influence of each oxide component remains underexplored, as most authors focus on one or two specific types of precursors, which limits the applicability of their models to other types of waste-derived raw materials.

Additionally, recent research addressed the fresh state of AABs using non-destructive test (NDT) techniques to monitor hardening processes, focusing on reaction kinetics, gel formation, and setting time (Tekle; Hertwig; Holschemacher, 2021; Park *et al.*, 2024). Amongst the available techniques, ultrasonic test is the most commonly employed and has demonstrated promising results (Hong; Choi, 2021; Lin *et al.*, 2022). For example, Park *et al.* (2024) proposed the existence hardening stages for geocement (a hybrid material between a Portland cement and a geopolymer obtained after mixing metakaolin) based on variations in ultrasonic wave amplitude across different frequencies. However, ultrasonic test remains limited in the range of parameters it can assess, primarily focusing on wave velocity and

amplitude, which may be enough for elastic materials but fail for more complex viscoelastic materials (Bezerra *et al.*, 2023; Carret; Babadopulos, 2025). In that context, and as suggested by Castillo, Hedjazi and Kabir (2022), impact resonance appears to be a more sensitive technique for studying the hardening process of AABs and Portland cement materials. However, its application in the fresh state, when the material may present high damping, still demands significant development, particularly regarding test apparatus and theoretical understanding. Currently, the technique is mainly employed in the hardened state to assess elastic modulus (Castillo; Hedjazi; Kabir, 2022; Song; Lange, 2022). Therefore, such technique may reveal relevant microstructural changes that contribute to understanding the hardening process of AABs.

In this context, rheological and microstructural analyses serve as critical tools for elucidating the mechanisms underlying mechanical wave propagation during the hardening process of cementitious materials. Rheological characterization provides quantitative information on the evolution of viscoelastic properties. In particular, flow behavior and stiffness development, which are intrinsically linked to physicochemical transformations occurring during setting and hardening, can be studied (Wang *et al.*, 2023; Abed *et al.*, 2024; Rahimpour; Esmaeili, 2025). The rheological evolution of AAB is strongly controlled by their hydration kinetics and associated microstructural transformations (Kou *et al.*, 2020; Jiang; Shi; Zhang, 2022). Previous studies have shown that rheological stiffening and the transition from viscous to elastic behavior by hydration-induced gel formation and microstructural percolation, which simultaneously modify the material's internal stiffness and damping, thereby influencing its wave propagation characteristics (Kou *et al.*, 2020; Kozhukhova *et al.*, 2021; Jiang; Shi; Zhang, 2022). Therefore, it is hypothesized that variations in resonance frequency and damping ratio obtained from IRT can be used as indirect indicators of hydration kinetics, as both rheological and microstructural evolution alter the dynamic stiffness that controls wave behavior.

Given the aforementioned scenario, the general objective of this work is to investigate the hardening mechanisms of AABs, combining machine learning models, mechanical wave propagation techniques and rheology, and microstructural analysis as a complementary support. The specific objectives for such work are: i) to investigate the use of machine learning techniques to estimate fresh and hardened state properties based on chemical composition; ii) to design, develop and validate a test apparatus for studying the hardening process by adapting non-destructive impact resonance techniques for test the material in the fresh state; iii) to investigate the hardening kinetics of AABs through impact resonance and

rheological tests, microstructural characterization, and thermal analyses. The method will include: i) test the main current machine learning models and validating them through laboratory experiments; ii) simulating impact resonance behavior in different geometries using FEM (Finite Element Method) in COMSOL software, followed by laboratory tests on the most promising configurations; iii) applying impact resonance test to AABs with varying mix parameters, supported by time-sweep rheological tests and advanced thermos-physical and chemical characterization techniques such as FTIR, TGA and isothermal calorimetry. The integration of experimental and computational approaches is anticipated to provide new tools for real-time monitoring and quality control of these materials, promoting their reliable and high-performance use in sustainable construction. This work is the result of a partnership between UFC - Fortaleza, Brazil and ENTPE - Vaulx-en-Velin, France.

1.1 Research objectives

1.1.1 Main objective

Investigate the hardening mechanisms of alkali-activated binders (AABs), combining machine learning models, mechanical wave propagation and rheology.

1.1.2 Specific objectives

To achieve the main objective, the specific objectives of this research are presented below. They are organized in such a way that they fit in different chapters in this work.

1. To investigate the use of machine learning techniques to estimate fresh and hardened state properties based on chemical composition;
2. To design, develop and validate a test apparatus for studying the hardening process by adapting non-destructive impact resonance techniques for test the material in the fresh state;
3. To investigate the hardening kinetics of alkali-activated binders through impact resonance and rheological tests, microstructural characterization, and thermal analyses.

1.2 MSc Thesis' structure

This manuscript is organized into six chapters to ensure a coherent and systematic presentation of the research. Chapter 1 introduces the research context and outlines the general

and specific objectives, concluding with a brief description of the dissertation structure. Chapter 2 provides a comprehensive literature review, discussing the composition and environmental relevance of AABs, the chemistry of reaction products, the mechanisms governing hardening and rheological evolution, and the roles of precursors and mix parameters. It also reviews current advances in machine learning and non-destructive techniques, with emphasis on the impact resonance test. Chapters 3, 4, and 5 correspond directly to the three specific objectives of the research and are structured as scientific papers: Chapter 3 investigates machine learning methods for predicting fresh and hardened properties based on chemical composition; Chapter 4 presents the design, development, and validation of an impact resonance apparatus for monitoring the hardening process; and Chapter 5 examines the hardening kinetics of AABs through a multi-technique approach combining impact resonance testing, rheology, calorimetry, FTIR, and TGA. Finally, Chapter 6 summarizes the main findings, followed by the list of references.

2 LITERATURE REVIEW

2.1 Alkali-activated binders: composition and environmental relevance

Alkali-activated binders are inorganic polymers that have emerged as an alternative to Ordinary Portland Cement (OPC) in the construction sector (Alouani *et al.*, 2024). They are produced by activating aluminosilicate materials (precursors) with alkaline solutions (activators), leading to the formation of semicrystalline gels (Aktürk *et al.*, 2025; Bahmani; Mostofinejad, 2025; Zhang, P. *et al.*, 2025). A major advantage of AABs lies in the possibility of using industrial waste as precursors, which significantly reduces CO_2 emissions compared to OPC (Segura *et al.*, 2023). Nonetheless, the production and application of AABs face several challenges, including the elevated cost and environmental impact of commercial alkaline activators, as well as the variability and unpredictability of raw materials (Aktürk *et al.*, 2025).

Figure 1 illustrates the main precursors and activators used in AABs. Among the most commonly used precursors are fly ash, ground granulated blast furnace slag, metakaolin (Xie *et al.*, 2020; Zhang *et al.*, 2020; Nodehi; Taghvaee, 2022). Regarding activators, sodium-based compounds are predominant: sodium hydroxide (NaOH) and sodium silicate ($Na_2O{\cdot}nSiO_2$). They are frequently combined to provide a high pH environment and soluble silicate content. Potassium-based analogues (such as KOH and potassium silicate) are also effective but are less commonly used due to their higher cost (Xie *et al.*, 2020; Zhang *et al.*, 2020; Luga *et al.*, 2024).

Figure 1 – Main precursors and activators

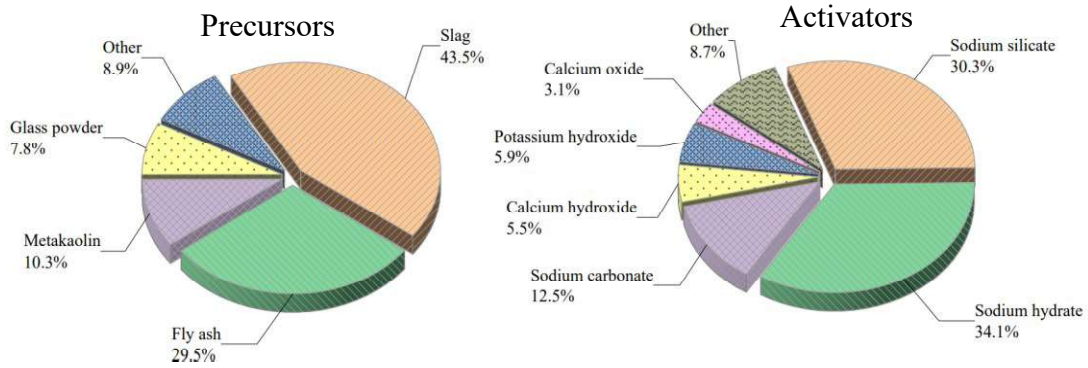

Source: Qin *et al.* (2022).

Reducing CO_2 emissions is the strongest motivation behind the development of AABs, as OPC production alone is responsible for approximately 5-7% of global CO_2 emissions (Singh; Middendorf, 2020). By utilizing industrial byproducts like fly ash and slag instead of relying on limestone calcination, AABs can reduce CO_2 emissions by 50-68%, contributing

significantly to global climate goals (Segura *et al.*, 2023). Additionally, AABs consume about 60% less energy and generate 60-80% fewer CO_2 emissions compared to OPC (Qureshi; Pal; Singh, 2025).

Nevertheless, several obstacles remain. Comprehensive life cycle assessments (LCA) are essential to ensure that AABs truly deliver sustainability benefits, considering that the production of activators like sodium silicate can carry a considerable carbon footprint (Luga *et al.*, 2024). Furthermore, cost remains a critical barrier: current estimates suggest that AAB concrete can be 2-3 times more expensive than OPC, primarily due to the high cost of activators (Segura *et al.*, 2023).

2.2 Reaction products and gel chemistry in AABs

The hardened matrix of AABs is composed predominantly of amorphous or semi-crystalline gel phases, analogous to the calcium silicate hydrate (C-S-H) gel in Portland cement systems (Nasir *et al.*, 2025). The principal gel phases are classified as sodium aluminosilicate hydrate (N-A-S-H) and calcium aluminosilicate hydrate (C-A-S-H), with intermediate or hybrid gels forming when both alkali and calcium are present in significant quantities (Provis; Bernal, 2014; Garcia-Lodeiro; Palomo; Fernández-Jiménez, 2015; Jia *et al.*, 2020; Azimi; Toufigh, 2023). The N-A-S-H gel predominates in low-calcium alkali-activated systems, such as those based on fly ash or metakaolin. It consists of a three-dimensional framework of SiO_4 and AlO_4 tetrahedra, charge-balanced by alkali cations (Ca^+, Na^+, K^+), and exhibits structural similarities to zeolite-like aluminosilicate gels (Vizureanu; Burduhos-Nergis, 2021). Figure 2 shows C-A-S-H and N-A-S-H, formed during the curing of AABs on ternary diagram.

Figure 2 – Evolution of N-A-S-H and C-A-S-H gels over time

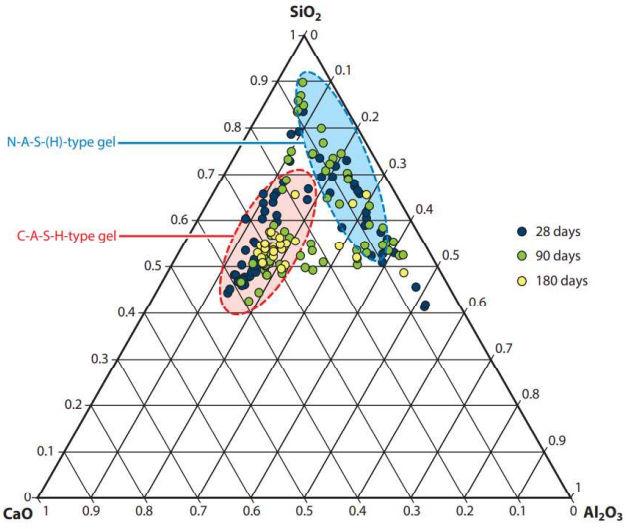

Source: Provis and Bernal (2014).

Conversely, C-A-S-H gel is the dominant binding phase in high-calcium systems, including activated slag and class C fly ash (Provis; Bernal, 2014). It shares similarities with the C-S-H gel of Portland cement but incorporates aluminum and alkalis into its structure (Garcia-Lodeiro; Palomo; Fernández-Jiménez, 2015; Qin *et al.*, 2022b). In addition to C-A-S-H, minor phases such as hydrotalcite and aluminosilicate hydrates frequently coexist in slag-activated systems (Wang, Xingang *et al.*, 2024). The Figure 3 illustrates the 2D schematic of C-S-H, C-A-S-H and N-A-S-H.

Figure 3 – 2D schematic of C-S-H, C-A-S-H and N-A-S-H

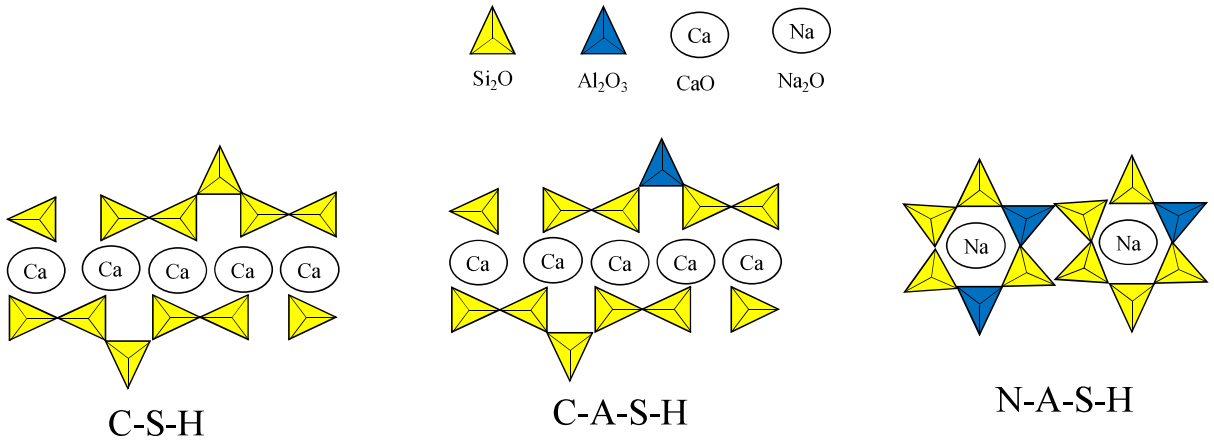

Source: Adapted by Zhang, Xi and Yang (2021).

In blended systems, such as mixtures of slag and fly ash, both gel types may co-develop, forming so-called hybrid gels denoted as C-(N)-A-S-H or N-(C)-A-S-H (Provis; Bernal, 2014; Qin *et al.*, 2022a; Ahmad *et al.*, 2023). High-resolution analyses have revealed that Ca^{2+} ions can be incorporated into N-A-S-H gels, resulting in a denser N-(C)-A-S-H phase that merges characteristics of both parent gels (Azimi; Toufigh, 2023). A key challenge is linking gel composition to macroscopic properties: even small variations in Si/Al or Ca content can significantly impact stiffness, shrinkage, and durability, yet these relationships are not yet fully quantified (Zhang *et al.*, 2017; Zhao *et al.*, 2019; Dinh *et al.*, 2024). Continued investigation into the evolution and structural refinement of AABs gels is essential for optimizing mix design and improving the prediction of long-term performance.

2.3 Hardening mechanisms and rheological evolution relationship in AABs

Before discussing the reaction mechanisms, it is necessary to define a few key terms: stiffness, hardening, setting, and curing. This clarification is essential because these terms are used continuously throughout the text and their definitions are often a source of confusion in the literature.

First, in mechanical terms, stiffness provides a quantitative measure of the material's resistance to deformation and is directly related to the elastic modulus. As such, stiffness depends on both the intrinsic material properties and the geometry of the specimen. By way of terminology, the term stiffness is used generically here to encompass modulus-related properties that evolve during hardening.

Hardening in AABs refers to the progressive physical and chemical transformation by which the material develops rigidity and mechanical strength as geopolymerization reactions proceed (Romano; Cincotto; Pileggi, 2018; Hong; Choi, 2021). The setting period is empirically determined using the Vicat test, which evaluates the penetration resistance of a standard needle, providing a practical indication of when the paste transitions from a plastic to a rigid state (Romano; Cincotto; Pileggi, 2018). Although setting is primarily a physical event, it signals the onset of chemical hardening, where the microstructure begins to evolve into a coherent and load-bearing network (Reinhardt; Grosse, 2004). It is important to note that setting, being empirically determined, is distinct from hardening, which is a physically and chemically grounded process linked to stiffness and strength development.

Finally, the curing process is defined as the maintenance of suitable moisture and temperature conditions that allow these reactions to proceed effectively (Rath; Deo; Ramtekkar, 2018; Ghostine *et al.*, 2022). Proper curing ensures adequate hydration and gel development, leading to improved strength, impermeability, and durability. Consequently, many researchers use hardening and curing almost interchangeably, since both describe the time-dependent strengthening and densification of the matrix.

With the main terms established, the relationship between hardening mechanisms and rheological evolution in AABs is now detailed. Duxson *et al*. (2007) proposed a conceptual model to describe the geopolymerization process (or alkali-activation), as illustrated in Figure 4. It comprises sequential yet interconnected stages: dissolution of the aluminosilicate source, speciation of dissolved species, gelation, reorganization, and final polymerization and hardening. The author makes it clear that, although the process is presented in a linear manner, it is strongly coupled, the stages occur simultaneously.

Figure 4 – Highly simplified reaction mechanism for geopolymerization

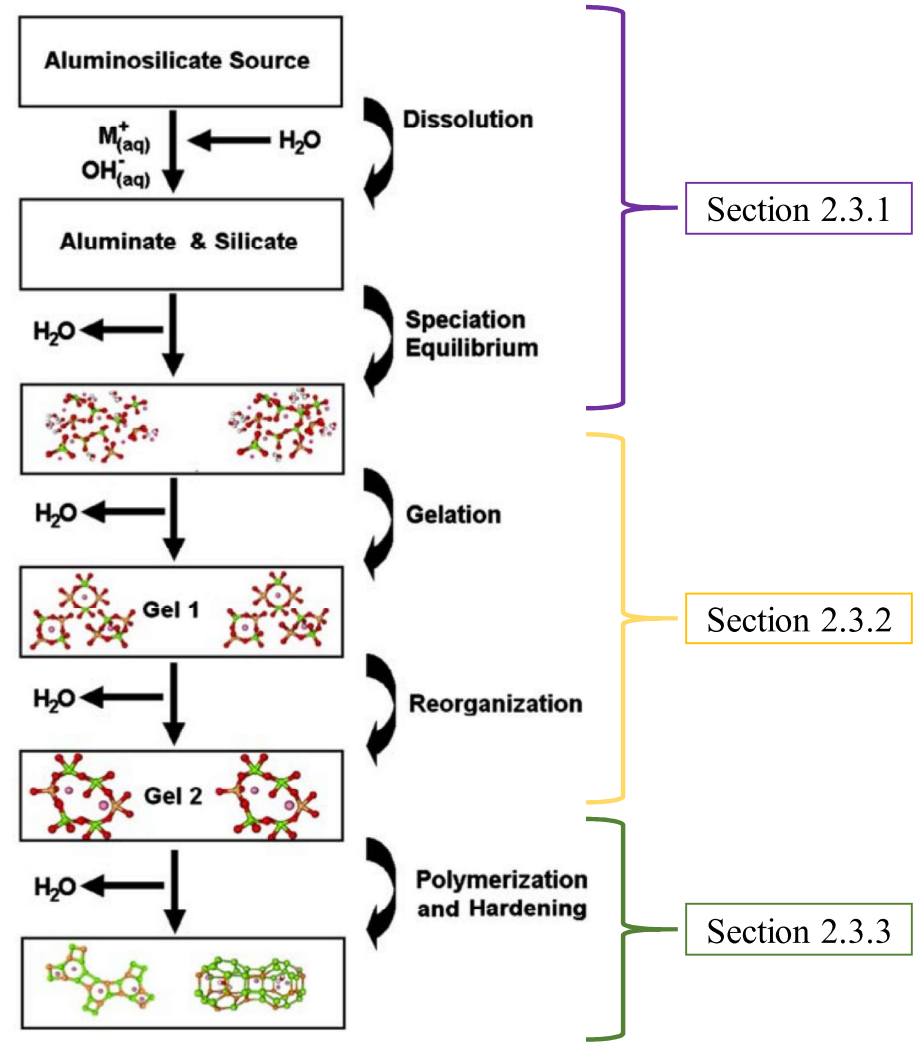

Source: Duxson *et al.* (2007)

2.3.1 Dissolution and speciation equilibrium

The alkaline activation process begins with the dissolution of solid precursor particles in alkali ambient. The covalent Si-O-Si and Al-O-Si bonds in the aluminosilicate source are broken, this occurs via OH^- attack on the solid, effectively "leaching" Si and Al into the liquid phase (Duxson *et al.*, 2007; Siyal *et al.*, 2024). The dissolution rate depends on precursor chemistry and activator composition (Liu *et al.*, 2023).

Low-calcium system often dissolve more slowly at ambient temperature, they may require very strong alkali or heat curing to achieve substantial dissolution in the early (Huang, G. *et al.*, 2024; Xu, D. *et al.*, 2024). By contrast, high-calcium precursors tend to have higher initial reactivity, Ca-O bonds are more easily hydrolyzed (Huang, G. *et al.*, 2024). In both cases, the dissolution step is endothermic and is reflected as an initial thermal signal in isothermal calorimetry (Keppert *et al.*, 2024). A key factor in AAB dissolution kinetics is whether

dissolution continues or is limited by early gel precipitation. Rapid gel formation on particle surfaces can create a passivating layer that slows further dissolution (Ma *et al.*, 2023; Cui *et al.*, 2024). After dissolution, the released silicate and aluminate species coexist in the solution and establish a speciation equilibrium, where different monomeric and oligomeric species continuously form, break, and reorganize depending on pH, Si/Al ratio, and ionic strength (Siyal *et al.*, 2024).

The initial dissolution of precursor particles in AABs has some impact on the rheological behavior of fresh binders. As OH^- ions break Si-O-Si and Al-O-Si bonds and leach species into solution, the ionic concentration and viscosity of the pore fluid evolve, altering yield stress and viscosity (Tran *et al.*, 2022). This can be observed via shear stress growth tests and small amplitude oscillatory shear (SAOS) measurements (Sun *et al.*, 2022; Tran *et al.*, 2022). This correlation between dissolution kinetics and rheological parameters offers a way to probe microstructural development in situ in fresh AAB systems (Tran *et al.*, 2022).

2.3.2 Gelation and reorganization

As the concentration of dissolved silicate and aluminate species increases, the solution becomes supersaturated, and condensation reactions begin to form small oligomeric structures that progressively assemble into a continuous aluminosilicate gel network (Duxson *et al.*, 2007; Aversa *et al.*, 2024). In low-calcium systems, this stage corresponds to the formation of an N-A-S-H gel (Provis; Bernal, 2014; Guan *et al.*, 2022). According to the conceptual model proposed by Duxson *et al*. (2007), this represents the gelation phase of geopolymerization, where a disordered, colloidal framework begins to develop. The onset of this nucleation and condensation process usually coincides with the end of the induction period and the beginning of the main exothermic peak observed in isothermal calorimetry (Keppert *et al.*, 2024).

Following gelation, the newly formed amorphous network undergoes progressive structural reorganization. The gel densifies as the degree of condensation increases, leading to greater connectivity between Si-O-Al and Si-O-Si units and the gradual development of a three-dimensional aluminosilicate framework (Duxson *et al.*, 2007; Tognonvi; Pascual; Tagnit-Hamou, 2022). This reorganization step involves redistribution of water within the pore structure and partial rearrangement of the gel domains (Duxson *et al.*, 2007; Aversa *et al.*, 2024). In calcium-rich systems, similar condensation reactions produce a C-A-S-H-type gel, which may coexist or intermix with the N-A-S-H network, but both follow the same fundamental

sequence of gel formation (Provis; Bernal, 2014; Egnaczyk; Quinn; Wagner, 2025).

From a rheological perspective, gel nucleation in AABs marks the onset of stiffening as the system evolves from a low-viscosity suspension into a percolated network (Liang; Yao; She, 2023). Rheologically, it is characterized by a rapid increase in the storage modulus (G′) and, in many cases, the point where G′ overtakes the loss modulus (G″), signaling a liquid-to-solid transition (Kamath; Prashant; Kumar, 2021; Sun *et al.*, 2022; Aversa *et al.*, 2024). In practical terms, this confirm that macroscopic setting is a direct manifestation of microscopic gel connectivity.

2.3.3 Polymerization and hardening

According to the conceptual model proposed by Duxson et al. (2007) (Figure 4), this is the final stage of geopolymerization, and corresponds to the continued growth and structural reorganization of the aluminosilicate gel. In this step, the small gel nuclei formed during gelation consume additional dissolved species and progressively develop into a continuous three-dimensional network. Chemically, this involves ongoing polycondensation, where SiO_4 and AlO_4 tetrahedra increasing the connectivity and rigidity of the structure (Keppert *et al.*, 2024; Yi; Boluk; Bindiganavile, 2024). This process is exothermic and typically coincides with the main calorimetric peak observed in alkali-activated systems (Egnaczyk; Quinn; Wagner, 2025).

As the process continues, residual condensation reactions and structural reorganization further reduce the gel porosity and increase the packing of the solid network (Tognonvi; Pascual; Tagnit-Hamou, 2022). In some systems, secondary reactions or limited crystallization may take place at later ages, refining the pore network and contributing to long-term stability (Yi; Boluk; Bindiganavile, 2024). The overall process results in a dense, cohesive aluminosilicate matrix whose mechanical and durability performance depend directly on the extent of polymerization and structural consolidation achieved during hardening (Duxson *et al.*, 2007).

Following this, polymerization sustains the progressive build-up of rigidity. The storage modulus (G′) continues to increase as new Si-O-Al linkages form and the gel clusters merge into a denser three-dimensional framework (Egnaczyk; Quinn; Wagner, 2025). Even beyond the final set determined by Vicat, G′ continues to rise, indicating that the system remains chemically active and that polymerization proceeds well into later ages (Tekle; Hertwig;

Holschemacher, 2021).

2.3.4 Influence of precursors

The chemistry of the precursor, plays a critical role in influencing the reaction pathway and the type of gel formed in alkali-activated binders. Figure 5 illustrates the main materials used as precursors and their chemical composition in the CaO-SiO_2-Al_2O_3 ternary diagram. Calcium availability accelerates the initial reactions, which in turn promotes faster setting and early strength development (Qin *et al.*, 2022). In contrast, low-calcium systems rely on the polymerization of dissolved silica and alumina species to form N-A-S-H networks.

Figure 5 – Variation of principal oxides in the chemical composition of precursors used in alkali-activated materials

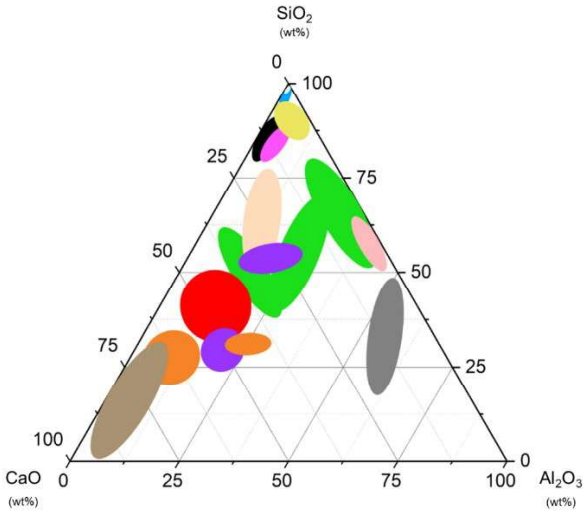

Primary industrial process	Resulting by-product – potential precursor
Production of steel and pig iron	Blast furnace slags
Thermal power plants	Coal fired fly ashes
Production of ceramic materials	Metakaolin
Biomass-derived ashes	Rice husk ashes
	Sugar cane bagasse ashes
	Palm oil fuel ashes
Production of aluminium	Red mud*
Production of Fe-Si alloys	Silica fume
Municipal wastes	Municipal solid waste incineration ashes
	Recycled glass
	Wood construction ashes
	Paper sludge ashes
	Sewage sludge ashes

Source: Adapted by Lima Junior (2025)

Blending precursors enables the tailoring of reaction kinetics and gel chemistry. According to Wang *et al.* (2023), when the CaO content is gradually increased in a fly ash-based alkali-activated binder, the gel products evolve in stages: initially forming a N-A-S-H network, then transitioning to a mixed N-(C)-A-S-H gel, and ultimately, under high calcium conditions, predominating in a C-A-S-H type gel.

Experimental results have demonstrated that incorporating calcium into aluminosilicate gels results in more compact structures and significantly higher compressive strengths (Myers *et al.*, 2013; Azimi; Toufigh, 2023). However, an excessive calcium content can trigger overly rapid reactions and induce shrinkage if not properly managed (Luga *et al.*, 2024). In addition to calcium, the silica and alumina content of the precursor also critically influences gel development: higher Si/Al ratios in low-calcium systems generally lead to the formation of more polymerized and mechanically robust N-A-S-H networks (Kamath;

Prashant; Kumar, 2021), while an optimal Ca/Si ratio of approximately 1.0-1.5 promotes the development of strong C-A-S-H gels in slag-based systems.

Nonetheless, several challenges remain. Many industrial precursors are chemically heterogeneous (Figure 5), making it difficult to predict their effects on setting behavior and mechanical strength. Minor oxides such as MgO, Fe_2O_3, and TiO_2, commonly present in precursors, can lead to the formation of secondary hydrate phases that influence the pore structure and durability, but these effects are less thoroughly studied (Mahmed; Zailan; Abdullah, 2020; Prusty; Pradhan, 2020; Kaya *et al.*, 2022).

2.3.5 Influence of mix parameters (alkali content, silica modulus, water content and curing temperature)

Alkali content (N/B) is defined as the ratio between the equivalent mass of Na_2O supplied by the activating solution and the mass of the precursor solids. An increase in the overall alkali concentration generally accelerates the reaction. For instance, raising the NaOH molarity or the percentage of solids shortens the setting time by increasing the pH and enhancing the dissolution rates. However, exceeding an optimum alkali concentration may induce rapid particle coagulation and immediate stiffening of the paste (Mahmed; Zailan; Abdullah, 2020; Yang; Zhang; Lin, 2022; Zhang *et al.*, 2023).

Silica modulus (S/N) corresponds to the molar ratio of SiO_2 to Na_2O within the activator. A lower value results in a higher initial pH, typically leading to faster setting but potentially causing early structural instability (Hung *et al.*, 2021). Conversely, a higher silica modulus moderates the initial pH and tends to extend the induction period. One study demonstrated that increasing the S/N ratio significantly prolonged the setting time of alkali-activated slag binders (Poggetto; Leonelli; Spinella, 2024).

Water content (W/B) is expressed as the total mass of water, originating from the activating solutions, relative to the precursor mass. Higher water content dilutes the activator and increases the spacing between particles, generally resulting in longer setting times and lower early-age strength. For example, in slag-fly ash blends, mixtures with higher W/B show slower stiffness development due to the dilution of reactants (Zhang *et al.*, 2023; Guo *et al.*, 2024; Han *et al.*, 2024). Conversely, reducing the water content accelerates setting, although at the expense of workability, by concentrating the alkalis and promoting faster gel percolation.

Curing temperature denotes the thermal regime applied during the early stages of

reaction. Elevated temperatures can dramatically accelerate setting. In low-calcium systems, raising the curing temperature can shorten the setting time from days to hours by enhancing the dissolution of precursors and accelerating polymerization rates (Siddique *et al.*, 2021; Mohamed, 2023; Statkauskas; Vaičiukynienė; Grinys, 2024).

2.3.6 Challenges in monitoring hardening process in AABs

Understanding and monitoring the hardening process of AABs is crucial because it provides direct guidance for mix design and formulation adjustments. By clarifying the steps showed, researchers can better control workability, setting time, and strength development. Yet, tracking these processes remains complex: the different reactions overlap, and conventional tests such as the Vicat needle often fail to capture the gradual transitions observed in AABs (Nedunuri; Muhammad, 2021; Shilton; Wang; Banthia, 2025; Zhang, P. *et al.*, 2025). Advanced methods, calorimetry, rheometry, FTIR, Raman, offer valuable insight but require costly equipment and expertise, and their signals often overlap, making interpretation difficult (Sun *et al.*, 2022; Zhong *et al.*, 2022; Keppert *et al.*, 2024). In addition, reproducibility is limited, since small changes in precursor chemistry or activator composition can lead to markedly different outcomes (Hung *et al.*, 2021; Kaze *et al.*, 2021).

To overcome these barriers, less expensive approaches are gaining attention. Machine learning models are being developed to link chemical composition with macroscopic properties such as setting time and compressive strength (Nguyen *et al.*, 2020; Ahmad *et al.*, 2022; Hsu *et al.*, 2024), while non-destructive techniques such as ultrasonic monitoring provide accessible ways to follow hardening in real time (Lee; Lee; Choi, 2020; Tian; Xu, 2022; Park *et al.*, 2024; Xu, D. *et al.*, 2024). Even so, the lack of standardized protocols for AAB characterization continues to hinder comparisons between studies. Overall, advancing monitoring strategies is essential, since a clearer understanding of hardening directly supports the design of more efficient and reliable AAB formulations.

2.4 Machine learning applications in AABs

In recent years, researchers have increasingly employed machine learning (ML) techniques to study and predict the properties of alkali-activated materials (AAMs) (Amin *et al.*, 2022; Fang *et al.*, 2024; Matsimbe *et al.*, 2024). ML is a subset of artificial intelligence (AI) that enables computers to learn from data patterns and make predictions or decisions without being explicitly programmed. In the context of materials science, ML models are trained using

large datasets of experimental results, to identify complex, often nonlinear relationships among variables that are difficult to capture through traditional regression or empirical equations (Völker *et al.*, 2021).

ML algorithms can generally be divided into supervised, unsupervised, and reinforcement learning methods. Supervised learning, the most common in AAM research, uses labeled data to predict target properties (e.g., compressive strength or setting time), while unsupervised learning focuses on identifying patterns or clusters in unlabeled datasets (Völker *et al.*, 2021; Amin *et al.*, 2022; Matsimbe *et al.*, 2024). Among supervised approaches, regression-based algorithms (e.g., linear, polynomial, or ridge regression) provide interpretable yet limited models, whereas nonlinear methods such as random forest (RF), support vector machines (SVM), and artificial neural networks (ANN) can capture complex feature interactions with higher accuracy (Amin *et al.*, 2022; Fang *et al.*, 2024). Furthermore, interpretability tools such as SHapley Additive exPlanations (SHAP) allow researchers to quantify the relative influence of input parameters, revealing that factors like silica modulus, slag/fly ash ratio, and curing temperature are the most influential variables controlling AAM strength (Fang *et al.*, 2024; Matsimbe *et al.*, 2024).

Ensemble methods, such as Random Forest and XGBoost, combine the predictions of multiple individual models to improve accuracy and robustness (Amin *et al.*, 2022). By integrating bagging or boosting strategies, these approaches effectively capture the nonlinear relationships inherent in AABs, leading to superior prediction performance compared to single-model approaches (Amin *et al.*, 2022; Fang *et al.*, 2024; Matsimbe *et al.*, 2024).

The most common models applied in the literature include artificial neural networks (ANNs), SVM, decision tree ensembles (e.g. random forests and gradient boosting), and other regression algorithms. For example, Cao *et al.* (2022) studied using an ANN (multilayer perceptron, MLP), an SVM, and an XGBoost gradient boosting model to predict the compressive strength of fly ash-based geopolymer concrete from mix composition. They found that the ensemble tree model (XGBoost) achieved the highest accuracy ($R^2 \sim 0.98$) compared to the ANN and SVM. This indicates that nonlinear ensemble approaches can capture the complex interactions in AAB mixes effectively. The Figure 6 presents the XGBoost results from this study. It illustrates a common issue in machine learning applied to this field: the limited amount of available data.

An example is a model that takes precursor chemistry and activator dosage as inputs

to estimate strength or setting time (Zhang *et al.*, 2024). Tree-based models (random forest, gradient boosting) have been popular for AAMs because they handle mixed data (categorical inputs like type of precursor, and continuous inputs like ratios) well and can rank variable importance. In one comprehensive study, over 600 mix-data points of slag/fly ash were used to train four different tree-based ML models, among them, gradient boosting regression gave the best predictions of 28-day strength. Notably, that model achieved a high correlation ($R^2 \sim 0.97$) between predicted and actual strength. As data from different studies are being combined, we see more robust models emerging. These successes demonstrate that ML can be a powerful tool to complement experimental and theoretical approaches in the AAB field.

Figure 6 – Experimental and predicted result of XGBoost model

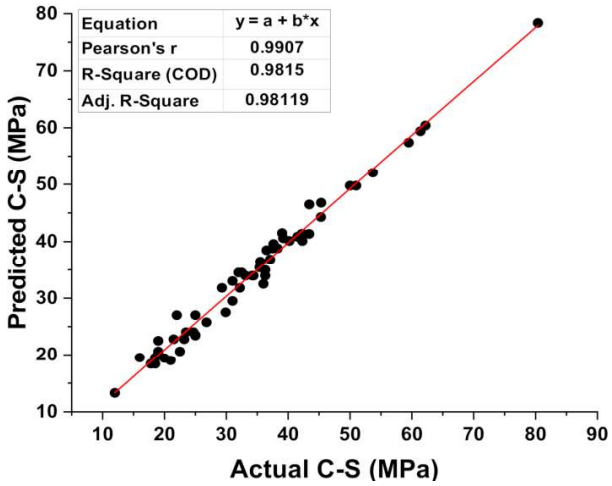

Source: Cao *et al.* (2022).

While ML models show promise, their performance is only as good as the data available. A major limitation is the scarcity of large, diverse datasets, many models are trained on a specific subset of materials (e.g. one type of fly ash and slag) and may not generalize to different precursors or activators. Also, results from different labs are not always directly comparable due to slight differences in conditions, which complicates data pooling.

2.5 Non-destructive techniques applications in AABs

2.5.1 Principles and general applications

Non-destructive tests (NDTs) refer to a range of techniques used to assess the properties, quality, or internal condition of a material or structure without causing damage or impairing its functionality (Peruń, 2024). One important class of NDT techniques relies on mechanical waves, such as ultrasonic or vibrational signals, which interact with the material's internal structure and provide insights based on wave speed, attenuation, or resonance behavior

(Silva *et al.*, 2023; Peruń, 2024).

In the mechanical wave literature, two types of body waves are reported: P-waves (primary waves) and S-waves (secondary waves). P-waves are compressional waves in which particles move in the same direction as the wave propagates. They are the fastest wave type and can travel through solids, liquids, and gases. S-waves, on the other hand, are shear waves with particle motion perpendicular to the direction of propagation; they are slower and can only propagate through solids. According to King and Stephens (1975), the propagation velocities of these waves, denoted as Vp for P-waves and Vs for S-waves, depend on the material's elastic modulus (E) and specific mass (ρ), as expressed in Equations 1 and 2, valid for homogeneous and isotropic materials.

$$v_p = \sqrt{\frac{E(1-\nu)}{\rho(1+\nu)(1-2\nu)}} \tag{1}$$

$$v_s = \sqrt{\frac{E}{2\rho(1+\nu)}} \tag{2}$$

Among mechanical wave-based techniques, the Ultrasonic Pulse Velocity (UPV) test is one of the most established. It involves transmitting high-frequency ultrasonic waves through a material and measuring the time it takes for the waves to travel between a transmitter and receiver (Silva *et al.*, 2023; Alqurashi *et al.*, 2025). The velocity of these waves is influenced by the material's stiffness, density, and homogeneity: higher velocities generally indicate greater compactness and strength, while lower values may suggest cracks, voids, or reduced stiffness (Peruń, 2024). In practical setups, transducers are placed on opposite sides of the sample with coupling gel to ensure effective contact (Figure 7).

Figure 7 – Ultrasonic test equipment and set up

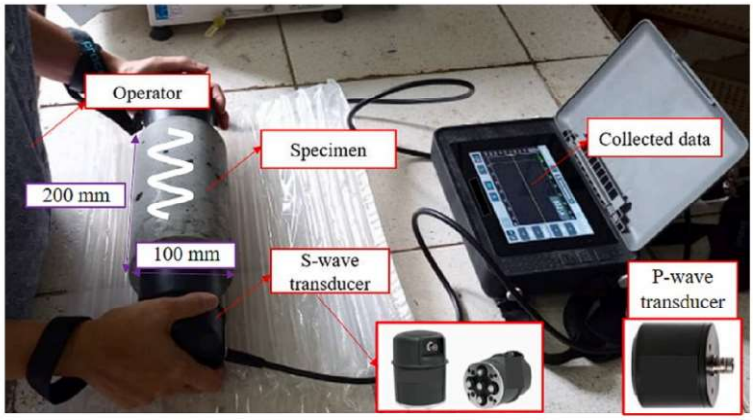

Source: Bezerra *et al.* (2023).

UPV test has long been standardized (ASTM C597, 2022) and used in conventional

and alkali-activated concretes for estimating dynamic elastic modulus, evaluating compactness, and detecting internal flaws (Tekle; Hertwig; Holschemacher, 2021; Silva *et al.*, 2023; Alqurashi *et al.*, 2025). More notably, UPV has been applied to monitor early-age behavior in alkali-activated materials. For example, Tekle, Hertwig and Holschemacher (2021) used ultrasonic pulses to monitor alkali-activated mixes from fresh to hardened states and found a strong correlation between the UPV curve and setting times determined via traditional Vicat needle tests.

Despite these advances, ultrasonic test in the fresh state still presents important limitations. While UPV techniques are effective in capturing structural transitions such as setting and early hardening, they provide limited information about the viscous or flow-related behavior of the material. This is due to the fact that the frequencies used are extremely high, resulting in responses that are almost purely elastic. For example, Park et al. (2024) conducted tests at 34 kHz, 100 kHz, and 400 kHz in the fresh state, limiting the analysis to wave velocity and amplitude. As a result, early-age measurements can miss key aspects of workability, thixotropy, or yield stress, which are critical for processing and placing alkali-activated binders.

In contrast, the Impact Resonance Test is particularly useful for evaluating more complex materials such as asphalt pavements, which are well known for their pronounced viscoelastic behavior (Carret, 2018; Bezerra *et al.*, 2023). It provides a fast, non-invasive means of assessing stiffness and mechanical response, and will be discussed in greater detail in the following section.

2.5.2 Impact resonance test (IRT)

Impact resonance test is a non-destructive method in which a specimen, such as a concrete beam or cylinder, is placed on soft foam supports, lightly struck with a small hammer, and its vibration response is captured by an accelerometer (Malone; Sun; Zhu, 2023). The Figure 8 shows the test setup on hardened specimen. The resulting signal is analyzed to identify the specimen’s natural resonant frequencies (after fast fourier transform) (Carret, 2018; Bezerra *et al.*, 2023). From these frequencies, and using known relationships involving the specimen's geometry, mass, and material properties, the dynamic modulus can be calculated, and when is more complex materials: finite element method (FEM) (Schmidt; Dethof; Kessler, 2023; Wang, Y. *et al.*, 2024).

This technique is particularly effective for quasi-elastic materials like hardened

Portland cement concrete, which respond with stable and well-defined vibrational modes (Kim *et al.*, 2022; Bezerra *et al.*, 2023; Feng; Ren; Wang, 2023) . According to (ASTM C215, 2019), the dynamic modulus of elasticity is given by Equation 3, where n' represents the fundamental longitudinal frequency (Hz), M is the mass of the specimen (kg), and D is a geometric factor equal to $5.093(L/d2)$ m^{-1} for a cylindrical specimen.

Figure 8 – Impact resonance test setup

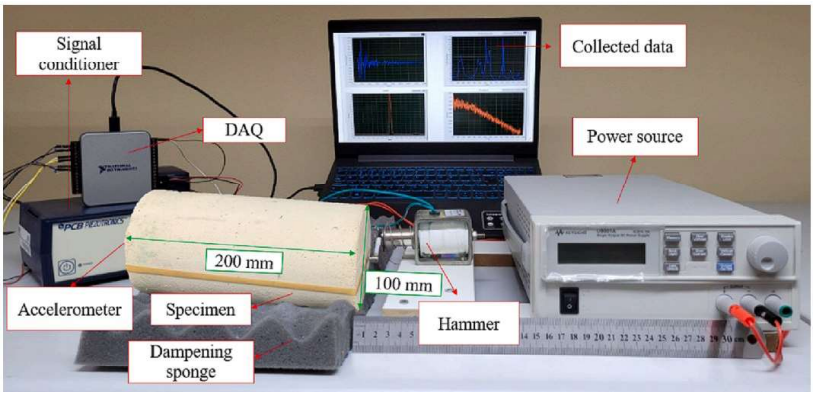

Source: Bezerra *et al.* (2023).

$$\text{Dynamic E} = \text{DM}(n')^2 \quad (3)$$

Recently, this technique has gained attention for its potential use in more complex materials like asphalt mixtures, which are inherently viscoelastic. In such cases, the time-temperature superposition principle is applied to build master curves of complex modulus over a wide range of temperatures and loading frequencies (Carret, 2018; Zhang; Sias; Dave, 2022; Bezerra *et al.*, 2023) . Although more challenging due to the dissipative nature of viscoelastic behavior, the appeal lies in the fact that impact resonance allows for stiffness evaluation without requiring large-scale mechanical equipment like a universal testing machine (UTM).

Although still unexplored in the fresh state of AABs, resonance by impact has the potential to capture viscoelastic behavior due to its broad frequency range (typically 0 to 50 kHz) (Carret, 2018; Bezerra *et al.*, 2023). This makes it a promising technique for monitoring the hardening process. By performing tests at short time intervals, it is possible to track the evolution of stiffness across a wide frequency spectrum as the material sets-something that conventional rheometers struggle to achieve. The challenge with rheometry is that frequency sweeps take time, and as the material hardens, its properties are continuously changing during the test (Maciel; Romano; Pileggi, 2023; Carvalho, I. D. C. *et al.*, 2024). Additionally, rheometers are expensive and not always practical for field or large-scale use. In contrast, impact resonance is fast, cost-effective, and could provide valuable high-frequency

characterization during early-age development in alkali-activated binders.

Exploring this technique in the fresh-to-hardened transition not only opens a new path for early-age monitoring but also creates opportunities to correlate resonance data with rheological behavior and microstructural evolution-deepening our understanding of the hardening mechanisms in these emerging binder systems.

3 INVESTIGATION OF MACHINE LEARNING METHODS FOR PREDICTING FRESH AND HARDENED PROPERTIES OF ALKALI-ACTIVATED BINDERS BASED ON CHEMICAL COMPOSITION

3.1 Introduction

Concrete is one of the most widely used manufactured materials worldwide, and its production relies fundamentally on Portland cement (PC) (Trindade *et al.*, 2020; Glanz *et al.*, 2023). Nevertheless, PC manufacturing accounts for roughly 7-8% of CO_2 emissions (Singh; Middendorf, 2020). As global PC consumption continues to rise, the need to develop alternative binders with markedly reduced environmental impact has become increasingly pressing (Lanjewar *et al.*, 2023). Within this context, alkali-activated binders (AABs) have emerged as a highly promising sustainable alternative, owing to their ability to incorporate industrial by-products and their potential to substantially lower CO_2 emissions while preserving competitive mechanical performance and durability (Provis, 2018; Segura *et al.*, 2023; Luga *et al.*, 2024).

AABs are synthesized by activating aluminosilicate precursors such as fly ash, metakaolin, and GGBS with alkaline solutions, typically sodium hydroxide (NaOH) and sodium silicate (Na_2SiO_3) (Provis, 2018; Xie *et al.*, 2020; Zhang; Sias; Dave, 2022). As a result, different gel networks are formed, including N-A-S-H in systems with low-calcium content and C-A-S-H to high-calcium availability (Guan *et al.*, 2022; Liu *et al.*, 2023; Siyal *et al.*, 2024). The development and structural characteristics of these gels are strongly influenced by the chemical composition of the precursor, particularly the SiO_2, Al_2O_3 and CaO content, as well as by the concentration and composition of the activating solution (Provis, 2018; Siyal *et al.*, 2024; Qader *et al.*, 2025). Because these parameters interact in complex and nonlinear ways, significant variability arises in the properties (Statkauskas; Vaičiukynienė; Grinys, 2024). For example, the effects of the individual oxide species on hardening mechanisms are still poorly resolved, making it difficult to design mixtures that simultaneously achieve suitable setting times and compressive strength without relying on empirical trial-and-error approaches for each new precursor (Zhao *et al.*, 2019; Jurado-Contreras *et al.*, 2022; Ma *et al.*, 2023). Consequently, machine learning (ML) frameworks have been introduced to address the high-dimensional parameter interactions and nonlinear reaction pathways inherent to AABs (Nguyen *et al.*, 2020; Ahmad *et al.*, 2023; Hsu *et al.*, 2024).

In the AABs the main ML methods employed include artificial neural networks (ANNs), support vector machines (SVMs), and tree-based ensemble algorithms (Zou *et al.*,

2022). Cao et al. (2022) showed that a gradient-boosted decision tree model (XGBoost) outperformed both the ANN and the SVM for predicting compressive strength of fly ash-based geopolymers ($R^2 \sim 0.98$), while Zhang et al. (2024) demonstrated that precursor mix proportion and activator dosage can be used effectively to estimate strength or setting time. Although ensemble models trained on larger combined datasets have reached high accuracy, the scarcity of diverse and standardized data continues to limit generalizability (Zou *et al.*, 2022; Feng; Ren; Wang, 2023; Zhang *et al.*, 2024). Most available datasets focus on fly ash and steel slag systems, meaning that models rarely incorporate other industrial by-products or alternative precursors (Nguyen *et al.*, 2020; Cao *et al.*, 2022; Han, T. *et al.*, 2022). As a result, predictions may not transfer well across different precursor chemistries, activator types, or laboratory conditions (Hsu *et al.*, 2024). Furthermore, many existing studies lack systematic sensitivity analyses, making it difficult to determine the true influence of each mixture parameter on AAB performance.

Based on this, the aim of the present study is to investigate the use of machine learning techniques to estimate fresh and hardened state properties of AABs from their chemical composition. For this purpose, several algorithms were applied, including Multivariate Polynomial Regression (MPR), Decision Tree (DT), Random Forest (RF), Bagging Regression (BR), AdaBoost (AB), and Artificial Neural Networks (ANN), with MPR used to benchmark linear-polynomial behavior against the nonlinear ensemble and neural network models. The models were trained using precursor oxide composition (Al_2O_3, SiO_2, P_2O_5, SO_3, Cl, K_2O, CaO, TiO_2, MnO, Fe_2O_3), the silica modulus S/N (SiO_2/Na_2O, mol ratio), the alkali content N/B (Na_2O/binder, mass ratio), the water-to-binder ratio W/B (mass ratio), and curing temperature. The output variables were initial and final setting times and compressive strength, obtained from datasets of 139 and 427 data points, respectively. Model performance was evaluated using a 70/30 train-test split and the metrics Coefficient of Determination (R^2), Mean Squared Error (MSE), Mean Absolute Error (MAE), after which the three models with the highest R^2 were selected for feature-importance and sensitivity analyses to determine the influence of each input parameter on the predicted property.

3.2 Materials

3.2.1 Data set description

3.2.1.1 Selected parameters as input

The dataset employed in this study comprised a comprehensive set of input parameters covering both precursor composition and mix design variables. Precursor oxides included Al_2O_3, SiO_2, P_2O_5, SO_3, Cl, K_2O, CaO, TiO_2, MnO, and Fe_2O_3 (obtained with X-ray fluorescence, XRF). These oxides were included as input variables in the present study, allowing the analysis to be generalized at the chemical level. In addition, mix design parameters were considered, such as the silica modulus (SiO_2/Na_2O, in mol/mol), the Na_2O/binder ratio (N/B, in %), and the water/binder ratio (H_2O/Binder, in g/g). These parameters were selected because they are commonly reported in the literature on alkali-activated materials and, moreover, they provide a comprehensive summary of the mix design (Amaludin *et al.*, 2024; Toobpeng; Thavorniti; Jiemsirilers, 2024; Yuan *et al.*, 2024). Curing conditions were represented by temperature (during 24 h after mixing), while fresh state behavior was assessed through initial and final setting time, and hardened state performance was evaluated through compressive strength.

In binder formulations containing two precursors, the equivalent oxide composition was determined using Equation 4. This procedure ensured a precise representation of the overall chemical composition of the binder system.

$$oxide_{n,res} = \sum_{n,p\,=\,1}^{n=10,\ \ p=2} oxide_{\,n,p} \cdot precursor_p \qquad (4)$$

Where $\mathrm{oxide_{n,res}}$ (%) is the resulting mass percentage of the *n*-th oxide in the mixture, $oxide_{\,n,p}$(%) is the mass percentage of the *n*-th oxide in the *p*-th precursor, and $precursor_p$ is the mass percentage of the *p*-th precursor in the mixture.

3.2.1.2 Initial and final setting time

The setting time of binders was evaluated using the Vicat apparatus, according to NBR 16607 (2018) or similar. This empirical penetration test is commonly employed in the literature for both Portland cement and AABs to assess the transition from the fresh to the hardened state. In this method, the initial setting time corresponds to the period required for the Vicat needle to remain at a distance of 6 ± 2 mm from the base plate, while the final setting

time is reached when the needle penetrates no deeper than 0.5 mm, indicating the loss of workability.

Table 1 presents the data overview of initial and final setting time. For each parameter, the table reports the average, standard deviation, minimum, and maximum values, providing an overview of the data distribution and variability among the collected samples. The outputs consist of the initial setting time, with an average of 237.54 min and a standard deviation of 463.68 min, and the final setting time, with an average of 404.15 min and a standard deviation of 742.12 min.

Table 1 – Dataset overview of initial and final setting time

Data	Type	Parameters	Average	Standard deviation	Min	Max
Inputs	Precursor oxides (%)	Al_2O_3	15.01	6.24	1.26	29.09
		SiO_2	43.31	13.18	6.94	67.08
		P_2O_5	0.12	0.33	0.00	2.21
		SO_3	1.10	0.86	0.00	4.86
		Cl	0.86	1.48	0.00	3.92
		K_2O	1.59	1.80	0.00	8.20
		CaO	21.92	11.30	0.87	45.12
		TiO_2	2.10	2.60	0.00	6.98
		MnO	0.08	0.41	0.00	3.18
		Fe_2O_3	5.03	6.77	0.50	39.86
	Activator	$\frac{S}{N} = \frac{SiO_2\ (mol)}{Na_2O\ (mol)}$	1.05	0.49	0.00	2.06
		$\frac{N}{B}(\%) = \frac{Na_2O\ (g)}{Binder\ (g)}$	7.96	2.81	1.00	12.00
		$\frac{W}{B} = \frac{H_2O\ (g)}{Binder\ (g)}$	0.38	0.09	0.25	0.50
	Curing condition	Temperature (°C)	26.60	11.03	20.00	65.00
Output	Fresh state	Initial setting time (min)	237.54	463.68	5.00	4080.00
		Final setting time (min)	404.15	742.12	25.00	6000.00
Total data					139	

Source: elaborated by the author.

A total of 139 setting-time data entries were compiled from the literature, as detailed in Table 2. The dataset integrates studies employing different aluminosilicate sources, including fly ash, coal bottom ash, GGBFS, BFS, waste brick, wood bottom ash, and titanium tailing slag, as well as blended precursor systems. This diversity in precursor chemistry and mixture design provides a robust foundation for developing ML models capable of capturing variations in setting behavior across different AABs systems.

Table 2 – Dataset of initial and final setting time literature sources

Source	Precursor system	Precursor 1	Precursor 2	Number of data
(Souza, 2024)	1	Fly ash	BSSF	5
(Araújo *et al.*, 2025)	1	Fly ash	BOF	3
(Li, J. *et al.*, 2023)	1	Coal bottom ash	Titanium tailing slag	36
(Wang *et al.*, 2023)	1	Fly ash	-	13
(Toobpeng; Thavorniti; Jiemsirilers, 2024)	1	Fly ash	-	1
(Allahverdi; Kani, 2009)	1	Waste brick	Waste concrete	15
(Yadollahi; Benli; Demirboğa, 2015)	1	Hasankale ground pumice	-	9
(Allahverdi; Shaverdi; Kani, 2010)	1	BFS	-	6
(Al Makhadmeh; Soliman, 2021)	1	GGBFS	-	9
(Tran Thi; Liao; Vo, 2023)	1	Fly ash + GGBFS	Wood bottom ash	12
(Amaludin *et al.*, 2024)	1	Palm Oil Fuel Ash	GGBFS	8
(Ghosh; Ghosh, 2020)	1	Fly ash	BFS	22
Total data				139

Source: elaborated by the author.

The Figure 9 presents the relative frequency distribution of all input variables used in the dataset for predicting initial and final setting time. Each subplot corresponds to one chemical or mix-design parameter included in the model. The histograms reveal substantial variability in the dataset, with certain parameters such as Cl, MnO, Fe_2O_3 and temperature displaying very narrow distributions, while others including SiO_2, CaO, Al_2O_3, S/N and N/B show broader and more heterogeneous ranges. Overall, the figure highlights the heterogeneity and chemical diversity of the compiled dataset, which is essential for training ML models capable of generalizing across different AABs systems.

Figure 9 – Relative frequency distribution of input variables dataset to initial and final setting time (a) Al_2O_3 (b) SiO_2 (c) P_2O_5 (d) SO_3 (e) Cl (f) K_2O (g) CaO (h) TiO_2 (i) MnO (j) Fe_2O_3 (k) S/N (l) N/B (m) W/B (n) Temperature

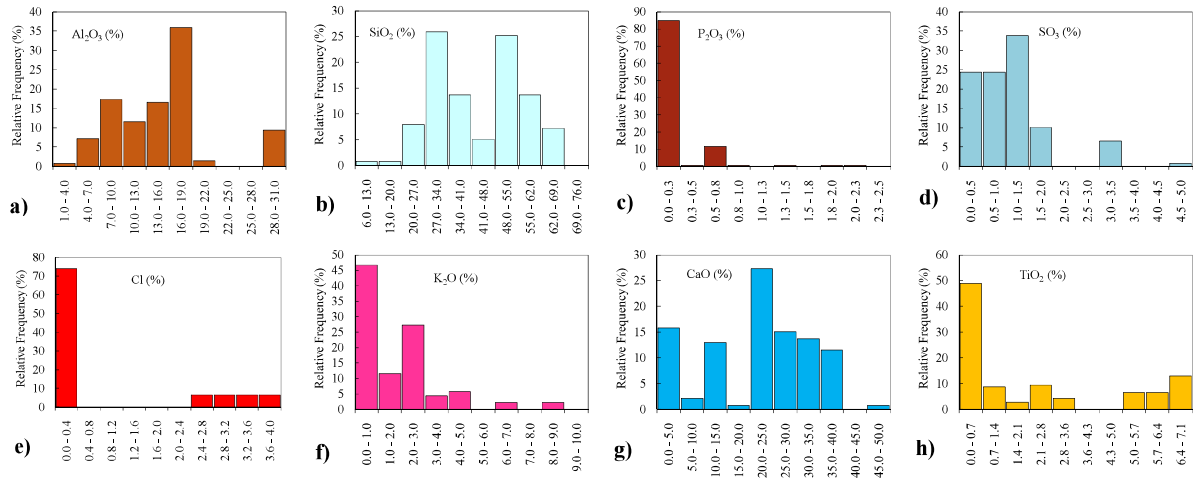

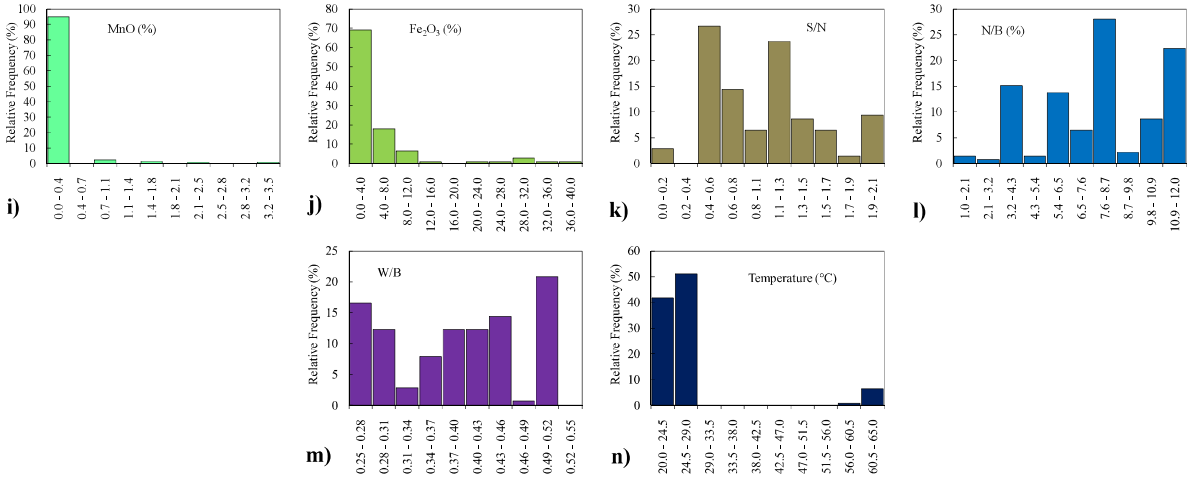

Source: elaborated by the author.

3.2.1.3 Compressive strength

The compressive strength is widely reported in the literature for AABs as a key indicator of mechanical performance and material development. It's determined through a uniaxial compression test on hardened specimens at 28 days. Table 3 shows the dataset overview for this property. As result the data set exhibit an average value of 28.59 MPa with a standard deviation of 18.72 MPa, ranging from 0.81 MPa to 110 MPa.

Table 3 – Dataset overview of compressive strength

Data	Type	Parameters	Average	Standard deviation	Min	Max
Inputs	Precursor oxides (%)	Al_2O_3	15.41	9.20	1.26	46.23
		SiO_2	38.77	14.76	6.94	67.08
		P_2O_5	0.28	0.43	0.00	2.21
		SO_3	1.28	1.31	0.00	4.86
		Cl	0.29	0.93	0.00	3.92
		K_2O	1.58	1.49	0.00	8.20
		CaO	22.39	14.00	0.09	63.00
		TiO_2	1.23	1.72	0.00	6.98
		MnO	0.49	0.92	0.00	4.53
		Fe_2O_3	11.64	10.69	0.50	39.86
	Activator	$\frac{S}{N} = \frac{SiO_2\ (mol)}{Na_2O\ (mol)}$	1.12	0.48	0.00	3.10
		$\frac{N}{B}(\%) = \frac{Na_2O\ (g)}{Binder\ (g)}$	9.05	4.83	1	36.47
		$\frac{W}{B} = \frac{H_2O\ (g)}{Binder\ (g)}$	0.40	0.17	0.06	1.44
	Curing condition	Temperature (°C)	43.56	24.13	20	85
Output	Hardened state	Compressive Strength (MPa, in 28-days)	28.59	18.72	0.81	110
Total data					427	

Source: elaborated by the author.

The compressive strength dataset comprises 427 data points compiled from a wide

range of literature sources, as presented in Table 4. The collected studies encompass both single-precursor and blended binder systems, incorporating materials such as fly ash, GGBFS, BFS, steel slag, bottom ash, waste brick, glass fiber powder and various industrial by-products.

Table 4 – Dataset compressive strength literature sources

Source	Binder system	Precursor 1	Precursor 2	Number of data
(Souza, 2024)	1	Fly ash	BSSF	27
(Araújo *et al.*, 2025)	1	Fly ash	BOF	36
(Costa, 2022)	1	KR	-	5
(Costa, 2022)	2	Fly ash	-	9
(Costa, 2022)	3	Bottom ash	-	5
(Costa, 2022)	4	BOF	-	9
(Costa, 2022)	5	Fly ash	Bottom ash	5
(Costa, 2022)	6	Fly ash	BOF	5
(Costa, 2022)	7	Bottom ash	BOF	5
(Carvalho, I. C. *et al.*, 2024)	1	Waste brick	BFS	6
(Wang, M. *et al.*, 2024)	1	Steel slag	Slag	27
(Li, J. *et al.*, 2023)	1	Coal bottom ash	Titanium tailing slag	36
(Wang *et al.*, 2023)	1	Fly ash	-	13
(Toobpeng; Thavorniti; Jiemsirilers, 2024)	1	Fly ash	-	33
(Yuan *et al.*, 2024)	1	Glass fiber powder	-	15
(Guo; Shi; Dick, 2010)	1	Fly ash	-	18
(Adu-Amankwah *et al.*, 2016)	1	Fly ash	-	30
(Allahverdi; Kani, 2009)	1	Waste brick	Waste concrete	15
(Yadollahi; Benli; Demirboğa, 2015)	1	Hasankale ground pumice	-	9
(Allahverdi; Shaverdi; Kani, 2010)	1	Blast-furnace slag	-	6
(Al Makhadmeh; Soliman, 2021)	1	GGBFS	-	9
(Tran Thi; Liao; Vo, 2023)	1	Fly ash + GGBFS	Wood bottom ash	12
(Nunes *et al.*, 2022)	1	BOF	-	6
(Amaludin *et al.*, 2024)	1	Palm Oil Fuel Ash	GGBFS	8
(Ruiz *et al.*, 2019)	1	Spent fluid catalytic cracking	-	19
(Joseph; Cizer, 2022)	1	Slag	Fly ash	9
(Ghosh; Ghosh, 2020)	1	Fly ash	BFS	50
Total data				427

Source: elaborated by the author.

The number of observations contributed by each reference ranges from a few individual measurements to several dozen, resulting in considerable variability in precursor chemistry and mixture design. The substantially larger volume of compressive strength data, in comparison with the more limited setting time dataset, reflects the fundamental importance of

this property in the assessment of AABs and the greater prevalence of such measurements in the existing literature.

The Figure 10 presents the distribution of the input variables incorporated into the compressive strength dataset. Each histogram represents the frequency with which a given chemical or mixture parameter appears across the collected studies. The oxide components display markedly different patterns: elements such as Cl, MnO and Fe_2O_3 occur in relatively limited concentration intervals, while oxides including SiO_2, CaO and Al_2O_3 span a wider range of values, reflecting the diversity of precursor types.

Figure 10 – Relative frequency distribution of input variables dataset to compressive strength (a) Al_2O_3 (b) SiO_2 (c) P_2O_5 (d) SO_3 (e) Cl (f) K_2O (g) CaO (h) TiO_2 (i) MnO (j) Fe_2O_3 (k) S/N (l) N/B (m) W/B and (n) Temperature

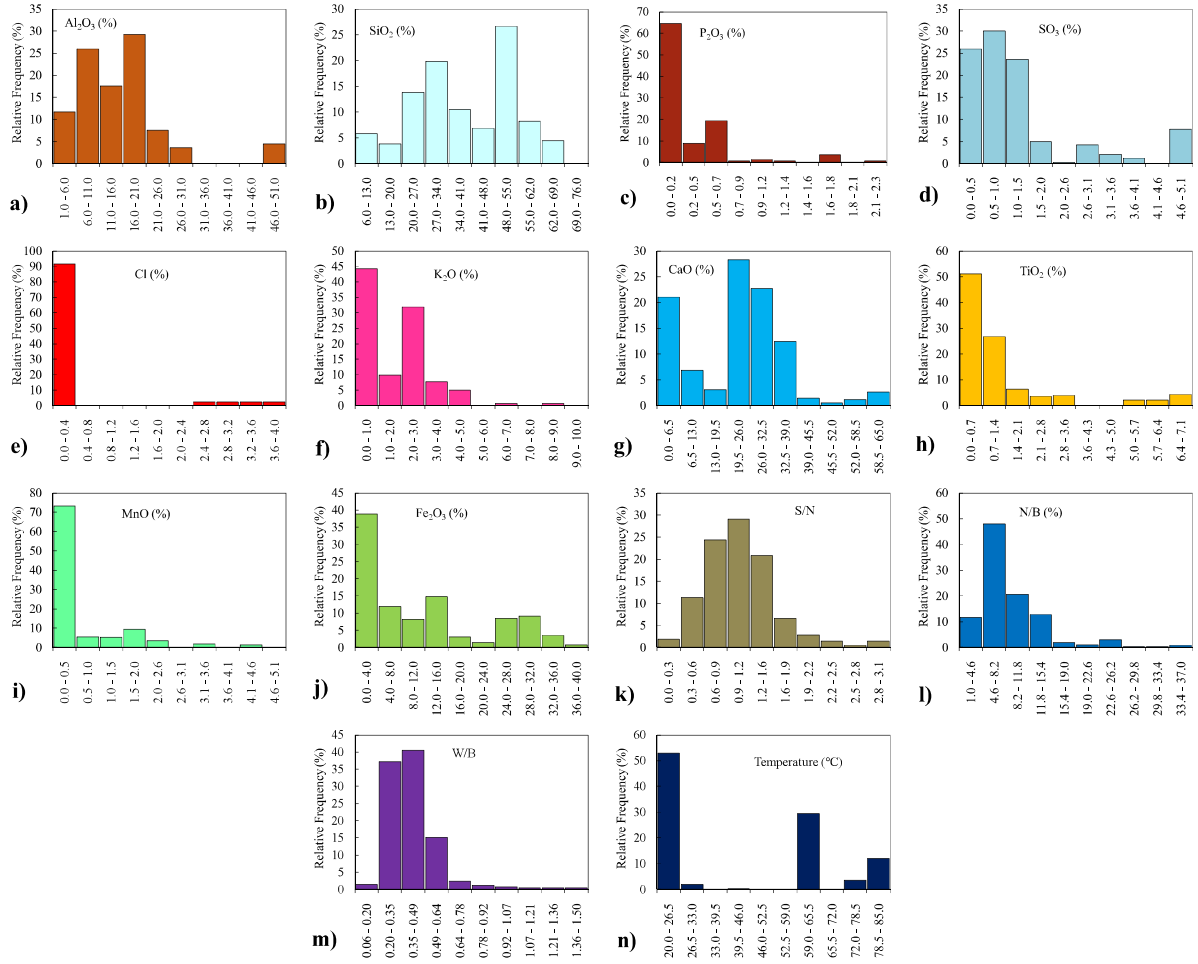

Source: elaborated by the author.

The mixture-related parameters, namely S/N, N/B and W/B, also cover multiple intervals. Curing temperature, although reported for fewer categories, still captures the conditions most commonly explored in the literature.

3.2.2 Laboratory validation binders

To validate the best machine learning models, a set of binder mixes will be produced in the laboratory using Class F fly ash (FA-BR) (ASTM C618, 2019) from the Pecém Thermoelectric Complex in Brazil and dry-pit slag (DP) supplied by ArcelorMittal Pecém (AMP). The chemical compositions of these precursors, determined by X-ray fluorescence (XRF), are presented in Table 5. FA-BR exhibited elevated SiO_2 (46.80%) and Al_2O_3 (15.64%) contents, with moderate Fe_2O_3 (21.05%) and comparatively low CaO (8.07%). In contrast, DP was characterized by a significantly higher CaO content (65.86%) and lower levels of SiO_2 (10.33%) and Al_2O_3 (2.38%), with Fe_2O_3 at 12.10%. The specific gravities of FA-BR and DP were 2.21 and 2.49, respectively.

Table 5 – Precursor oxides composition

Precursor	Al_2O_3	SiO_2	P_2O_5	SO_3	Cl	K_2O	CaO	TiO_2	MnO	Fe_2O_3
DP	**2.38**	**10.33**	1.03	4.76	0.11	0.76	**65.86**	1.12	1.32	**12.10**
FA-BR	**15.64**	**46.80**	0.44	1.91	0.03	3.72	**8.07**	1.77	0.12	**21.05**

Source: elaborated by the author.

The crystalline phases of the precursors were identified through X-ray diffraction (XRD), as shown in Figure 11. The fly ash (FA-BR) pattern exhibited predominant peaks associated with silicon oxide and iron oxide, consistent with its high SiO_2 and Fe_2O_3 contents determined by XRF. In contrast, the dry-pit slag (DP) presented more intense reflections of calcium-based phases, which corroborates its elevated CaO content.

Figure 11 – Precursors XRD

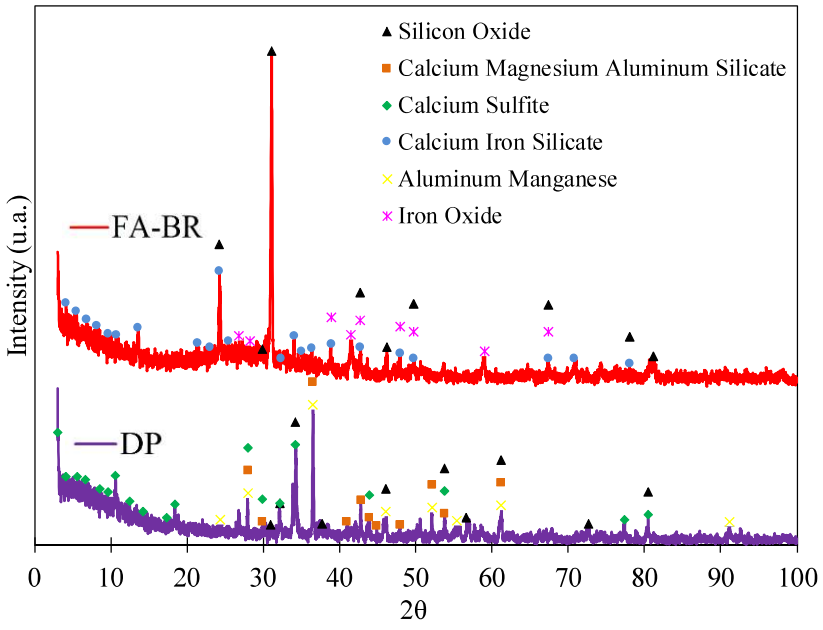

Source: elaborated by the author.

Additionally, the DP pattern displayed a markedly lower amorphous contribution compared to FA-BR, evidenced by the reduced background hump, which reflects its predominantly crystalline nature. As shown in Figure 12, the particle-size distribution curves reveal a clear distinction between the two precursors selected for the validation group. The analysis was performed using a Shimadzu SALD-2300 laser diffraction particle-size analyzer. FA-BR exhibits a finer profile, with characteristic diameters of D10 = 3.6 µm, D50 = 22.7 µm and D90 = 66.1 µm, whereas the DP material presents substantially coarser particles, with D10 = 16.2 µm, D50 = 56.8 µm and D90 = 124.2 µm. In its as-received condition, DP is supplied as a coarse aggregate, requiring mechanical beneficiation prior to use. Ball milling followed by sieving at 150 µm was therefore applied; however, this process showed limited efficiency, with only about 8–10% of the material being converted into fine particles. As a result, the DP precursor retained a comparatively coarser particle size distribution than the other FA-BR.

Figure 12 – Particle size distribution of the precursors

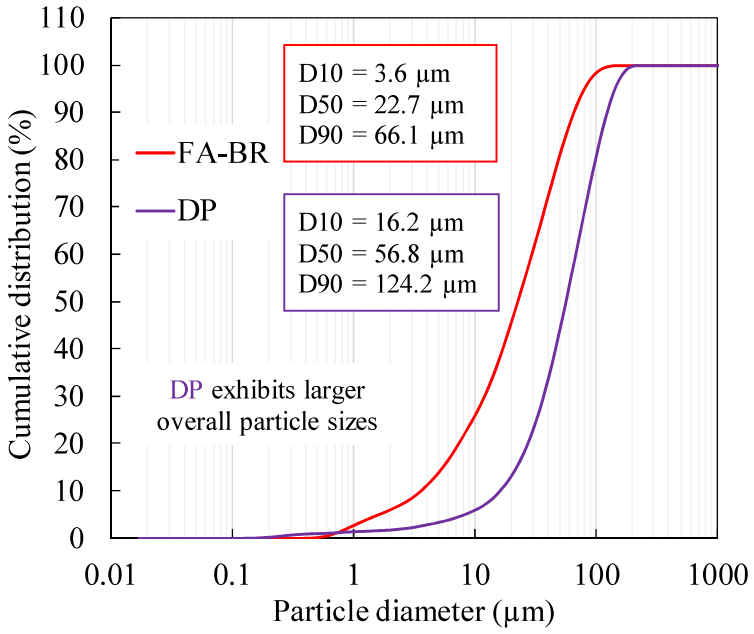

Source: elaborated by the author.

Based on the two precursors characterized, Table 6 presents the 20 binder formulations developed for the validation group. The mixtures were designed by systematically varying key compositional and mix-design parameters, including the relative oxide proportions of the precursors, the S/N, N/B) and W/B. All mixtures were prepared at a controlled temperature of 25 °C. The inclusion of DP is particularly relevant, as none of the data used for training the models contained this type of precursor.

Table 6 – Laboratory validation mix proportion binders

ID	DP-FA	Oxides composition (%)										S/N	N/B (%)	W/B
		Al_2O_3	SiO_2	P_2O_5	SO_3	Cl	K_2	CaO	TiO_2	MnO	Fe_2O_3			
1	**0-100**	15.64	46.80	0.44	1.91	0.03	3.72	8.07	1.77	0.12	21.05	0.75	8%	**0.23**
2	**25-75**	12.33	37.68	0.59	2.62	0.05	2.98	22.52	1.61	0.42	18.81	0.75	8%	**0.23**
3	**50-50**	9.01	28.57	0.74	3.34	0.07	2.24	36.96	1.44	0.72	16.57	0.75	8%	**0.23**
4	**75-25**	5.70	19.45	0.89	4.05	0.09	1.50	51.41	1.28	1.02	14.34	0.75	8%	**0.23**
5	**100-0**	2.38	10.33	1.03	4.76	0.11	0.76	65.86	1.12	1.32	12.10	0.75	8%	**0.23**
6	**0-100**	15.64	46.80	0.44	1.91	0.03	3.72	8.07	1.77	0.12	21.05	0.75	8%	**0.38**
7	**25-75**	12.33	37.68	0.59	2.62	0.05	2.98	22.52	1.61	0.42	18.81	0.75	8%	**0.38**
8	**50-50**	9.01	28.57	0.74	3.34	0.07	2.24	36.96	1.44	0.72	16.57	0.75	8%	**0.38**
9	**75-25**	5.70	19.45	0.89	4.05	0.09	1.50	51.41	1.28	1.02	14.34	0.75	8%	**0.38**
10	**100-0**	2.38	10.33	1.03	4.76	0.11	0.76	65.86	1.12	1.32	12.10	0.75	8%	**0.38**
11	50-50	9.01	28.57	0.74	3.34	0.07	2.24	36.96	1.44	0.72	16.57	**0.25**	8%	0.38
12	50-50	9.01	28.57	0.74	3.34	0.07	2.24	36.96	1.44	0.72	16.57	**0.50**	8%	0.38
13	50-50	9.01	28.57	0.74	3.34	0.07	2.24	36.96	1.44	0.72	16.57	**1.00**	8%	0.38
14	50-50	9.01	28.57	0.74	3.34	0.07	2.24	36.96	1.44	0.72	16.57	**1.25**	8%	0.38
15	50-50	9.01	28.57	0.74	3.34	0.07	2.24	36.96	1.44	0.72	16.57	**1.50**	8%	0.38
16	50-50	9.01	28.57	0.74	3.34	0.07	2.24	36.96	1.44	0.72	16.57	1.00	**4%**	0.38
17	50-50	9.01	28.57	0.74	3.34	0.07	2.24	36.96	1.44	0.72	16.57	1.00	**6%**	0.38
18	50-50	9.01	28.57	0.74	3.34	0.07	2.24	36.96	1.44	0.72	16.57	1.00	**10%**	0.38
19	50-50	9.01	28.57	0.74	3.34	0.07	2.24	36.96	1.44	0.72	16.57	1.00	**12%**	0.38
20	50-50	9.01	28.57	0.74	3.34	0.07	2.24	36.96	1.44	0.72	16.57	1.00	**14%**	0.38

Source: elaborated by the author.

3.3 Methods

Figure 13 illustrates the workflow adopted in this study for developing and evaluating the predictive models.

Figure 13 – Schematic representation of the analysis methodology

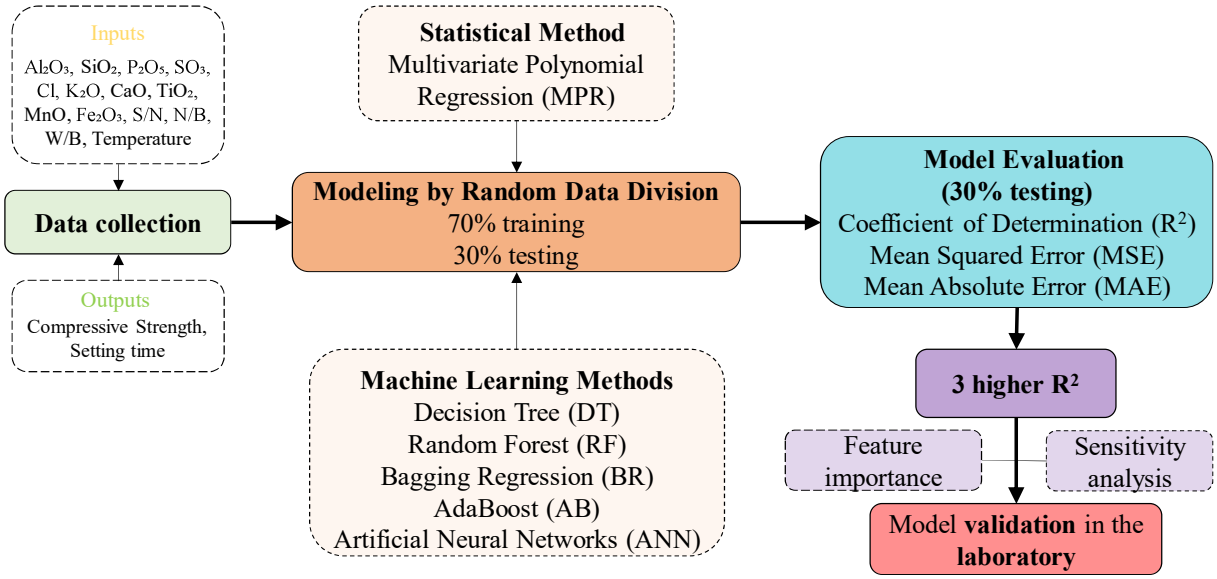

Source: elaborated by the author.

The procedure begins with data collection, followed by the application of a statistical baseline model using Multivariate Polynomial Regression (MPR) and a set of ML algorithms. The dataset is then randomly divided into training (70%) and testing (30%) subsets

to ensure unbiased model assessment, as done by other authors (Han, T. *et al.*, 2022; Hsu *et al.*, 2024; Zhang *et al.*, 2024). Each model is implemented in Python using specialized libraries for statistical analysis and machine learning.

Model performance is evaluated on the testing subset based on the coefficient of determination (R^2), mean squared error (MSE) and mean absolute error (MAE). The three promising models, identified by their higher R^2 values, are further analyzed through feature importance and sensitivity analyses. Finally, the selected models are validated experimentally through laboratory testing to assess their predictive capability under real conditions.

3.3.1 Multivariate Polynomial Regression (MPR)

Polynomial regression extends linear regression by including higher-order terms of the input variables, allowing the model to capture nonlinear effects. For a single predictor, a kth-order (k > 1) can be written as Equation 5 (Su; Zhong; Peng, 2021).

$$\hat{y} = \omega_0 + \omega_1 x + \omega_2 x^2 + \omega_3 x^3 + \cdots + \omega_k x^k \tag{5}$$

Where $\hat{y}$ is the predicted value, x is the input variable, ω_0 is the intercept term, and ω_1, ω_2, ω_3,… ω_k are the regression coefficients for each polynomial term. When extended to multiple predictors, the method becomes multivariate polynomial regression (MPR), which incorporates both power terms and interaction terms (Wei *et al.*, 2016). The kth-order MPR can be expressed in Equation 6.

$$\hat{y} = \omega_0 + \sum_{l_1=1}^{m} \omega_{l_1} x_{l_1} + \sum_{l_1=1}^{m} \sum_{l_2=l_1}^{m} \omega_{l_1 l_2} x_{l_1} x_{l_2} + \cdots + \sum_{l_1=1}^{m} \times \sum_{l_2=l_1}^{m} \cdots \sum_{l_k=l_{k-1}}^{m} \omega_{l_1 l_2 \cdots l_k} x_{l_1} x_{l_2} \cdots x_{l_k} \tag{6}$$

Where $\omega_{l_1}, \omega_{l_1 l_2}, \ldots, \omega_{l_1 l_2 \cdots l_k}$ are the polynomial coefficients and $x_{l1}, x_{l2}, \cdots, x_{lk}$ are the input variables. To determine the coefficients of the equation, the least squares method is applied, based on the database.

3.3.2 Machine learning models

AABs exhibit complex behavior resulting from the strong interaction between chemistry, reaction kinetics, and microstructural evolution, which can be difficult to represent using linear models. Otherwise, machine learning methods are often considered nonlinear because they employ nonlinear transformations, decision rules, or kernel mappings that enable

the capture of complex interactions and non-additive relationships between variables, which cannot be represented by classical linear models (Pilario *et al.*, 2019; Woodman; Mangoni, 2023).

3.3.2.1 Decision Tree (DT)

As supervised learning algorithms, decision tree (DT) is employed in both classification and regression contexts (Karbassi *et al.*, 2014). The Figure 14 represent the regression decision tree structure.

Figure 14 – Regression decision tree structure

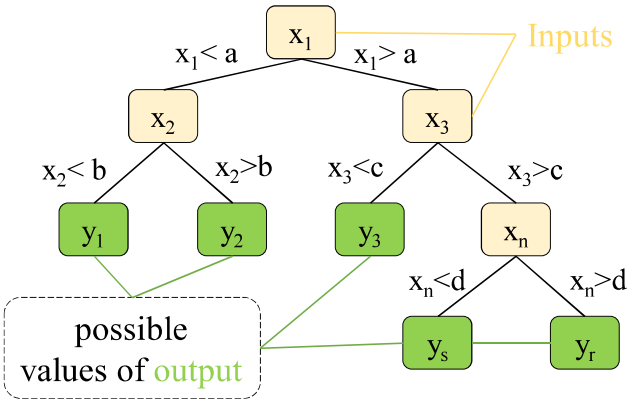

Source: elaborated by the author.

As showed, the DT is organized hierarchically, composed of internal nodes that correspond to predictor attributes, branches that represent the decision rules, and terminal leaves that provide the predicted outcomes (Ahmad *et al.*, 2022). The construction process involves recursively dividing the dataset into increasingly homogeneous subsets, usually guided by impurity criteria such as the Gini index or information gain (Nazar *et al.*, 2024). Data partitioning is executed through decision nodes, whereas the final prediction is assigned at the leaf nodes. However, due to the discontinuous structure of the model, small variations in the input data can produce substantial fluctuations in the predictions, resulting in inefficiencies (Syarif *et al.*, 2012).

3.3.2.2 Random Forest (RF)

Random forest (RF) represents an ensemble-based extension of DTs designed to improve generalization and reduce overfitting (Nazar *et al.*, 2024). The algorithm constructs multiple trees, each trained on a bootstrap sample of the dataset, while random subsets of features are evaluated at each split, and this dual randomization strategy decreases inter-tree correlation and enhances predictive performance (Schonlau; Zou, 2020). Final outputs are

obtained through aggregation, majority voting in classification tasks or averaging in regression tasks, resulting in a model that is more accurate and robust than individual decision trees (Nazar *et al.*, 2024).

3.3.2.3 AdaBoost (AB)

Adaptive Boosting (AdaBoost) is a sequential ensemble technique that iteratively combines multiple weak learners to form a stronger predictive model (Nazar *et al.*, 2024). In this study, AdaBoost was implemented using decision trees as base estimators. During training, higher weights are assigned to samples that are mispredicted, forcing subsequent learners to focus on these harder cases (Ahmad *et al.*, 2022). The outputs of all trees are then aggregated through weighted averaging, with each learner's contribution determined by its accuracy (Ding *et al.*, 2022). This reweighting strategy reduces bias, improves accuracy, and enhances generalization compared to a single decision tree.

3.3.2.4 Bagging Regression (BR)

Bagging Regression (BR) is an ensemble method that constructs multiple bootstrap samples from the dataset, trains a separate model on each subset, and aggregates their outputs by averaging to produce the final prediction (Ahmad *et al.*, 2022). This procedure reduces variance, mitigates overfitting, and enhances model robustness (Sharafati; Asadollah; Al-Ansari, 2021). In this study, BR was implemented with decision trees as base estimators, allowing the ensemble to benefit from their high variance while improving stability through aggregation.

3.3.2.5 Artificial Neural Networks (ANN)

Inspired by the structure and functioning of the human brain, Artificial Neural Networks (ANNs) are computational models designed to recognize complex patterns. The general structure is showed on Figure 15. They consist of interconnected artificial neurons arranged in layers: an input layer, one or more hidden layers, and an output layer (Nazar *et al.*, 2024). Each neuron aggregates several inputs into a weighted sum, incorporates a bias term, and then applies a nonlinear activation (transfer) function to produce a single output (López; López; Crossa, 2022).

Figure 15 – ANN structure

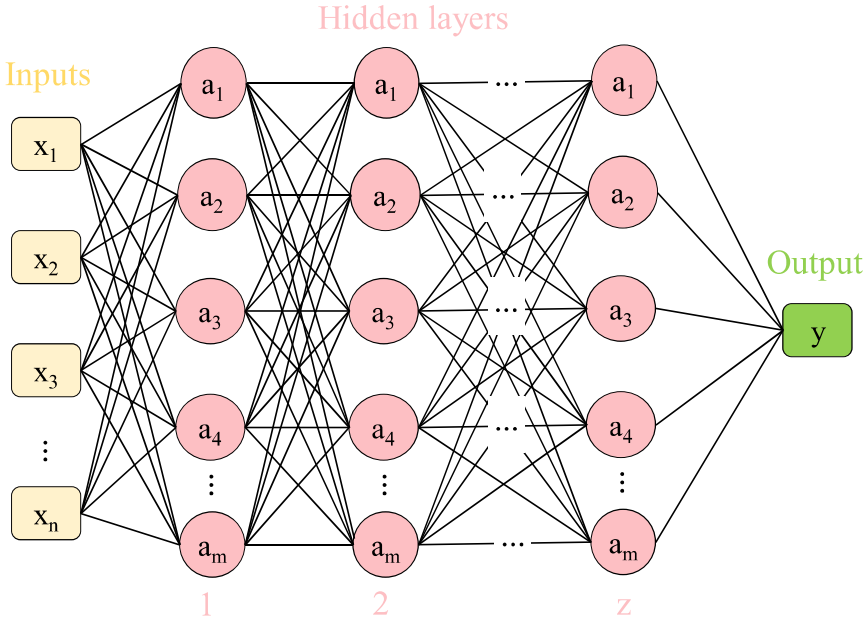

Source: elaborated by the author.

The learning process in ANNs is usually carried out through backpropagation, where weights and biases are updated iteratively to minimize the discrepancy between predicted and observed values (Nazar *et al.*, 2024). This allows the network to learn linear as well as nonlinear dependencies, making it a flexible tool for regression and classification problems. The representational capacity of an ANN depends on its architecture: larger hidden layers or deeper networks increase flexibility but also raise the risk of overfitting, requiring careful parameter design and regularization (Mienye; Swart, 2024). In this research, the ANN was implemented with a Multi-Layer Perceptron (MLPRegressor, scikit-learn). The rectified linear unit (ReLU) activation function and the Adam optimizer were employed.

3.3.3 Parameter's evaluation

To evaluate the predictive performance of the models, three standard statistical metrics were computed using the random test dataset (30% of the total data), as used by other authors (Aydın *et al.*, 2023; Abdullah *et al.*, 2024; Zhang *et al.*, 2024). As decrypted by Abdullah *et al.* (2024) the coefficient of determination (R^2) (Equation 7), the mean absolute error (MAE) (Equation 8) and the mean squared error (MSE) (Equation 9) are the main parameters. These metrics were automatically calculated through Python using the scikit-learn library, ensuring consistency across all evaluated algorithms.

$$R^2 = 1 - \frac{\sum_{i=1}^{m}(\hat{y}_i - y_i)^2}{\sum_{i=1}^{m}(\bar{y}_i - y_i)^2} \quad (7)$$

$$MAE = \frac{1}{m}\sum_{i=1}^{m}|\hat{y}_i - y_i| \quad (8)$$

$$MSE = \frac{1}{m}\sum_{i=1}^{m}(\hat{y}_i - y_i)^2 \quad (9)$$

Where y_i and $\hat{y}_i$ represent the experimental and predicted values, respectively, and $\bar{y}_i$is the mean of the experimental data.

3.3.4 Feature importance

Feature importance was evaluated using a permutation-based approach applied consistently across all machine-learning models. First, the baseline predictive score (R^2) was obtained using the test dataset (Mandler; Weigand, 2024). Then, each input variable was permuted independently while all others were kept unchanged, and the resulting drop in model performance was interpreted as the importance of that feature (Biswas *et al.*, 2024).

For oxide variables (Al_2O_3, SiO_2, CaO, Fe_2O_3), a compositionally-aware permutation was used: after shuffling one oxide, the remaining oxides in the same sample were rescaled proportionally to preserve the original total oxide content, as done by Borgonovo, Plischke, Prieur (2024). Non-compositional parameters (S/N, N/B, W/B) were permuted directly. Each permutation was repeated ten times, and the mean reduction in R^2 was used to generate the final importance ranking.

3.3.5 Sensitivity analysis

Sensitivity analysis was performed using a representative "artificial binder," defined by the average values of the compressive strength dataset. The same binder configuration was used for the setting time sensitivity analysis to maintain consistency between outputs. For each input parameter, its value was independently varied from the minimum to the maximum limits observed in the experimental database.

For the oxide variables, this variation was carried out under a compositional constraint: when one oxide was perturbed, the remaining oxides were proportionally adjusted so that the total oxide sum in each evaluation remained less than or equal to 100%. To avoid model extrapolation, predictions exceeding the upper 90th percentile of the real dataset were excluded from the analysis, corresponding to values above approximately 800 minutes for setting time and 60 MPa for compressive strength.

3.4 Results and discussion

3.4.1 Initial and final setting time

3.4.1.1 Pearson correlation matrix

Figure 16 presents the Pearson correlation matrix, which quantifies the linear association between variables through a coefficient ranging from -1 to 1, where values close to ±1 indicate strong linear relationships (positive or negative trend) and values near zero reflect weak or no linear dependence (Yaseen *et al.*, 2024; Han *et al.*, 2023).

Figure 16 – Pearson correlation matrix for initial and final setting time

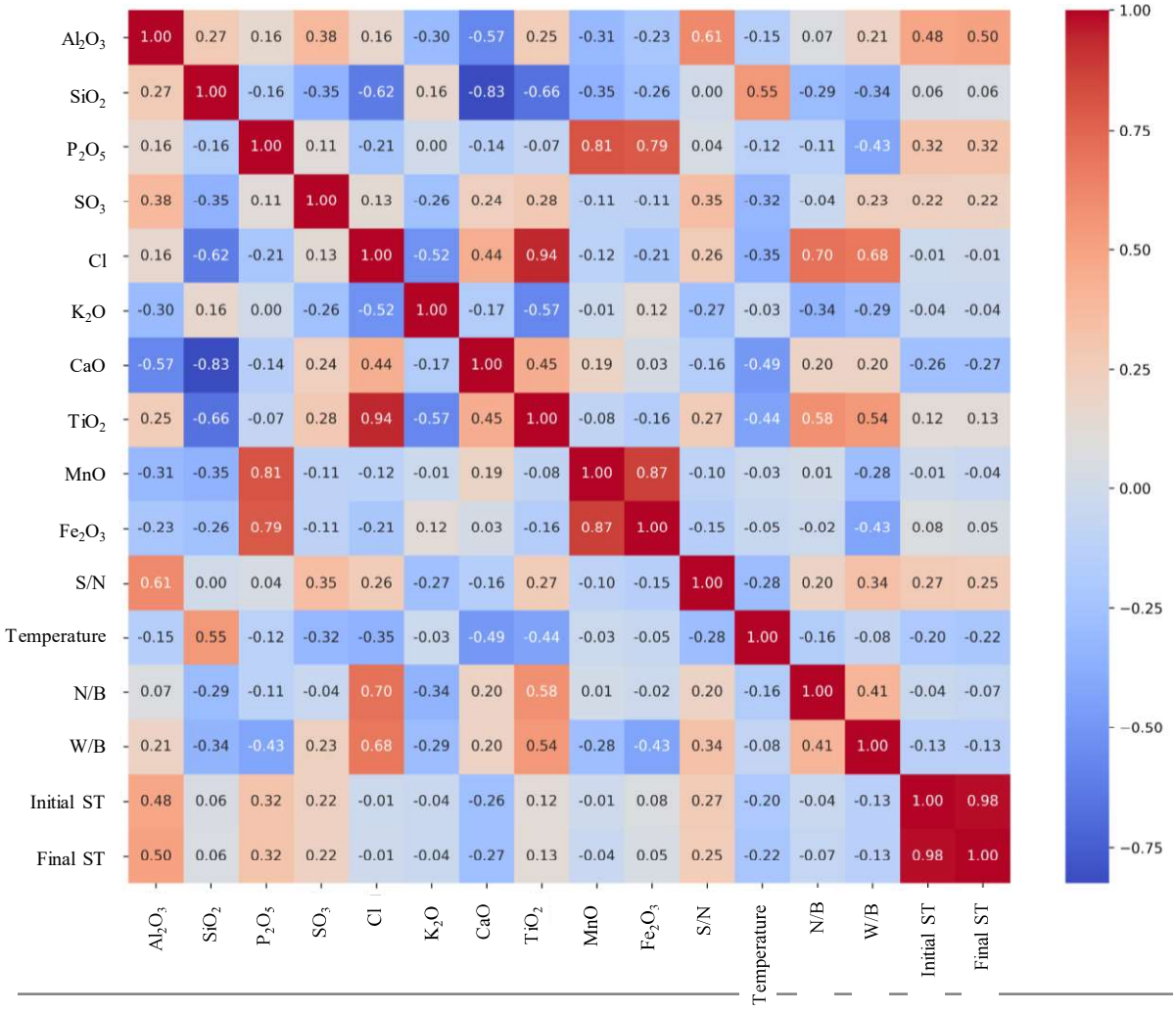

Source: elaborated by the author.

Considering that the Pearson coefficient captures only linear relations, this analysis was conducted as an initial exploratory step to provide a preliminary understanding of variable interactions. Notably, the highest positive correlation reaching 0.50 (Al_2O_3) and the most

negative correlation was -0.27 (CaO), indicating that the relationships between the chemical composition and the setting behavior are generally weak from a linear standpoint. This is similar to the findings of Nofalah *et al.* (2023), who reported weak correlations in polynomial linear prediction models. Even so, some meaningful tendencies can be observed. Al_2O_3, P_2O_5 (0.32) and S/N (0.27) display moderate positive correlations with the initial and final setting time, suggesting as other authors, a delayed in hardening mechanism (Huang, Y. *et al.*, 2024). In contrast, CaO correlates negatively with both outputs (-0.27), reinforcing its role in accelerating early-age reactions due to rapid C-A-S-H gel formation, process already knew in the literature (Provis, 2018; Zhao *et al.*, 2019; Toobpeng; Thavorniti; Jiemsirilers, 2024). SiO_2, Cl, K_2O, MnO, Fe_2O_3 and N/B show weak or negligible correlations within the studied range.

3.4.1.2 Model evaluation

Table 7 presents the evaluation metrics (R^2, MAE, and MSE) obtained for all models tested, as done by other authors in alkali-activated materials (Fang *et al.*, 2018; Nguyen *et al.*, 2020; Abuhussain *et al.*, 2024). Overall, the results reveal substantial variation in predictive performance across algorithms. The MPR model exhibited the lowest accuracy (R^2 = 0.04) and the highest error values (MAE = 164.95 min; MSE = 153,160.90 min^2), indicating that linear-polynomial relationships are insufficient to represent the complex behavior, that is due to highly nonlinear chemical-microstructural interactions (Fang *et al.*, 2018; Nofalah *et al.*, 2023; Abuhussain *et al.*, 2024). The first model parameters for the MPR are presented in Appendix A. Since the model comprises 14 parameters and the polynomial model with degree 5 provided the best performance, it was not possible to include all data; therefore, only the first parameters are presented as an example.

Table 7 – Evaluation parameters setting time

Model	Parameters		
	R^2	**MAE (min)**	**MSE (min^2)**
Multivariate Polynomial Regression (MPL)	0.04	164.95	153160.90
Decision Tree (DT)	0.80	110.07	94181.59
Random Forest (RF) - **2nd higher R^2**	**0.95**	**52.10**	**5928.17**
AdaBoost (AB)	0.87	103.34	30617.52
Bagging Regression (BR) - **3rd higher R^2**	**0.89**	**82.23**	**26649.38**
Artificial Neural Networks (ANN) - **1st higher R^2**	**0.96**	**47.27**	**17199.03**

Source: elaborated by the author.

In contrast, the ANN delivered the best overall performance, achieving the highest average R^2 (0.96) and the lowest MAE (47.27 min), this type of model are repeatedly shown to outperform other ML predicting of alkali-activated materials behavior due to their ability to

capture nonlinearities in multivariate data (Nofalah *et al.*, 2023; Li, Q. *et al.*, 2023; Dodo *et al.*, 2024). Ensemble methods also enhanced predictive capacity, particularly the RF, which achieved the second-highest R^2 (0.95), followed by BR with the third-highest R^2 (0.89), such models are generally effective in capturing the behavior and properties of AABs (Li, Q. *et al.*, 2023; Abuhussain *et al.*, 2024; Khan *et al.*, 2025). Tree-based models showed notable improvement compared to MPR, as illustrated by the DT with $R^2 = 0.80$, whereas AB presented moderate accuracy ($R^2 = 0.87$) but higher prediction errors. Table 8 presents the ANN hyperparameters that yielded the best performance.

The hyperparameters of the tree-based and ensemble models were tested, and the best-performing configurations are reported below. The DT showed optimal performance with a maximum tree depth of 13, no pruning ($\alpha = 0$), 1 sample per leaf, and 2 samples for node splitting. The BR performed best with 150 estimators, using all samples and features. The RF achieved optimal performance with 100 trees, no depth restriction, 1 sample per leaf, and 2 samples for splitting. The AB yielded the best results with a linear loss function, a learning rate of 0.1, and 100 estimators.

Table 8 – ANN hyperparameters initial and final setting time

Parameter	Value
Activation function	relu
Regularization parameter (alpha)	0.0001
Batch size	auto
Adam first moment coefficient (β_1)	0.9
Adam second moment coefficient (β_2)	0.999
Early stopping criterion	FALSE
Numerical stability constant (epsilon)	0.00000001
Hidden layer size(s)	(500, 300, 150)
Learning rate schedule	constant
Initial learning rate	0.001
Maximum number of function evaluations	15000
Maximum number of iterations	1000
Momentum coefficient	0.9
Maximum iterations without improvement	10
Nesterov's momentum	TRUE
Learning rate power parameter (power-t)	0.5
Data shuffling	TRUE
Optimization solver	adam
Convergence tolerance	0.0001
Validation data fraction	0.1

Source: elaborated by the author.

The inherent variability of the Vicat setting time measurement introduces

uncertainty into the dataset, which may affect ML model performance. Because setting time is obtained from discrete measurements at non-fixed intervals, the results are subject to resolution and interpolation errors, particularly near the setting points, potentially increasing prediction dispersion and biasing model sensitivity to input parameters.

These trends are visually consistent with Figure 17, which shows the real versus predicted values for initial and final setting times for each model ((a) MPR, (b) DT, (c) RF, (d) AB, (e) BR, (f) ANN).

Figure 17 – Real vs. predicted values obtained for the initial and final setting time prediction (a) MPL (b) DT (c) RF (d) AB (e) BR (f) ANN

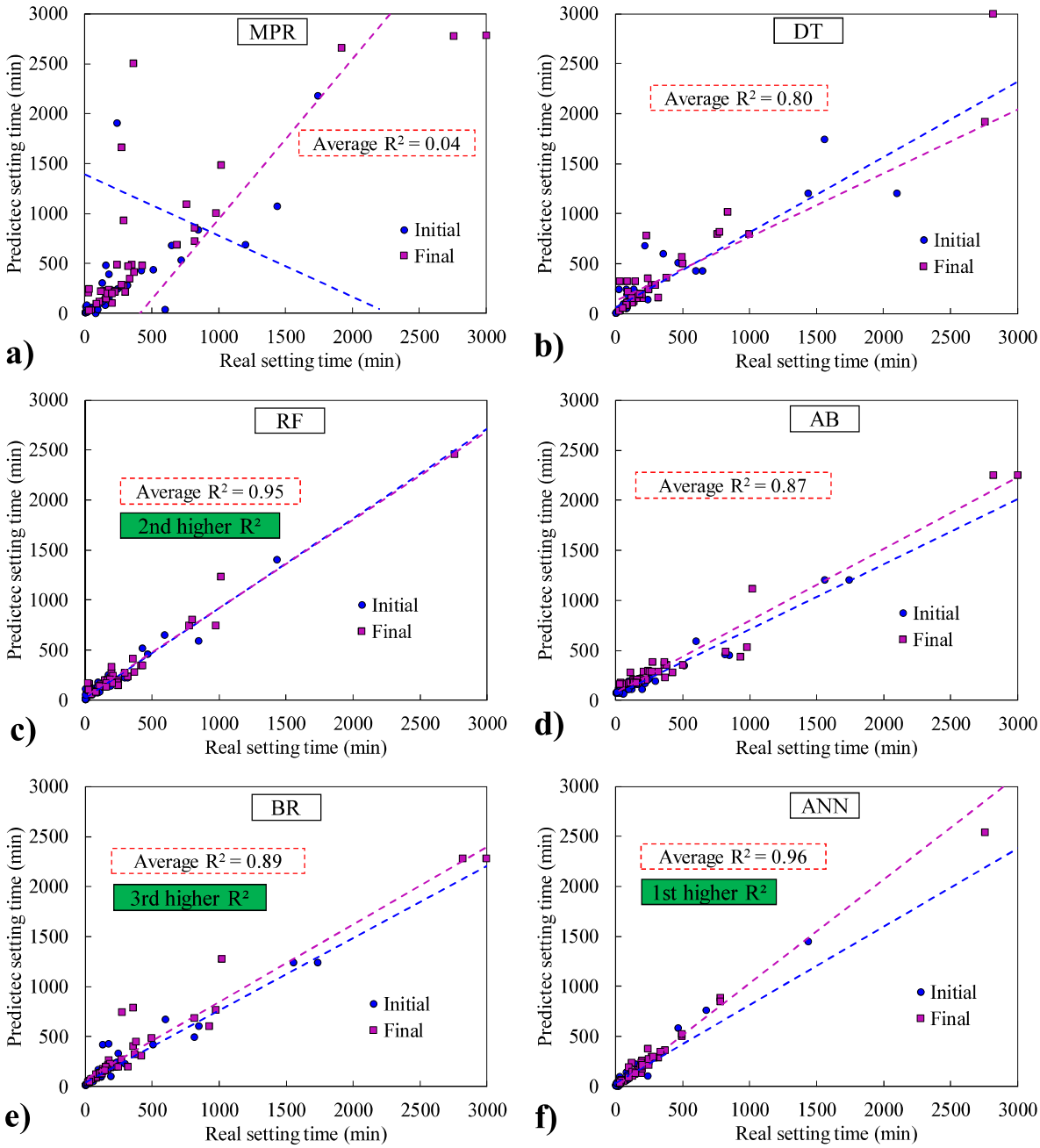

Source: elaborated by the author.

In the best-performing models, particularly the ANN and RF, the scatter points align closely with the 45° reference line, indicating strong agreement between measured and predicted values. Conversely, the MPR plot shows significant dispersion and deviation from the 45° line, visually reinforcing its low predictive accuracy. The intermediate performance of the DT, AB and BR models is also evident in their respective panels, where the point clouds partially align with but still deviate from the ideal trend.

3.4.1.3 Feature importance three higher R^2

Figure 18 illustrates the normalized feature importance values obtained from the ANN models. The variables were ranked according to their relative influence on the ANN predictions, with importance values normalized from 0 to 1. The N/B ratio emerges as the most dominant parameter (1.00), followed by SiO_2 (0.76), P_2O_5 (0.60), and K_2O (0.58). Temperature appears at the lower end of the ranking (0.07), indicating a comparatively minor effect within the temperature range represented in the dataset.

Interestingly, some variables traditionally associated with strong control of setting kinetics exhibit relatively modest importance in the ANN. For example, CaO typically accelerates setting through the rapid formation of C-A-S-H or hybrid C-(N)-A-S-H phases (Provis, 2018; Qin *et al.*, 2022b; Xu, X. *et al.*, 2024). Yet in this dataset CaO shows a moderate importance rather than being among the dominant variables. A similar pattern is observed for Al_2O_3, which plays a well-established structural role in gel formation but appears with low importance (Gong; White, 2023).

Figure 18 – Feature importance ANN

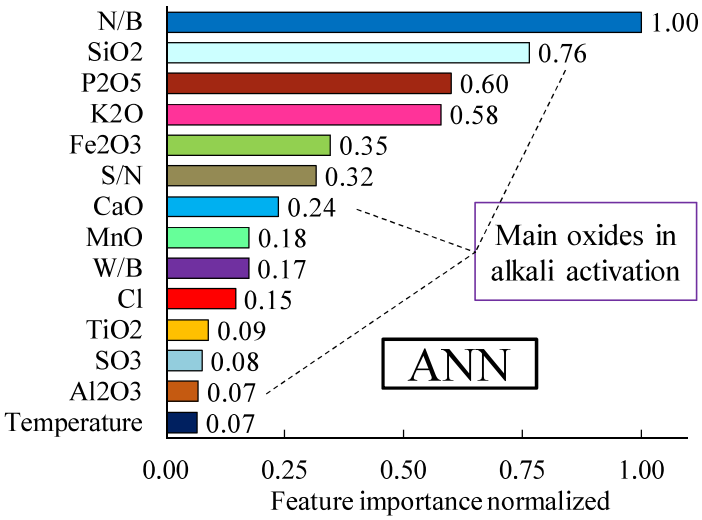

Source: elaborated by the author.

In contrast, the ANN attributes the highest sensitivity to the N/B ratio, which is

consistent with the fact that alkalinity strongly affects the rate of precursor dissolution and early gel formation (Mohamed, 2023; Siyal *et al.*, 2024). The high importance of SiO_2 and P_2O_5 is also chemically meaningful. Soluble silica enhances crosslinking and increases the rate of polycondensation (Provis, 2018).While P_2O_5 is reported to modify gel connectivity and reaction pathways, depending on concentration and precursor chemistry (Prochon; Piotrowski; Kępniak, 2024).

Figure 19a presents the normalized feature-importance values obtained from the RF model for setting time prediction. The RF identifies SiO_2 as the most influential variable (1.00), followed by CaO (0.33), Al_2O_3 (0.22), and N/B (0.18). Moderate but lower importance is observed for S/N (0.05), whereas all other parameters, including TiO_2, Cl, Fe_2O_3, W/B, SO_3, P_2O_5, K_2O, MnO, and temperature display negligible contributions (<0.01). Figure 19b shows the results obtained from the BR model, which exhibit a very similar pattern, reflecting the shared decision-tree architecture of both methods (Abdullah *et al.*, 2024). BR likewise emphasizes SiO_2 (1.00), Al_2O_3 (0.80), and N/B (0.53) as dominant parameters, followed by a secondary influence of CaO (0.18) and S/N (0.12), while all remaining variables contribute minimally (<0.01). Despite architectural differences from the ANN, both tree-based models (RF and BR) converge with the ANN in some points, these observations are in agreement with prior studies (Hoayek *et al.*, 2023; Ngo; Nguyen; Tran, 2023). All models consistently identify SiO_2 and N/B as central predictors of setting time, reinforcing their relevance in dissolution, early gel formation, and polycondensation kinetics (Siyal *et al.*, 2024). Similarly, all three models attribute very low importance to variables such as SO_3, TiO_2, Cl, MnO, and temperature.

Figure 19 – Feature importance (a) RF and (b) BR

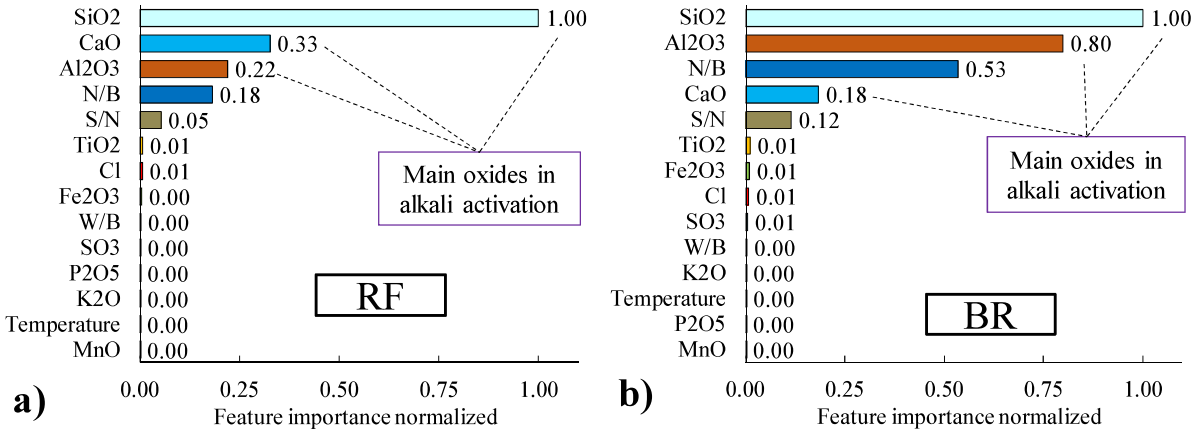

Source: elaborated by the author.

However, notable distinctions emerge when comparing tree-based models with the ANN. While the ANN places N/B as the single most dominant parameter, RF and BR give

higher prominence to SiO_2 and, to varying degrees, to CaO and Al_2O_3. From a chemistry perspective, the prominence of this oxides in tree-based models is consistent with their known roles in controlling setting kinetics, as discussed previously.

3.4.1.4 Sensitivity analysis three higher R^2

As described in the methodology, the sensitivity analysis was performed using an artificial binder, characterized by the average values of all input parameters. Each parameter was then individually varied around this baseline to evaluate its specific influence on the setting time. The detailed sensitivity analysis was performed for selected key parameters, as shown in Figure 20: (a) Al_2O_3, (b) SiO_2, (c) CaO, and (d) P_2O_5. The first three oxides were chosen due to their fundamental roles in alkali-activated binder chemistry. In addition, P_2O_5 was included because it exhibited high importance in the ANN feature importance analysis.

For Al_2O_3 (Figure 20a), all three models exhibit a similar qualitative trend, though with different magnitudes. At low alumina contents, the predicted initial and final setting times remain relatively stable, with minimal differences between models. RF and BR begin to show a progressive increase after approximately 15 wt%, whereas the ANN displays this transition only at higher contents, around 33 wt%. In all cases, elevated Al_2O_3 concentrations produce a sharp rise in setting time, indicating that higher alumina levels significantly retard the setting process. This behavior is consistent with recent literature showing that elevated alumina contents reduce precursor dissolution and lower early reaction heat, thereby delaying gel nucleation and extending the setting time, particularly under low Si/Al ratios (Zhong *et al.*, 2022; Guo *et al.*, 2025). Chemically, Marvila, Azevedo and Vieira (2021) explained that high-alumina systems generate abundant AlO_4^- tetrahedra, which slow condensation when the supply of charge-balancing alkalis (Na^+, K^+) is insufficient.

Figure 20b presents the sensitivity analysis for SiO_2. The ANN exhibits a steep decrease in setting time as SiO_2 increases from low levels, followed by a prolonged region of minimal values at intermediate contents and a gradual rise at higher SiO_2 percentages. In contrast, the RF and BR models display smoother curves with moderate variability across the entire SiO_2 range, maintaining higher predicted setting times than the ANN. At low silica contents, all models predict delayed setting, with the ANN showing the strongest increase in setting time. This trend is chemically expected: low silicate availability limits the supply of polymerization nuclei, slowing the formation of Si-O-Al bonds and delaying network percolation (Kaze *et al.*, 2018; Lahlou Nouha *et al.*, 2019). At higher silica contents, all models

eventually predict slower setting, though the ANN shows this reversal more clearly. This behavior is also supported by experimental research. Silica-rich activators retard setting due to diffusion barriers and over-polymerized silicate species (Dineshkumar; Umarani, 2020; Han, Q. *et al.*, 2022).

Figure 20 – Sensitivity analysis precursor oxides (a) Al_2O_3 (b) SiO_2 (c) CaO and (d) P_2O_5

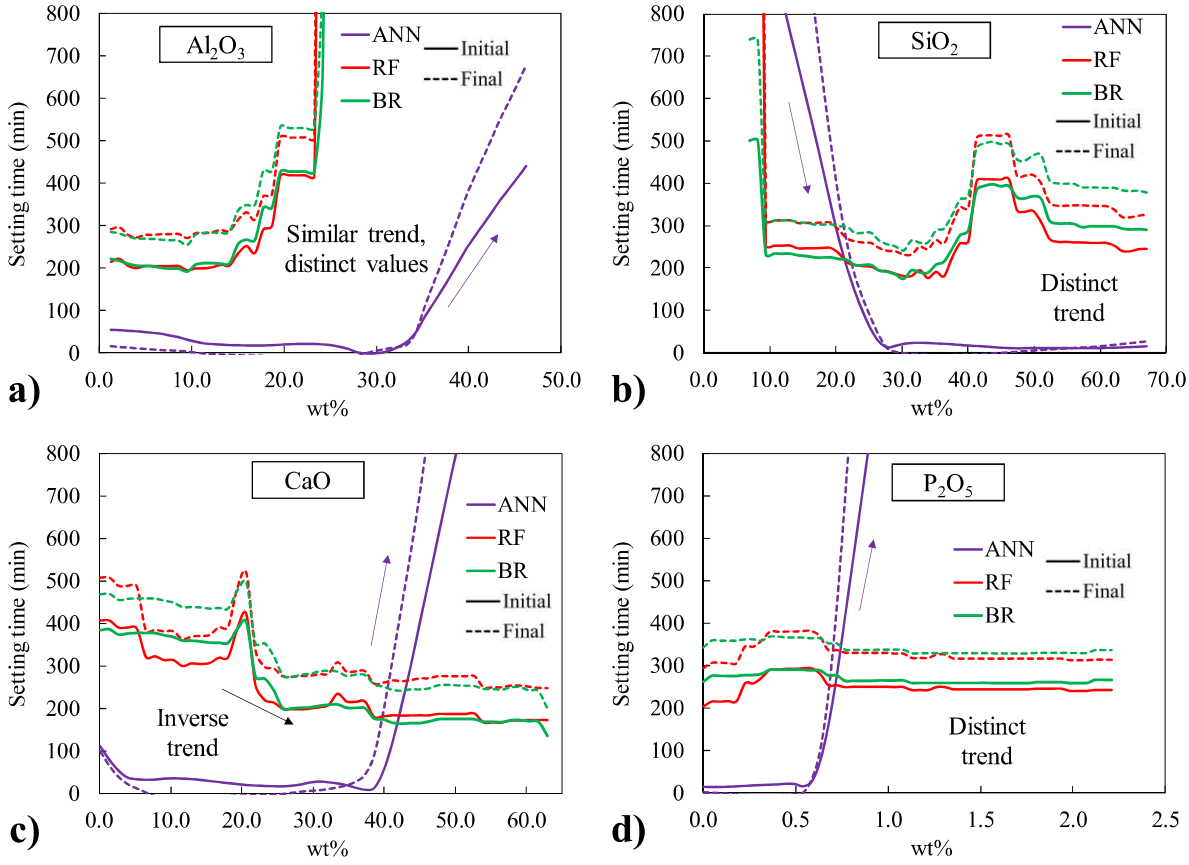

Source: elaborated by the author.

Figure 20c presents the sensitivity analysis for CaO. The ANN displays a distinct nonlinear pattern with sharp variations at both low and high CaO levels. In that case, the RF and BR models capture the most chemically coherent trend: setting time decreases as CaO content increases, indicating faster hardening. Extensive evidence confirms that higher CaO availability accelerates early-age reactions through rapid nucleation of C-A-S-H and hybrid C-(N)-A-S-H gels, which form much more quickly than the aluminosilicate N-A-S-H networks typical of low-calcium systems (Provis, 2018; Kusumastuti; Ariati; Atmaja, 2020; Siyal *et al.*, 2024).

The Figure 20d shows the variation of setting time with P_2O_5 content. The ANN model exhibits a distinct upward trend, with both initial and final setting times remaining low up to approximately 0.5 wt% before increasing sharply beyond this point. In contrast, the RF

and BR models display relatively stable behavior. Based on the available literature, no studies have isolated the independent effect of P_2O_5 content on the setting time of AABs. But are a few relevant studies investigating phosphate-based geopolymers (Djobo; Stephan, 2021; Yankwa Djobo; Nkwaju, 2021; Zribi; Baklouti, 2021). In these studies, the reaction behavior is governed not by the bulk P_2O_5 content but especially the P/Al molar ratio and the reaction mechanism. For example, Zribi and Baklouti (2021) provided a detailed kinetic and mechanistic analysis of metakaolin-phosphoric acid geopolymers, showing that the early-age evolution is controlled by a sequence of dealumination, condensation, and polycondensation reactions, but they did not perform any setting time analysis.

Figure 21 presents the sensitivity analysis for the main activator parameters (a) S/N, (b) N/B and (c) W/B. Their effects on AABs are among the most extensively explored in the literature. The Figure 21a shows the influence of the S/N. The ANN model remains at very low values up to approximately 1.5, after which both initial and final setting times increase sharply. In contrast, the RF and BR models remain comparatively stable across the entire S/N range. Across multiple studies, increasing the S/N consistently leads to longer setting times (Adewumi *et al.*, 2021; Kaze *et al.*, 2021; Dai *et al.*, 2022a; Sun *et al.*, 2024). Sun *et al.* (2024) and Huo *et al.* (2024) reported delays in slag systems due to reduced pH and slower dissolution at high silicate contents. Considering this consistent experimental evidence, the ANN model provides the most chemically plausible prediction.

Figure 21 – Sensitivity analysis activator parameters (a) S/N (b) N/B and (c) W/B

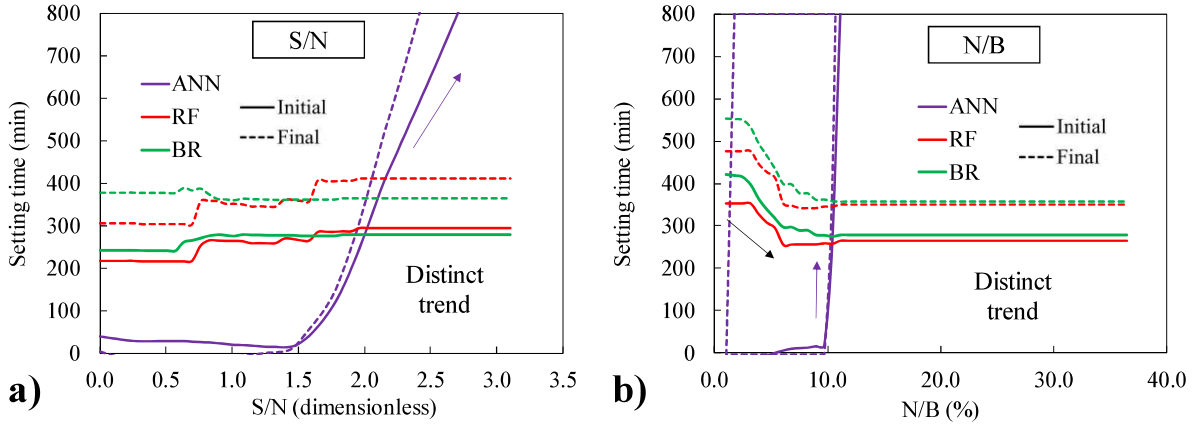

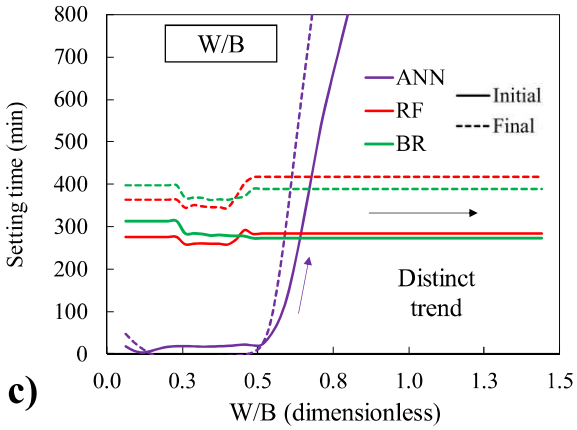

Source: elaborated by the author.

Figure 21b shows the influence of N/B. The ANN model stays very low until around 10%, then increases sharply, while the RF and BR models decrease, and then remain mostly stable across the range. Multiple works have shown that increasing N/B accelerates dissolution and geopolymerization, resulting in shorter setting times (Liu *et al.*, 2020; Naqi *et al.*, 2022; Tekle; Holschemacher, 2022). In this case, the RF and BR models align more closely with the trends reported in the literature.

Figure 21c shows the influence of W/B. The ANN model remains at very low values up to approximately 0.5, after which both initial and final setting times rise sharply. In contrast, the RF and BR models stay mostly stable across the entire W/B range. Numerous studies show that increasing W/B dilutes the activator and slows geopolymerization, leading to longer setting times at higher water contents (Dai *et al.*, 2020; Liu *et al.*, 2020; Yusslee; Beskhyroun, 2023). For the authors, this effect occurs because the excess free water reduces the effective contact between the precursor and activator, substantially delaying the hardening process.

Figure 22 presents the sensitivity analysis for the remaining parameters: (a) SO_2, (b) Cl, (c) K_2O, (d) TiO_2, (e) MnO, (f) Fe_2O_3, and (g) Temperature. A detailed analysis for each parameter is not discussed here; however, it can be observed that the RF and BR models produce very similar and closely aligned trends, indicating consistent behavior. In contrast, the ANN model deviates noticeably across all cases, showing distinct sensitivity patterns compared to the ensemble-based models.

Figure 22 – Sensitivity analysis others parameters (a) SO_2 (b) Cl (c) K2O (d) TiO_2 (e) MnO (f) Fe_2O_3 and (g) Temperature

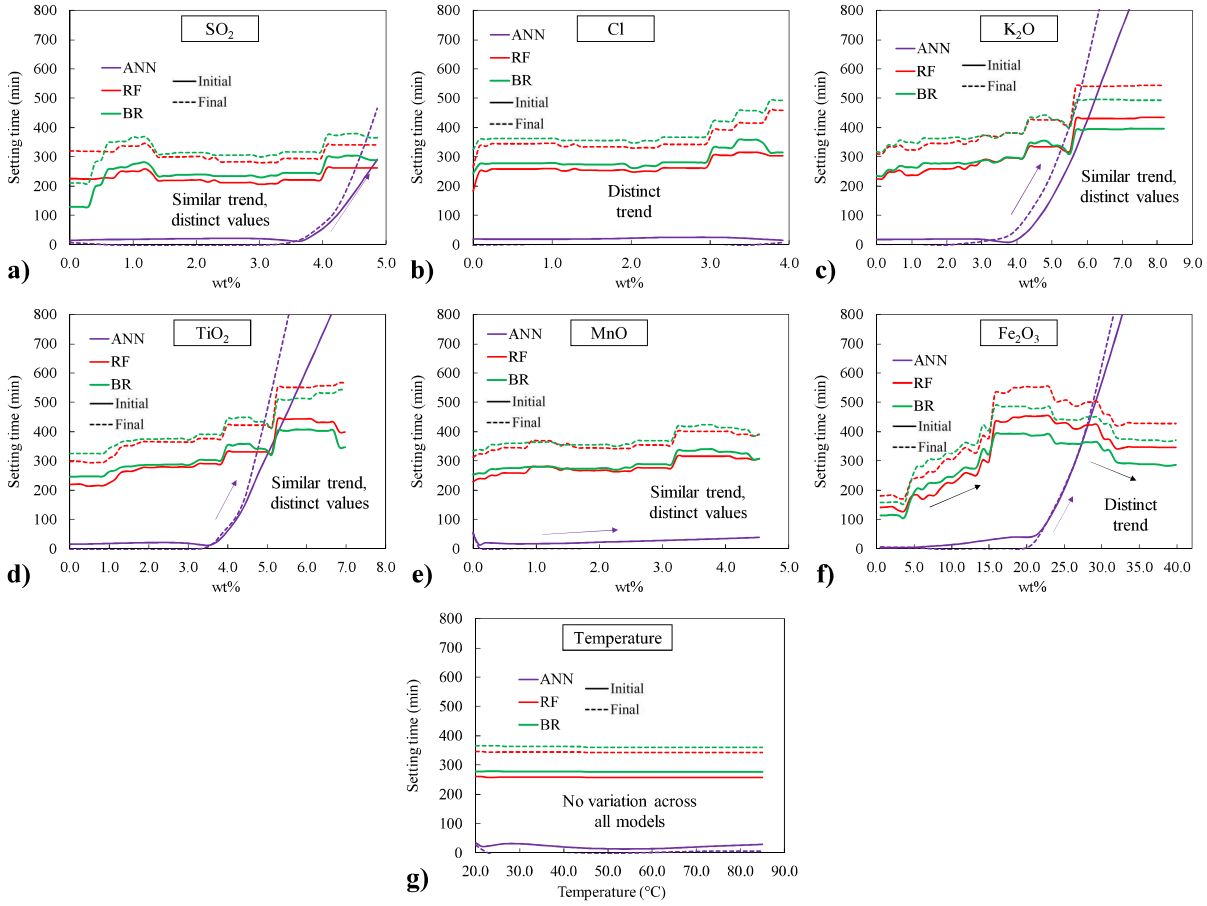

Source: elaborated by the author.

The sensitivity analysis reveals that the ANN model exhibits nonlinearity and extrapolation sensitivity, particularly when predicting outside the range of experimental data. For parameters such as P_2O_5 content and N/B, the ANN shows a sharp and unrealistic increase in setting time beyond approximately 0.55 wt% P_2O_5 and 10% N/B, respectively. This behavior likely stems from the scarcity of training data in those regions, causing the ANN to overfit and generate unstable predictions outside the calibrated domain. In contrast, the RF and BR models display much more stable and flattened trends beyond these limits. This difference can be attributed to the tree-based decision structure of the RF model and the regularization inherent in BR, both of which limit sensitivity to out-of-range inputs.

3.4.1.5 Laboratory validation

The laboratory validation using the dry-pit/fly ash AAB formulations provides a robust external test of the models, since these mixtures were not included in the training or testing dataset. The Figure 23 shows the results to initial setting time prediction. As expected,

the RF and BR models show very similar predictions. For the oxide-based formulations, the ANN reproduces the experimental trend at low setting times but deviates substantially when the mixtures fall outside the chemical space represented in the training data, resulting in a high global Mean Absolute Error (611 min). In contrast, RF and BR follow the general trend of the laboratory results, although with different magnitudes, and yield lower, yet still considerable errors (170, 166 min), especially when compared with their internal model errors calculated for the original dataset (52.10 for RF, 82.23 for BR, and 47.27 for ANN).

Figure 23 – Laboratory and model-predicted dry-pit binders' initial setting time results

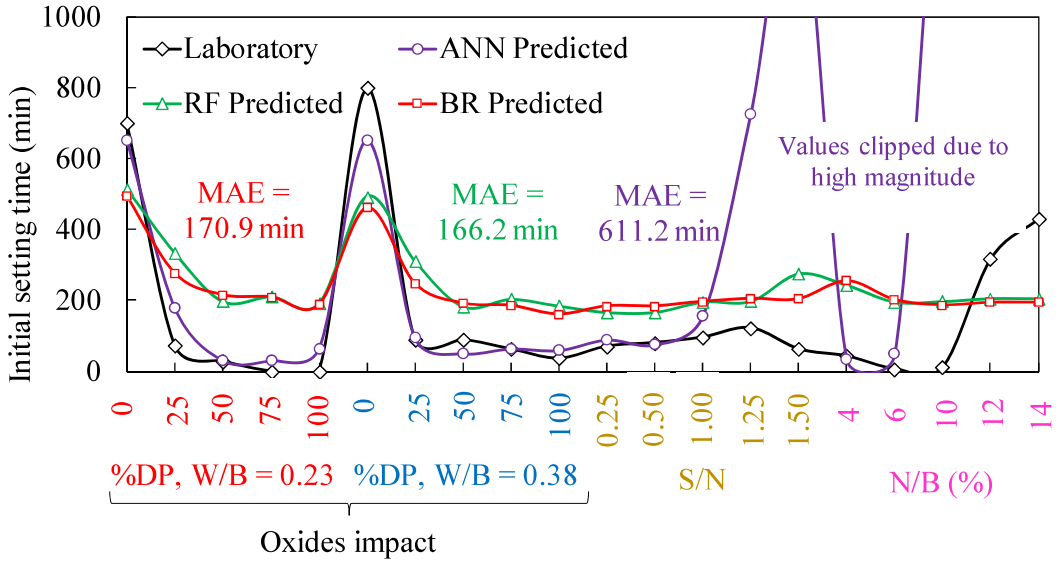

Source: elaborated by the author.

In resume, the ANN captures the nonlinear transitions observed experimentally, but becomes unstable at extreme values of S/N (>1.25) and N/B (>10%), likely due to the limited number of samples in these regions during training. Crucially, when these overfitted regions are excluded, the ANN's MAE drops dramatically from 611.2 min to 40.3 min, demonstrating that the network is highly accurate within its valid chemical range (S/N < 1.25 and N/B < 10%).

The Figure 24 it presents the final setting time results, the same behavior observed for initial setting. RF and BR remain stable, with moderate errors (193.0 and 198.7 min) and trends that generally follow the laboratory data. The ANN, however, becomes highly unstable outside its trained domain, generating very large errors (1234.4 min) and even negative final setting time predictions at high S/N and N/B values due to severe extrapolation. When these out-of-range points are removed, the ANN MAE drops sharply to 88.1 min, confirming that the model performs well within its valid chemical limits but must not be applied beyond them (S/N < 1.25 and N/B < 10%).

Figure 24 – Laboratory and model-predicted dry-pit binders' final setting time results

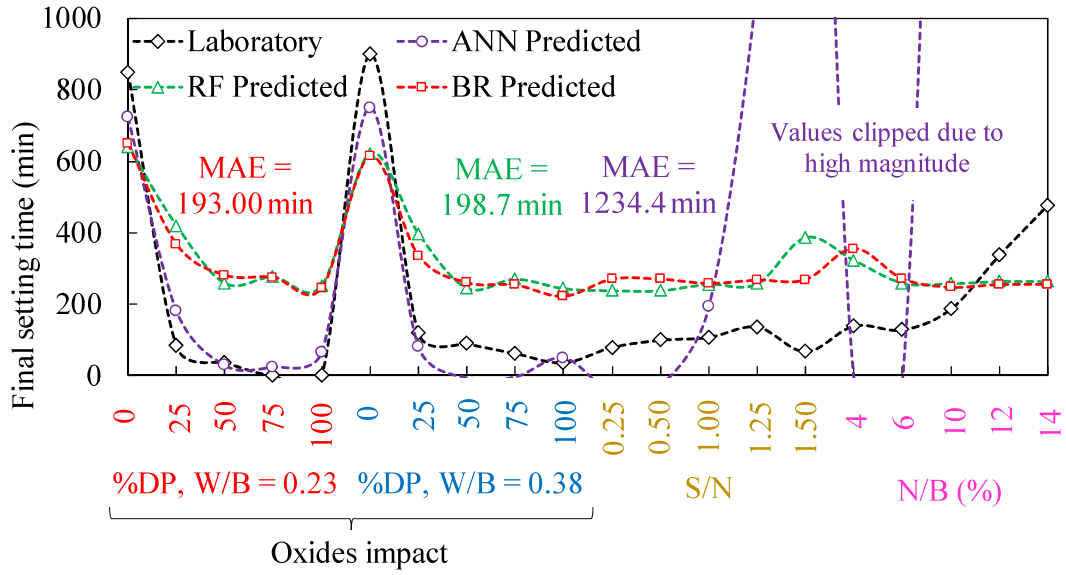

Source: elaborated by the author.

3.4.2 Compressive Strength

3.4.2.1 Pearson correlation matrix

Figure 25 presents the Pearson correlation matrix for compressive strength. Overall, the correlations between individual parameters and compressive strength are weak, indicating limited linear predictability. The highest positive correlation is 0.16 for CaO, suggesting only a slight tendency for strength to increase with higher calcium content. Conversely, the strongest negative correlations are -0.24, for Al_2O_3 and for N/B, implying a modest reduction in compressive strength when alumina proportion or alkali dosage increases. These low coefficients are consistent with previous findings that linear models perform poorly when describing mechanical development in AABs (Shah *et al.*, 2022).

Figure 25 – Pearson correlation matrix for initial compressive strengths

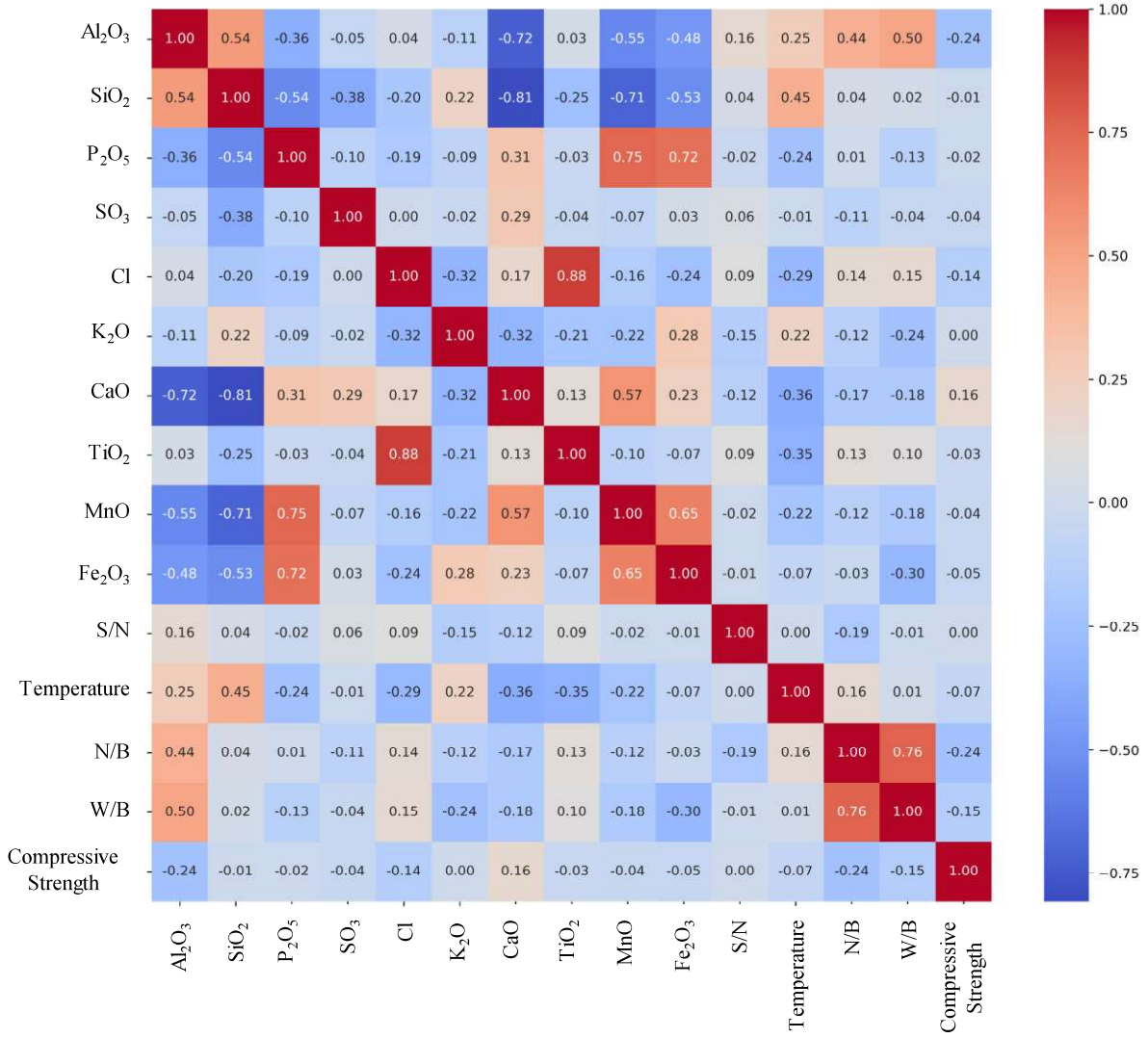

Source: elaborated by the author.

Other parameters, including SiO_2, P_2O_5, SO_3, Cl, K_2O, TiO_2, MnO, Fe_2O_3, S/N, W/B and temperature display near-zero correlations, further reinforcing that compressive strength emerges from complex, nonlinear interactions among composition, activator chemistry, and reaction kinetics, rather than simple linear relations. Some authors demonstrated that linear relationships were more evident when the model considered only the precursor category (e.g., fly ash, steel slag), without integrating chemical characterization into the inputs (Ahmed *et al.*, 2022; Ngo; Nguyen; Tran, 2023; Garcia *et al.*, 2024).

3.4.2.2 Model evaluation

Table 9 presents the evaluation metrics (R^2, MAE, and MSE) for all models applied to compressive strength prediction. Similar results were found when predicting setting time, where the same group of models showed the highest accuracy. The results show clear

differences in predictive capability across algorithms. The MPR model exhibits moderate performance ($R^2 = 0.74$) but relatively high errors (MAE = 7.99 MPa; MSE = 104.48 MPa²).

Table 9 – Evaluation parameters compressive strength

Model	Parameters		
	R^2	MAE (MPa)	MSE (MPa^2)
Multivariate Polynomial Regression (MPL)	0.74	7.99	104.48
Decision Tree (DT)	0.88	5.19	47.16
Random Forest (RF) - **2nd higher R^2**	**0.90**	**4.97**	**35.49**
AdaBoost (AB)	0.68	8.77	108.65
Bagging Regression (BR) - **3rd higher R^2**	**0.89**	**4.95**	**36.60**
Artificial Neural Networks (ANN) - **1st higher R^2**	**0.96**	**3.12**	**16.52**

Source: elaborated by the author.

The model parameters for the MPR are presented in Appendix B. Since the polynomial model with degree 2 provided the best performance, all parameter data are included. The ANN model achieved the best overall performance, reaching the highest R^2 (0.96) and the lowest error values (MAE = 3.12 MPa; MSE = 16.52 MPa²). This aligns with earlier compressive strength studies demonstrating that ANNs reliably surpass other methods in capturing the complex multivariate behavior of AABs (Bai *et al.*, 2023; Ngo; Nguyen; Tran, 2023; Katatchambo; Bingöl, 2025). Table 10 presents the ANN hyperparameters that yielded the best performance.

Table 10 – ANN hyperparameters compressive strength

Parameter	Value
Activation function	relu
Regularization parameter (alpha)	0.0001
Batch size	auto
Adam first moment coefficient (β_1)	0.9
Adam second moment coefficient (β_2)	0.999
Early stopping criterion	FALSE
Numerical stability constant (epsilon)	0.00000001
Hidden layer size(s)	(500, 300, 150)
Learning rate schedule	constant
Initial learning rate	0.001
Maximum number of function evaluations	15000
Maximum number of iterations	1000
Momentum coefficient	0.9
Maximum iterations without improvement	10
Nesterov's momentum	TRUE
Learning rate power parameter (power-t)	0.5
Data shuffling	TRUE
Optimization solver	adam
Convergence tolerance	0.0001
Validation data fraction	0.1

Source: elaborated by the author.

Ensemble methods also performed strongly: RF obtained the second-highest R^2

(0.90) with MAE = 4.97 MPa, while BR achieved the third-highest R^2 (0.89) and MAE = 4.95 MPa. The hyperparameters of the tree-based and ensemble models were evaluated, and the best-performing configurations are reported below. The DT achieved optimal performance with a maximum tree depth of 13, no cost-complexity pruning ($\alpha = 0$), a minimum of 2 samples per leaf, and 2 samples required for node splitting. The RF performed best with 100 trees, a minimum of 1 sample per leaf, and 2 samples for node splitting, with no restriction on maximum tree depth. The AB yielded the best results using a learning rate of 1 and 100 estimators. Finally, the BR achieved optimal performance with 200 estimators, using all samples and all features for training. Overall, the performance hierarchy for compressive strength mirrors the results obtained for setting time, with ANN > RF > BR > DT > MPR > AB, confirming the consistent superiority of ANN and ensemble models across different AAB behaviors.

A similar pattern can be observed in Figure 26, which compares the experimental compressive strength to the predicted values for each model ((a) MPR, (b) DT, (c) RF, (d) AB, (e) BR, (f) ANN). The highest-performing algorithms, most notably ANN and RF, display point distributions that lie very close to the 45° reference line.

Figure 26 – Real vs. predicted values obtained for the compressive strength (a) MPL (b) DT (c) RF (d) AB (e) BR and (f) ANN

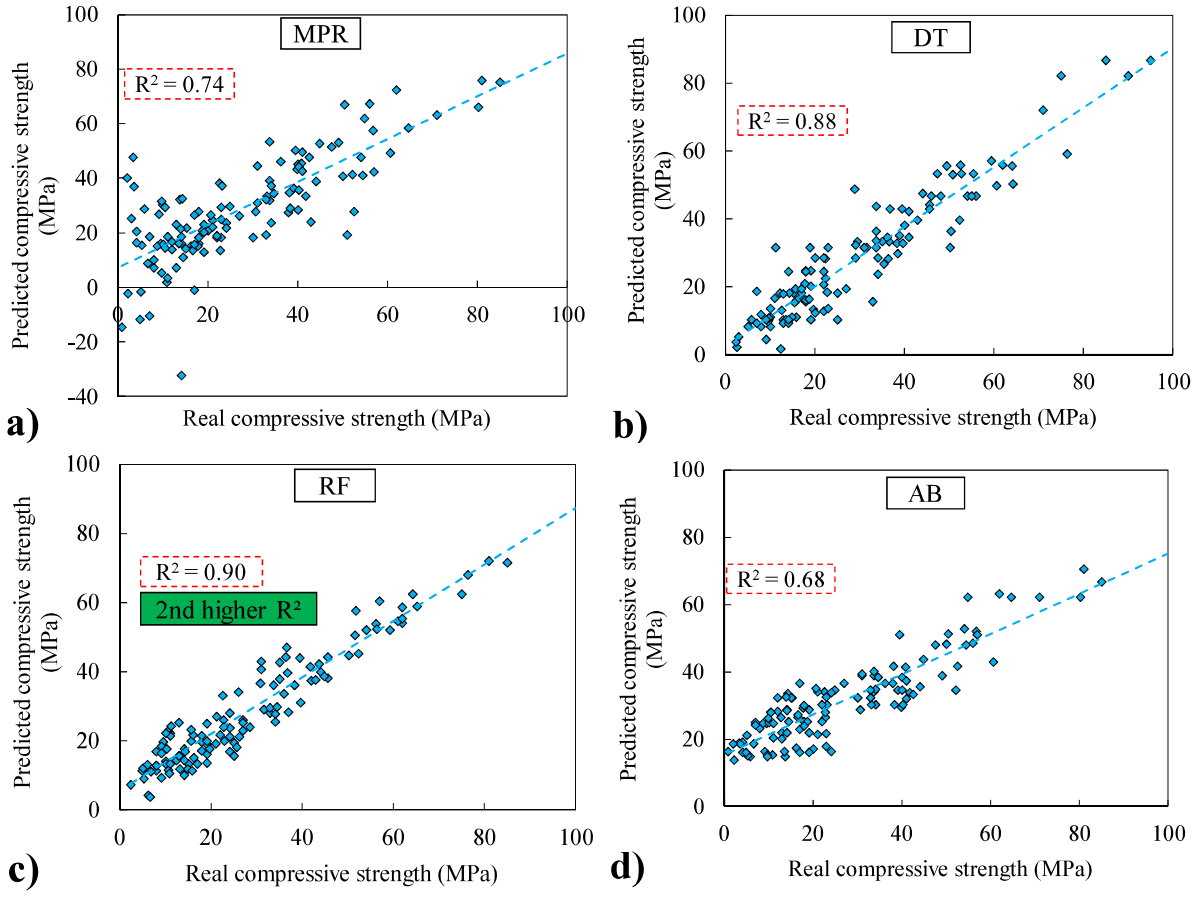

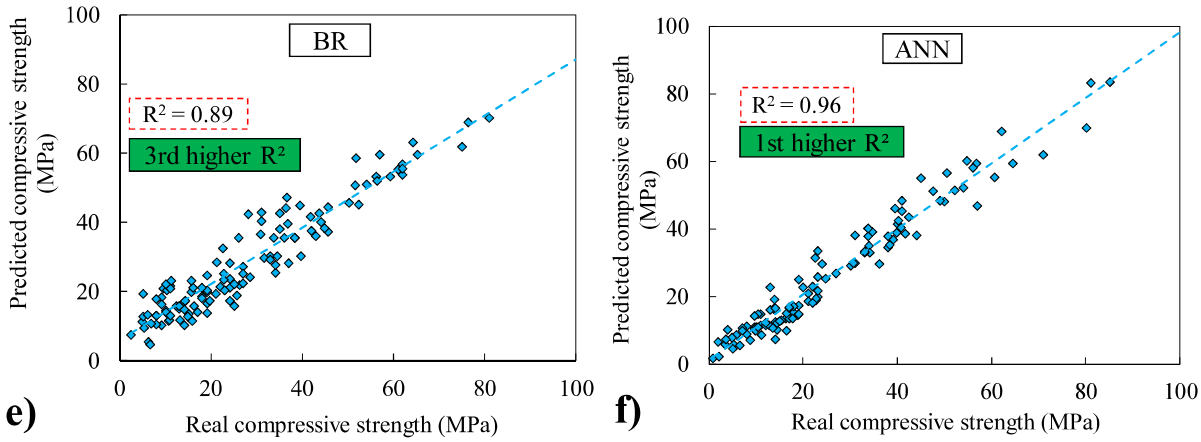

Source: elaborated by the author.

In contrast, the MPR panel reveals a broad scatter and clear divergence from the ideal line, highlighting its limited ability to capture the nonlinear behavior of AAB strength development (and with negative values in compressive strength). The DT, AB, and BR models demonstrate intermediate performance: although their point clusters generally follow the correct trend, the spread around the bisector line remains more pronounced, indicating reduced predictive precision relative to ANN and RF.

3.4.2.3 Feature importance three higher R^2

Figure 27 presents the normalized feature importance values obtained from the ANN model for compressive strength prediction. Chloride (Cl) is identified as the most influential parameter (1.00), followed by CaO (0.82), Fe_2O_3 (0.59), and TiO_2 (0.56). A second group of variables with intermediate influence includes temperature (0.29), N/B (0.25), SiO_2 (0.24), W/B (0.23), and Al_2O_3 (0.20). The parameters P_2O_5, SO_3, K_2O, and MnO show low importance (< 0.12). Several interesting patterns emerge from these results. CaO appears as the second most influential feature, which is consistent with its central role in promoting rapid reaction kinetics and forming calcium-rich binding phases that strongly enhance compressive strength. In contrast, SiO_2 and Al_2O_3, typically considered the primary structural oxides in geopolymer gel formation, appear with only moderate importance in this dataset. This suggests that their isolated effect on strength becomes less dominant when other strong contributors such as Ca, Fe, and Ti are present.

An unexpected outcome of the ANN feature importance analysis is the extremely high influence assigned to chloride (Cl). Although Cl is not usually considered a primary precursor component in AABs, but recent studies show that chloride can modify strength development, the effect depends on the content (Siddique; Jang, 2020; Zulkarnain *et al.*, 2021;

Yang *et al.*, 2022; Shen *et al.*, 2023). However, the elevated importance observed here may be influenced by the highly skewed and low-variability distribution of Cl in the dataset (Figure 10), as suggested by its relative frequency, which could bias feature-importance metrics and potentially amplify its apparent relevance (Nascimento; Cavalcanti; Costa-Abreu, 2025). A more comprehensive assessment of the influence of chloride will be addressed in the sensitivity analysis presented in the next section.

Figure 27 – Feature importance to compressive strength ANN model

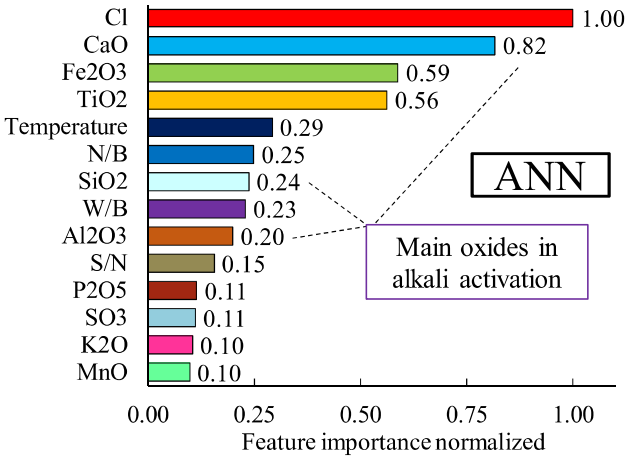

Source: elaborated by the author.

The prominence of Fe_2O_3 in the ANN is less unexpected. Evidence from iron-rich precursors shows that high Fe_2O_3 levels tend to shift the chemistry away from highly polymerized aluminosilicate networks. Nkwaju *et al.* (2023), working with lateritic soils containing ~45% Fe_2O_3, reported that such systems develop lower compressive strength because iron promotes the formation of less cohesive Fe-silicate phases. Similar observations appear in studies using industrial residues rich in iron, reinforcing the notion that iron does not participate as effectively as Al in building a robust three-dimensional network (Mishra *et al.*, 2022; Polydorou *et al.*, 2022; Nkwaju *et al.*, 2023).

Figure 28(a–b) shows that the RF and BR models produced very similar importance rankings. In both models, CaO emerges as the dominant variable, followed by Fe_2O_3 and SiO_2. These three parameters clearly form the core chemical indicators for strength prediction in the tree-based approaches. Secondary contributors such as S/N, Al_2O_3, and TiO_2 present moderate importance values. Unlike the ANN model, which placed Cl among the most influential variables, both RF and BR rank chloride at the very bottom of the feature hierarchy, together with K_2O and P_2O_5. Overall, RF and BR display a consistent and chemically intuitive pattern, emphasizing oxide-driven reactivity based on CaO, SiO_2, Al_2O_3, and also the Fe_2O_3.

Figure 28 – Feature importance to compressive strength models (a) RF and (b) BR

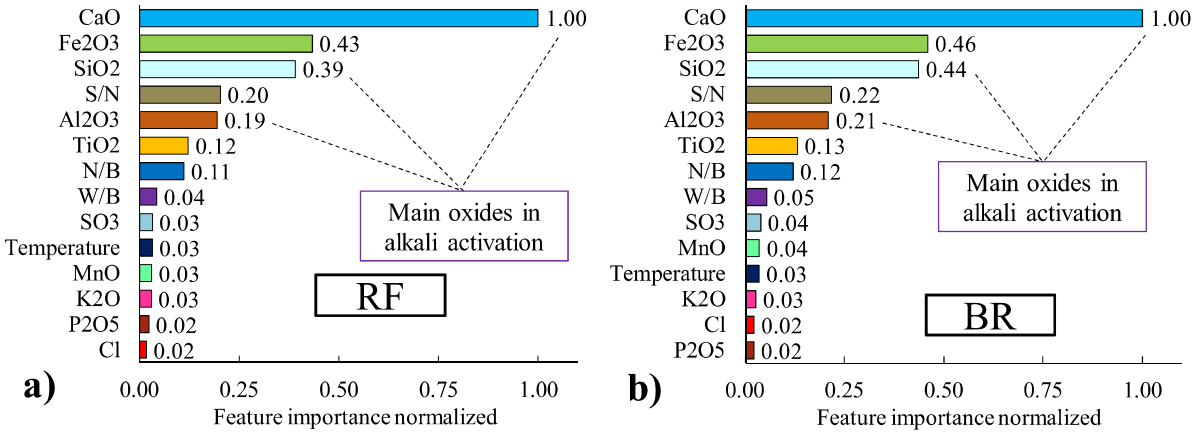

Source: elaborated by the author.

3.4.2.4 Sensitivity analysis three higher R^2

Figure 29 shows the sensitivity analysis for the precursor parameters (a) Al_2O_3, (b) SiO_2, (c) CaO, and (d) Cl. The first three oxides were selected because they are consistently reported in the literature as the main components in AABs. Chloride was included due to its unexpectedly high importance in the ANN feature importance. The Al_2O_3 (Figure 29a) sensitivity curve shows that the ANN model exhibits a marked variation, reaching its lowest predicted strength near 15 wt% before increasing steadily at higher contents. Meanwhile, the RF and BR models maintain nearly constant predictions. The effect of Al_2O_3 on compressive strength is rarely evaluated in isolation, instead, its influence is primarily interpreted through SiO_2/Al_2O_3 (Si/Al) ratio trends (Ali; Al-Attar; Abbas, 2022; Dinh *et al.*, 2024). Experimental studies consistently show that optimal mechanical performance occurs at balanced Si/Al ratios, where moderate Al availability enhances cross-linking and promotes the formation of well-connected aluminosilicate gels (Wu *et al.*, 2020; Guo *et al.*, 2025; Zhang, G. *et al.*, 2025). Thus, the effect is non-monotonic, which is more consistent with the ANN model.

Figure 29b shows the effect of SiO_2 content on compressive strength. RF and BR predict nearly constant and higher strength values, indicating a weak influence of SiO_2, while the ANN curve remains lower and shows only slight nonlinearity. Similarly, to Al_2O_3, the effect of SiO_2 is governed by chemical interactions that often produce non-monotonic trends. Consequently, the ANN demonstrates better sensitivity to this behavior, evidenced by the maxima and minima captured in its output.

Figure 29 – Sensitivity analysis to precursors parameters (a) Al_2O_3 (b) SiO_2 (c) CaO and (d) Cl

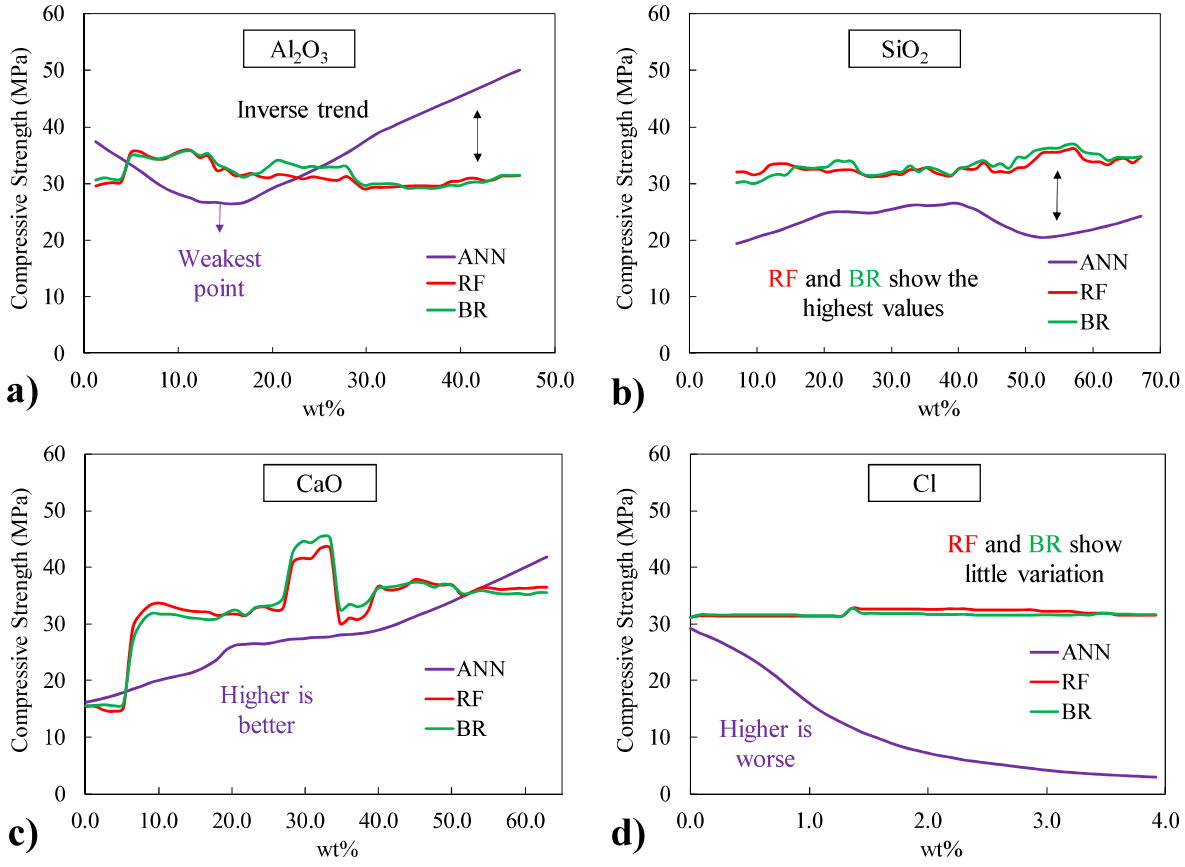

Source: elaborated by the author.

Figure 29c shows that increasing CaO generally raises compressive strength. RF and BR capture a sharp strength increase around 25-35 wt% and predict the highest values, while the ANN shows a smoother but consistent upward trend. Overall, the literature demonstrates a nonlinear effect of CaO on compressive strength. Moderate CaO enhances reaction kinetics and promotes the formation of dense hybrid C-A-S-H/N-A-S-H gels, leading to higher strength, however, when CaO content exceeds the optimal range, the aluminosilicate network is disrupted due to rapid precipitation, and increased porosity, resulting in reduced strength (Görhan; Danishyar, 2022; Zhan *et al.*, 2022; Zerzouri *et al.*, 2024).

Figure 29d shows the effect of Cl content on compressive strength. RF and BR predict almost no variation across the range, while the ANN model displays a clear decrease in strength as chloride increases. Shen *et al.* (2023) demonstrated that small NaCl additions (~2%) can increase early compressive strength of slag-based geopolymers by nearly 67%, attributing this to accelerated condensation of aluminosilicate species and the formation of zeolitic structures. Similar results was found by other authors (Siddique; Jang, 2020; Yang *et al.*, 2022). As a counterpoint, Zulkarnain *et al.*, (2021) showed that the effect of chloride is highly dose-dependent, beneficial at low contents but detrimental at higher levels. Despite these findings, it

is important to note that almost all available studies evaluate chloride in the form of NaCl or $CaCl_2$, or through chloride-rich solutions such as seawater. Consequently, the isolated contribution of the chloride ion itself is difficult to determine, since the accompanying cation (Na^+ or Ca^{2+}) also alters dissolution behavior, ionic balance, and gel chemistry. The apparent importance of chloride in the ANN model may stem from its uneven distribution, as about 90% of the data points are below 0.04%. Such imbalance can distort the model's assessment of its global relevance. If consider that the literature indicates an optimal chloride content, none of the models capture this variation.

Figure 30 shows the sensitivity analysis of the activator parameter (a) S/N (b) N/B and (c) W/B. Figure 30a show a nonlinear relationship between S/N and compressive strength.

Figure 30 – Sensitivity analysis to activators parameters (a) S/N (b) N/B and (c) W/B

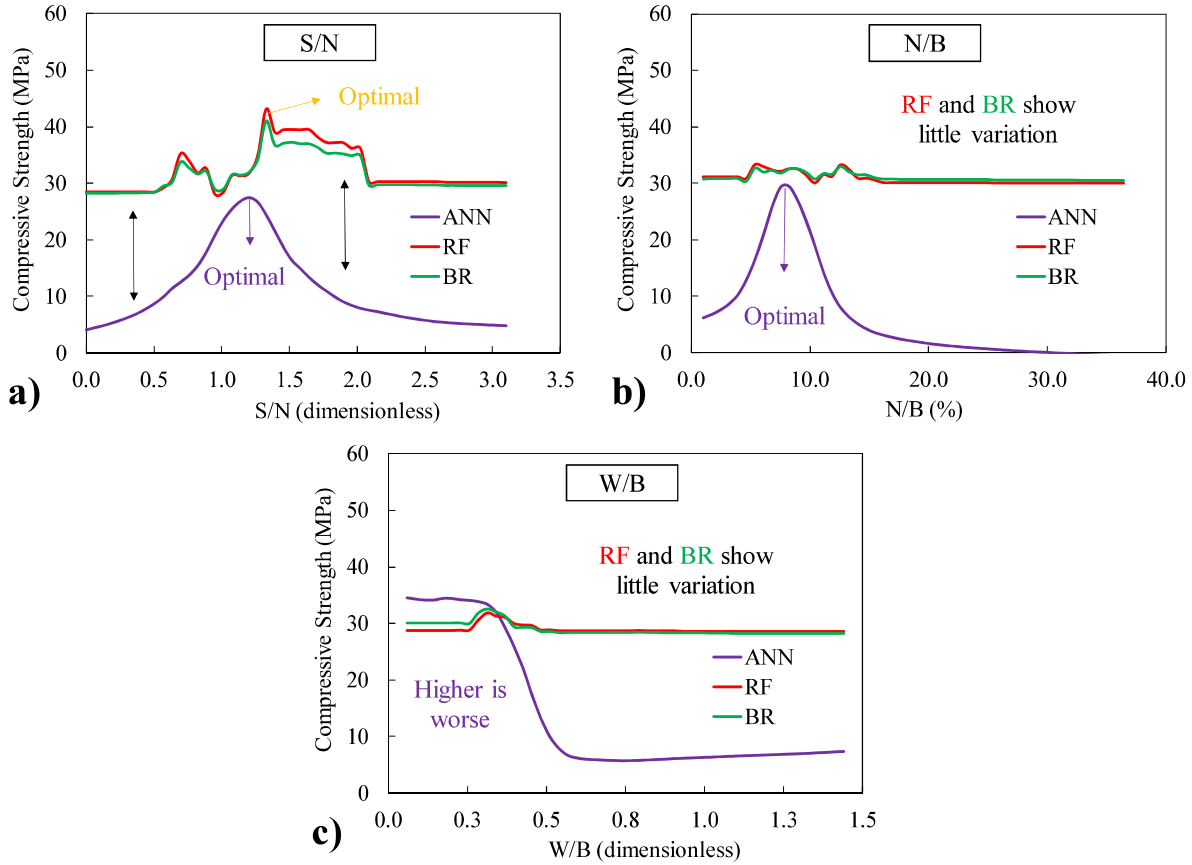

Source: elaborated by the author.

Many studies identify an optimal S/N range, where soluble silica promotes stronger and denser C-A-S-H/N-A-S-H gels (Gado *et al.*, 2020; Ukritnukun *et al.*, 2020; Adewumi *et al.*, 2021; Gao *et al.*, 2021). However, this optimum is not universal, it varies with other formulation parameters, especially precursor type. The ANN, RF, and BR curves all reflect this general nonlinear behavior.

Figure 30b presents the N/B results. As with S/N, the literature indicates that N/B does not follow a universal trend but instead shows an optimum that varies with precursor type (Leong *et al.*, 2016; Xu *et al.*, 2023; Wang, Xiaoping *et al.*, 2024). For this reason, the ANN is better able to capture the associated nonlinear response. Figure 30c shows the effect of the W/B on compressive strength. The RF and BR models predict almost no variation in strength. In contrast, the ANN model shows a strong negative trend. The negative trend is consistent with the material behavior, where higher W/B ratios reduce compressive strength because excess water increases porosity in the hardened matrix (Al-Husseinawi *et al.*, 2022; Teo *et al.*, 2022; Pham *et al.*, 2023). Based on this, the ANN model looks more consistent with the expected behavior.

Figure 31 presents the sensitivity analysis for the remaining parameters: (a) P_2O_5, (b) SO_3, (c) K_2O, (d) TiO_2, (e) MnO, (f) Fe_2O_3, and (g) temperature. Although each case is not discussed in detail here, it is evident that the RF and BR curves remain very close to each other and generally stable across the evaluated ranges, indicating low sensitivity in these models. In contrast, the ANN model shows much greater variability, displaying fluctuations and distinct response patterns for each parameter, which suggests a higher sensitivity to these inputs compared with the ensemble-based models.

Figure 31 – Sensitivity analysis to others parameters (a) P2O5 (b) SO3 (c) K2O (d) TiO2 (e) MnO (f) Fe2O3 and (g) Temperature

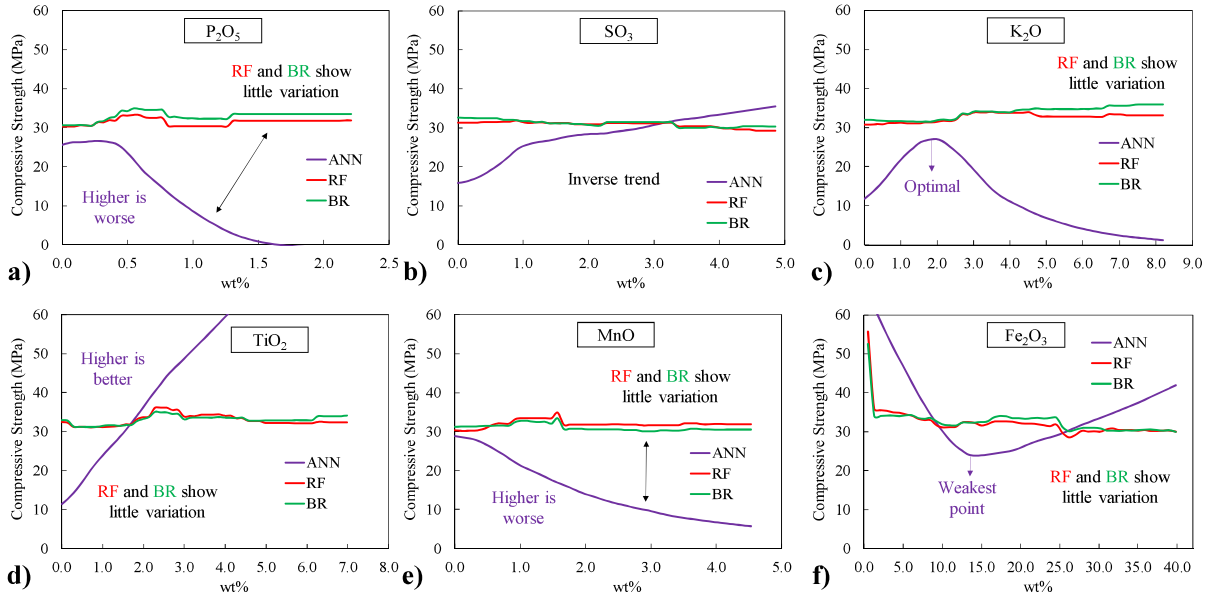

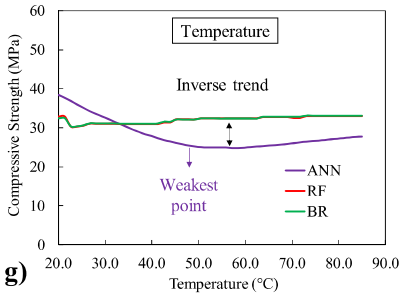

Source: elaborated by the author.

3.4.2.5 Laboratory validation

Figure 32 presents the laboratory compressive strength results for the dry-pit binders alongside the predictions generated by the ANN, RF, and BR models. The three models exhibit similar predictive patterns, and in several regions, they follow the general tendency of the experimental curve, although not in numerical terms. Among them, the ANN model shows the lowest error (MAE = 21.2 MPa), followed by RF (23.9 MPa) and BR (26.2 MPa); however, these error values are still considerably high, indicating that the models did not perform well in predicting the compressive strength for this specific dataset.

Figure 32 – Dry-pit binders compressive strength results in laboratory and model predicted

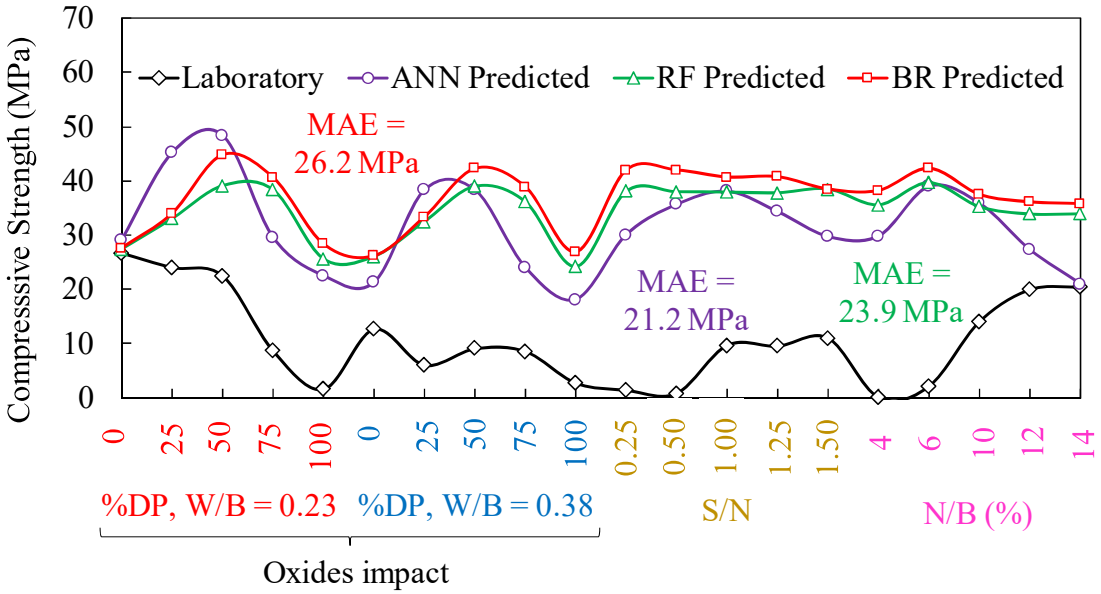

Source: elaborated by the author.

Given that the dry-pit binders exhibited low compressive strength and unsatisfactory predictive performance, additional experimental data from the literature were incorporated to further assess the behavior of the models under alternative formulation conditions. For this purpose, the dataset reported by Liu *et al.* (2020) was selected, as it includes AABs based on landfilled fly ash (LFA) and ground-granulated blast-furnace slag (GGBS) with higher strength levels and parameters variability. Figure 33 presents the laboratory compressive

strength results from this reference dataset together with the predictions obtained from the ANN, RF, and BR models. In this case, the models reproduce the experimental trends more closely, with the ANN achieving the lowest prediction error (MAE = 5.8 MPa), followed by RF (24.4 MPa) and BR (26.0 MPa).

Figure 33 – Liu *et al*. (2020) compressive strength results and model predicted

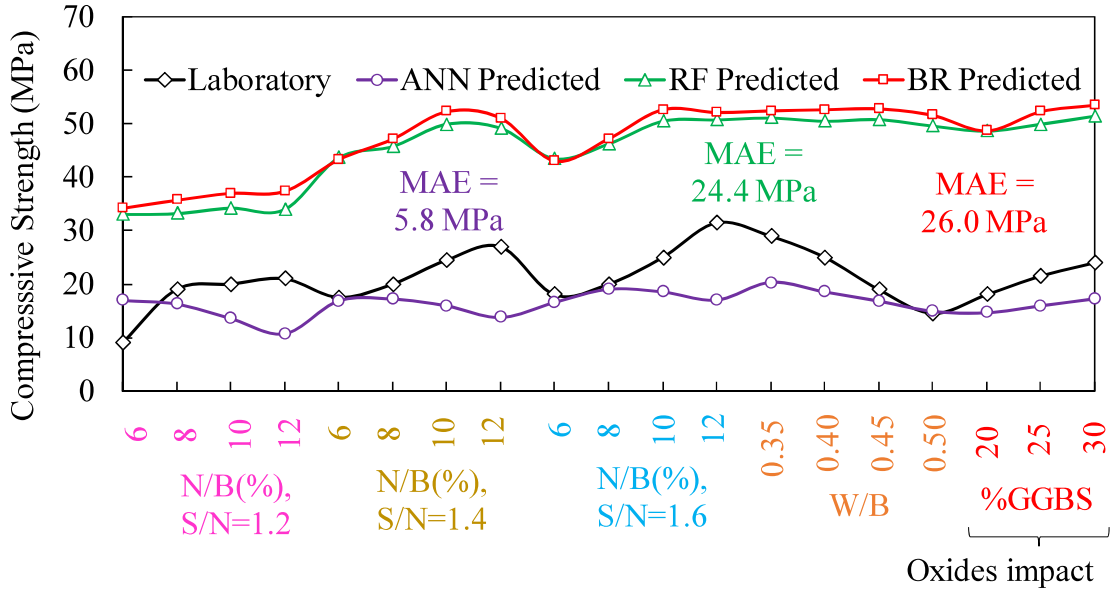

Source: elaborated by the author.

A similar procedure was applied to an additional reference dataset reported by Sachet *et al.* (2020), which includes AABs with varying proportions of ground granulated blast-furnace slag (GGBFS). Figure 34 presents the corresponding laboratory results alongside the predictions models. In this dataset, the ANN again demonstrates the best predictive performance (MAE = 11.4 MPa), capturing the increasing trend in compressive strength as the GGBFS content rises. In contrast, the RF and BR models exhibit substantially higher errors (45.6 MPa and 45.2 MPa, respectively) and fail to reproduce the experimental strength evolution, remaining almost constant over most of the range.

The difference in predictive performance between the dry-pit binders and the literature datasets (Liu *et al.*, 2020; Sachet *et al.*, 2020) can be hypothesized to arise from material characteristics not represented in the oxide-based inputs used in the models. The XRD results suggest that the dry-pit precursor may contain a higher proportion of crystalline phases than the predominantly amorphous fly ash typically present in the database, which could imply lower reactivity and reduced dissolution of Si and Al species. Likewise, the much coarser particle-size distribution observed for the dry-pit material may slow dissolution kinetics and limit gel development. The very short setting times of the dry-pit binders could also hinder the

formation of a continuous reaction network due to rapid CaO dissolution and premature hardening.

Figure 34 – Sachet *et al*. (2020) binders compressive strength results and model predicted

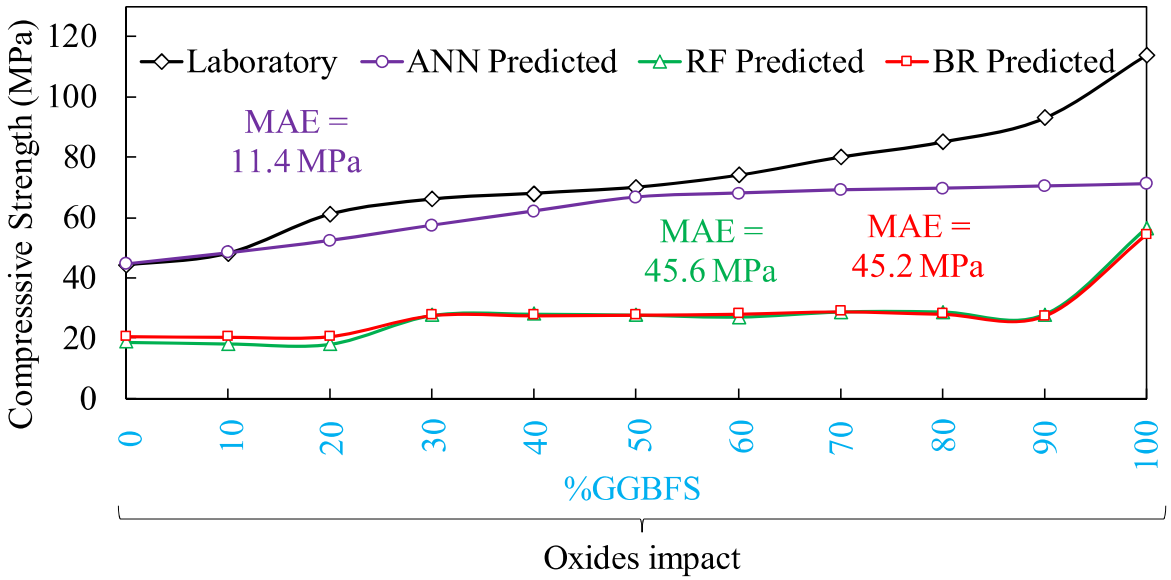

Source: elaborated by the author.

These characteristics, crystallinity, particle size, are not included as input variables because such characterizations are rarely reported across the studies that compose the database, adding them would drastically reduce the usable dataset and compromise the model's statistical robustness. In contrast, the reference datasets from Liu *et al.* (2020) and Sachet *et al.* (2020) rely on precursors such as GGBS/GGBFS, which are well known for their high amorphous content and reactivity, making them more compatible with the chemical and physical domain represented in the original data. These hypotheses may help explain why the models perform well for these systems but poorly for the dry-pit binders, however, they require further experimental confirmation. Overall, the results indicate that the model can be reliably applied, but only under formulation conditions that fall within the reactive and compositional domain represented by the training dataset.

3.1 Section conclusions

This study investigated the use of ML models to predict the fresh state (initial and final setting time, 139 data) and hardened state (compressive strength, 427 data) properties of AABs based on their chemical composition and mix design parameters. Five ML algorithms were used: DT, RF, AB, BR and ANN, along with MPR as linear statistical model.

The main initial and final setting time prediction conclusion are summarized as

follows:

- ANN, RF, and BR achieved the best predictive performances (R^2 = 0.96, 0.95, and 0.89, respectively), while MPR showed very low accuracy (R^2 = 0.04), suggesting the strongly nonlinear nature of the setting time behavior;
- The ANN identifies N/B, SiO_2, P_2O_5, and K_2O as the most influential variables, while RF and BR consistently highlight SiO_2, Al_2O_3, N/B, and CaO, a ranking that aligns more closely with expected chemical behavior in AABs;
- Comparison with literature shows that no model consistently matches with all expected trends. Agreement varies by parameter, with ANN sometimes better capturing nonlinear effects and RF/BR aligning more closely in other cases;
- Laboratory validation showed the ANN performs well only within S/N < 1.25 and N/B < 10% (MAE = 40.3 and 88.1 min), outside this domain, errors rise sharply (up to 611.2 and 1243.4 min);
- Expanding the predictive capacity of the models across wider parameter ranges depends on increasing the dataset size, since the current 139 samples are not enough.

The main conclusions regarding the compressive strength predictions are summarized as follows:

- ANN, RF, and BR showed the highest predictive accuracy for compressive strength (R^2 = 0.96, 0.90, and 0.89), while AB performed the worst;
- The ANN highlights Cl, CaO, Fe_2O_3, and TiO_2 as most influential, while RF and BR consistently emphasize CaO, Fe_2O_3, SiO_2, and S/N, which better reflect expected AABs chemical behavior;
- Although the ANN ranked Cl as the most important feature, its isolated effect is rarely studied, and the skewed, low-variability distribution of Cl may bias feature importance estimates;
- The ANN captured expected nonlinear behaviors, such as optimum points for N/B and S/N, showing greater sensitivity, while RF and BR remained more stable and less responsive to these variations;
- The laboratory validation for the dry-pit binders showed poor agreement with the model predictions, probably because their crystallinity and larger particle size are not

considered in the model;

- Laboratory validation with external datasets, Liu *et al*. (2020) and Sachet *et al*. (2020), showed better agreement, with good results only for the ANN (MAE = 5.8 MPa and 11.4 MPa, respectively), indicating that the model performs better when the materials exhibit good alkali-activation behavior.

4 DESIGN, DEVELOPMENT, AND VALIDATION OF AN IMPACT RESONANCE APPARATUS FOR STUDYING THE HARDENING PROCESS OF ALKALI-ACTIVATED BINDERS

4.1 Introduction

Alkali-activated binders (AABs) have emerged as an alternative to Portland cement and are produced by activating aluminosilicate precursors, such as fly ash, steel slag, and industrial residues with alkaline solutions like sodium hydroxide (NaOH) and sodium silicate (Na_2SiO_3) (Provis, 2018; Xie *et al.*, 2020; Siyal *et al.*, 2024). Their hardening behavior varies with precursor chemistry and activator composition, forming N-A-S-H and/or C-A-S-H gels through reaction mechanisms that remain only partially understood (Siyal *et al.*, 2024). Because these early transformations strongly affect the final mechanical performance, improved monitoring tools are needed (Park *et al.*, 2024). Conventional methods for hardening assessment are often limited when applied to AABs, especially given their complex kinetics and rheology (Tekle; Hertwig; Holschemacher, 2021).

Between these techniques, the Vicat test, an empirical method that determines initial and final setting times based on needle penetration, is useful for comparing binders but provides only two discrete points and does not capture the continuous evolution of hardening (Naqi *et al.*, 2022). Isothermal calorimetry and Fourier Transform Infrared Spectroscopy (FTIR), while capable of providing information on reaction progress, involve high experimental costs and specialized equipment, limiting their application (Kaze *et al.*, 2020; Dai *et al.*, 2021; Hoyos-Montilla *et al.*, 2022). Given these constraints, there is a clear need for more accessible and cost-effective techniques capable of capturing the physical evolution of the material and enabling correlation with microstructural and chemical development. In this context, rheological measurements have been explored, and some studies attempt to relate setting and hardening behavior to the evolution of viscoelastic properties measured with Dynamic Shear Rheometer (DSR) (Alrefaei *et al.*, 2022; Dai *et al.*, 2022b; Egnaczyk; Quinn; Wagner, 2025). In parallel, non-destructive techniques (NDT) are increasingly being applied in an effort to complement these approaches.

Ultrasonic waves propagation is NDT, and has been used to monitor the early-age behavior of binders. Some advanced approaches, like the multi-frequency method proposed by Park *et al.* (2024), improved the method sensitivity by using 34, 100, and 400 kHz to capture the material evolution, supported by SEM and FTIR analyses. However, ultrasound still

presents limitations in the fresh state: the high frequencies used lead to predominantly elastic responses, reducing sensitivity to viscous effects, mainly reflects bulk modulus changes (Ryu *et al.*, 2020). Given these limitations, the impact resonance test (IRT) emerges as a promising alternative.

Building on this need for alternative approaches, the IRT shows potential for application in the fresh state of AABs, particularly because of its proven effectiveness in characterizing viscoelastic materials (such bituminous materials). The IRT is NDT in which a specimen (usually cylindrical) is placed on soft supports, lightly impacted with a hammer, and its vibrational response is recorded using an accelerometer (Boz *et al.*, 2017; Barbosa *et al.*, 2024; Sadeghi *et al.*, 2024). The frequency content of this response, obtained via fast Fourier transform, allows identification of resonant frequencies related to stiffness (Carret, 2018; Bezerra *et al.*, 2023). IRT provides rapid, low-cost mechanical characterization without the need for large testing machines (Barbosa *et al.*, 2024). Its broad excitation frequency range (typically 0-50 kHz) makes it particularly suitable for capturing viscoelastic effects in materials with substantial damping (Carret; Babadopulos, 2025; Herozi *et al.*, 2025). Although still unexplored in the fresh state binders, it is hypothesized that IRT may be advantageous because it provides access to the frequency domain at each measurement interval, potentially enabling continuous tracking of stiffness evolution throughout the hardening process. This remains to be experimentally demonstrated, and the use of IRT in the fresh state requires the development of a specific test apparatus, including an appropriate geometry capable of containing the binder during early-age measurements.

In this context, the objective of this study is to design, develop, and validate an impact resonance test apparatus to monitoring the hardening process of AABs in the fresh state. The test geometries used throughout the development are manufactured by 3D printing in polylactic acid (PLA), allowing precise dimensional control and rapid prototyping. The methodology follows four stages: first, a reference PLA cylindrical specimen is fabricated and tested using impact resonance, together with 2D finite element method (FEM) simulations, to calibrate the viscoelastic 2S2P1D model; second, multiple geometries are evaluated through FEM to assess how dimensional variations influence the frequency response and to pre-select designs (the lower number of resonant peaks is the criteria); third, these geometries are 3D-printed and experimentally tested, and the selection of the optimal geometry is guided by two criteria: (i) a lower number of detectable resonant peaks in the frequency domain and (ii) high signal coherence (~1), ensuring a clear and stable dynamic response and the overall objective

of minimizing geometric influence on the measured response after in the binder. Finally, the chosen geometry is used as a container for fresh AABs so that the vibrational signature predominantly reflects the hardening behavior of the binder system. This work is expected to provide new experimental insight into the hardening mechanisms of AABs and support the development of more robust, physics-based interpretations of their hardening process.

4.2 Materials

4.2.1 Geometry material

4.2.1.1 Polylactic acid (PLA)

To adapt the test to the fresh state, it was necessary to design and manufacture a specific geometry capable of containing the binder during the resonance measurements. The geometry was produced using a 3D printer (Figure 35a). Several different geometries were produced in polylactic acid (PLA) filament (Figure 35b) to evaluate the influence of shape on wave propagation.

Figure 35 – 3D printing (a) 3D printer K1 Max and (b) PLA roll

a) 


b)

Source: elaborated by the author.

PLA was selected because it is one of the most widely studied and documented thermoplastic materials in the literature (Matos *et al.*, 2019; Adibeig; Vakili-Tahami; Saeimi-Sadigh, 2023; Song *et al.*, 2024). The printing parameters adopted for manufacturing the PLA geometries are presented in Table 11. These values were provided by the filament manufacturer and were followed to ensure the reliability of the printing process and the dimensional precision of the geometries.

The detailed 3D printing parameters employed in the production of the PLA geometries are presented in Table 12. These settings, based on the manufacturer's recommendations and the printer's default calibration, ensured consistent printing quality and

dimensional stability across all specimens. The use of standardized print speeds for external and internal perimeters (60 mm/s) further contributed to uniform layer deposition.

Table 11 – Polylactic Acid (PLA) properties

Parameter	Value
Printing Temperature	215 °C (range: 190 °C – 220 °C)
Bed Temperature	60 °C
Retraction Distance	Direct Extruder: 4 mm • Bowden Extruder: 9 mm
Retraction Speed	~45 mm/s
Fan Speed	100% (225 PWM)
Diameter	1.75 mm
Filament Length (per 1 kg)	330 m

Source: provided by the manufacturer.

Table 12 – 3D printing parameters

Parameter	Setting	Parameter	Setting
Filament Type	PLA	External perimeter speed	60 mm/s
Filament Diameter	1.75 mm	Internal perimeter speed	60 mm/s
Heat Deflection Temperature (HDT)	60 °C	First-layer travel speed	100 %
Idle Temperature	0 °C	Infill Density	99 %
Recommended Nozzle Temperature	190 – 240 °C	Infill Pattern	Rectilinear
Chamber Temperature	0 °C	Infill Anchor Length	400 %
Automatic Temperature Adjustment	Disabled	Small Gap Filtering	0 mm
Build-Plate Type	PEI smooth / High-temp bed	Infill/Perimeter Overlap	15 %
Bed Temperature (First Layer)	60 °C	Infill Density	99 %
Bed Temperature (Other Layers)	60 °C	Infill Pattern	Rectilinear

Source: provided by the manufacturer.

4.2.1.2 Polyurethane

In addition to the PLA geometry, polyurethane was employed in specific configurations to attenuate unwanted vibrations and improve the accuracy of the resonance measurements. Widely used in civil construction for dilation joints in structures, the material provided the necessary damping support for the tests (Yuan; Wei; Ni, 2021; Babkina *et al.*, 2023; Chen *et al.*, 2024). The main properties of the polyurethane used in this study are summarized in Table 13. With a density of (1.53 ± 0.02) g/cm³ and a hardness of 25-30 Shore A, the material combined flexibility and resilience, while its high elongation at break (>600%) and broad temperature resistance (-20 °C to 120 °C) guaranteed stable performance during test.

Table 13 – Polyurethane properties

Property	Value
Density (Pycnometer)	(1.53 ± 0.02) g/cm³
Skin Formation Time	~35 minutes (25°C and 50% RH)
Curing Time	3mm/24h (25°C and 50% RH)
Flow Time (NBR 9278, 2019)	50-70 seconds (20 g - 1.5 kgf/cm² - 2.8 mm²)

Hardness (ASTM D2240, 2015)	25-30 Shore A
Elongation at Break (ASTM D412, 2016)	>600%
Tensile Strength 100% deformation (ASTM D412, 2016)	~0.46 N/mm²
Tensile Strength at Break (ASTM D412)	~0.90 N/mm²
Working Temperature	10°C to 40°C

Source: provided by the manufacturer.

4.2.2 Alkali-activated binder tested

Two aluminosilicate precursors were employed in the AAB composition at 50%/50% mass proportion: ground granulated blast-furnace slag (GGBS) and fly ash (FA). The both chemical compositions determined by X-ray fluorescence (XRF), is presented in Table 14. The GGBS exhibited a high CaO content (55.84%), with moderate lsevels of SiO_2 (27.91%) and Al_2O_3 (7.42%). Minor oxides such as TiO_2, MnO, and Fe_2O_3 were also detected in smaller proportions. The FA precursor showed a high SiO_2 content (58.15%), accompanied by a substantial amount of Al_2O_3 (19.61%), reflecting its predominantly aluminosilicate nature. Smaller quantities of CaO (4.60%), Fe_2O_3 (9.33%), and K_2O (2.60%) were present, along with minor levels of TiO_2, MgO, MnO, and SO_3. A measurable amount of P_2O_5 (1.87%) was also detected. The density of the GGBS was 2.90 g/cm³, while the fly ash presented a density of 2.21 g/cm³. The material binder was freshly prepared during the author's internship in France.

Table 14 – Precursor oxides composition

Precursor	Al_2O_3	SiO_2	P_2O_5	SO_3	MgO	K_2O	CaO	TiO_2	MnO	Fe_2O_3
GGBS	**7.42**	**27.91**	0.72	1.52	2.96	0.58	**55.84**	1.53	0.58	**0.78**
FA	**19.61**	**58.15**	1.87	0.58	0.67	2.60	**4.60**	1.93	0.09	**9.33**

Source: elaborated by the author.

Figure 36 illustrates the cumulative particle size distributions of the FA and GGBS precursors, measured using a laser diffraction particle size analyzer (SALD-2300, Shimadzu). The technique is based on laser light scattering, allowing the determination of particle size distribution over a wide range and providing a reliable comparison of the granulometric characteristics of both precursors. FA presents larger characteristic diameters (D10 = 2.5 μm, D50 = 16.6 μm, D90 = 72.2 μm), indicating a generally coarser profile. In contrast, GGBS shows finer sizes (D10 = 1.6 μm, D50 = 12.6 μm, D90 = 33.0 μm), reflecting a narrower distribution. These differences highlight the greater overall particle size of FA compared to GGBS.

Figure 36 – Precursor's particle size

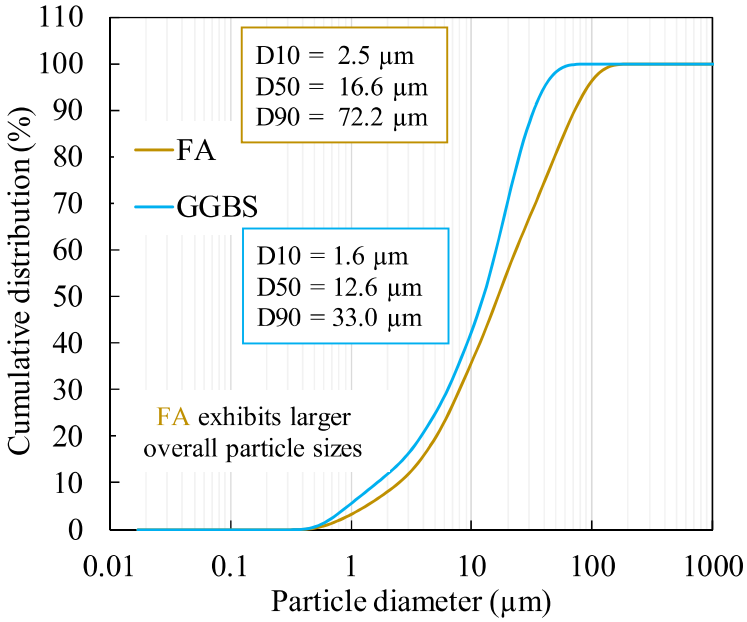

Source: elaborated by the author.

Figure 37 presents the FTIR spectra of the raw precursors, highlighting the distinct structural environments of FA and GGBS. The most notable difference appears in the main Si-O-T (T = Al or Si) asymmetric stretching region: FA shows a band at 1086 cm^{-1}, characteristic of a more polymerized Si-O network, whereas GGBS displays this vibration at a lower wavenumber (974 cm^{-1}), indicating a more depolymerized silicate structure (Bondar; Vinai, 2022). FA presents Si-O-Si vibrations at 795 cm^{-1} and Si-O/Al-O at 465 cm^{-1} (Zhou *et al.*, 2023), whereas GGBS displays a broad 500-700 cm^{-1} band due to overlapping Si-O/Al-O bending modes (Bondar; Vinai, 2022).

Figure 37 – Precursor's FTIR

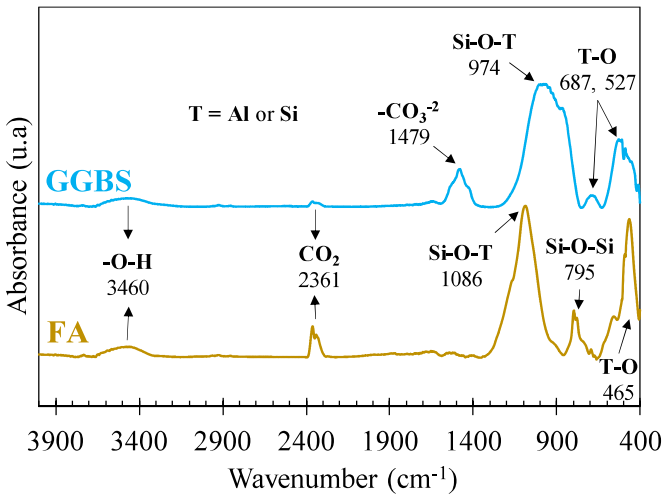

Source: elaborated by the author.

A carbonate ($-CO_3^{-2}$) band at 1479 cm^{-1} (Zhang; Çopuroğlu, 2022) is observed only in GGBS, indicating partial surface carbonation associated with its higher CaO content. These

spectral trends are consistent with XRF data (Table 12), confirming the higher SiO_2 and Al_2O_3 content of FA and the CaO-rich composition of GGBS

The mix binder proportion is descripted on the Table 15. The alkaline activator consisted of sodium hydroxide (NaOH) and sodium silicate (Na_2SiO_3) solutions.

Table 15 – Mix proportion

GGBS-FA (%)	GGBS (g/L)	FA (g/L)	Na_2SiO_3 solution (g/L)	NaOH solution (g/L)
50-50	562.90	562.90	137.11	558.81

Source: elaborated by the author.

The NaOH solution was prepared at a concentration of 10 mol/L, using analytical-grade pellets with 98% purity. The sodium silicate solution had a density of 1.493 g/cm³ and contained 27.86% SiO_2, 11.14% Na_2O, and 61.00% H_2O. The silica modulus (S/N) was fixed at 0.25, the alkali content (N/B) at 14%, and the water-to-binder ratio (W/B) at 0.40.

4.3 Methods

4.3.1 Classical binder tests in fresh state

Before advancing to the impact resonance test, a set of classical characterization methods is first performed to establish the fundamental behavior of the binder system. These preliminary tests include setting time measurements and time-sweep rheology, which together provide essential information in early-age behavior, and viscoelastic evolution. These conventional tests form the baseline against which the dynamic response obtained from IRT can later be interpreted.

4.3.1.1 Setting time and time sweep rheology

The initial and final setting time was measured using the Vicat apparatus, in accordance to NBR 16607, (2018). The setting time is determined through an empirical penetration test. In practice, these values represent, in the field, the period of workability of the material. The initial setting time corresponds to the interval between the contact of the cement (precursors in AABs) with water (alkalinity solutions in AABs) and the moment when the needle of the apparatus, inserted into the binder, remains at a distance of 6 ± 2 mm from the base plate, while the final setting time is defined as the interval until the needle penetrates no deeper than 0.5 mm. The standard indicates that Vicat needle penetration measurements are performed at non-fixed, suitably spaced time intervals. Intervals of about 10 minutes are typically used for the initial setting time and may be extended up to 30 minutes for the final

setting time, with shorter intervals adopted near the end of the test to improve accuracy.

A time sweep rheological test was conducted to characterize the time-dependent behavior of the binder and to provide fundamental parameters (G', G" and δ) for comparison with impact resonance measurements and COMSOL simulations. Tests were carried out on a dynamic shear rheometer (Advanced Rheometer AR2000) using a plate-plate geometry (40 mm diameter, 1 mm gap). The evolution of viscoelastic properties was monitored through the storage modulus (G′), loss modulus (G″), and phase angle (δ), under constant frequency and strain conditions, as showed in Figure 38. For this purpose, a frequency of 10 Hz was selected, and the strain was determined by performing a strain sweep to identify the linear viscoelastic region. The total duration of the test was set to 300 min (5 h), in accordance with the approximate final setting time (~200 min) determined by the Vicat test for the investigated binders. The test will be conducted at 10 Hz and 25 °C.

Figure 38 – Time sweep signals

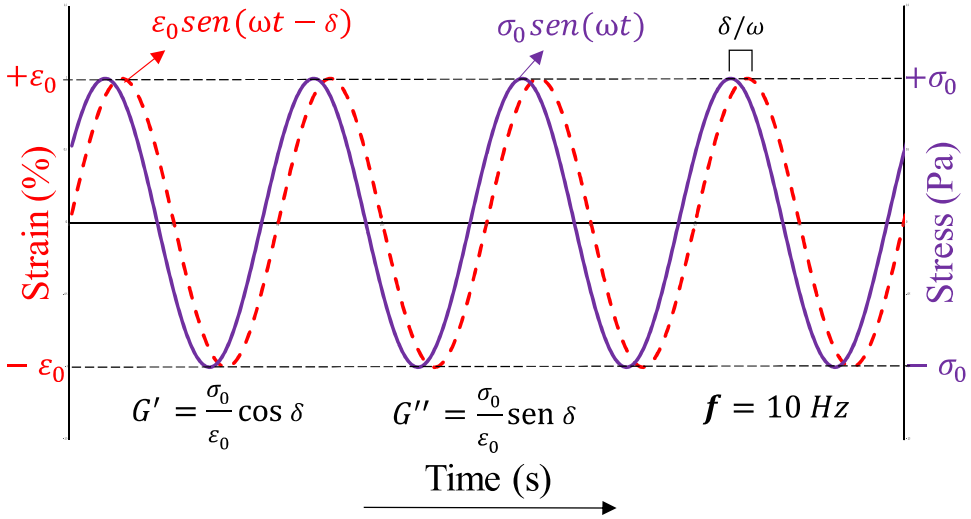

Source: elaborated by the author.

4.3.1.2 *Isothermal calorimetry*

Isothermal calorimetry is a thermal analysis method that quantifies the heat flow released or absorbed by a material maintained at constant temperature (Egnaczyk; Quinn; Wagner, 2025). In AABs, it is a powerful tool to investigate hardening kinetics, since the dissolution of precursors and subsequent gel formation are exothermic processes (Caron; Patel; Dehn, 2022; Sun *et al.*, 2022; Cui *et al.*, 2024). In this study, measurements were conducted under controlled temperature conditions (25 °C) using an eight-channel TAM Air heat-conduction calorimeter (TA Instruments). Immediately after mixing, the binder was transferred into sealed 20 mL ampoules, and heat evolution was monitored continuously for 7 days. The

raw heat-flow data (mW/kg of binder) were integrated over time to obtain the cumulative heat release (J/kg of binder). These calorimetric profiles were then used to characterize reaction kinetics and were correlated with complementary techniques to provide a comprehensive understanding of binder hardening.

4.3.2 Impact resonance test (IRT)

4.3.2.1 Experimental setup and analysis procedure

The IRT is a non-destructive technique based on wave propagation, used to estimate mechanical properties such as the elastic modulus (or complex modulus). At present, the technique is mainly restricted to the hardened state (Carret, 2018; Bezerra *et al.*, 2023), however, in this work it will be employed to study materials in the fresh state during the hardening process.

Figure 39 illustrates the schematic of the IRT setup for both hardened and fresh states. The experimental configuration employed a miniature impact hammer (PCB model 086E80, 222 N load cell) to excite the specimen, while its response was recorded using a bonded accelerometer (PCB model 353B15).

Figure 39 – Schematic IRT in hardened and fresh state materials

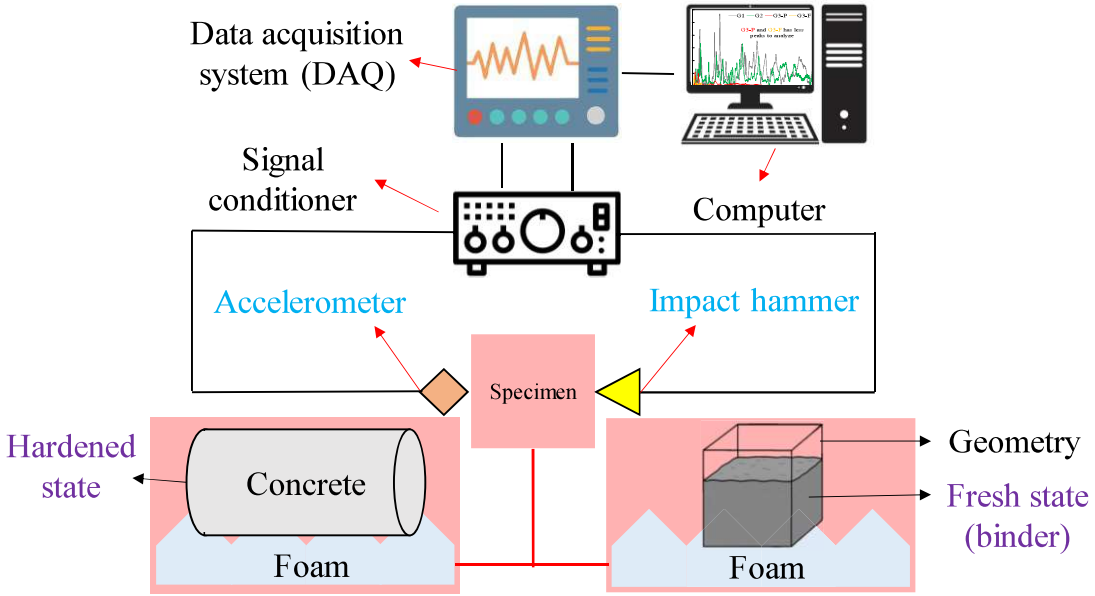

Source: elaborated by the author.

The signals from both sensors were conditioned and amplified through a PCB 482C15 unit, and data acquisition was performed with an NI USB-6002 system at a sampling rate of 50 kS/s. The digitized force and acceleration records were transferred to a computer for post-processing. The time-domain signals were converted into the frequency domain using the

Fast Fourier Transform (FFT), from which the frequency response function (FRF) was computed as the ratio between the response spectrum (Y), typically acceleration, and the input force spectrum (X), as defined in Equation 11 (Berjamin *et al.*, 2018; Carret, 2018).

$$H*(f) = \frac{S_{xy}(f)}{S_{xx}(f)} = \frac{X^*(f)Y(f)}{X^*(f)X(f)} \tag{11}$$

Where $H^*(f)$ is the FRF in the frequency domain, but in this present study, the analysis is always performed using the amplitude of the FRF, $|H^*(f)|$. S_{xy} is the cross-power spectrum between the input and output, S_{xx} is the auto-power spectrum of the input, X(f) and X*(f) represent the input signal in the frequency domain and its complex conjugate, respectively; and Y(f) corresponds to the output signal in the frequency domain. The coherence function (CF), calculated using Equation 12, was employed to assess the reliability of the measurements, with coherence values approaching 1.0 indicating a high signal-to-noise ratio and consistent excitation during testing (Bezerra *et al.*, 2023).

$$CF\ (f) = \frac{S_{xy}^2}{S_{xx} \cdot S_{yy}} \tag{12}$$

Where S_{xy} is the cross-power spectrum, S_{xx} is the auto-power spectrum of the input, and S_{yy} = Y*(f)Y(f) is the auto-power spectrum of the output. The terms Y(f) and Y*(f) denote the output signal in the frequency domain and its complex conjugate, respectively.

However, as shown in Figure 39, it is necessary to use a geometry to contain the binder in the fresh state. To obtain this result, an activity flowchart is described in Figure 40. Accordingly, was followed our main steps: (1) The reference cylindrical specimen is produced by 3D printing, being chosen specifically for the initial determination of the 2S2P1D parameters, since its reduced complexity facilitates parameter identification compared to more complex geometries. (2) 2D FEM simulations are performed to assess the influence of geometric dimensions, followed by the selection of candidate geometries for laboratory testing. (3) Based on these steps, the most suitable geometry is identified, and optimization of the 2S2P1D parameters is carried out. (4) Finally, binder parameters are optimized via LiveLink, which connects COMSOL and MATLAB. To evaluate the evolution over time, resonance impact tests are performed every 15 minutes, with the geometry parameters fixed and only the binder parameters being identified.

Figure 40 – Schematic representation for the definition of test geometry and binder analysis

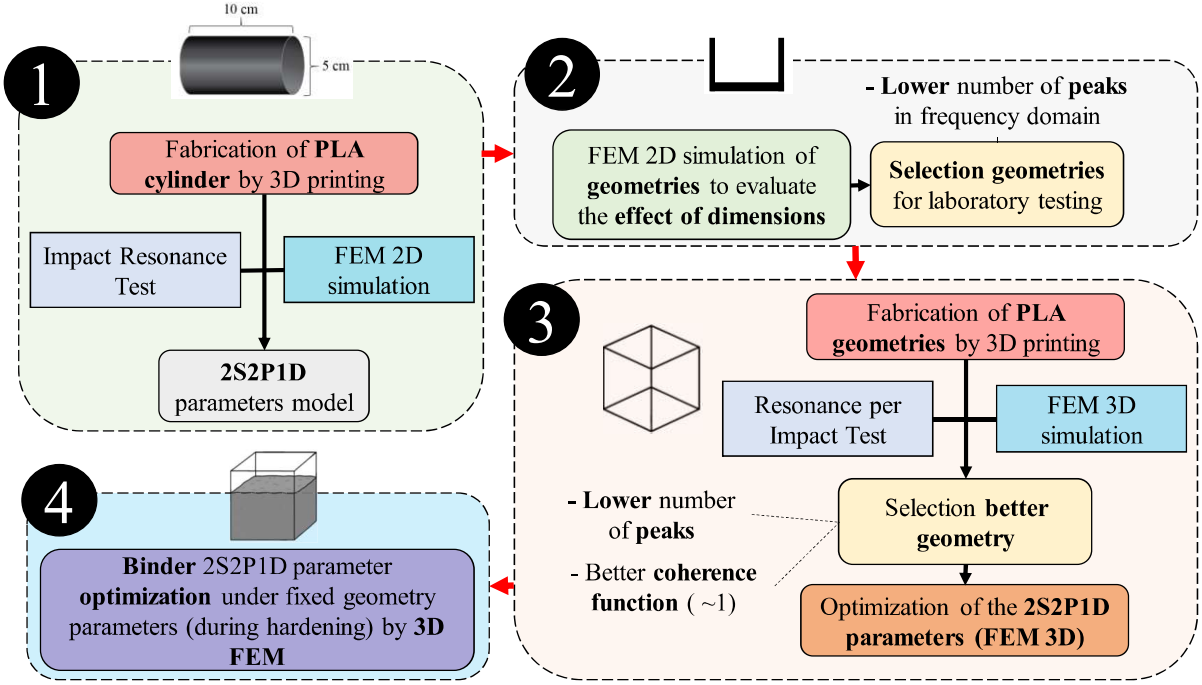

Source: elaborated by the author.

4.3.2.2 2S2P1D model

The 2S2P1D is a rheological model, with a mechanical analog composed of two springs, two parabolic elements, and one dashpot, all connected in series (Figure 41). It was developed to extend the applicability of earlier viscoelastic models, particularly for accurately representing bituminous materials at low frequencies or high temperatures (Olard; Di Benedetto, 2003; Di Benedetto *et al.*, 2004).

Figure 41 – 2S2P1D model analogical representation

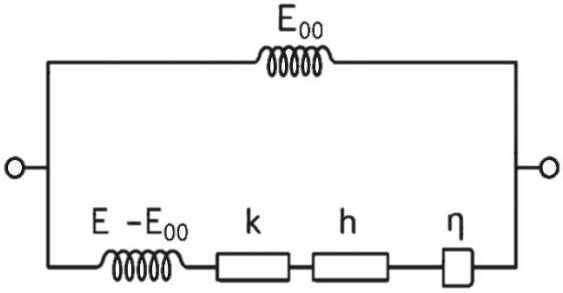

Source: Carret (2018).

Equations 13 and 14 give the 2S2P1D laws for the complex modulus $E^*(\omega)$ and the complex Poisson's ratio $\nu^*(\omega)$. The angular frequency is $\omega=2\pi f$. The limits of $E^*(\omega)$ are E_{00} at very low frequency ($\omega\rightarrow 0$) and E_0 at very high frequency ($\omega\rightarrow\infty$). The fractional exponents k and h (with $0<k<h<1$) shape the two parabolic branches; δ is a dimensionless weighting factor; β scales the Newtonian branch. The characteristic time is $\tau_e > 0$. The Poisson-ratio law $\nu^*(\omega)$

uses the same spectral skeleton but with bounds ν_{00} (static) and ν_0 (glassy), and τ_v is time constant linked to that of the modulus ($\tau_v=\tau_e/\gamma$ where γ is a dimensionless constant). When the spectral parameters are the same, the model has 10 independent constants (Carret, 2018).

$$E^*(\omega) = E_{00} + \frac{E_0 - E_{00}}{1 + \delta\,(i\omega\tau_e)^{-k} + (i\omega\tau_e)^{-h} + (i\omega\beta\tau_e)^{-1}} \quad (13)$$

$$\nu^*(\omega) = \nu_{00} + \frac{\nu_0 - \nu_{00}}{1 + \delta\,(i\omega\tau_v)^{-k} + (i\omega\tau_v)^{-h} + (i\omega\beta\tau_v)^{-1}} \quad (14)$$

This model was chosen because it provides a continuous formulation in the frequency domain, allowing the representation of several decades of frequency while capturing both the viscous and elastic characteristics of the material. The aim of this approach is to evaluate how the binder properties evolve with frequency and, consequently, how they influence the simulated mechanical response.

4.3.2.3 Finite element method (FEM)

In order to obtain the frequency domain numerically calculated, a modeling was performed using the FEM software COMSOL Multiphysics. The material behavior was considered linear elastic, but the modulus introduced at each frequency was not constant. Instead, the rheological model 2S2P1D (Equation 13 and 14) previously defined, was employed to calculate the complex modulus, which varies with frequency.

As showed in Figure 40, the FEM procedure was first applied to a PLA cylinder to characterize the material, then extended to different geometries to assess shape influence, and finally to binders, where geometry was fixed and only rheological properties were optimized using the 2S2P1D model. The geometry was reproduced in COMSOL, and the mesh was generated with a maximum element size of 5 mm (Figure 42 illustrates a FEM geometry example).

Free boundary conditions were applied on all surfaces, except at the impact position where a unitary load was imposed as a function of time. The frequency domain calculated was then obtained by solving the wave propagation Equation 15 at each of the specified frequencies of interest. Where u is the displacement vector, ω the angular frequency, Δ the gradient tensor operator, σ the Cauchy stress tensor, and ρ the bulk density.

Figure 42 – Finite element mesh

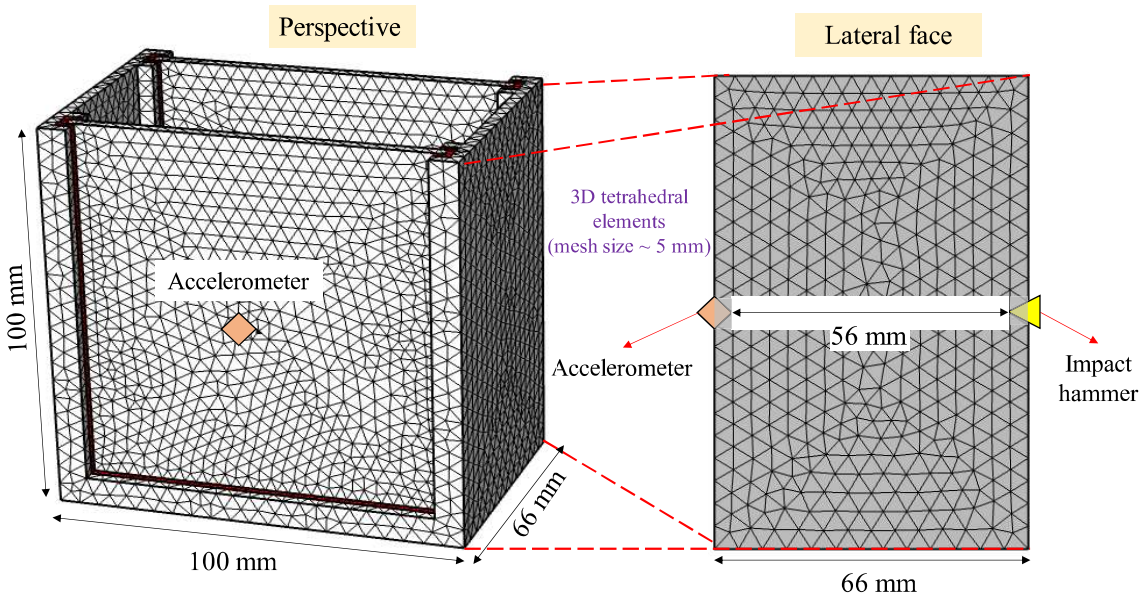

Source: elaborated by the author.

$$-\rho\omega^2 u - \nabla\sigma = 0 \tag{15}$$

4.3.3 Inverse analysis to rheological parameter's optimization

The inverse analysis developed in this work follows the methodology originally proposed by Carret *et al.* (2018), with adjustments as necessary due to the complex vibration behavior of non-cylindrical geometries. The analysis was implemented through a MATLAB code connected to COMSOL Multiphysics by the LiveLink interface, enabling iterative calculations of the frequency domain while updating model parameters automatically.

In the present work, some modifications were introduced. First, it was the first time that the 2S2P1D model was applied to PLA and AABs, so it was necessary to adjust all the model parameters instead of restricting the optimization to a reduced set. Moreover, both the complex modulus (Equation 13) and the complex Poisson's ratio (Equation 14) were considered in the formulation, which required a higher number of parameters to be optimized (total of 10). Second, instead of selecting an artificial frequency window, the simulated FRF was evaluated exactly at the 11 points of interest (Figure 43) corresponding to the experimental measurements, selected within the half-power bandwidth (0.707 of the peak amplitude) around the resonance peak, ensuring direct point-to-point comparability.

Figure 43 – 11 data points example

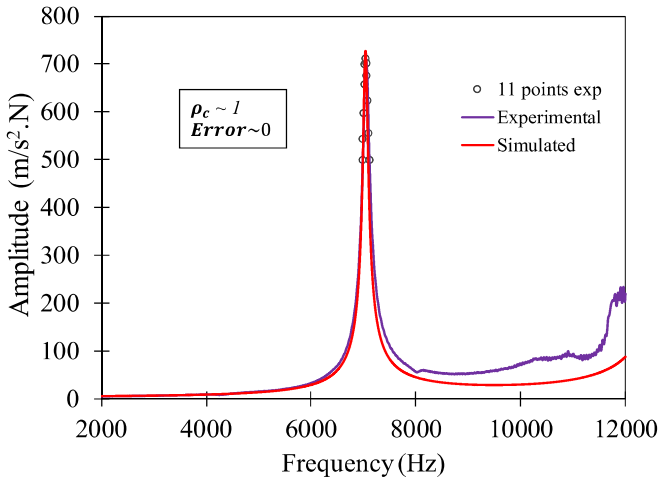

Source: elaborated by the author.

Third, instead of the original error function proposed by Carret *et al.* (2018), the optimization was performed using a new error function, defined in Equation 16, which depends on the Concordance Correlation Coefficient (ρc) given in Equation 17. Where $\rho_{exp,FEM}$ is the Pearson correlation coefficient (Equation 18) between the two groups of data, σ represents the standard deviation, and μ denotes the mean result. The subscripts "exp" and "FEM" refer to the experimental data and the data calculated by the finite element method, respectively.

$$Error = (1 - \rho_c) \cdot 100 \tag{16}$$

$$\rho_c = \frac{2 \cdot \rho_{exp,FEM} \cdot \sigma_{exp}\sigma_{FEM}}{\sigma_{exp}^2 + \sigma_{FEM}^2 + (\mu_{exp} - \mu_{FEM})^2} \tag{17}$$

$$\rho_{exp,FEM} = \frac{\mathrm{cov}(|H * (f)|_{exp}, |H * (f)|_{FEM})}{\sigma_{exp}\,\sigma_{FEM}} \tag{18}$$

The Pearson correlation coefficient ($\rho_{exp,FEM}$) quantifies the linear relationship between the experimental values ($|H * (f)|_{exp}$) and the numerical values ($|H * (f)|_{FEM}$), the group data are the 11 points selected. The ρ_c measures both precision and accuracy between datasets, quantifying their agreement. Values range from -1 to 1, when is closer to 1 indicate stronger concordance between the experimental and simulated FEM data. The main difficulty in extending the methodology to the geometries and the binders is that these simulations were carried out in 3D FEM, which requires significantly more processing time. Therefore, all modifications introduced in this work were designed to improve computational efficiency and reduce simulation time, while still ensuring accurate agreement between experimental and simulated results.

4.4 Results and discussion

4.4.1 Classical tests

4.4.1.1 Setting time and time sweep rheology

The binder exhibited an initial setting time of 170 min and a final setting time of 230 min, values that indicate a relatively well-developed early-age reaction process. Similar setting time ranges have also been reported in the literature for GGBS-FA based AABs (Dineshkumar; Umarani, 2020; Paul; Gunneswara Rao, 2022). To complement these measurements, a time-sweep rheology test (Figure 44) was conducted for 300 min (5 hours). This duration was deliberately selected to capture the material's evolution at three key stages: (i) the period preceding the initial setting, (ii) the interval between initial and final setting, and (iii) approximately one hour after final set. This approach makes it possible to monitor changes in viscoelastic behavior throughout the critical hardening phases.

The Figure 44a shows the evolution of the storage modulus (G′), loss modulus (G″), and phase angle (δ), while (b) displays their first derivatives (dG′/dt and dG″/dt), highlighting the rate at which the microstructure develops over time. In the early stage (0-150 min), both G′ and G″ remain close to zero and the phase angle is initially high, decreasing slightly in the first ~50 min and then rising gradually toward the end of the test. A slight, discrete increase in dG′/dt is already visible around 20-115 min, suggesting early microstructural reorganization even before G′ begins its significant rise in Figure 44a. In the pre-initial setting stage, the material behaves as a predominantly viscous suspension, with low G′ and G″ values indicating minimal particle-particle interactions (Bílek *et al.*, 2021; Siddique *et al.*, 2021)

A more pronounced change occurs around 170 min (initial setting time). At this point, both G′ and G″ begin to increase, and the derivatives in Figure 44b show a clear acceleration. The setting stage initiates as dissolution of slag and fly ash elevates the ionic concentration of the pore solution, triggering accelerated gel formation and network percolation that produce a sharp increase in both G′ and G″ (Dai *et al.*, 2020; Nedunuri; Muhammad, 2021). The derivative curves capture this transition earlier and more sharply than the shear modulus themselves, demonstrating their sensitivity to the kinetics of early microstructure development.

Between 170 and 230 min, both the measured modulus and their derivatives increase substantially. The G' grows faster than G". During this same interval, the phase angle, after its initial drop, continues a progressive increase toward 300 min. In the post-setting stage,

continued polymerization and densification of C-A-S-H and N-A-S-H gels increase stiffness (Yin *et al.*, 2022; Lv *et al.*, 2023), while the rise in G″ indicates that viscous dissipation remains significant during hardening.

Figure 44 – Time sweep rheology (a) Measured values and (b) first derivative values

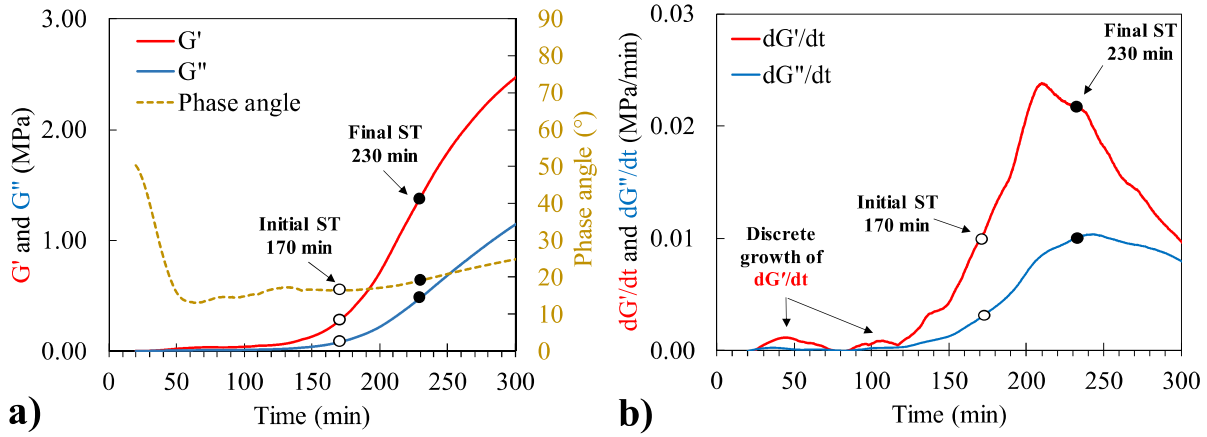

Source: elaborated by the author.

Importantly, the peak of dG′/dt occurs 20 minutes before the final setting time (230 min). The system is still hardening, but the acceleration of gel formation and network densification has begun to slow. In contrast, dG″/dt does not follow the same trend, with its peak occurring approximately 10 minutes after the final setting time. After that, both dG′/dt and dG″/dt continue to decline. Although the absolute modulus keeps increasing, the rate of structural development progressively decreases as the binder transitions into a more consolidated solid.

Overall, the combined analysis of the measured modulus and their derivatives provides a view of the hardening kinetics of the binder. Figure 44a captures the global viscoelastic evolution, while Figure 44b highlights subtle acceleration and deceleration phases, which are essential for understanding the progressive microstructural development of AABs.

4.4.1.2 Isothermal calorimetry

The Figure 45 shows the isothermal calorimetry results at (a) 300 min and (b) 7 days, where the initial fluctuations observed between 0 and 45 minutes are disregarded because they are strongly affected by environmental stabilization when the sample is placed into the calorimeter at approximately 20 minutes. Despite this disturbance, the early behavior is governed by rapid wetting of the precursor and dissolution of reactive glassy phases, which release Si^{4+}, Al^{3+}, and Ca^{2+} into the pore solution and generate a short-lived exothermic response

mainly associated with physical dissolution processes (Ascensão *et al.*, 2020; Joseph; Cizer, 2022). As the reaction progresses (~45-180 min), the pore solution becomes supersaturated, producing the main exothermic peak at roughly 155 minutes, which marks the onset of gel polymerization and the precipitation of N-A-S-H or C-A-S-H structures, representing the principal chemical reaction period (Sun; Vollpracht, 2018; Chithiraputhiran; Neithalath, 2013).

Figure 45 – Isothermal calorimetry (a) 300 min and (b) 7 days

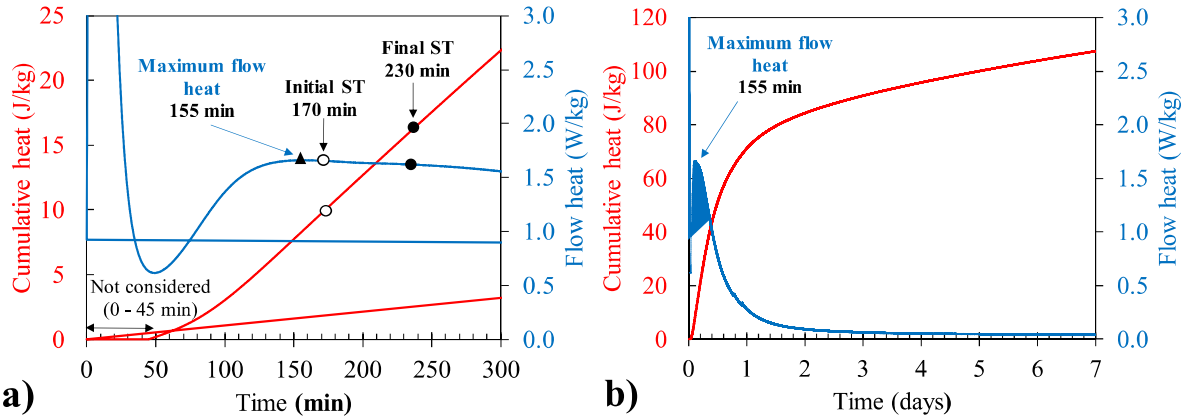

Source: elaborated by the author.

In the following interval (170-230 min), the heat flow decreases as the developing gel network interconnects and progressively immobilizes remaining ions, corresponding to the experimentally observed initial and final setting times and aligning with the deceleration behavior previously described for alkali-activated slag-fly ash binders (Ascensão *et al.*, 2020; Joseph; Cizer, 2022). Over extended durations (1-7 days), the heat flow stabilizes at a low but persistent level after the main exothermic process has fully dissipated-ending at approximately 3 days-while cumulative heat continues to increase, reflecting ongoing condensation reactions, structural reorganization of the gel, and the potential formation of secondary crystalline phases, consistent with long-term polymeric evolution in AABs (Sun; Vollpracht, 2018; Ascensão *et al.*, 2020).

4.4.2 Impact resonance test (IRT)

4.4.2.1 FEM 2D for PLA characterization using cylinder

Figure 46 shows the frequency response function (FRF) comparison between the experimental and simulated results for the PLA cylindrical specimen (100 mm in length and 50 mm in diameter, 99% infill). The specimen was produced to identify the 2S2P1D viscoelastic model parameters, which describe the material's dynamic mechanical behavior under excitation.

Figure 46 – FRF experimental and simulated for PLA cylinder 99% infill

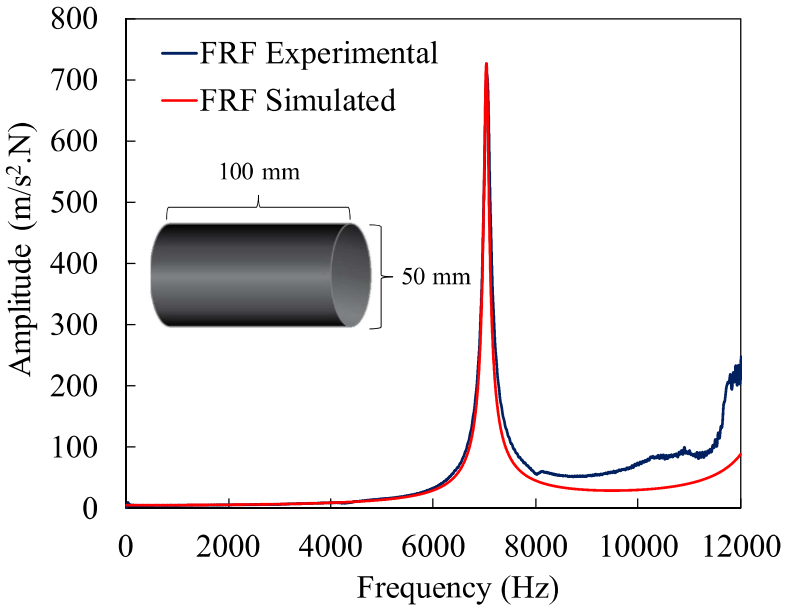

Source: elaborated by the author.

As observed in Figure 46, the simulated FRF (red curve) shows excellent agreement with the experimental results (blue curve), particularly around the main resonance frequency near 7000 Hz, confirming that the identified model accurately reproduces the material's dynamic response. The final calibrated 2S2P1D parameters, obtained from the optimization process, are summarized in Table 16. The fitted parameters demonstrate consistent stiffness and damping characteristics representative of high-density PLA material.

Table 16 – PLA cylinder 2S2P1D parameters

2S2P1D parameter	PLA Cylinder
E_{00} (Pa)	574945752
E_0 (Pa)	2482262849
τ_e	7.770858
α	0.548684
k	0.143893
h	0.641324
β	0.070557
v_{00}	0.360395
v_0	0.407043
τ_v	1.688496

Source: elaborated by the author.

4.4.2.2 FEM 2D for determining the geometries to be tested in the laboratory

Before conducting experimental measurements, selecting an appropriate specimen

geometry is essential to ensure accurate and reliable results in IRT. While this aspect has received limited attention in previous IRT research, most related studies on ultrasonic testing of cementitious materials have relied on conventional specimen geometries without prior optimization (Trtnik; Valič; Turk, 2013; Park *et al.*, 2024; Xu, D. *et al.*, 2024). Dumoulin and Deraemaeker (2017), however, demonstrated through finite element simulations that geometry plays a crucial role in wave propagation and resonance behavior. Nevertheless, such simulation-based optimization has not been systematically applied to IRT. Therefore, in this study, preliminary simulations were performed to determine the most suitable specimen geometry capable of producing distinct and stable resonance modes, ensuring accurate and reproducible experimental results.

The Figure 47 illustrates the finite element model (FEM) geometry used for the analysis. A three-dimensional (3D) specimen with width (W), height (H), and wall thickness (t) was represented in two dimensions (2D) to evaluate the influence of geometric parameters on the vibration response. In this study, the specimen length was fixed at 100 mm, while width, height, and thickness were varied individually, keeping the other dimensions constant for each simulation. The analysis was performed on an empty geometry to identify the configuration that produces the lowest vibration amplitude (i.e., fewer resonance peaks), providing insight into the most stable geometry for the subsequent Impact Resonance Test (IRT).

Figure 47 – FEM empty geometry analyzed in 2D

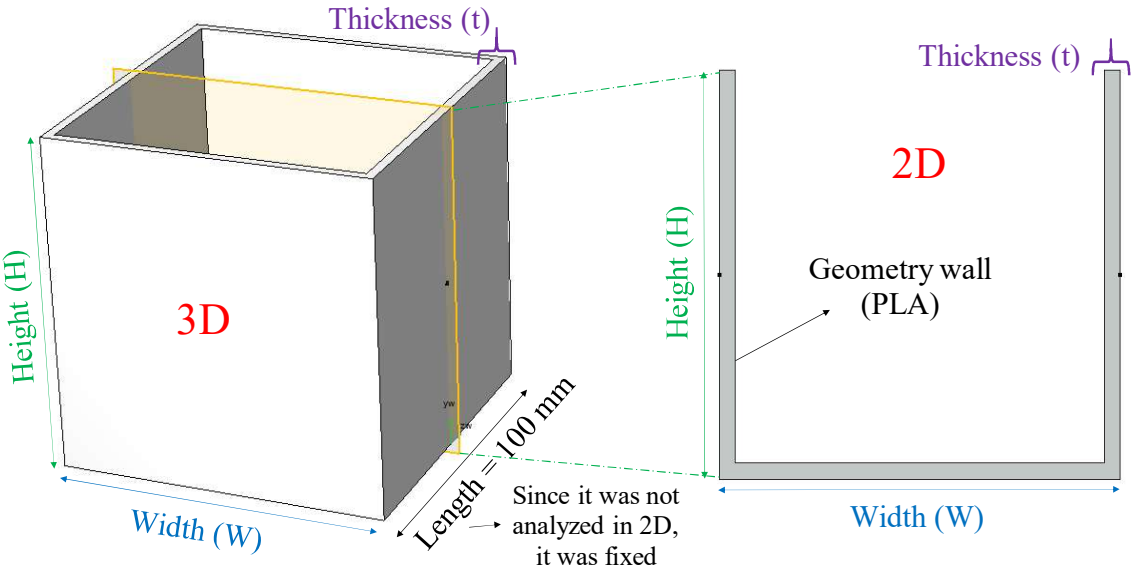

Source: elaborated by the author.

The Figure 48 shows the results of the finite element method (FEM) analysis used to evaluate how geometric dimensions influence the vibration response of the empty specimen.

Figure 48(a) presents a representative frequency response for fixed dimensions (W = 100 mm, H = 150 mm, t = 4 mm), where 46 resonance peaks were identified. Figure 48b illustrates that reducing the width leads to fewer resonance peaks, indicating a decrease in vibration intensity. Figure 48c shows that decreasing the height also reduces the number of peaks, suggesting greater vibrational stability. Figure 48d demonstrates that increasing the thickness significantly lowers the number of peaks, further stabilizing the frequency response. Overall, the results indicate that specimens with smaller width and height and greater thickness exhibit fewer resonance peaks, thereby minimizing vibration and enhancing stability for subsequent IRT analyses.

Based on the results obtained from the FEM simulations, the geometries shown in Figure 51 were selected for laboratory testing. Figures 51a and b represent the chosen configurations, G1 and G2, selected because they followed the tendency observed in the numerical analysis, showing fewer resonance peaks and, consequently, lower vibration intensity.

Figure 48 – Influence of geometric dimensions on the frequency response domain (a) frequency domain example (b) width (c) height and (d) thickness

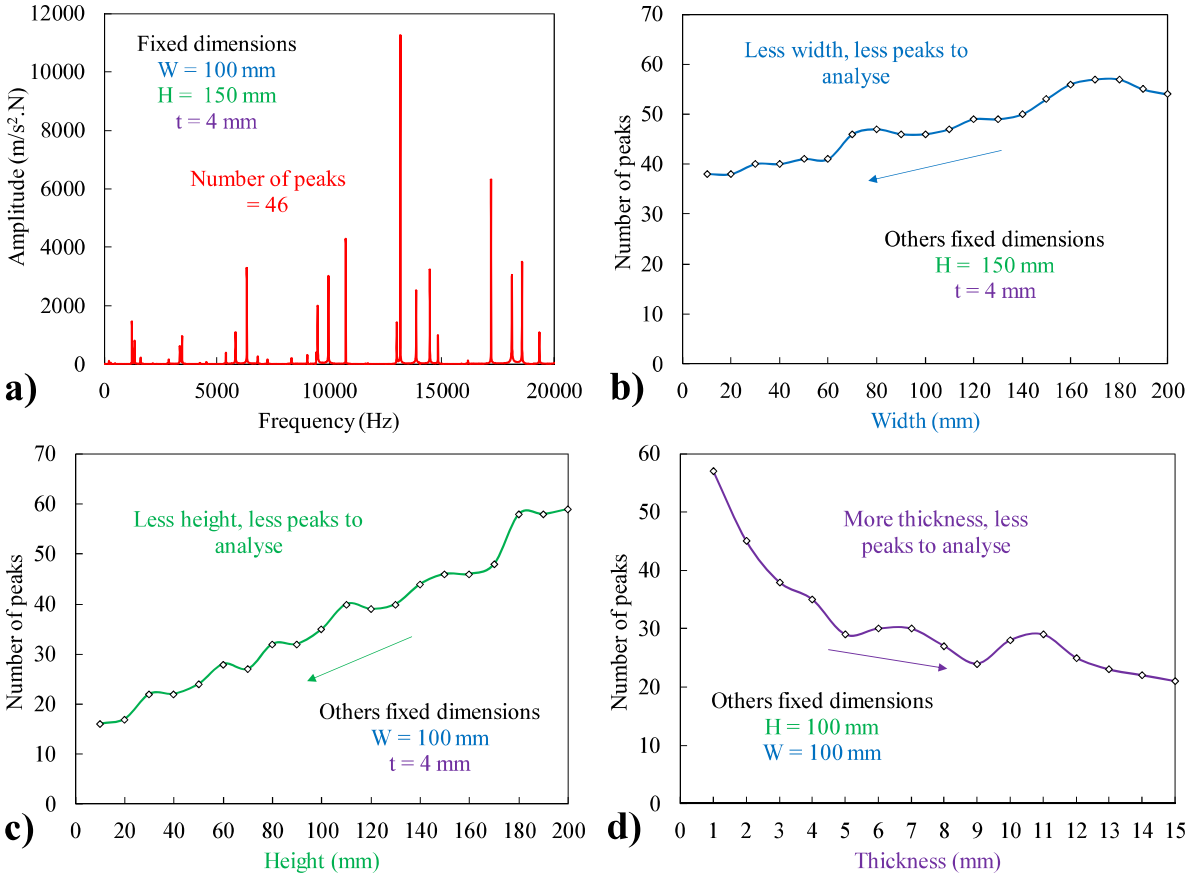

Source: elaborated by the author.

These geometries were designed to minimize the number of resonance peaks while maintaining suitable wall thickness for structural integrity. In addition, the height limitation was defined considering the subsequent ultrasonic tests, since this dimension is compatible with the transducer setup and allows efficient signal transmission and detection. In addition, the height limitation was defined considering the subsequent ultrasonic tests, as this dimension is compatible with the transducer size and allows proper coupling during measurements. Thus, the selected geometries provide a practical balance between vibration stability and experimental feasibility for both the Impact Resonance Test (IRT) and the planned ultrasonic evaluations.

The Figure 49 illustrates the modified geometry designed with vibration-reduction joints at the base. The use of these joints aims to decrease the vibration amplitude of the empty PLA box, ensuring that, in subsequent tests, the mechanical energy from the impact is primarily transmitted through the binder rather than through the PLA structure itself. This approach is intended to better simulate the real behavior of the binder material during the Impact Resonance Test (IRT). To identify a suitable material for the damping joint, a parametric study was conducted by varying the elastic modulus and density of the joint material while keeping the geometry fixed. This analysis allowed the evaluation of how different joint properties influence the vibration response, helping to determine the optimal combination for effective vibration reduction without compromising structural stability.

Figure 49 – Geometry incorporating a damping joint to reduce vibrations

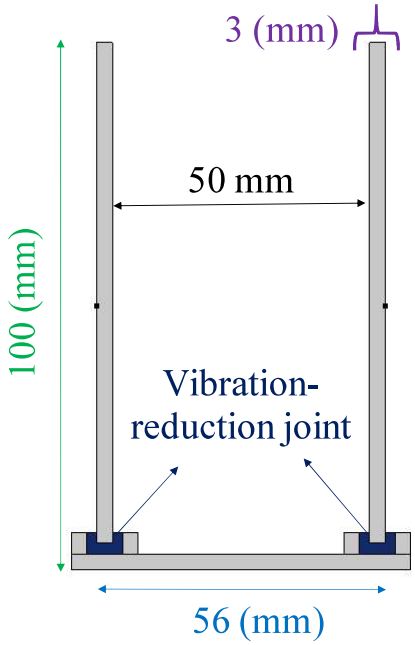

Source: elaborated by the author.

The Figure 50 shows that the number of resonance peaks depends strongly on the

joint material properties. In (a), the variation with elastic modulus is non-monotonic, very soft or very stiff materials reduce vibrations, while intermediate stiffness increases the number of peaks. In (b), increasing specific mass leads to more resonance peaks, indicating higher vibration intensity. Thus, joints made of lightweight materials with moderate stiffness are more effective in minimizing vibrations in the IRT setup.

Figure 50 – Impact of joint properties (a) Elastic modulus and (b) Specific mass

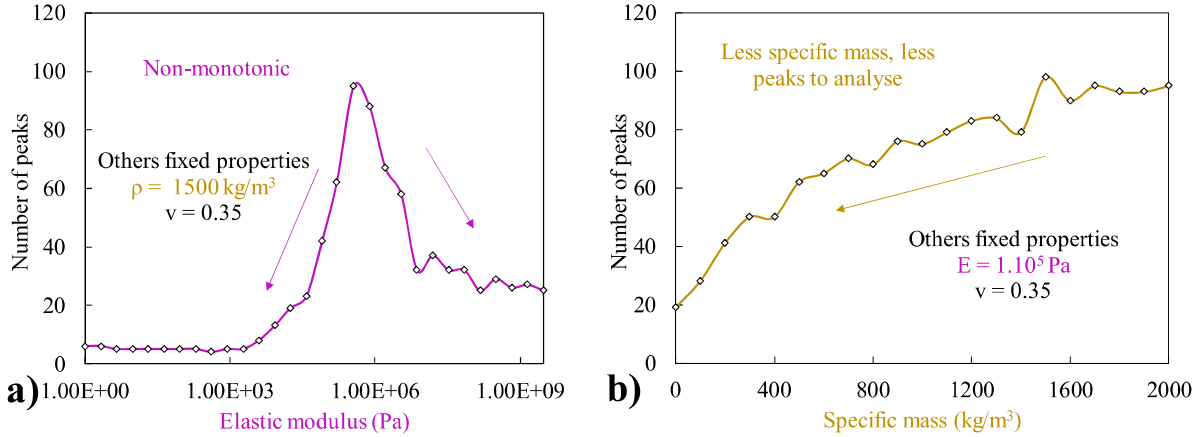

Source: elaborated by the author.

To evaluate how the joint material influences the vibration response in the laboratory, polyurethane and foam were selected as candidate materials. Both materials exhibit distinct combinations of density and stiffness that influence their vibration damping behavior. As shown in Figure 51c and 51d, the G3-P configuration employs polyurethane joints, while the G3-F configuration incorporates foam joints with identical geometry, respectively.

Figure 51 – Geometries tested in the laboratory (a) G1 (b) G2 (c) G3-P and (d) G3-F

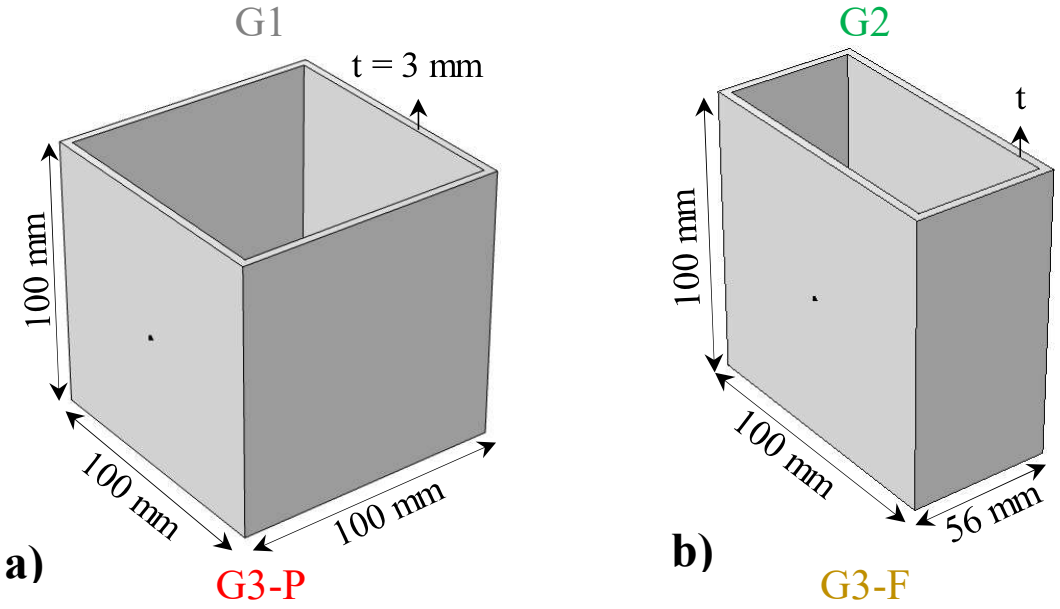

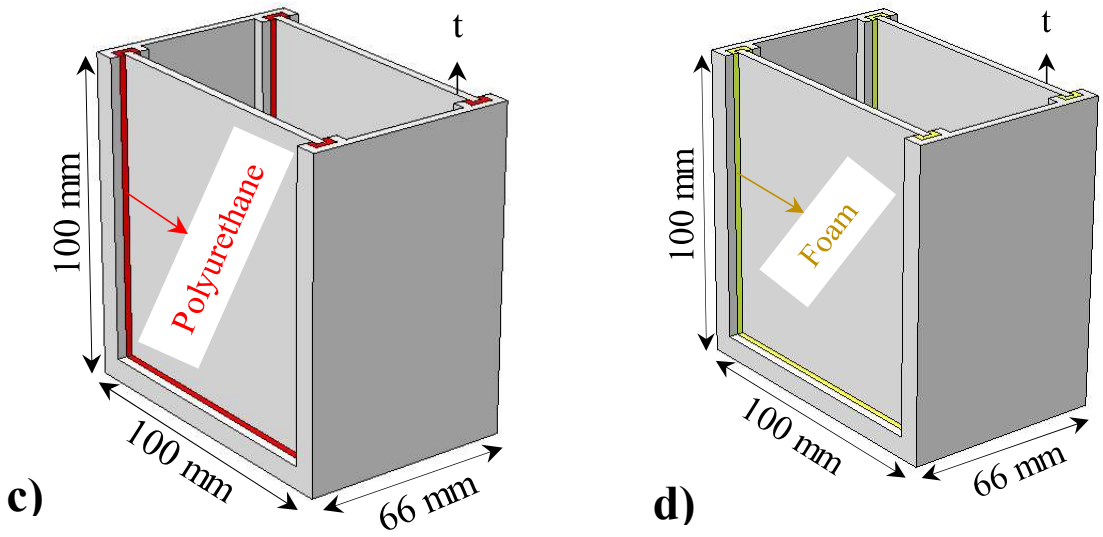

Source: elaborated by the author.

These materials were chosen because polyurethane typically presents an elastic modulus ranging from 0.06 to 2.1 MPa, depending on formulation low density (Domingos *et al.*, 2018), providing moderate stiffness and high energy absorption capacity. And, foams exhibit low elastic modulus and density, which enhances vibration damping through greater deformability and energy dissipation (Chen *et al.*, 2023).

4.4.2.3 Experimental results of the selected geometries

Figure 52 shows the experimental response of the empty geometries, presenting the frequency response functions (FRF) in Figure 52a and the coherence functions in Figure 52b. The FRF curves reveal that the G1 and G2 geometries exhibit a large number of vibration peaks, making peak identification and tracking more difficult. In contrast, the G3-based geometries display a reduced number of resonant peaks, which simplifies the analysis of frequency domain in later stages. The coherence plots further support this selection: G3-P maintains a high coherence level (close to 1) up to approximately 7000 Hz, indicating a more reliable and stable vibrational response.

Although G3-F also shows a reduced number of resonant peaks, its coherence function does not present any frequency range with consistently high values. This behavior does not necessarily indicate poor measurement quality, but rather reflects a strong attenuation of vibration transmission to the accelerometer, leading to coherence values close to 0 when no measurable response is detected. Nevertheless, in the absence of a stable frequency band with high coherence, reliable peak identification becomes impractical. Furthermore, despite its potential vibrational suitability, the G3-F geometry was excluded from subsequent analyses because the foam interface allows pore solution and free water from the fresh binder to leak

outside the geometry, thereby altering the effective formulation and compromising the repeatability of the measurements.

Based on the combination of fewer peaks (7) and higher coherence, G3-P was selected as the optimal geometry for subsequent binder analyses. Before performing the tests with the fresh binder, the empty G3-P geometry will be simulated to determine its 2S2P1D viscoelastic parameters using a full 3D FEM model. Once these parameters are calibrated, they will be fixed, allowing the following analyses to focus exclusively on the evolution of the binder's behavior.

Figure 52 – Experimental empty geometries results (a) FRF and (b) coherence function

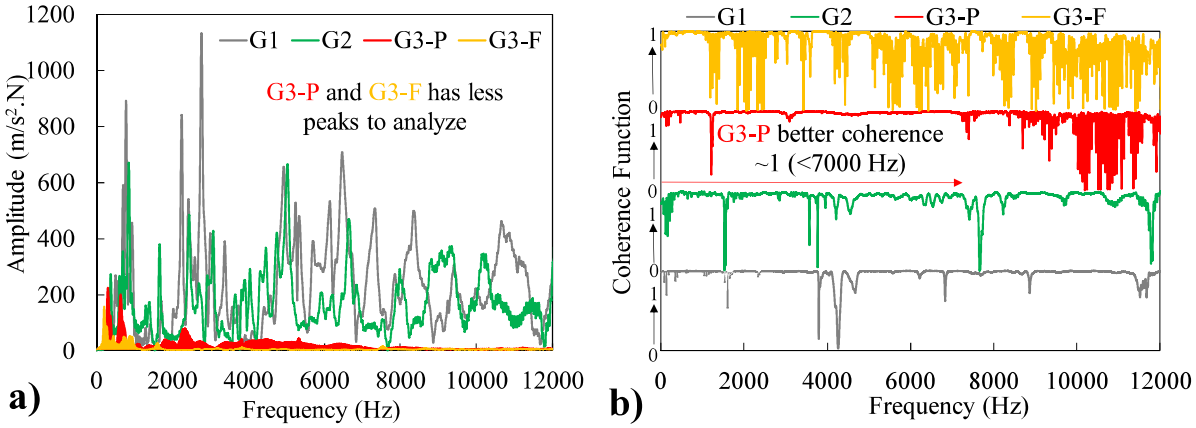

Source: elaborated by the author.

Figure 53 presents the experimental and simulated FRF of the empty G3-P geometry, together with the corresponding coherence function. The experimental and numerical curves show strong agreement across the analyzed frequency range, reflected by the high concordance correlation coefficient (CCC = 0.975). Among all identifiable modes, three resonant peaks, labelled as the 1st, 2nd, and 3rd peaks, are the most clearly defined in both experimental and simulated FRFs. These well-resolved peaks were therefore selected as the reference points for the 2S2P1D optimization.

Because the empty geometry is composed of two materials with distinct viscoelastic behavior, PLA forming the structural body and polyurethane acting as the damping joint, two independent 2S2P1D parameter groups were required. For each material, 10 viscoelastic parameters were calibrated, resulting in a total of 20 parameters used in the harmonic simulation. This separation was essential to accurately represent the mechanical contribution of each material and to achieve a reliable calibration.

Figure 53 – Experimental and simulated FRF of the empty G3-P geometry with coherence function

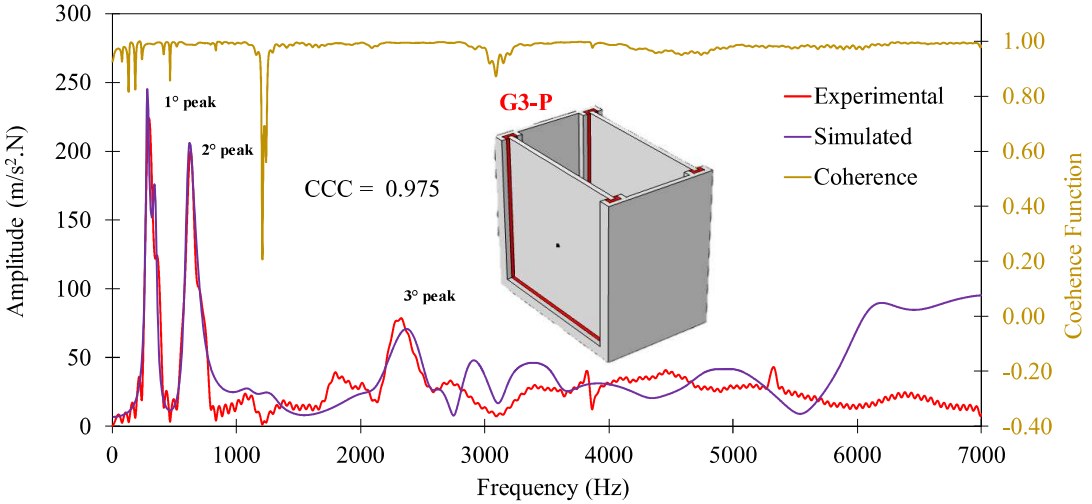

Source: elaborated by the author.

Table 17 presents the calibrated 2S2P1D parameters for the two materials composing the G3-P geometry: polyurethane (joint material) and PLA (structural body). The optimized 2S2P1D parameters from the PLA cylinder were also added to the table to compare the geometric influence using the same material. As expected, PLA exhibits much higher instantaneous and long-term moduli (E_{00} and E_0) compared to polyurethane. Conversely, polyurethane shows a much lower relaxation time (τ_e) and a substantially higher α exponent, consistent with its softer, more dissipative viscoelastic character.

Table 17 – 2S2P1D parameters materials to G3-P geometry

Parameter	Polyurethane	PLA		
		Cylinder	G3-P	Difference
E_{00} (Pa)	228323	574945752	176234756	-69.3%
E_0 (Pa)	2595825	2482262849	2800213241	12.8%
τ_e	0.049666	7.770858	0.472162	-93.9%
α	25.002689	0.548684	0.609907	11.2%
k	0.304845	0.143893	0.10496	-27.1%
h	0.976217	0.641324	0.978795	52.6%
β	0.000348	0.070557	0.03174	-55.0%
ν_{00}	**0.495137**	**0.360395**	**0.357957**	**-0.7%**
ν_0	**0.496968**	**0.407043**	**0.390254**	**-4.1%**
τ_ν	**0.43916**	**1.688496**	**12.946642**	**666.8%**

Source: elaborated by the author.

The PLA parameters obtained for the G3-P geometry differ noticeably from those determined previously using the solid PLA cylinder. This discrepancy is expected, because although both elements were printed with the same 99% infill, the G3-P geometry consists of thin 3 mm walls and when the printed dimensions are smaller, the filament paths, layer orientation, and inter-layer bonding have a strong influence on stiffness and damping, leading to different deformation modes during vibration. The essential point, however, is whether the

calibrated model reproduces the experimental behavior within the frequency range of interest, which will be demonstrated in the Figure 54.

Figure 54 compares the 2S2P1D viscoelastic response of PLA calibrated from the solid cylinder and from the G3-P geometry. In Figure 54a, the largest differences in the complex modulus |E*| appear at low frequencies, where the thin-walled geometry shows a softer response due to its reduced dimensions and greater filament influence. Above 100 Hz, both curves converge and become very similar, indicating that the geometric differences have minimal effect within the frequency range used in the resonance simulations.

Figure 54 – Differences of 2S2P1D model on PLA as cylinder and geometry (a) Complex modulus as function of frequency and (b) Cole-Cole

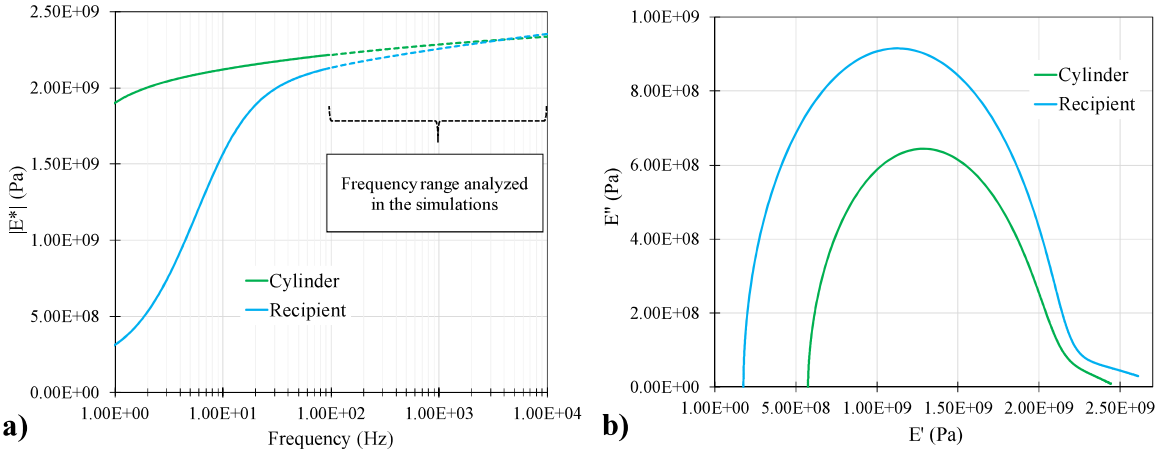

Source: elaborated by the author.

Figure 54b, the Cole-Cole diagram, highlights the main distinction between the two calibrations: the PLA parameters optimized for the recipient produce a larger and wider loop, indicating a more viscous character compared to the cylinder calibration. The slight distortion at high E′ is associated with the lower β value obtained during parameter fitting, which affects the tail of the relaxation spectrum.

4.4.2.4 Rheological binder evolution based on 2S2P1D parameters approach

Figure 55 presents the time-dependent evolution of the storage modulus (E′), loss modulus (E″), and phase angle for four excitation frequencies (a) 10 Hz, (b) 100 Hz, (c) 1000 Hz, and (d) 10000 Hz, obtained from IRT measurements performed every 15 minutes on the fresh binder. The purpose of these analyses is to evaluate whether IRT can provide usable viscoelastic information in the fresh state and to examine its potential as an alternative or complementary technique to conventional shear rheometer.

In this case, the curves do not display a clear or physically consistent evolution over

time, and no coherent trend can be identified for E′, E″, or phase angle across the different frequencies. Several factors may contribute to this behavior. First, the numerical simulation involves three different materials (PLA, polyurethane, and the evolving binder) within a full 3D model, making the problem computationally demanding and limiting the ability to refine the analysis. Second, the sensor may not have sufficient sensitivity to capture well-defined peak shapes during the very early, highly dissipative stages, resulting in noisy or inconsistent responses.

Figure 55 – Time-dependent evolution of E′, E″, and phase angle for different frequencies (a) 10 Hz (b)100 Hz (c) 1000 Hz and (d) 10000 Hz

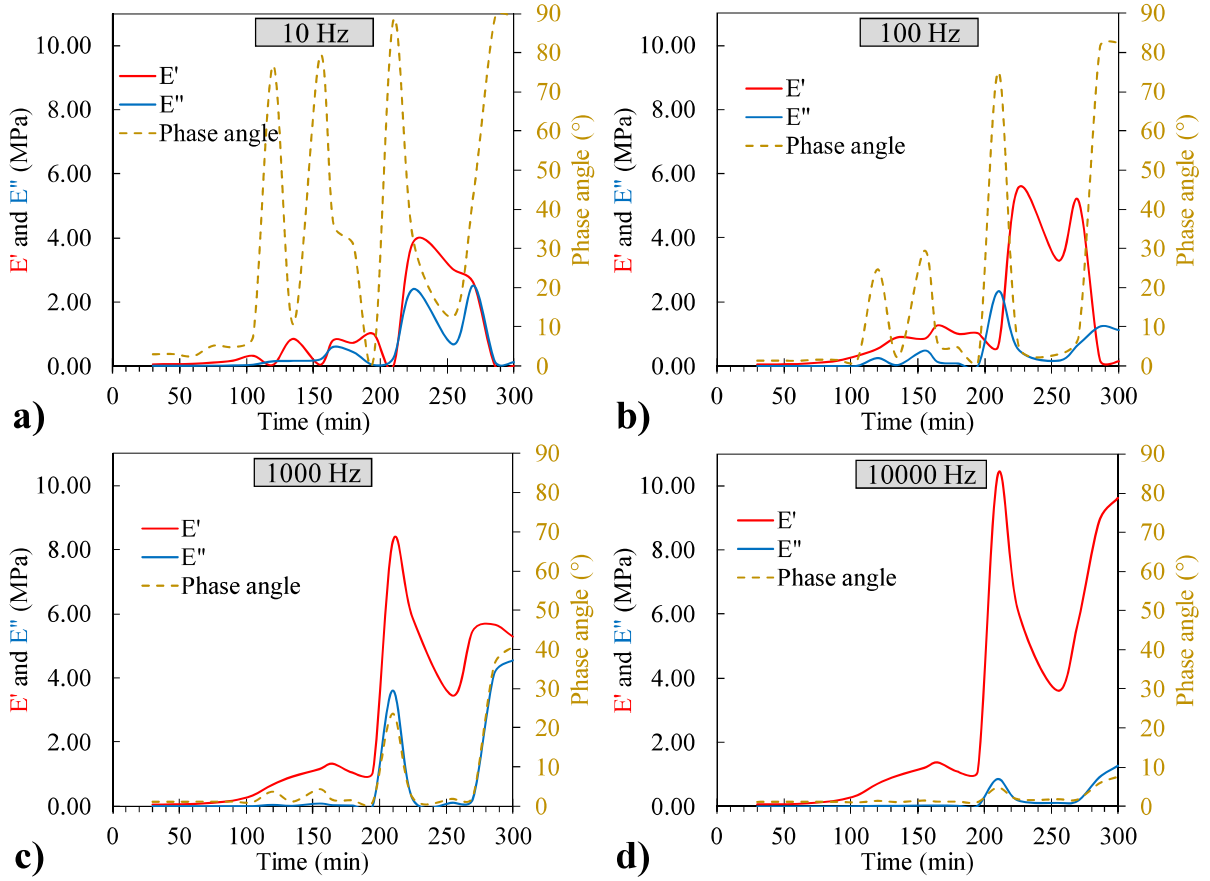

Source: elaborated by the author.

Additionally, because the resonance peaks shift significantly as the material hardens, the effective frequency range of interest evolves over time; as a result, the 2S2P1D extrapolation becomes unsuitable across the entire frequency domain, further reducing the reliability of the fitted parameters. Finally, the use of the 2S2P1D model may not be the most suitable representation for such a soft material, and exploring alternative rheological formulations could lead to more interpretable trends.

Even with these limitations, the numerical magnitudes of E′ and E″ obtained from

the IRT-based model remain broadly comparable to those measured by the rheometer, indicating that the method is not fundamentally incompatible with the binder's mechanical behavior. Although IRT does not yet reproduce the rheological evolution with the clarity or reliability of shear rheometers, the results suggest partial potential, particularly in capturing the correct order of stiffness, which supports further refinement of the approach for fresh-state characterization.

Since the 2S2P1D fitting procedure did not produce a coherent rheological tendency over time, the IRT data will be examined using an alternative strategy. Instead of relying on viscoelastic parameter optimization, the analysis will focus directly on the measurable vibration features extracted from the resonance response of the binder. This includes evaluating the impact wave velocity, as well as the evolution of resonance frequencies, peak amplitudes, and peak widths throughout the setting process. These quantities are closely related to stiffness development and energy dissipation and may provide more robust indicators of early-age behavior than the viscoelastic model alone. This alternative approach and its implications for monitoring the hardening of the binder are presented and discussed in the following results section.

4.4.2.5 Hardening behavior of the binder assessed through impact-wave velocity

Figure 56 presents the evolution of the impact wave velocity over time. Although many studies commonly employ ultrasonic pulse velocity to assess hardening, the present work determines velocity directly from the IRT. Here, the wave travel time was obtained from the difference between the input impact (hammer) and the output response (accelerometer), with the velocity computed using the linear distance between the opposite container walls.

A clear increase in wave velocity is observed as the binder hardens. This behavior aligns with numerous ultrasonic studies that demonstrate a strong link between velocity and microstructural evolution. For instance, Park *et al.* (2024) showed that longitudinal wave velocity increases as the material hardens due to densification and growth of stiffness, noting that velocity correlates with compressive strength and density as hardening proceeds. Similarly, Xu, D. *et al.* (2024) reported that at early ages cement paste behaves like a water-like viscous suspension, resulting in low velocity, but as hardening accelerates, the amplitude and velocity of the transmitted wave rise sharply, reflecting the formation of a stronger internal structure. These trends are further supported by classical UPV work.

Figure 56 – Impact wave velocity evolution over time

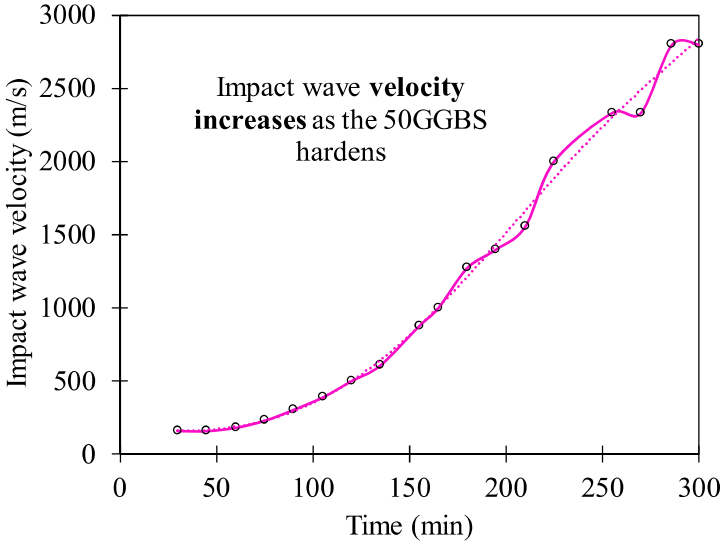

Source: elaborated by the author.

At later ages, the velocity continues to rise more gradually, accompanying microstructural densification, consistent with the theoretical dependence of wave velocity on elastic modulus and density described in ultrasonic frameworks. In the present binder, this behavior mirrors the complex modulus evolution previously observed in the time-sweep rheology (Figure 44). As G′ and G″ increase, the material acquires stiffness, enabling faster mechanical wave propagation.

Table 18 presents the Pearson correlation coefficients between the impact wave velocity and the rheological and calorimetric properties of the alkali-activated binder up to 300 min.

Table 18 – Pearson correlation between binder rheological and calorimetric properties and impact wave velocity (until 300 min)

	Pearson correlation
|G*|(MPa)	0.96
G' (MPa)	0.97
G" (MPa)	0.94
δ (°)	0.24
Cumulative heat (J/kg)	**0.99**

Source: elaborated by the author.

The Pearson correlation coefficient (r) measures the strength and direction of the linear relationship between two variables, with values close to 1 indicating a strong positive correlation, values near -1 a strong negative correlation, and values around 0 little or no linear relationship. The impact wave velocity shows a high positive correlation with the rheological stiffness parameters (|G|*, G′, G″; r = 0.96, 0.97, 0.94, respectively) and with the cumulative

heat (r = 0.99). In contrast, the phase angle (δ) exhibits a weak correlation (r = 0.24). Overall, these correlations confirm that impact wave velocity is a reliable and sensitive indicator of the hardening and reaction evolution of AABs.

4.4.2.6 Hardening behavior of the binder assessed through resonance frequency, amplitude, and peak width

This section evaluates the hardening of the 50GGBS binder by tracking the first three resonance peaks obtained from the impact resonance tests. Since the 2S2P1D model did not provide clear rheological trends in the fresh state, the analysis focuses instead on peak characteristics that can be directly extracted from the frequency response: resonance frequency, amplitude, and peak width. These parameters offer practical indicators of stiffness development, energy dissipation, and structural evolution during setting.

Figure 57 presents the temporal evolution of the first three resonance frequencies (1st RF, 2nd RF, and 3rd RF) of the 50GGBS binder obtained from IRT. Overall, all resonance frequencies show a progressive increase over time, indicating a continuous rise in stiffness.

Figure 57 – Resonance frequency of the first three resonance peaks over time

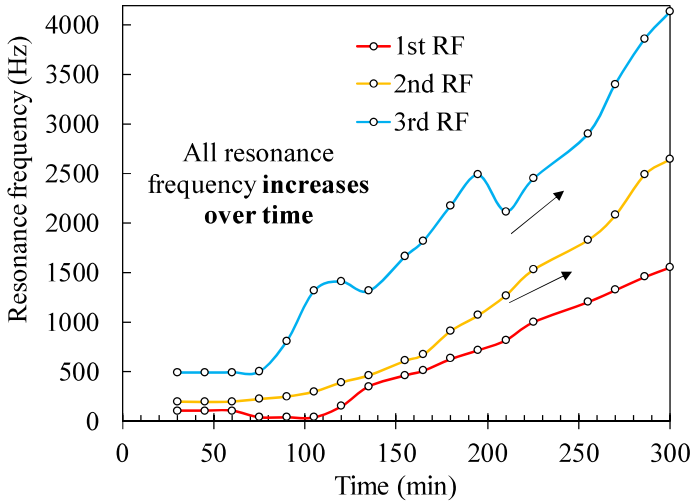

Source: elaborated by the author.

However, the onset and progression of the increase differ among the modes, which may indicate differences in their sensitivity to changes within the binder matrix. At the early stage (0-60 min), all resonance frequencies remain nearly constant, consistent with a fluid-like response and negligible elastic stiffness. The 2nd resonance frequency begins to increase first, at approximately 70 minutes, followed by the 3rd resonance frequency and then the 1st resonance frequency, which starts to rise more clearly after about 110 minutes. This sequence could suggest that the higher modes, are more responsive to early structural changes, while the

1st mode appears to capture the overall stiffening behavior of the material.

1st and 2nd resonance frequencies exhibit a clearer and more continuous increase. In contrast, the 3rd resonance frequency shows intermittent fluctuations, including a temporary decrease around 210 minutes, before continuing its upward trend. Such non-monotonic variations may result from transient microstructural adjustments, minor heterogeneities, or measurement sensitivity at higher modes. Overall, the evolution of resonance frequencies provides a consistent indication of stiffness development during the hardening, as also demonstrated by the time-sweep rheology and calorimetry results. Comparable multi-stage trends, initial plateau, rapid increase, and later stabilization, have been reported in ultrasonic monitoring studies of cementitious materials (Hong; Choi, 2021; Park *et al.*, 2024; Xu, D. *et al.*, 2024). These results demonstrate that resonance frequency monitoring can effectively capture the progressive hardening behavior of binders in a non-destructive manner.

Figure 58 shows the evolution of the peak amplitude of the first three resonance frequencies. In contrast to the clear increase observed in the resonance frequencies, the amplitude responses do not display a consistent or pronounced trend across all modes. The 1st resonance frequency exhibits a gradual decrease in amplitude over time, although the variation is relatively small. For the 2nd and 3rd resonance frequencies, the amplitude values fluctuate considerably, showing no clear monotonic behavior throughout the measurement period.

Figure 58 – Amplitude of the first three resonance peaks over time

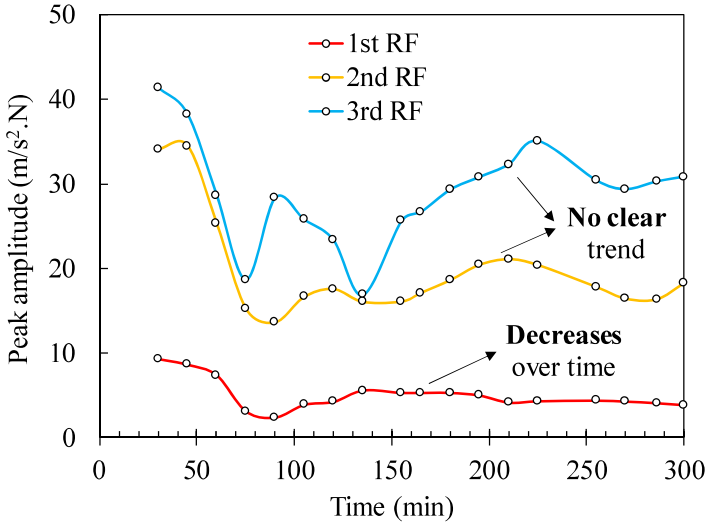

Source: elaborated by the author.

Similar irregular amplitude responses have been reported in ultrasonic monitoring of early-age cementitious systems, where scattering and microstructural rearrangements produce unstable signal magnitudes (Hong; Choi, 2021; Xu *et al.*, 2023).

Figure 59 shows the evolution of the peak width of the first three resonance frequencies, calculated at 0.707 of the peak amplitude. The peak width represents the damping or energy dissipation of the system, broader peaks indicate higher internal losses (Carret, 2018). The 1st resonance frequency shows a clear and steady increase over time, consistent with the rise in the viscous component (G″) observed in rheology, suggesting growing internal friction during hardening. The 2nd resonance frequency increases up to about 280 minutes and then decreases, while the 3rd resonance frequency shows no defined trend and fluctuates throughout the test. Overall, only the 1st mode exhibits a consistent increase, indicating a gradual enhancement of damping as the binder structure develops.

Figure 59 – Peak width of the first three resonance peaks over time

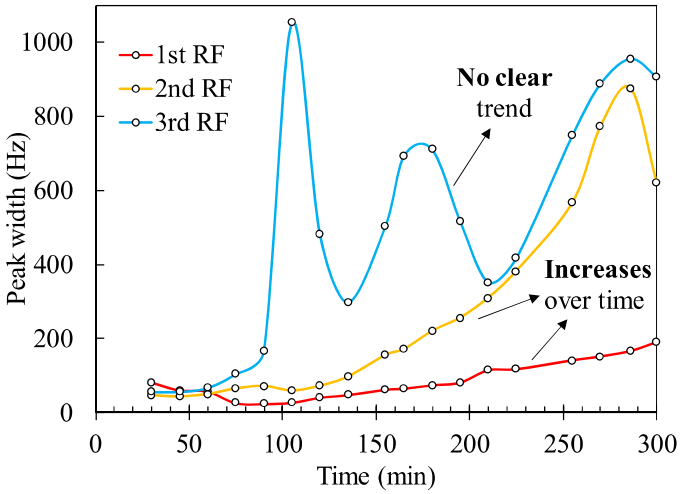

Source: elaborated by the author.

Table 19 presents the Pearson correlation coefficients between the resonance parameters (frequency, amplitude, and width) and the binder's rheological and calorimetric properties. The main objective of this analysis was to identify which resonance-based parameters best represent the binder's hardening behavior.

The phase angle (δ) does not show a strong correlation with any of the resonance parameters. When δ is not considered, the resonance frequency shows the highest and most consistent correlations with the rheological stiffness parameters and calorimetric response. Among the modes, the 2nd resonance frequency correlates most strongly with the rheological parameters |G|*, G′, and G″ (r = 0.99, 0.99, and 0.98, respectively), while the 1st resonance frequency shows the strongest relationship with the cumulative heat (r = 0.99). These results confirm that the resonance frequency closely follows both the mechanical stiffening and the reaction progress of the AABs.

Table 19 – Pearson correlation between binder rheological and calorimetric properties and resonance peak metrics (until 300 min)

	Resonance frequency (Hz)			Amplitude (m/s².N)			Width (Hz)		
Resonance Peak	1st	2nd	3rd	1st	2nd	3rd	1st	2nd	3rd
|G*|(MPa)	0.96	**0.99**	0.93	-0.35	-0.24	0.22	0.95	0.97	0.63
G' (MPa)	0.97	**0.99**	0.93	-0.35	-0.24	0.22	0.96	0.97	0.63
G" (MPa)	0.95	**0.98**	0.92	-0.33	-0.24	0.20	0.95	0.96	0.64
δ (°)	0.29	0.29	0.21	0.47	0.52	0.63	0.49	0.31	0.03
Cumulative heat (J/kg)	**0.99**	0.97	0.98	-0.43	-0.39	0.11	0.90	0.93	0.72

Source: elaborated by the author.

The peak width also correlates positively with these parameters, particularly for the 1st and 2nd resonance peaks (r ~ 0.95-0.97), while the correlation weakens for the 3rd peak (r ~ 0.63-0.64). This suggests that the width can reflect damping and viscous effects but with lower consistency at higher modes. In contrast, the peak amplitude shows weak or negative correlations with the reference properties, indicating that it is not a reliable indicator of the hardening process and is likely influenced by transient coupling or measurement variability.

Overall, these results indicate that the resonance frequency is the most representative parameter for monitoring the hardening of AABs, with the 2nd mode best reflecting rheological stiffening and the 1st mode showing the strongest relationship with cumulative heat, while the peak width provides complementary but less stable information related to energy dissipation during structural development.

4.5 Section conclusions

The objective of this study was to design, develop, and validate an impact resonance test apparatus capable of monitoring the hardening process of AABs in the fresh state. The tests were performed on an AAB formulated with GGBS and fly ash. The test geometries were manufactured by 3D printing in polylactic acid (PLA). In the resonance tests, a 2S2P1D rheological model was applied to analyze the binder's viscoelastic evolution over time. The resonance data were evaluated in terms of frequency, amplitude, and peak width, and correlated with rheological (|G*|, G′, G″, δ) and calorimetric parameters to assess their suitability as NDT indicators of microstructural development. The main conclusions are summarized as follows:

- The G3-P geometry, which uses a polyurethane-filled joint, was the most suitable, reducing unwanted vibrations and yielding fewer resonance peaks with a stable coherence function up to 7000 Hz;
- The evolution of E′, E″, and phase angle (by IRT) between 10 and 10,000 Hz showed

no consistent trends compared with rheology, possibly due to limited sensor sensitivity in the early highly dissipative stages, the suitability of the 2S2P1D model for very soft binders, and the continuous shift of resonance peaks during hardening, which alters the effective frequency range and compromises the stability of the fitted parameters;

- The impact wave velocity showed strong correlations with rheological stiffness parameters (|G*|, G′, G″; $r \geq 0.94$) and cumulative heat ($r = 0.99$), confirming its sensitivity to the binder's hardening and reaction progress;
- The resonance frequency proved to be the most representative parameter for monitoring the hardening of AAB. The 2nd mode showed the strongest correlation with the rheological stiffness parameters (|G|*, G′, G″; $r \geq 0.98$), while the 1st mode correlated best with the cumulative heat ($r = 0.99$);
- The peak width exhibited moderate correlations ($r \sim 0.95$-0.97) for the first two modes, suggesting partial sensitivity to damping and viscous effects, while the amplitude showed weak or inconsistent relationships with the reference properties;

5 HARDENING KINETICS OF ALKALI-ACTIVATED BINDERS EVALUATED THROUGH IMPACT RESONANCE TEST, RHEOLOGY, AND CHEMICAL CHARACTERIZATION

5.1 Introduction

The hardening of alkali-activated binders (AABs) follows the interconnected stages described by Duxson *et al*. (2007), where dissolution, speciation, gelation, and polymerization occur simultaneously. OH^- ions break Si-O-Si and Al-O-Si bonds, releasing reactive species into solution (Duxson *et al*., 2007; Siyal *et al*., 2024), with dissolution rates governed by precursor chemistry and activator composition (Liu *et al*., 2023). Low-calcium precursors dissolve more slowly, whereas calcium-rich systems show higher early reactivity (Huang *et al*., 2024; Xu *et al*., 2024). As dissolved species accumulate, condensation reactions produce N-A-S-H or hybrid C-A-S-H/N-A-S-H gels (Guan *et al.,* 2022; Provis; Bernal, 2014), which progressively reorganize and densify (Aversa *et al*., 2024; Tognonvi; Pascual; Tagnit-Hamou, 2022). Continued polycondensation strengthens the aluminosilicate network (Keppert *et al.,* 2024), further consolidating the gel structure during hardening. Given the complexity of these coupled mechanisms, advanced techniques capable of monitoring hardening in real time are needed to better characterize AAB early-age behavior.

A range of techniques has been used, although many face practical limitations related to high cost, equipment complexity, and the difficulty of performing continuous measurements (Jiang; Shi; Zhang, 2022; Park *et al.*, 2024). FTIR spectroscopy provides valuable insight into chemical and structural evolution but requires specialized instrumentation and is not easily adapted for real-time monitoring (Keppert *et al.*, 2024; Park *et al.*, 2024). Isothermal calorimetry is a powerful tool for assessing reaction kinetics, yet calorimeters are expensive and mainly offer indirect information about mechanical development (Keppert *et al.*, 2024; Siyal *et al.*, 2024).

In response to these challenges, non-destructive techniques (NDT) have gained increasing attention for early-age monitoring, as they allow continuous assessment of mechanical evolution without interrupting the material (Xu, D. *et al.*, 2024; Park *et al.*, 2024). Among these methods, ultrasonic testing has been widely adopted for tracking stiffness development during hardening (Xu, D. *et al.*, 2024; Park *et al.*, 2024). However, wave-based methods, such as impact resonance test (IRT), offer low-cost, simple, and effective alternatives, providing sensitivity to stiffness and damping changes through frequency-domain analysis.

These advantages make impact resonance an attractive option for expanding real-time and affordable monitoring of AAB hardening. However, this technique remains unexplored in fresh state applications, it has only been applied to hardened materials (Carret, 2018; Bezerra *et al.*, 2023; Herozi *et al.*, 2025).

Nevertheless, one key point must be highlighted: integrating multiple experimental techniques is essential for identifying meaningful relationships between chemical, thermal, rheological, and mechanical indicators of hardening. Early-age FTIR and TGA provide essential chemical and thermal evidence of gel formation and water evolution (Keppert et al., 2024; Park et al., 2024), while calorimetry and rheology clarify how reaction kinetics translate into progressive stiffness development (Aversa et al., 2024; Siyal et al., 2024). IRT can capture the mechanical manifestation of these transformations by tracking stiffness evolution through frequency-domain responses. The combined interpretation of these complementary datasets strengthens the overall understanding of early-age behavior in AAs, although such integrated analyses remain largely unexplored in the current literature.

Based on this context, the objective of this study is to investigate the hardening kinetics of AABs through an integrated experimental program combining IRT, rheological measurements, chemical characterization, thermal analyses, and conventional fresh state tests. To achieve this, three AABs are evaluated, varying the proportion of GGBS and fly ash to obtain binders containing 50%, 75%, and 100% GGBS, allowing assessment of how calcium content influences early-age reactions and mechanical evolution. The experimental program includes setting time measurements, and time-sweep rheology, alongside continuous impact resonance test to monitoring to obtain resonance frequency during the hardening. Reaction kinetics are assessed through isothermal calorimetry, while microstructural evolution is examined using FTIR and TGA. All techniques are applied at very early ages, up to approximately 5 hours, to capture dissolution, gel nucleation, and early polymerization. By correlating wave-based mechanical indicators with chemical, thermal, and viscoelastic evolution, this study aims to identify the most sensitive descriptors of early-age hardening and to evaluate the potential of impact resonance as a low-cost, real-time monitoring technique for AABs.

5.2 Materials

The raw materials used for producing the AABs in this study were the same as those described previously in Section 4.2.2, namely ground granulated blast-furnace slag (GGBS) and fly ash (FA). Based on these precursors, three binders were formulated by varying the

GGBS content to 50%, 75%, and 100%, while maintaining a constant silica modulus (SiO_2/Na_2O, mol/mol) of 0.25, an alkali content (Na_2O/Binder, g/g) of 14% Na_2O and a water content (H_2O/Binder, g/g) ratio of 0.40, as summarized in Table 20. Sodium hydroxide (NaOH) and sodium silicate (Na_2SiO_3), described earlier, were used as activators.

Table 20 – Alkali-activated binder mix proportion

ID	GGBS-FA (%)	GGBS (g/L)	FA (g/L)	Na_2SiO_3 solution (g/L)	NaOH solution (g/L)
50GGBS	50-50	562.90	562.90	137.11	558.81
75GGBS	75-25	870.74	290.25	141.40	576.27
100GGBS	100-0	1198.44	0.00	145.96	594.86

Source: elaborated by the author.

The decision to vary the precursor proportions was made to more clearly reveal differences in reaction kinetics among the binders, since the contrasting oxide compositions of GGBS and FA, particularly their CaO, influence early-age chemical and mechanical evolution (Siyal *et al.*, 2024). The characterization of particle size distribution, oxide composition, and FTIR for these precursors was already presented in the preceding sections.

5.3 Methods

5.3.1 Setting time

According to the methodology detailed in Section 4.3.1.1.

5.3.2 Time sweep rheology

According to the methodology detailed in Section 4.3.1.1.

5.3.3 Isothermal calorimetry

According to the methodology detailed in Section 4.3.1.2.

5.3.4 Impact resonance test (IRT)

The development and validation of the apparatus for applying the impact resonance test (IRT) in the fresh state, as well the processing procedures, were detailed in Chapter 3. Based on those results, the optimized geometry configuration was selected for the present study to ensure reliable detection of early-age mechanical evolution. Using this configuration, the impact signals were recorded at each 15 min and processed using MATLAB to extract the

impact wave velocity (IWV) and the first and second resonance frequencies, which serve as indicators of stiffness development and structural transition during the hardening of the AABs.

5.3.4.1 Impact wave velocity (IWV)

Figure 60a shows the experimental configuration adopted for the IRT in the fresh state. The binder is placed inside a rectangular geometry and a impact hammer is positioned on one wall to generate the input pulse, while a uniaxial accelerometer is mounted on the opposite face to capture the transmitted signal. This geometry minimizes early-age boundary reflections and improves the accuracy of wave-arrival detection. Figure 60b illustrates the procedure used to determine the Time of Flight (ToF) between the hammer impact and the arrival of the mechanical wave at the accelerometer. The first force signal (t_1) marks the exact moment of impact, while the beginning of the first distinguishable acceleration peak (t_2) corresponds to the wave arrival. The difference ($\Delta t = t_2 - t_1$) defines the ToF.

Figure 60 – IRT in the fresh state (a) geometry used and (b) Time of flight (ToF)

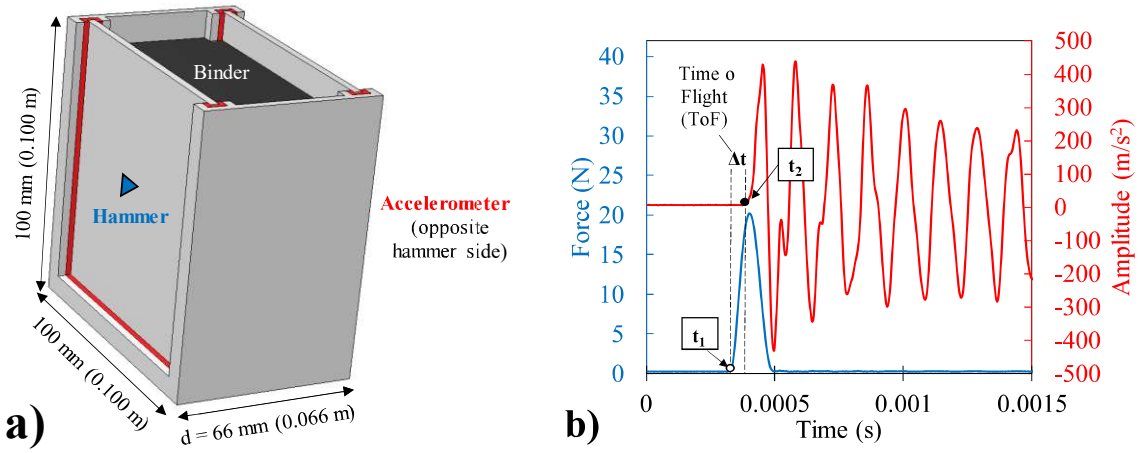

Source: elaborated by the author.

The IWV was then computed using Equation 19, which relates the travel distance between the hammer and the sensor (0.056 m) to the measured ToF (Δt):

$$IWV\ (m/s) = \frac{0.056\ (m)}{\Delta t\ (s)} \tag{19}$$

5.3.4.2 Resonance frequency

Figure 61 presents a representative FRF used to illustrate the procedure for identifying the first and second resonant peaks of the system (more details about FRF was presented in the section 3.3.2). For all measured times, this same peak-identification procedure was systematically applied to the FRFs. The processing was performed using custom MATLAB

scripts developed to automatically locate local maxima, assign the 1st and 2nd resonant modes, and extract their corresponding frequencies with high precision. Since resonant mode is governed by the rheological properties of the material (Bezerra *et al.*, 2023), changes in resonant frequency provide a reliable indicator of stiffness evolution throughout the hardening process.

Figure 61 – Identification of the 1st and 2nd resonant peaks by FRF

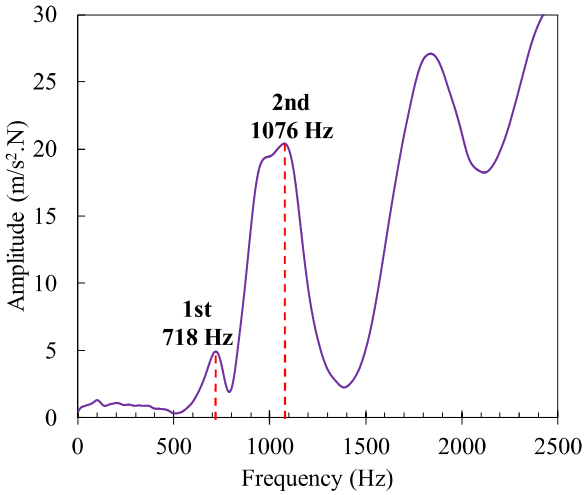

Source: elaborated by the author.

5.3.5 Fourier Transform Infrared Spectroscopy (FTIR)

Fourier transform infrared (FTIR) spectroscopy is a technique that records the interaction between infrared radiation and matter, allowing the identification of functional groups through their characteristic vibrational bands (Nguyen *et al.*, 2022). In this study, it was followed FTIR methodology proposed by Hoyos-Montilla *et al.* (2022), with the difference that earlier hardening ages were investigated. This approach was used to monitor the temporal evolution of the main bands in AABs, with measurements collected every 30 minutes from mixing up to 5 hours. Complemented by 1, 7 and 28 days of curing to evaluate the stability of the formed products. FTIR spectra were acquired using a Shimadzu IR Prestige 21 spectrometer, operating with 4 cm^{-1} resolution over the 400-4000 cm^{-1} range.

5.3.6 Thermogravimetric Analysis (TGA)

Thermogravimetric analysis (TGA) monitors mass changes of a sample under controlled heating, providing information on decomposition events, thermal stability, and material composition (Yu *et al.*, 2024; Bílek *et al.*, 2025; Luo *et al.*, 2025). Unlike FTIR, which allows rapid sequential measurements, TGA is a slower technique; therefore, only two

measurement was performed in the fresh state, the first at 30 min and another one 300 min (5 h) after mixing, complemented by another at 28 days of curing to evaluate the stability of the formed products. Analyses were conducted using a Shimadzu DTG-60H, with samples heated from 25 to 1000 °C at 10 °C/min under an inert nitrogen atmosphere (50 mL/min). The derivative thermogravimetric curves (DTG) were analyzed to identify characteristic decomposition steps, quantify bound water, and assess microstructural transformations during hardening and long-term stabilization.

5.3.7 Compressive strength

At 28 days, compressive strength was determined using a universal test machine operating at a loading rate of 0.5 mm/min with a 300 kN load cell. For each condition, three cubic specimens of 40 mm were tested, and the average value obtained was employed to compare the binders in the hardened state.

5.4 Results and discussion

5.4.1 Setting time

The Figure 62 illustrates the evolution of initial and final setting times of ABBs. Increasing the GGBS content consistently accelerates setting. The 50% GGBS mixture shows the slowest kinetics, with an initial setting time of approximately 170 min and final setting at 230 min. When the GGBS proportion increases to 75%, both values decrease substantially to 95 min (initial) and 150 min (final). The binder composed entirely of GGBS exhibits the fastest reaction, reaching initial set at 80 min and final set at 130 min.

Figure 62 – Initial and final setting times

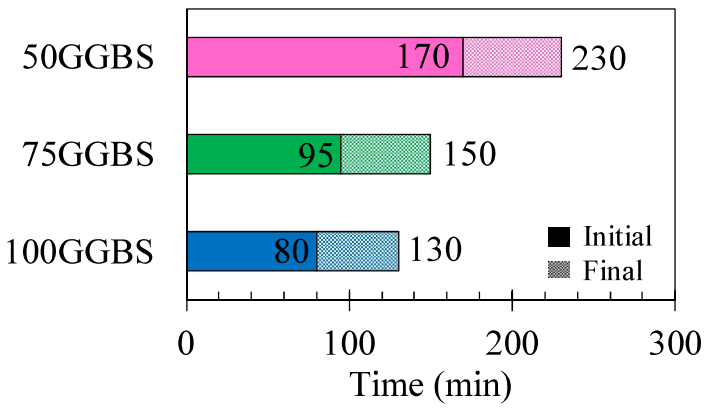

Source: elaborated by the author.

These results are consistent with the findings of previous studies (Huang, G. *et al.*,

2024; Siyal *et al.*, 2024; Shi *et al.*, 2022). This acceleration is primarily attributed to the higher calcium content provided by GGBS, which enhances the formation of C-A-S-H gels and promotes rapid hardening under alkaline conditions (Huang, G. *et al.*, 2024; Siyal *et al.*, 2024).

5.4.2 Time sweep rheology

Figure 63 shows the evolution of G′, G″, and phase angle for the binders with (a) 50GGBS, (b) 75GGBS, and (c) 100GGBS. An increase in GGBS content accelerates the development of G′, indicating an earlier gain in stiffness, which is consistent with the setting-time results. This behavior agrees with previous research showing that slag-rich binders exhibit faster geopolymerization kinetics because of their higher calcium content (55.84 wt% CaO for GGBS vs. 4.60 wt% for fly ash) and finer particle size (D_{90} = 33.0 μm for GGBS vs. 72.2 μm for fly ash), which together enhance dissolution and early gel formation (Dai *et al.*, 2020; Alnahhal; Kim; Hajimohammadi, 2021; Shi *et al.*, 2022).

Before the initial setting, all mixtures show predominantly viscous behavior characterized by low G′ and G″ and high phase angles. This period corresponds to precursor dissolution and ion accumulation (Palacios *et al.*, 2021; Egnaczyk; Quinn; Wagner, 2025), where the system remains fluid and unconnected. The higher surface area (due the lowest particle size) of GGBS accelerates ion release and initial gel nucleation, producing noticeable rheological responses even before network formation (Alnahhal; Kim; Hajimohammadi, 2021; Huang, G. *et al.*, 2024). In contrast, the 50GGBS binder remains more fluid because the lower-Ca, coarser fly ash dissolves slowly and contributes less to early C-A-S-H gel formation (Siyal *et al.*, 2024).

Between the initial and final setting times, the binders transition from a viscous suspension to a percolated solid network. The sharp increase of G′ and its overtaking of G″ mark the formation of a continuous gel skeleton, similar to the structural build-up patterns reported by Alnahhal, Kim and Hajimohammadi (2021). The 100GGBS mixture exhibits the fastest transition (80-130 min), followed by 75GGBS (95-150 min) and 50GGBS (170-230 min). The phase angle (δ) stabilizes or slightly increases during this interval but remains lowest for slag-rich binders. Thus, the higher GGBS content compress the setting window and accelerate mechanical percolation (Sun *et al.*, 2022; Zhang; Liu; Liu, 2024).

Figure 63 – Time sweep rheology with G', G" and phase angle over time at 10Hz and 20°C (a) 50GGBS (b) 75GGBS and (c) 100GGBS

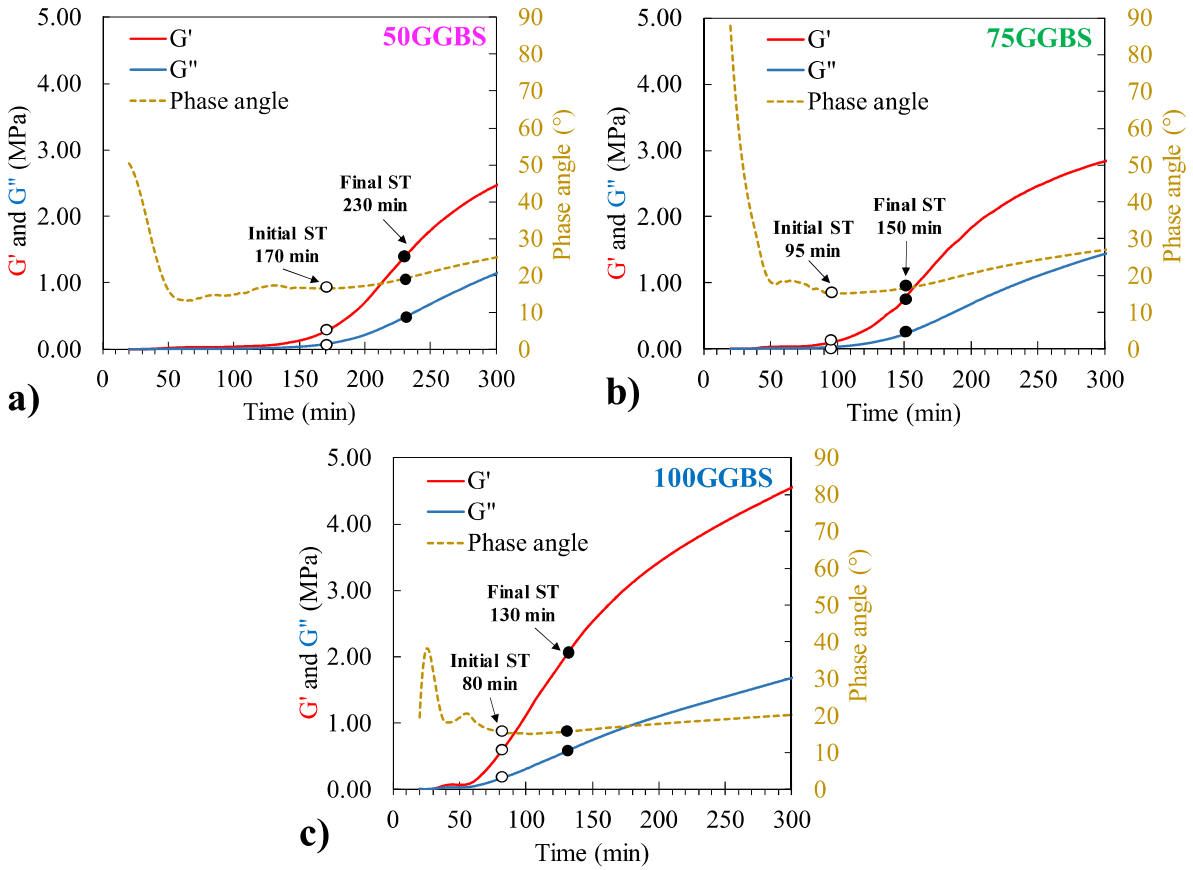

Source: elaborated by the author.

After the final setting, all binders exhibit predominantly elastic behavior, but their hardening rate and stiffness magnitude depend on GGBS content. The 50GGBS binder shows gradual G′ growth. The 75GGBS reaches intermediate stiffness, while 100GGBS exhibits the steepest and highest post-setting increase in G′, forming a dense and rigid structure within a shorter period. This behavior promotes rapid gel interconnectivity and structural densification (Shi *et al.*, 2022; Egnaczyk; Quinn; Wagner, 2025).

Figure 64 shows the derivative evolution of (a) dG′/dt and (b) dG″/dt for the binders. In Figure 64 (a), the dG′/dt curves highlight how the rate of elastic-network formation increases with slag content. The 100GGBS binder presents the earliest and most intense peak, indicating the fastest stiffening, followed by 75GGBS, while 50GGBS shows the slowest evolution. Although higher GGBS contents clearly accelerate the rate of modulus development, the position and shape of the dG′/dt peaks do not show a direct correlation with the empirically measured initial and final setting times.

Figure 64 – Derivative evolution of (a) G′ and (b) G″ for binders with different GGBS contents

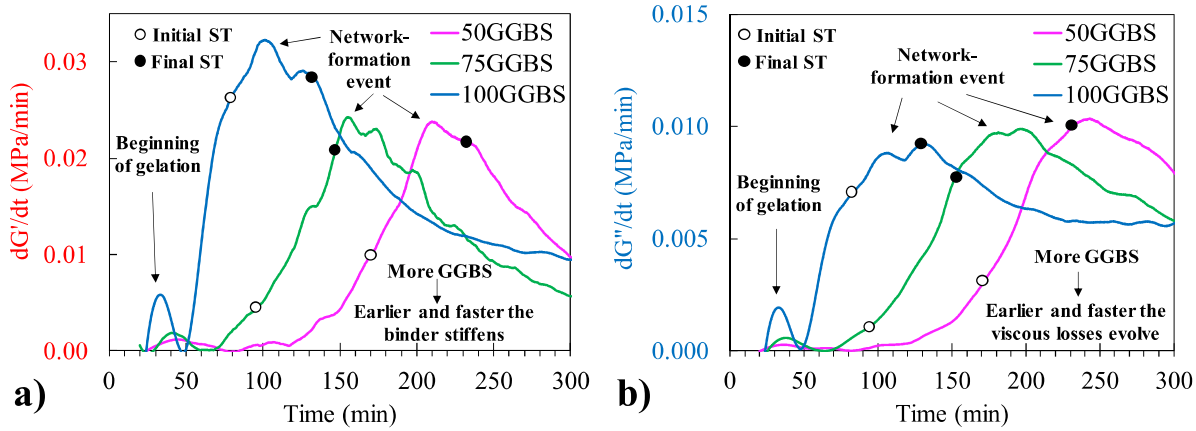

Source: elaborated by the author.

The Figure 64b, the dG″/dt curves show how the rate of viscous-loss evolution is influenced by GGBS content. The evolution of dG″/dt clarifies the different phase-angle behaviors. In 50GGBS, dG″ reaches a higher and later peak, meaning viscous losses continue to grow for a longer period; this produces the more pronounced increase in phase angle. The 75GGBS binder shows the same trend but with lower intensity. In contrast, 100GGBS exhibits a much earlier and smaller dG″ peak, and after this point the rate changes only slightly, so viscous losses do not rise significantly. As a result, the phase angle remains almost constant for 100GGBS, while it increases clearly in the mixtures with lower slag content.

A possible explanation for the differences in phase-angle evolution is related to how the gel network may develop as the GGBS content varies. For the binders 50GGBS and 75GGBS, it is plausible that a slower and less cross-linked C-A-S-H network allows a greater amount of long, partially connected polymeric species, sustaining viscous dissipation during hardening. This would justify the higher and later dG″ peaks and the more pronounced increase in phase angle, as the viscous contribution continues to grow even while G′ increases. In contrast, for the 100GGBS, the rapid and denser gel formation may limit the presence of mobile polymeric chains, reducing viscous losses at later ages. This would explain why dG″ peaks earlier and remains small and why the phase angle stays nearly constant. Although this interpretation requires further validation.

5.4.3 Isothermal calorimetry

The Figure 65 shows the isothermal calorimetry over 300 min: (a) Flow heat and (b) Cumulative heat. Figure 65 a) demonstrate that the reaction kinetics are strongly influenced by the GGBS content, with higher slag proportions leading to greater heat evolution and faster

reaction rates. The initial dissolution peak (0-45 min) was disregarded due to thermal disturbance from sample insertion (Sun; Vollpracht, 2018).

After that, the dormant period is the short stage after the initial dissolution when reaction heat temporarily stabilizes before gel formation begins (Sun; Vollpracht, 2018). In all binders, it is very short, showing that dissolution and polycondensation occur almost simultaneously (Dai *et al.*, 2020; Huang, G. *et al.*, 2024). After this initial period, a clear main exothermic peak is observed, corresponding to the polycondensation and gelation stages of the reaction, during which the N-A-S-H and C-A-S-H gels form and begin to crosslink (Chithiraputhiran; Neithalath, 2013; Sun; Vollpracht, 2018; Dai *et al.*, 2020; Siyal *et al.*, 2024). The increase in the peak magnitude with increasing GGBS content indicates a higher overall reaction rate and heat release due to the greater availability of reactive CaO from slag, which promotes rapid formation of calcium aluminosilicate hydrate networks (Dai *et al.*, 2020; Sun; Vollpracht, 2018). After the main peak, the heat flow decreases, indicating the diffusion-controlled stage, where residual particles slowly react and the gels densifies (Sun; Vollpracht, 2018; Keppert *et al.*, 2024).

Figure 65 – Isothermal Calorimetry 300 min (a) Flow heat and (b) Cumulative heat

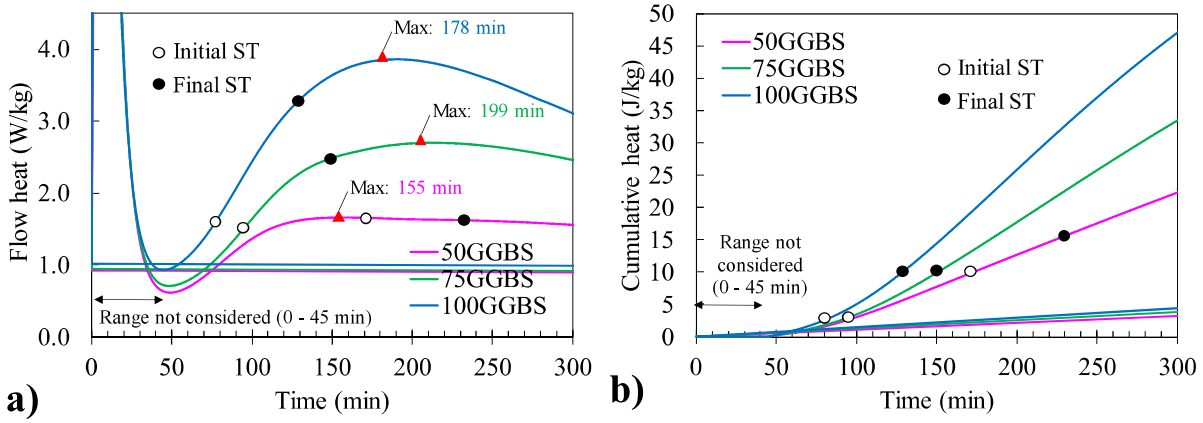

Source: elaborated by the author.

The timing of the main calorimetric peaks (155 min for 50GGBS, 178 min for 100GGBS, and 199 min for 75GGBS) indicates that the reaction rate does not scale linearly with slag content. Similar non-monotonic behavior has been reported in several studies, where the competition between dissolution, ion diffusion, and gel growth determines the apparent rate of heat evolution (Sun; Vollpracht, 2018; Dai *et al.*, 2020). Higher slag content supplies more reactive calcium and alkalinity, accelerating dissolution and the early formation of C-A-S-H gels (Sun; Vollpracht, 2018; Huang, G. *et al.*, 2024). However, when calcium concentration becomes very high, rapid precipitation of early gels nuclei can create localized surface

passivation layers, temporarily reducing the availability of reactive sites and slowing further polycondensation (Chithiraputhiran; Neithalath, 2013; Dai *et al.*, 2020). This self-limiting effect explains why the 100GGBS mixture, although richer in reactive slag, does not reach its maximum heat release as quickly as 50GGBS.

As the flow heat increased with higher GGBS content (Figure 65a), it is natural that the cumulative heat curves in Figure 65b followed the same trend. Through the cumulative curves, the differences between the mixtures become even clearer, reinforcing that GGBS-rich binders react more extensively and develop faster than those with lower slag proportions (Keppert *et al.*, 2024; Egnaczyk; Quinn; Wagner, 2025).

At 7 days (Figure 66), the calorimetry curves show that most of the reaction occurred within the first 3 days, as the heat flow (Figure 66a) rapidly dropped to near zero after the main peak. This indicates that the binder reached its stable reaction stage early, typical of AABS with high calcium reactivity (Sun; Vollpracht, 2018). The cumulative heat curves (Figure 66b) confirm this behavior. Even though no new thermal phenomena are observed after this stage, the mechanical and microstructural properties of the AABs continue to develop, following the ongoing gel densification and structural reorganization (Egnaczyk; Quinn; Wagner, 2025).

Figure 66 – Isothermal Calorimetry 7 days (a) Flow heat and (b) Cumulative heat

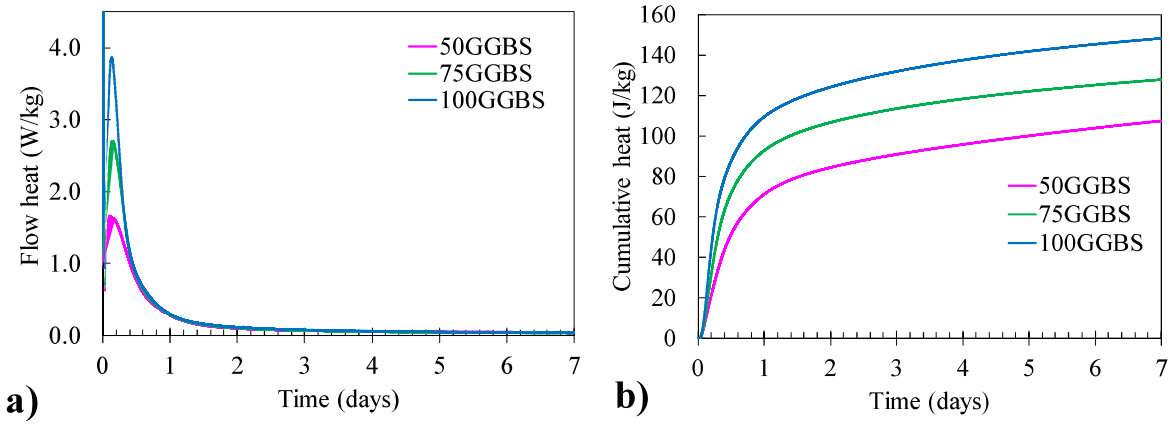

Source: elaborated by the author.

5.4.4 Impact resonance test (IRT)

5.4.4.1 Impact wave velocity (IWV)

Figure 67 shows the evolution of IWV over time for the binders. The velocity was obtained by measuring the time difference between the hammer impact and the first arrival of

the accelerometer signal (Figure 60), and then dividing the linear distance between the sensors by the calculated travel time. The segment labeled measures without resolution (100GGBS and 75GGBS at late ages) corresponds to situations where the travel time between hammer and accelerometer becomes too short to be accurately distinguished, this occurs because the linear distance between sensors is insufficient to resolve very small-time differences. A possible improvement in future geometries would be to increase the sensor distance, allowing longer travel times and thus higher sensitivity.

Figure 67 – Impact wave velocity over time

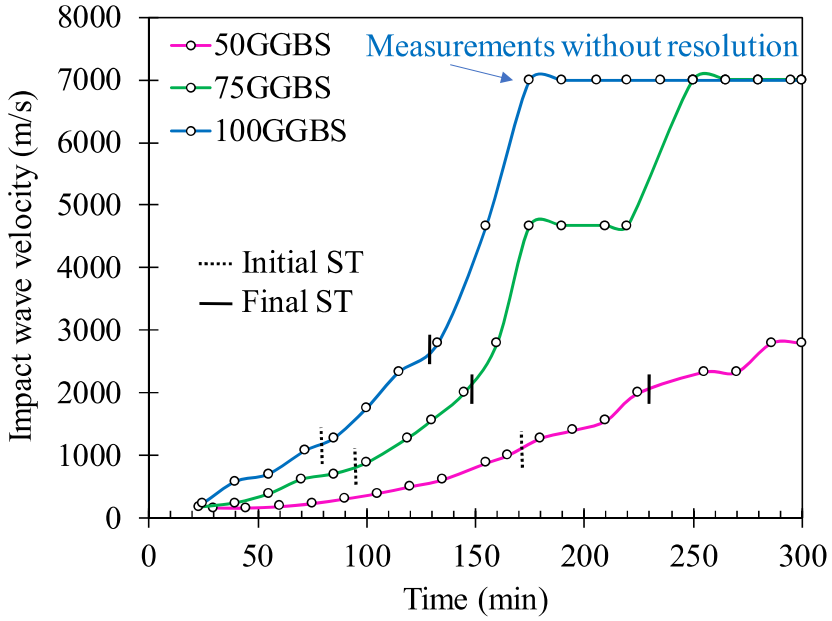

Source: elaborated by the author.

As seen in the figure, the initial and final setting times align with characteristic velocity ranges, with initial setting occurring around 800-1200 m/s and final setting near 2000-2500 m/s for all binders. Higher slag content leads to a faster rise in IWV. The evolution of IWV provides a clear NDT representation of the hardening kinetics of AABs, described by Park *et al*. (2024) and Tian and Xu (2022). Initially, the low velocities (<500 m/s) reflect a fluid suspension dominated by ionic dissolution, where waves propagate mainly through the liquid phase (Banouni *et al.*, 2022; Xu, D. *et al.*, 2024). As the reaction proceeds, the sharp velocity increase marks the formation of a percolating C-A-S-H/N-A-S-H gel network and coincides with the defined setting period (Shi *et al.*, 2022; Park *et al.*, 2024). The subsequent increase indicates the establishment of a continuous, elastic solid matrix and microstructural densification. Overall, impact wave velocity provides a reliable, NDT measure of hardening kinetics. However, to achieve greater sensitivity in high velocity binders, such 100GBBS, it is necessary to adapt the geometry.

5.4.4.2 Resonance frequency

The resonance frequency is directly linked to the material's fundamental rheological properties, especially its stiffness and ability to store elastic energy. Because of this relationship, the evolution of resonance frequency provides meaningful insight into the hardening process.

The Figure 68 shows the resonance frequency over time for two peaks (a) 1st and (b) 2nd. Both the 1st and 2nd modes exhibit a similar overall behavior: the resonance frequency increases progressively as the binder hardens, and mixtures with higher GGBS content consistently develop stiffness earlier and more rapidly. This general trend agrees with the time-sweep rheology, calorimetry and with the IWV.

Figure 68 – Resonance frequency over time (a) 1st and (b) 2nd

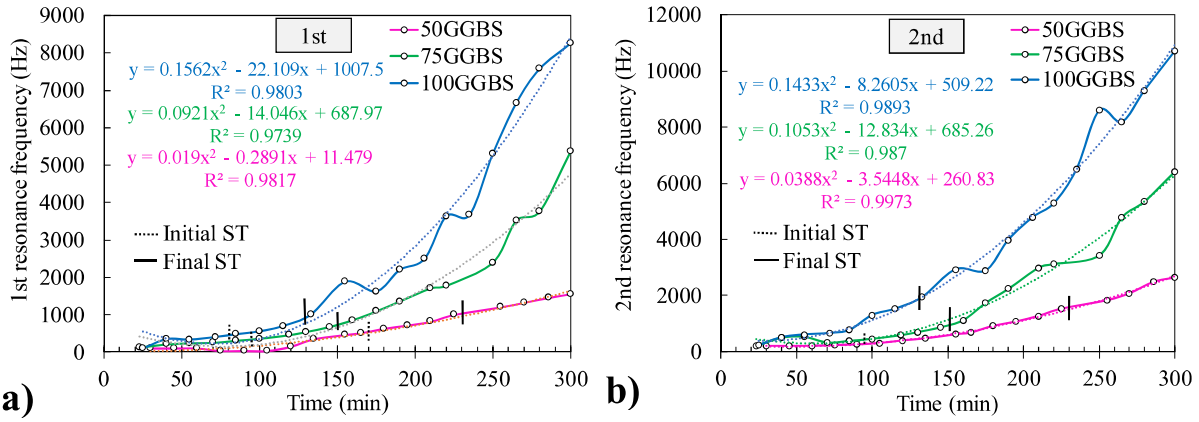

Source: elaborated by the author.

Despite the similar overall behavior in both modes, the 2nd resonance frequency is more sensitive to evolution, as indicated by its polynomial coefficients. Identifying whether each resonance peak corresponds to a compressional, flexural, or mixed mode is difficult because the vibration modes overlap and are not cleanly separated. The geometry causes multiple deformation mechanisms to occur in similar frequency ranges, meaning each peak likely represents a mixed vibration mode. Despite this, the frequency evolution still provides reliable insight into early-age stiffness development.

During the acceleration phase, the sharp rise in resonance frequency parallels the rapid formation of gels, as described by Rouyer and Poulesquen (2015) in their observation of a fractal percolating network marking the transition from a viscous suspension to a rigid solid. The dependence of resonance evolution on GGBS content, where higher slag percentages produce earlier and steeper frequency increases, agrees with the findings of Egnaczyk, Quinn and Wagner (2025), who demonstrated that reaction rate governs the rate of modulus

development through rheokinetic coupling. Collectively, these findings confirm that resonance frequency acts as a sensitive, non-destructive descriptor of early-age mechanical evolution, integrating the chemical kinetics, microstructural transitions.

5.4.4.3 Time-dependent correlation of impact resonance test, rheological parameters, and calorimetric response

Table 21 summarizes the Pearson correlation coefficients (r) between impact resonance parameters, rheological properties, and cumulative heat. The r quantifies the strength and direction of linear relationships between variables. Values closer to +1 indicate a very strong positive correlation, meaning both parameters evolve synchronously over time.

Table 21 – Pearson correlation coefficients between impact resonance parameters, rheological properties, and cumulative heat

Binder	Parameters	IWV (m/s)	Resonance frequency (Hz)	
			1st	2nd
50GGBS	|G*| (MPa)	0.96	0.96	0.99
	G' (MPa)	0.97	0.97	0.99
	G" (MPa)	0.94	0.95	0.98
	Cumulative heat (J/kg)	0.99	0.99	0.97
75GGBS	|G*| (MPa)	0.99	0.92	0.96
	G' (MPa)	0.99	0.91	0.95
	G" (MPa)	0.97	0.95	0.98
	Cumulative heat (J/kg)	0.98	0.94	0.97
100GGBS	|G*| (MPa)	0.97	0.87	0.92
	G' (MPa)	0.97	0.86	0.92
	G" (MPa)	0.96	0.91	0.95
	Cumulative heat (J/kg)	0.92	0.95	0.98
Average		0.97	0.93	0.96

Source: elaborated by the author.

The results indicate that all binders present very strong positive correlations between impact resonance parameters, rheological stiffening, and cumulative heat, showing that the three techniques capture highly synchronized hardening behavior. IWV exhibits the highest correlations ($r \sim 0.97$), reflecting its strong dependence on the development of the elastic gel network. G′ and |G*| show the strongest rheological alignment with resonance frequencies, while G″ remains slightly lower but still highly correlated. Cumulative heat also correlates strongly with mechanical and rheological evolution, particularly for 50GGBS and 75GGBS ($r = 0.97$-0.99). In 100GGBS, the second resonance mode correlates more closely with cumulative heat than IWV. Overall, Table 21 confirms that impact resonance parameters, mainly IWV and 2nd resonance frequency, captures the same hardening process reflected by rheology and calorimetry, supporting its use as a reliable NDT method for monitoring early-age kinetics in

AABs.

5.4.5 Fourier Transform Infrared Spectroscopy (FTIR)

The Table 22 FTIR band assignments summarize the main vibrational bands identified across all AABs studied. These bands appeared consistently in the spectra, with only minor shifts observed within narrow wavenumber ranges. Such variations, especially noticeable at later ages, reflect subtle differences in gel formation and the evolving chemical environment progress from early dissolution to advanced reaction stages.

Table 22 – FTIR band assignments

Wavenumber (cm^{-1})	Chemical species / group	Type of vibration	Reference
3418	–OH (structural or adsorbed water)	Stretching	(Finocchiaro *et al.*, 2020; Hoyos-Montilla *et al.*, 2022)
2970	HCO_3^- (bicarbonate species)	Stretching	(Xu *et al.*, 2023)
2361	CO_2	Asymmetric stretching	(Hoyos-Montilla *et al.*, 2022)
1454	CO_3^{2-} (carbonate)	Asymmetric stretching	(Finocchiaro *et al.*, 2020; D'Elia *et al.*, 2023)
1034	Si–O–T (T = Si, Al)	Asymmetric stretching	(Hoyos-Montilla *et al.*, 2022; Poggetto; Leonelli; Spinella, 2024)
866	CO_3^{2-} (carbonate)	Bending (out-of-plane)	(Finocchiaro *et al.*, 2020; Xu *et al.*, 2023)
471	Si–O–Al	Bending	(Archez *et al.*, 2020; D'Elia *et al.*, 2023)

Source: elaborated by the author.

5.4.5.1 FTIR Analysis at early ages (0-300 min)

The Figure 69 shows the FTIR spectra of the 50GGBS during the first 300 min in two configurations (a) non-overlapped (b) overlapped. The Si-O-T vibration band (typically 950-1050 cm^{-1}) is a key spectral feature in AABs, as it represents the asymmetric stretching of Si-O-Al/Si linkages within the aluminosilicate gel and its position reflects the degree of polymerization and Al incorporation in the network (Archez *et al.*, 2020; Finocchiaro *et al.*, 2020; Poggetto; Leonelli; Spinella, 2024). Although the calorimetry and rheology results clearly indicate ongoing reaction activity and a progressive increase in stiffness during the first five hours of activation, the FTIR spectra show that the main Si-O-T band at 1034 cm^{-1} remains essentially unchanged in both position and intensity throughout this period. This is particularly noteworthy given that the initial and final setting times are approximately 170 min and 230 min,

respectively, when the system is already undergoing significant mechanical stiffening.

The absence of changes in the 1034 cm^{-1} band indicates that, although dissolution and early gel nucleation occur, they do not produce long-range structural reorganization detectable by FTIR. This suggests that FTIR has limited sensitivity to early-age reactions dominated by short-range ionic rearrangements, with significant spectral evolution typically observed only after ~24 h of curing as the geopolymer network becomes more cross-linked (Finocchiaro *et al.*, 2020; Hoyos-Montilla *et al.*, 2022; D'Elia *et al.*, 2023). The 471 cm^{-1} Si-O-Al bending band was not analyzed in detail due to limited spectral quality in the low-wavenumber region of the KBr FTIR spectrum (Krivoshein *et al.*, 2022).

Figure 69 – FTIR spectra 50GGBS during the first 300 min: (a) non-overlapped (b) overlapped

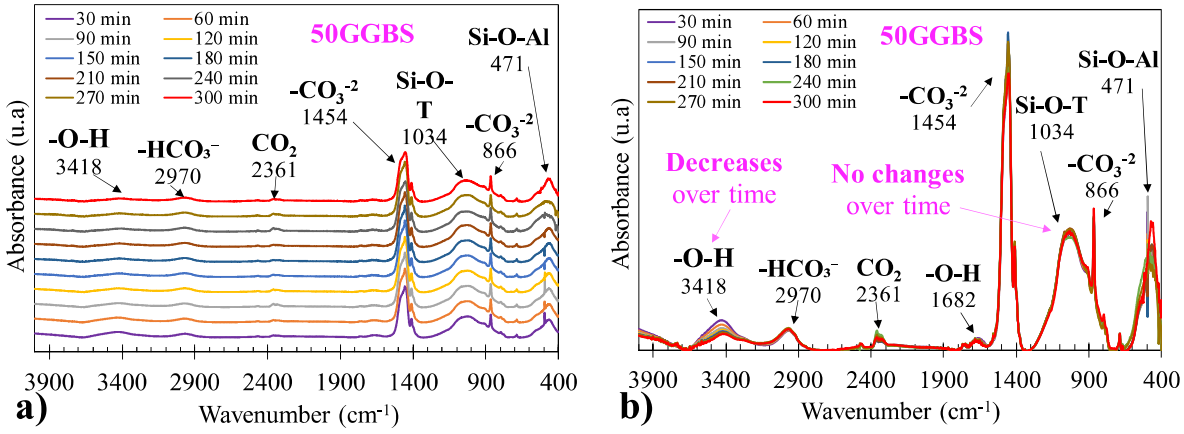

Source: elaborated by the author.

A decrease in the O-H stretching band at 3418 cm^{-1} was observed during the first five hours, indicating a progressive reduction of free and bound water as the alkali activation progressed. In the present case, the attenuation of the O-H region is more likely related to water evaporation from the sample surface rather than complete chemical consumption. The FTIR detects both free and bound water, the reduction in intensity suggests that part of the physically adsorbed or loosely retained moisture was lost during curing or measurement, while the molecular water structurally incorporated into the gels remains detectable in the spectra (Rüscher *et al.*, 2021). The more pronounced change in the O-H band, compared with the stable Si-O-T vibration at 1034 cm^{-1}, suggests that water participates directly in early-age processes such as precursor dissolution and charge transport, while the aluminosilicate framework remains largely unchanged at the long range.

As shown in Figure 69, the FTIR spectra of the 75GGBS (Figure 70) exhibit a behavior very similar to that of the 50GGBS system. The main Si-O-T band at 1034 cm^{-1} remains nearly unchanged during the first 300 min, with only a very slight and almost

imperceptible variation in position or intensity. The O-H stretching band at 3418 cm^{-1} also gradually decreases over time.

Figure 70 – FTIR spectra 75GGBS during the first 300 min: (a) non-overlapped (b) overlapped

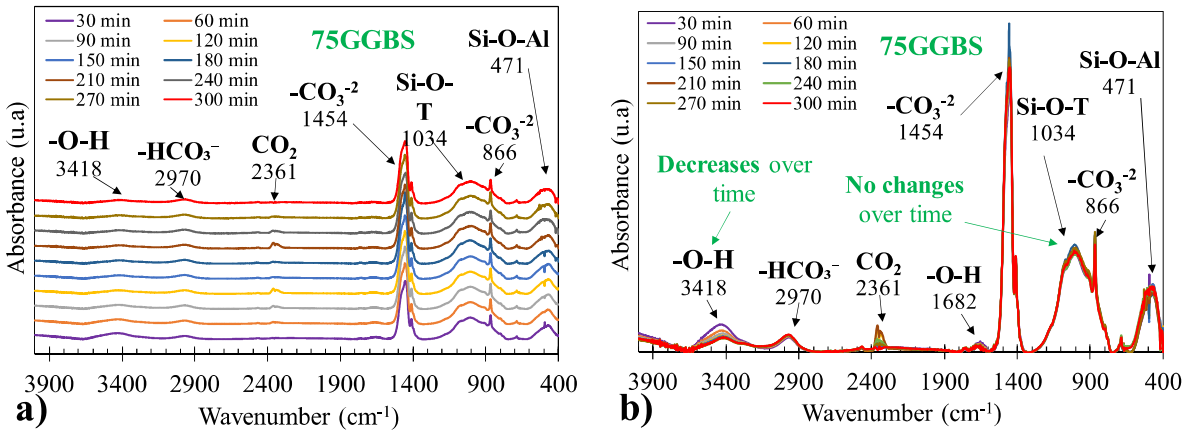

Source: elaborated by the author.

As shown in Figure 71, the FTIR spectra of the 100GGBS binder exhibit a distinct behavior compared to the 50GGBS and 75GGBS systems. The main Si-O-T band at 1034 cm^{-1}, shows a slight but clear increase in intensity over time, indicating progressive development and densification of the reaction products. This vibration is widely recognized as the fingerprint of C-A-S-H, N-A-S-H, or hybrid (N,C)-A-S-H gels, depending on the Ca/Si ratio and the precursor composition (Archez *et al.*, 2020; Finocchiaro *et al.*, 2020; Hoyos-Montilla *et al.*, 2022).

Figure 71 – FTIR spectra 100GGBS during the first 300 min: (a) non-overlapped (b) overlapped

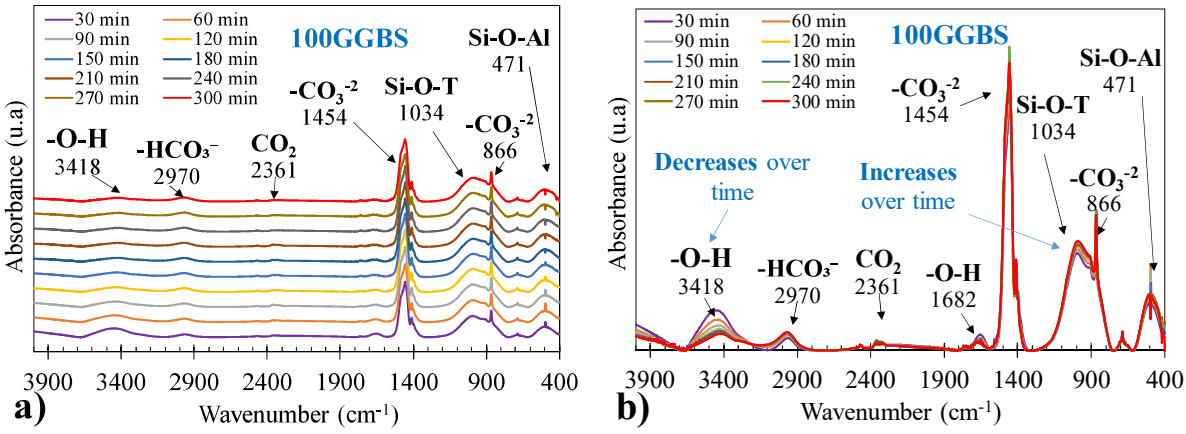

Source: elaborated by the author.

The observed increase in the 1034 cm^{-1} band agrees with the earlier setting times of the 100GGBS mixture (~80 min initial and ~130 min final) and with the calorimetry results, which showed a higher cumulative heat release compared to the other binders. This correlation confirms that a higher slag content accelerates gel formation and structural reorganization.

Meanwhile, the O-H stretching band at 3418 cm^{-1} decreases due to water consumption and condensation of the gel network.

5.4.5.2 FTIR Analysis at later ages (up to 28 Days)

As illustrated in Figure 72, the FTIR spectra of the 50GGBS binder over the first 28 days displayed as (a) non-overlapped and (b) overlapped plots, clearly demonstrate the gradual structural evolution of the system. From 1 day to 28 days of curing, the Si-O-T band (initially centered near 1034 cm^{-1}) shows a progressive increase in intensity accompanied by a slight shift toward lower wavenumbers. This evolution reflects the ongoing polymerization and condensation of the aluminosilicate framework, a process that becomes increasingly evident at later curing ages (Hoyos-Montilla *et al.*, 2022). The shift of this band toward lower wavenumbers indicates the progressive incorporation of Al into the silicate network and the increase in the polymerization degree of the gel (Finocchiaro *et al.*, 2020). As Al substitutes for Si in the tetrahedral sites, the Si-O bond environment becomes more ionic, lowering the bond energy and thus the corresponding vibration frequency (Rüscher *et al.*, 2021; Hoyos-Montilla *et al.*, 2022). This trend is characteristic of C-A-S-H-type gel growth in slag-rich binders, where Ca^{2+} balances the negative charge created by Al substitution, promoting the formation of a denser, more interconnected structure (Mikhailova *et al.*, 2019).

Figure 72 – FTIR spectra 50GGBS during 28 d: (a) non-overlapped (b) overlapped

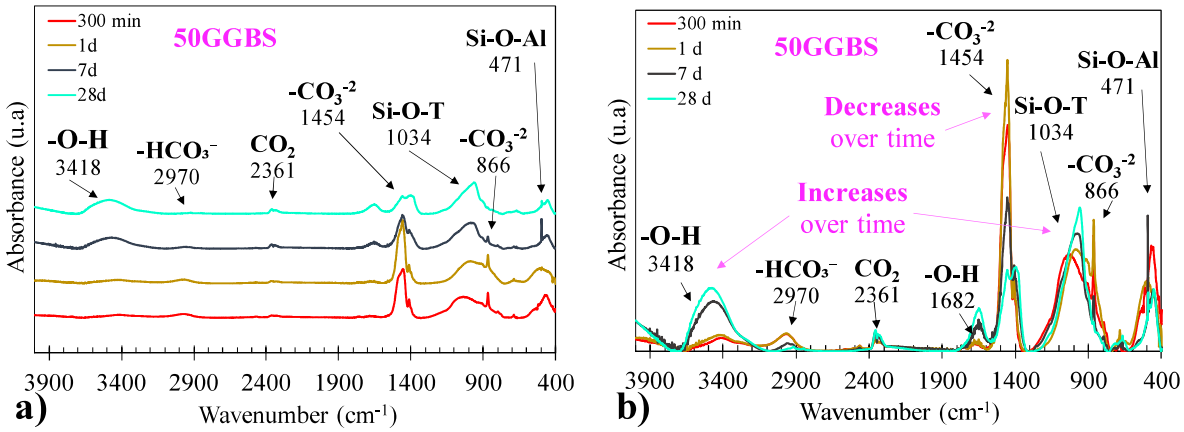

Source: elaborated by the author.

The decrease of the 1454 cm^{-1} band and 866 cm^{-1} ($-CO_3^{-2}$) over time, coinciding with the increase in the Si-O-T band, has been associated with the progressive consumption or encapsulation of carbonate species as gel polymerization advances. According to Finocchiaro *et al.* (2020), carbonate vibrations in this region originate mainly from the partial carbonation of alkaline cations and Ca-rich phases during the initial stages of activation, leading to transient CO_3^{2-} stretching near 1454 cm^{-1}. As hardening proceeds, the growth of C-A-S-H and (N,C)-A-

S-H gels incorporates available calcium and silica into the aluminosilicate network, reducing the amount of free or weakly bound carbonate species (Finocchiaro *et al.*, 2020; Hoyos-Montilla *et al.*, 2022; D'Elia *et al.*, 2023). In resume, the increase in mechanical properties over time is directly related to the growth and shift of the Si-O-T band toward lower wavenumbers, indicating progressive gel polymerization and structural densification, together with the decrease of the carbonate band (~1454 cm^{-1}) as calcium and alkalis are incorporated into the aluminosilicate framework.

The Figure 73 shows the FTIR spectra of the 75GGBS binder during 28 days: (a) non-overlapped and (b) overlapped presentation. The spectral evolution of the 75GGBS binder follows the same general trends observed for the 50GGBS system. As this behavior has already been discussed in detail for the 50GGBS composition, only the evolution of the O-H stretching region (3418 cm^{-1}) is further considered here.

In this case, the O-H band, which initially decreased during the first 300 min due to water consumption during early condensation and gel formation, shows a gradual increase at later curing ages (1-28 days). This apparent re-intensification is likely not related solely to additional structural hydroxylation but rather to moisture uptake from the environment, since the binder showed clear hygroscopic behavior when the samples were collected. The high alkalinity and the presence of residual NaOH in the pore solution can promote rapid adsorption of atmospheric humidity, increasing the O-H signal intensity even after the main hydration reactions have slowed.

Figure 73 – FTIR spectra 75GGBS during 28 d: (a) non-overlapped (b) overlapped

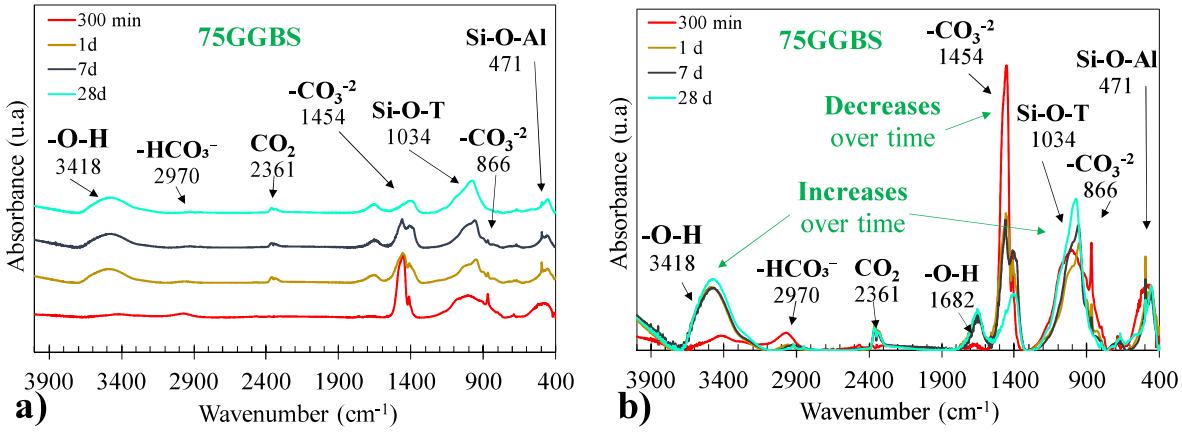

Source: elaborated by the author.

The Figure 74 illustrate the FTIR spectra of the 100GGBS until 28 days: (a) non-overlapped and (b) overlapped presentation. The spectra of the 100GGBS binder follow the same overall behavior observed for the 50GGBS and 75GGBS systems, showing an increase

in the Si-O-T band (~1034 cm^{-1}) and a decrease in the carbonate peaks (1454 and 866 cm^{-1}) over time. To obtain more detailed information and enable a quantitative comparison between the binders, it is necessary to perform a deconvolution analysis of the main Si-O-T band, which would allow for a clearer evaluation of the structural evolution and the degree of polymerization among the different mixtures, as did for Hoyos-Montilla *et al.* (2022).

Figure 74 – FTIR spectra 100GGBS during 28 d: (a) non-overlapped (b) overlapped

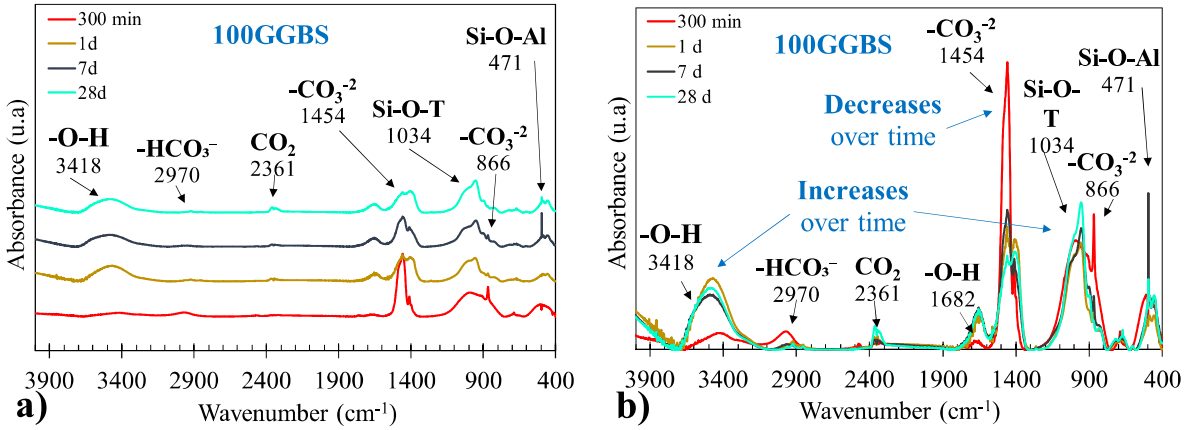

Source: elaborated by the author.

5.4.6 Thermogravimetric Analysis (TGA)

Thermogravimetric analysis of alkali-activated systems typically shows three main weight-loss stages. The first, from room temperature to ~150 °C, corresponds to the evaporation of free and physically bound water (Caballero *et al.*, 2019; Abdellatief *et al.*, 2022). Between 150 °C and 400 °C, the dehydration and dehydroxylation of C-A-S-H and N-A-S-H gels occur, marking structural densification of the aluminosilicate network (Rezzoug; Ayed; Leklou, 2024; Yan *et al.*, 2024). At higher temperatures, around 600-900 °C, carbonate decomposition and crystalline phase formation (e.g., mullite, spinel) take place (Caballero *et al.*, 2019; Poggetto; Leonelli; Spinella, 2024).

The TGA (Figure 75a) and DTG curves (Figure 75b) of the 50GGBS system present the typical thermal behavior of slag-based geopolymers at three curing ages: 30 min, 300 min (5 h), and 28 days. At 30 min, the pronounced mass loss and sharp DTG peak indicate a high content of free and weakly bound water, reflecting an immature and porous gel structure (Abdellatief *et al.*, 2022). After 300 min, both mass loss and DTG peak intensity decrease, showing that early geopolymerization reduces water retention and initiates gel condensation. At 28 days, the amount of released water continues to decrease, and a broader tail appears above 150 °C, suggesting the presence of a higher proportion of stable gels and a more consolidated

C-A-S-H network.

Figure 75 – Thermal decomposition of the 50GGBS (a) TGA and (b) DTG

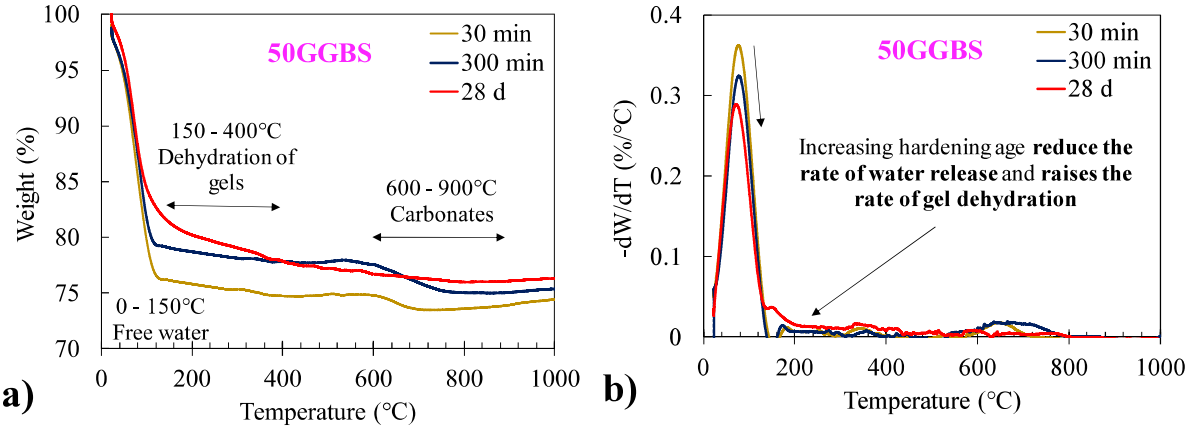

Source: elaborated by the author.

Figure 76 shows the (a) TGA and (b) DTG curves of the 75GGBS system, which follow the same overall thermal behavior observed for the 50GGBS mixture, with progressive reductions in water-related mass loss and DTG peak intensity as curing time increases. But, unlike the 50GGBS system, where total loss decreased continuously with curing time (30 min > 300 min > 28 d), the 75GGBS mixture exhibits an irregular trend (28 d > 30 min > 300 min). This behavior can be related to the higher slag content, which enhances calcium availability and promotes the formation of more hydrated C-A-S-H phases at longer curing times, resulting in slightly greater total weight loss upon heating (Rezzoug; Ayed; Leklou, 2024).

Figure 76 – Thermal decomposition of the 75GGBS (a) TGA and (b) DTG

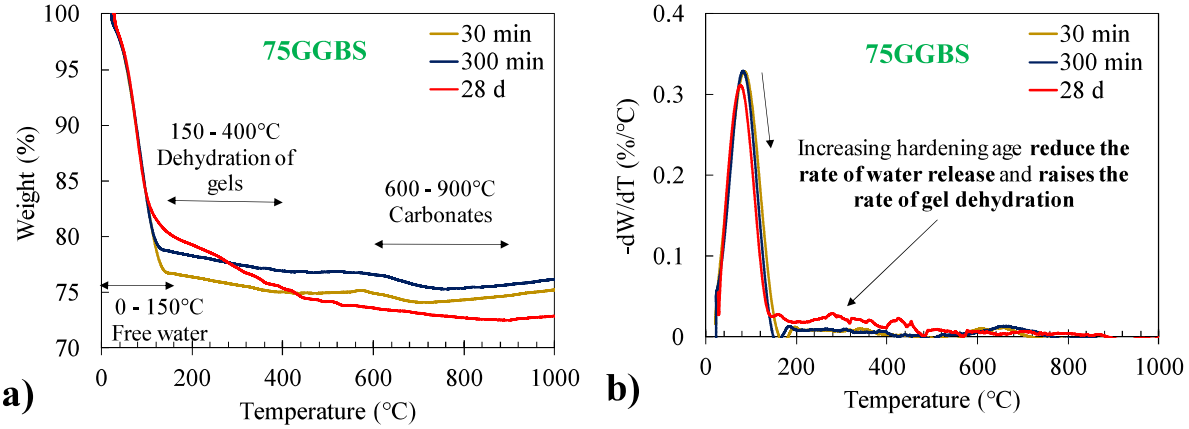

Source: elaborated by the author.

Figure 77 shows the (a) TGA and (b) DTG curves of the 100GGBS system, which maintain the same general decomposition pattern observed in the 50GGBS and 75GGBS mixtures. However, unlike the previous mixtures, the 100GGBS sample does not present a clear trend in total water-related mass loss with hardening time. This behavior may result from the

higher slag content, which promotes the formation of additional C-A-S-H gel capable of retaining more bound water. A partial reabsorption of atmospheric moisture by the 28-day sample could also contribute to the higher apparent water release, as occasionally observed in dense, calcium-rich alkali-activated systems (Abdellatief *et al.*, 2022).

Figure 77 – Thermal decomposition of the 100GGBS (a) TGA and (b) DTG

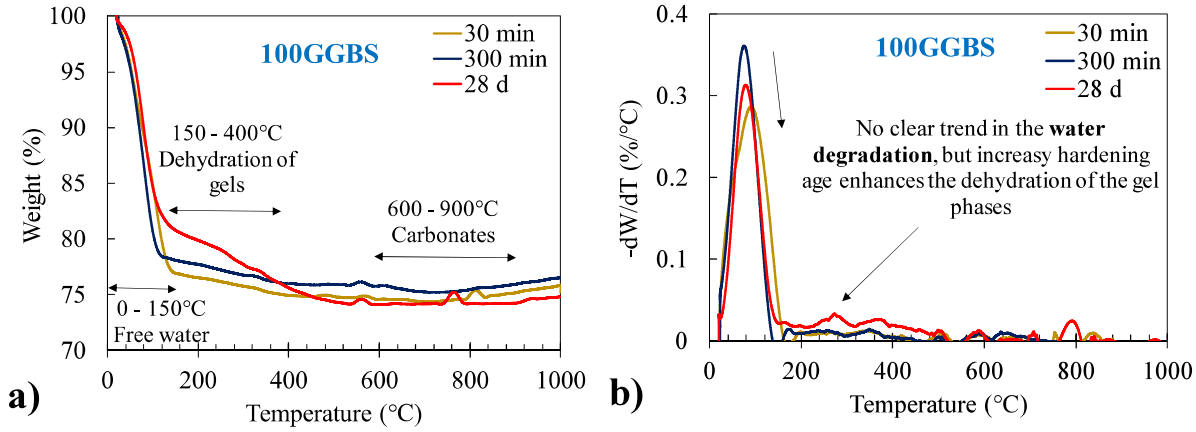

Source: elaborated by the author.

Figure 78 summarizes the thermogravimetric weight-loss behavior of AABs) at different curing ages for (a) free water and (b) gels. The values were obtained by subtracting the mass loss in the 0-150°C range (free water) from that in the 150-400°C range (gel dehydration). The Figure 78a shows that the trend of free-water loss varies

Figure 78 – Thermogravimetric weight loss of AABs over time (a) free water evaporation and (b) gel dehydration

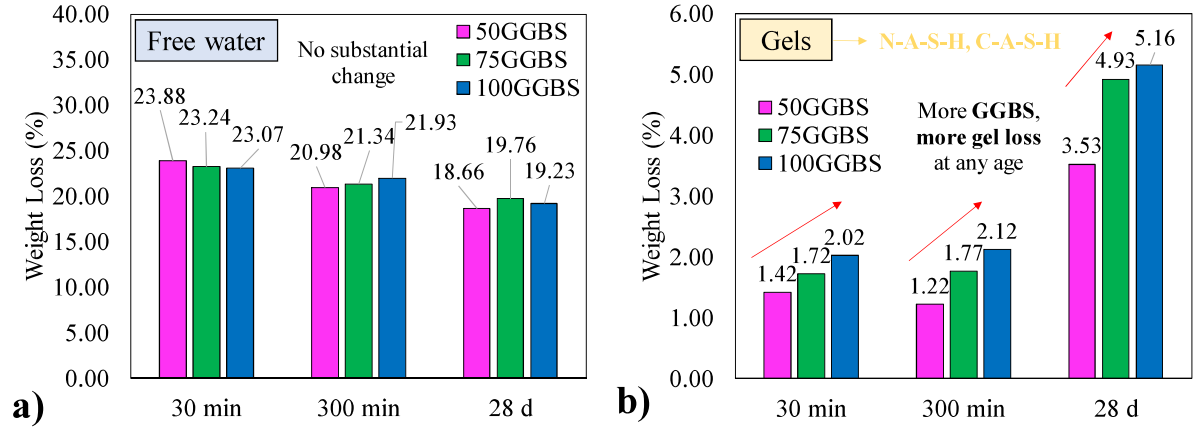

Source: elaborated by the author.

. When comparing the same binder over time, the amount of free water decreases as hardening progresses, reflecting microstructural densification and reduced porosity. However, no clear trend is observed when comparing between different binders, as the values fluctuate with GGBS content, additionally, no substantial change was observed. This irregular behavior may be influenced by the hygroscopic nature of the samples, since partial moisture

reabsorption from the atmosphere before testing could affect the measured water content (Abdellatief *et al.*, 2022; Rezzoug; Ayed; Leklou, 2024). The Figure 78b shows that gel-related mass loss increases consistently with both curing age and GGBS content, confirming that higher slag levels promote the formation of more C-A-S-H and/or N-A-S-H gels with larger amounts of bound water. The 100GGBS mixture shows the greatest gel-related loss at 28 days, consistent with a higher degree of reaction showed in the calorimetry and a denser, more polymerized structure.

5.4.7 Compressive strength

Figure 79 shows the compressive strength results of the AABs after 28 days, which correspond to the only tests conducted in the hardened state. As expected, the increase in GGBS content led to a progressive rise in compressive strength, with values of 33.2 MPa, 48.9 MPa, and 54.3 MPa for 50GGBS, 75GGBS, and 100GGBS, respectively. This trend agrees with previous results from FTIR, calorimetry, impact resonance test, and TGA analyses, all of which indicated that higher GGBS contents promote greater formation of C-A-S-H gels. These gels are known to form a denser and more cohesive microstructure, which enhances the mechanical strength (Dal Poggetto *et al.*, 2021; Abdellatief *et al.*, 2022; Rezzoug; Ayed; Leklou, 2024).

Figure 79 – Compressive strength at 28 d

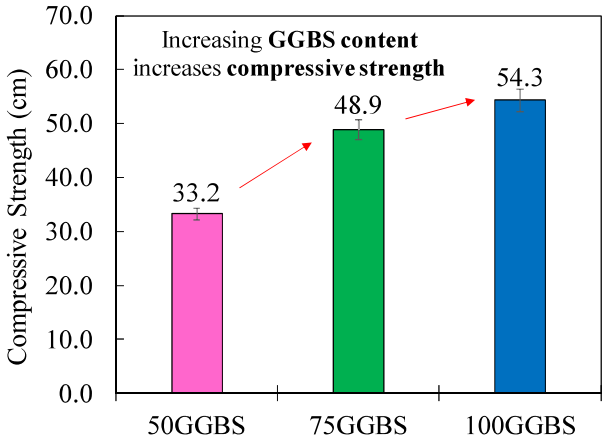

Source: elaborated by the author.

5.5 Section conclusions

This study investigated the hardening kinetics of AABs through an integrated experimental program that combined setting time measurements, time-sweep rheology, continuous monitoring of resonance frequency through IRT, isothermal calorimetry to characterize reaction kinetics, and FTIR and TGA to track microstructural evolution. Three

binders were evaluated with 50%, 75%, and 100% GGBS, to elucidate how calcium availability influences early-age reactions and mechanical development. These combined methodologies provided a comprehensive understanding of the early-age processes governing the hardening behavior of AABs. The main conclusions are summarized below:

- Calcium availability is the dominant factor controlling early-age behavior, dictating dissolution rate, gel connectivity, and stiffness evolution;
- Higher GGBS content accelerates hardening, driven by greater calcium availability and finer particle size, which enhance dissolution, ion release, and early gel nucleation;
- Viscous losses decrease more rapidly in slag-rich binders, as reflected in smaller and earlier dG″/dt peaks, leading to lower and more stable phase angles during hardening;
- The timing of calorimetric peaks does not scale linearly with GGBS content, due to competing effects such as rapid dissolution followed by temporary surface passivation in very slag-rich systems;
- Both impact wave velocity (IWV) and the two first resonance frequency increased consistently over time, confirming their sensitivity to stiffness development during early-age reactions;
- Impact resonance parameters correlated strongly with complex, storage and loss modulus and cumulative heat, demonstrating that mechanical, chemical, and thermal indicators evolve synchronously during hardening;
- FTIR is not highly sensitive for monitoring early hardening (first 300 min) in low- and medium-slag systems (50GGBS and 75GGBS), but it reliably captures structural development at later stages and differentiates mixtures when polymerization becomes more advanced (100GGBS);
- Significant FTIR evolution became evident only at later ages (1-28 days), when all binders exhibited increased Si-O-T intensity and shifts to lower wavenumbers, reflecting gel polymerization, Al incorporation, and network densification;
- Gel-related mass loss, by TGA, increased with both hardening age and slag content, demonstrating that higher GGBS levels promote greater formation of C-A-S-H/N-A-S-H gels and a more polymerized aluminosilicate network;
- Higher GGBS content leads to more advanced microstructural development, greater gel

formation, and improved mechanical performance.

6 FINAL CONSIDERATIONS

This research was structured into three papers, each aligned with one of the specific objectives.

The first paper investigated the application of machine learning models to predict both fresh state (initial and final setting time) and hardened state (compressive strength) properties of AABs and concluded:

- ANN, RF, and BR were the most accurate models, indicating that setting-time behavior is highly nonlinear and not suitable for linear approaches such as MPR;
- RF and BR produced chemically coherent variable rankings and stable sensitivities, while ANN captured stronger nonlinearities but showed greater variability when extrapolating;
- The limited setting time dataset (139 samples) restricts model generalization, meaning broader predictive reliability requires expanding the setting-time database;
- In compressive strength, ANN, RF, and BR achieved the highest predictive performance, with ANN additionally capturing key nonlinear behaviors such as optimal N/B and S/N ratios;
- RF and BR highlighted variables consistent with expected AAM chemistry (CaO, Fe_2O_3, SiO_2, S/N), while ANN showed higher sensitivity to complex nonlinear interactions;
- Model accuracy depends on the activation quality of the material, performing well for external datasets but poorly for dry-pit binders whose characteristics fall outside the trained domain;

The second paper focused on the design, development, and validation of an impact resonance test apparatus capable of monitoring the hardening process of AABs in the fresh state and concluded:

- The G3-P geometry was the most suitable configuration, presenting fewer spurious peaks and stable coherence up to 7000 Hz, making it the best option for early-age resonance monitoring;
- E′, E″, and phase angle from the 2S2P1D model showed no clear trends, probably due to early-age sensor limitations, the shift of the peak approached over time, and the model's reduced applicability to very soft binders;

- Resonance frequency was the most sensitive indicator of hardening, with the 2nd mode strongly related to stiffness and the 1st mode closely following reaction heat;
- Peak width showed moderate sensitivity to damping and viscous effects, while amplitude did not present consistent or meaningful correlations.

The third paper examined the early-age hardening kinetics of alkali-activated binders using impact resonance as the central monitoring technique and concluded:

- Calcium availability is the key driver of early-age behavior, controlling dissolution, gel nucleation, network connectivity, and stiffness evolution;
- Higher GGBS content accelerates hardening, producing faster stiffness gain, reduced viscous losses, and earlier mechanical percolation.
- Mechanical, thermal, and rheological indicators evolve synchronously, as shown by the strong correlations between IWV, resonance frequencies, moduli, and cumulative heat;
- FTIR has low sensitivity during the first 300 min, except for 100GGBS, but clearly captures gel polymerization and structural densification at later ages (1-28 days);
- TGA and compressive strength results show increased gel formation and improved mechanical performance with higher GGBS content, confirming more advanced microstructural development in slag-rich binders.

This research achieved its objectives by advancing both the understanding and the monitoring of early-age behavior in alkali-activated binders, combining data-driven prediction, rheological insight, and non-destructive mechanical evaluation. The findings demonstrate that the hardening process of AABs is strongly governed by precursor composition, which controls reaction kinetics, gel formation, and stiffness development. Machine learning tools proved capable of capturing the nonlinear relationships between chemistry, mix design, and performance, while resonance-based methods provided sensitive real-time indicators of microstructural evolution. Together, these approaches strengthen the scientific basis for designing, predicting, and assessing AABs, contributing to their advancement as sustainable and technically robust alternatives to conventional binders.

REFERENCES

ABDELLATIEF, M. *et al.* Multiscale characterization at early ages of ultra-high performance geopolymer concrete. **Polymers**, Basel, vol. 14, no. 24, p. 5504, 2022.

ABDULLAH, G. M. S. *et al.* Boosting-based ensemble machine learning models for predicting unconfined compressive strength of geopolymer stabilized clayey soil. **Scientific Reports**, London, vol. 14, no. 1, p. 2323, 2024.

ABED, F. H. *et al.* Enhancing geopolymer binder reactivity and performance via mechanochemical activation: A comprehensive study of rheological, mechanical, and microstructural properties. **Construction and Building Materials**, Amsterdam, vol. 430, p. 136456, 2024.

ABUHUSSAIN, M. A. *et al.* Data-driven approaches for strength prediction of alkali-activated composites. **Case Studies in Construction Materials**, Amsterdam, vol. 20, p. e02920, 2024.

ADEWUMI, A. A. *et al.* Influence of silica modulus and curing temperature on the strength of alkali-activated volcanic ash and limestone powder mortar. **Materials**, Basel, vol. 14, no. 18, p. 5204, 2021.

ADIBEIG, M. R.; VAKILI-TAHAMI, F.; SAEIMI-SADIGH, M.-A. Numerical and experimental investigation on creep response of 3D printed Polylactic acid (PLA) samples. Part I: The effect of building direction and unidirectional raster orientation. **Journal of the Mechanical Behavior of Biomedical Materials**, Amsterdam, vol. 145, p. 106025, 2023.

ADU-AMANKWAH, S. *et al.* Effect of synthesis parameters on the performance of alkali-activated non-conformant EN 450 pulverised fuel ash. **Construction and Building Materials**, Amsterdam, vol. 121, pp. 453–459, 2016.

AHMAD, M. R. *et al.* A multiscale study on gel composition of hybrid alkali-activated materials partially utilizing air pollution control residue as an activator. **Cement and Concrete Composites**, Amsterdam, vol. 136, p. 104856, 2023.

AHMAD, A. *et al.* Compressive strength prediction of fly ash-based geopolymer concrete via advanced machine learning techniques. **Case Studies in Construction Materials**, Amsterdam, vol. 16, p. e00840, 2022.

AHMED, H. U. *et al.* Statistical methods for modeling the compressive strength of geopolymer mortar. **Materials**, Basel, vol. 15, no. 5, p. 1868, 2022.

AKTÜRK, B. *et al.* Influence of nano-silica and r-MgO on rheological properties, 3D printability, and mechanical properties of one-part sodium carbonate-activated slag-based mixes. **Journal of Building Engineering**, Amsterdam, vol. 104, p. 112245, 2025.

AL MAKHADMEH, W.; SOLIMAN, A. Effect of activator nature on property development of alkali-activated slag binders. **Journal of Sustainable Cement-Based Materials**, Abingdon, vol. 10, no. 4, pp. 240–256, 2021.

AL-HUSSEINAWI, F. N. *et al.* The impact of molar proportion of sodium hydroxide and water amount on the compressive strength of slag/metakaolin (waste materials) geopolymer Mortar. **Advances in Civil Engineering**, London, vol. 2022, no. 1, p. 5910701, 2022.

ALI, A. A.; AL-ATTAR, T. S.; ABBAS, W. A. A statistical model to predict the strength development of geopolymer concrete based on SiO2/Al2O3 ratio variation. **Civil Engineering Journal**, Tehran, vol. 8, no. 3, pp. 454–471, 2022.

ALLAHVERDI, A.; KANI, E. N. Construction wastes as raw materials for geopolymer binders. **International Journal of Civil Engineering**, Tehran, vol. 7, no. 2, pp. 154–160, 2009.

ALLAHVERDI, A.; SHAVERDI, B.; KANI, E. N. Influence of sodium oxide on properties of fresh and hardened paste of alkali-activated blast-furnace slag. **International Journal of Civil Engineering**, Tehran, vol. 8, no. 4, pp. 304–314, 2010.

ALNAHHAL, M. F.; KIM, T.; HAJIMOHAMMADI, A. Distinctive rheological and temporal viscoelastic behaviour of alkali-activated fly ash/slag pastes: A comparative study with cement paste. **Cement and Concrete Research**, Amsterdam, vol. 144, p. 106441, 2021.

ALOUANI, M. E. *et al.* A comprehensive review of synthesis, characterization, and applications of aluminosilicate materials-based geopolymers. **Environmental Advances**, Amsterdam, vol. 16, p. 100524, 2024.

ALQURASHI, I. *et al.* A review of ultrasonic testing and evaluation methods with applications in civil NDT/E. **Journal of Nondestructive Evaluation**, Cham, vol. 44, no. 2, p. 53, 2025.

ALREFAEI, Y. *et al.* Effects of solid activator and fly ash on rheology and thixotropy of one-part alkali-activated pastes. **Journal of Advanced Concrete Technology**, Tokyo, vol. 20, no. 3, pp. 139–151, 2022.

AMALUDIN, A. *et al.* Fresh and hardened properties of alkali-activated POFA-GGBFS pastes cured in ambient temperature – an initial mix design. **Journal of Advanced Research in Applied Mechanics**, Johor Bahru, vol. 125, pp. 103–115, 2024.

AMERICAN SOCIETY FOR TESTING AND MATERIALS. **ASTM C215**: Standard test method for fundamental transverse, longitudinal, and torsional resonant frequencies of concrete specimens. West Conshohocken, Philadelphia, 2019a.

AMERICAN SOCIETY FOR TESTING AND MATERIALS. **ASTM C597**: Standard test method for ultrasonic pulse velocity through concrete. West Conshohocken, Philadelphia, 2022.

AMERICAN SOCIETY FOR TESTING AND MATERIALS. **ASTM C618**: Standard specification for coal fly ash and raw or calcined natural pozzolan for use as a mineral admixture in concrete. West Conshohocken, Philadelphia, 2019b.

AMERICAN SOCIETY FOR TESTING AND MATERIALS. **ASTM D412**: Standard test methods for vulcanized rubber and thermoplastic elastomers — tension. West Conshohocken, Philadelphia, 2016.

AMERICAN SOCIETY FOR TESTING AND MATERIALS. **ASTM D2240**: Standard test method for rubber property — durometer hardness. West Conshohocken, Philadelphia, 2015.

AMIN, M. N. *et al.* Compressive strength estimation of geopolymer composites through novel computational approaches. **Polymers**, Basel, vol. 14, no. 10, p. 2128, 2022.

ARAÚJO, L. B. R. *et al.* Impact of curing temperature and steel slag aggregates on high-strength self-compacting alkali-activated concrete. **Buildings**, Amsterdam, vol. 15, no. 3, p. 457, 2025.

ARCHEZ, J. *et al.* Influence of the wollastonite and glass fibers on geopolymer composites workability and mechanical properties. **Construction and Building Materials**, Amsterdam, vol. 257, p. 119511, 2020.

ASCENSÃO, G. *et al.* Reaction kinetics and structural analysis of alkali activated Fe–Si–Ca rich materials. **Journal of Cleaner Production**, Amsterdam, vol. 246, p. 119065, 2020.

ASSOCIAÇÃO BRASILEIRA DE NORMAS TÉCNICAS. **ABNT NBR 9278**: Adesivos e selantes — determinação do tempo de escoamento — método do fluxômetro de pressão. Rio de Janeiro, 2019.

ASSOCIAÇÃO BRASILEIRA DE NORMAS TÉCNICAS. **ABNT NBR 16607**: Cimento Portland — determinação dos tempos de pega. Rio de Janeiro, 2018.

AVERSA, R. *et al.* Thermokinetic and chemorheology of the geopolymerization of an alumina-Rich alkaline-activated metakaolin in isothermal and dynamic thermal scans. **Polymers**, Basel, vol. 16, no. 2, p. 211, 2024.

AYDIN, Y. *et al.* Neural network predictive models for alkali-activated concrete carbon emission using metaheuristic optimization algorithms. **Sustainability**, Basel, vol. 16, no. 1, p. 142, 2023.

AZIMI, Z.; TOUFIGH, V. Influence of blast furnace slag on pore structure and transport characteristics in low-calcium fly-ash-based geopolymer concrete. **Sustainability**, Basel, vol. 15, no. 18, p. 13348, 2023.

BABKINA, N. *et al.* Effect of polyurethane material design on damping ability. **Polymers for Advanced Technologies**, Hoboken, vol. 34, no. 11, pp. 3426–3437, 2023.

BAHMANI, H.; MOSTOFINEJAD, D. Microstructural characterization of alkali-activated concrete using waste-derived activators from industrial and agricultural sources: A review. **Case Studies in Construction Materials**, Amsterdam, vol. 22, p. e04632, 2025.

BAI, M. *et al.* Prediction of compressive strength of fly ash-slag based geopolymer paste based on multi-optimized artificial neural network. **Materials**, Basel, vol. 16, no. 3, p. 1090, 2023.

BANOUNI, H. *et al.* Ultrasound non-destructive characterization of early hydration of cement pastes: the effects of water-cement ratio and curing temperature. **Annales de Chimie - Science des Matériaux**, Paris, vol. 46, no. 6, pp. 307–312, 2022.

BARBOSA, E. *et al.* Mechanical analysis through non-destructive testing of recycled porous friction course asphalt mixture. **Buildings**, Amsterdam, vol. 14, no. 9, p. 2907, 2024.

BERJAMIN, H. *et al.* Modeling longitudinal wave propagation in nonlinear viscoelastic solids with softening. **International Journal of Solids and Structures**, Amsterdam, vol. 141–142, pp. 35–44, 2018.

BEZERRA, A. K. L. *et al.* Determination of modulus of elasticity and Poisson's ratio of cementitious materials using S-wave measurements to get consistent results between static, ultrasonic and resonant testing. **Construction and Building Materials**, Amsterdam, vol. 398, p. 132456, 2023.

BÍLEK, V. *et al.* Comparison of thermogravimetry response of alkali-activated slag and Portland cement pastes after stopping their hydration using solvent exchange method. **Journal of Thermal Analysis and Calorimetry**, Budapest, vol. 150, no. 2, pp. 1013–1037, 2025.

BÍLEK, V. *et al.* Experimental study of slag changes during the very early stages of its alkaline activation. **Materials**, Basel, vol. 15, no. 1, p. 231, 2021.

BISWAS, S. *et al.* Target permutation for feature significance and applications in neural networks. *In*: 2024 INTERNATIONAL CONFERENCE ON MACHINE LEARNING AND APPLICATIONS (ICMLA), 2024, Miami, FL, USA. **2024 International Conference on Machine Learning and Applications (ICMLA)**. Miami, FL, USA: IEEE, 2024. pp. 1115–1120. Available at: https://ieeexplore.ieee.org/document/10903452/. Accessed on: 2 dec. 2025.

BONDAR, D.; VINAI, R. Chemical and microstructural properties of fly ash and fly ash/slag activated by waste glass-derived sodium silicate. **Crystals**, Basel, vol. 12, no. 7, p. 913, 2022.

BORGONOVO, E.; PLISCHKE, E.; PRIEUR, C. Total effects with constrained features. **Statistics and Computing**, Cham, vol. 34, no. 2, p. 87, 2024.

BOZ, I. *et al.* Validation of model order assumption and noise reduction method for the impact resonance testing of asphalt concrete. **Journal of Nondestructive Evaluation**, Cham, vol. 36, no. 3, p. 58, 2017.

CABALLERO, L. R. *et al.* Thermal, mechanical and microstructural analysis of metakaolin based geopolymers. **Materials Research**, São Paulo, vol. 22, no. 2, p. e20180716, 2019.

CAO, R. *et al.* Application of machine learning approaches to predict the strength property of geopolymer concrete. **Materials**, Basel, vol. 15, no. 7, p. 2400, 2022.

CARON, R.; PATEL, R. A.; DEHN, F. Activation kinetic model and mechanisms for alkali-activated slag cements. **Construction and Building Materials**, Amsterdam, vol. 323, p. 126577, 2022.

CARRET, J.-C. **Linear viscoelastic characterization of bituminous mixtures from dynamic tests back analysis**. 2018. 218 f. Thesis (Doctor in Civil Engineering) - Tribology and Dynamics of Systems Laboratory, University of Lyon, Lyon, France, 2018. Available at: https://theses.hal.science/tel-02170515. Accessed on: 5 oct. 2025.

CARRET, J.-C.; BABADOPULOS, L. Opening letter of RILEM TC MWP: Mechanical wave propagation to characterize bituminous mixtures. **RILEM Technical Letters**, Paris, vol. 10, pp. 15–21, 2025.

CARVALHO, I. D. C. *et al.* Early-age structural build-up and rheological assessment of alkali-activated slag-red clay brick waste pastes: Influence of silica modulus and precursors proportions. **Cement and Concrete Composites**, Amsterdam, vol. 153, p. 105730, 2024.

CARVALHO, I. C. *et al.* Mechanical, rheological, and microstructural study of ternary alkali-activated pastes using BOF slag, metakaolin, and glass powder as Precursors. **Journal of Materials in Civil Engineering**, Reston, vol. 36, no. 6, p. 04024121, 2024.

CASTILLO, D.; HEDJAZI, S.; KABIR, E. Study on early-age elastic modulus of FRC using electrical resistivity and resonance frequency. **International Journal of Concrete Structures and Materials**, Seoul, vol. 16, no. 1, p. 53, 2022.

CHEN, W. *et al.* Interface optimizing core–shell PZT@carbon/polyurethane composites with enhanced passive piezoelectric vibration damping performance. **ACS Applied Materials & Interfaces**, Washington, vol. 16, no. 6, pp. 7742–7753, 2024.

CHEN, H. *et al.* Mechanical behavior of closed-cell ethylene-vinyl acetate foam under compression. **Polymers**, Basel, vol. 16, no. 1, p. 34, 2023.

CHITHIRAPUTHIRAN, S.; NEITHALATH, N. Isothermal reaction kinetics and temperature dependence of alkali activation of slag, fly ash and their blends. **Construction and Building Materials**, Amsterdam, vol. 45, pp. 233–242, 2013.

COSTA, H. N. **Cimento álcali ativado à base de cinzas do carvão mineral e escória de aciaria**. 2022. 217 f. Thesis (Doctor in Materials Science and Engineering) - Department of Metallurgical and Materials Engineering, Federal University of Ceará, Fortaleza, Brazil, 2022. Available at: http://repositorio.ufc.br/handle/riufc/64793. Accessed on: 5 oct. 2025.

CUI, C. *et al.* Mechanical properties and reaction kinetics of alkali-activated metakaolin. **Materials**, Basel, vol. 17, no. 2, p. 367, 2024.

DAI, X. *et al.* Effect of Ca(OH)2 addition on the engineering properties of sodium sulfate activated slag. **Materials**, Basel, vol. 14, no. 15, p. 4266, 2021.

DAI, X. *et al.* Influence of water to binder ratio on the rheology and structural Build-up of Alkali-Activated Slag/Fly ash mixtures. **Construction and Building Materials**, Amsterdam, vol. 264, p. 120253, 2020.

DAI, X. *et al.* Rheology and microstructure of alkali-activated slag cements produced with silica fume activator. **Cement and Concrete Composites**, Amsterdam, vol. 125, p. 104303, 2022a.

DAI, X. *et al.* Rheology and structural build-up of sodium silicate- and sodium hydroxide-activated GGBFS mixtures. **Cement and Concrete Composites**, Amsterdam, vol. 131, p. 104570, 2022b.

DAL POGGETTO, G. *et al.* FT-IR study, thermal analysis, and evaluation of the antibacterial activity of a MK-geopolymer mortar using glass waste as fine aggregate. **Polymers**, Basel, vol. 13, no. 17, p. 2970, 2021.

D'ELIA, A. *et al.* Alkali-activated binary binders with carbonate-rich illitic clay. **Polymers**, Basel, vol. 15, no. 2, p. 362, 2023.

DI BENEDETTO, H. *et al.* Linear viscoelastic behaviour of bituminous materials: From binders to mixes. **Road Materials and Pavement Design**, Abingdon, vol. 5, no. sup1, pp. 163–202, 2004.

DINESHKUMAR, M.; UMARANI, C. Effect of alkali activator on the standard consistency and setting times of fly ash and GGBS-based sustainable geopolymer pastes. **Advances in Civil Engineering**, London, vol. 2020, no. 1, p. 2593207, 2020.

DING, Y. *et al.* An efficient AdaBoost algorithm with the multiple thresholds classification. **Applied Sciences**, Amsterdam, vol. 12, no. 12, p. 5872, 2022.

DINH, H. L. *et al.* Influence of Si/Al molar ratio and ca content on the performance of fly ash-based geopolymer incorporating waste glass and GGBFS. **Construction and Building Materials**, Amsterdam, vol. 411, p. 134741, 2024.

DJOBO, J. N. Y.; STEPHAN, D. Control of the setting reaction and strength development of slag-blended volcanic ash-based phosphate geopolymer with the addition of boric acid. **Journal of the Australian Ceramic Society**, Hoboken, vol. 57, no. 4, pp. 1145–1154, 2021.

DODO, Y. *et al.* Estimation of compressive strength of waste concrete utilizing fly ash/slag in concrete with interpretable approaches: optimization and graphical user interface (GUI). **Scientific Reports**, London, vol. 14, no. 1, p. 4598, 2024.

DOMINGOS, I. J. *et al.* Polyurethane foams from liquefied Eucalyptus globulus branches. **BioResources**, Amsterdam, vol. 14, no. 1, pp. 31–43, 2018.

DUMOULIN, C.; DERAEMAEKER, A. Design optimization of embedded ultrasonic transducers for concrete structures assessment. **Ultrasonics**, Amsterdam, vol. 79, pp. 18–33, 2017.

DUXSON, P. *et al.* Geopolymer technology: the current state of the art. **Journal of Materials Science**, Cham, vol. 42, no. 9, pp. 2917–2933, 2007.

EGNACZYK, T. M.; QUINN, C. M.; WAGNER, N. J. Relating the early-age reaction kinetics and material property development in a model metakaolin geopolymer. **Journal of the American Ceramic Society**, Hoboken, vol. 108, no. 8, p. e20531, 2025.

FANG, G.-H. *et al.* Optimized machine learning model for predicting compressive strength of alkali-activated concrete through multi-faceted comparative analysis. **Materials**, Basel, vol. 17, no. 20, p. 5086, 2024.

FANG, G. *et al.* Workability and mechanical properties of alkali-activated fly ash-slag concrete cured at ambient temperature. **Construction and Building Materials**, Amsterdam, vol. 172, pp. 476–487, 2018.

FENG, Q.; REN, Z.; WANG, D. Detection of frost-resistance property of large-size concrete based on impact-echo method. **Structural Durability & Health Monitoring**, Hong Kong, vol. 17, no. 1, pp. 71–88, 2023.

FINOCCHIARO, C. *et al.* FT-IR study of early stages of alkali activated materials based on pyroclastic deposits (Mt. Etna, Sicily, Italy) using two different alkaline solutions. **Construction and Building Materials**, Amsterdam, vol. 262, p. 120095, 2020.

GADO, R. A. *et al.* Alkali activation of waste clay bricks: influence of the silica modulus, SiO2/Na2O, H2O/Na2O molar ratio, and liquid/solid ratio. **Materials**, Basel, vol. 13, no. 2, p. 383, 2020.

GAO, Y. *et al.* Influences of sodium silicate modulus on mechanical properties and microstructure of fly ash geopolymer. **IOP Conference Series: Earth and Environmental Science**, Bristol, vol. 760, no. 1, p. 012056, 2021.

GARCIA, C. *et al.* The quintenary influence of industrial wastes on the compressive strength of high-strength geopolymer concrete under different curing regimes for sustainable structures; a GSVR-XGBoost hybrid model. **Frontiers in Built Environment**, Lausanne, vol. 10, p. 1433069, 2024.

GARCIA-LODEIRO, I.; PALOMO, A.; FERNÁNDEZ-JIMÉNEZ, A. Crucial insights on the mix design of alkali-activated cement-based binders. *In*: HANDBOOK OF ALKALI-ACTIVATED CEMENTS, MORTARS AND CONCRETES. Amsterdam: Elsevier, 2015. pp. 49–73. Available at: https://linkinghub.elsevier.com/retrieve/pii/B9781782422761500034. Accessed on: 5 oct. 2025.

GHOSH, K.; GHOSH, P. **Alkali-activated fly ash blast furnace slag composites**. 1. ed. Boca Raton, United States: CRC Press, 2020. Available at: https://www.taylorfrancis.com/books/9781000287004. Accessed on: 11 nov. 2025.

GHOSTINE, R. *et al.* Curing effect on durability of cement mortar with GGBS: experimental and numerical study. **Materials**, Basel, vol. 15, no. 13, p. 4394, 2022.

GLANZ, D. *et al.* Comparative environmental footprint analysis of ultra-high-performance concrete using Portland cement and alkali-activated materials. **Frontiers in Built Environment**, Lausanne, vol. 9, p. 1196246, 2023.

GONG, K.; WHITE, C. E. Development of physics-based compositional parameters for predicting the reactivity of amorphous aluminosilicates in alkaline environments. **Cement and Concrete Research**, [*s. l.*], vol. 174, p. 107296, 2023.

GÖRHAN, G.; DANISHYAR, F. The effect of silicate modulus on the properties of polypropylene fiber-reinforced geopolymer composite material. **Periodica Polytechnica Civil Engineering**, Budapest, 2022. Available at: https://pp.bme.hu/ci/article/view/19417. Accessed on: 4 dec. 2025.

GUAN, X. *et al.* Molecular simulations of the structure-property relationships of N-A-S-H gels. **Construction and Building Materials**, Amsterdam, vol. 329, p. 127166, 2022.

GUO, K. *et al.* Experimental study of alkali-activated cementitious materials using thermally activated red mud: effect of the Si/Al ratio on fresh and mechanical properties. **Buildings**, Amsterdam, vol. 15, no. 4, p. 565, 2025.

GUO, A. *et al.* Monitoring early-stage evolution of free water content in alkali-activated slag systems by using 1H low-field NMR. **Buildings**, Amsterdam, vol. 14, no. 10, p. 3079, 2024.

GUO, X.; SHI, H.; DICK, W. A. Compressive strength and microstructural characteristics of class C fly ash geopolymer. **Cement and Concrete Composites**, Amsterdam, vol. 32, no. 2, pp. 142–147, 2010.

HAN, Q. *et al.* Comprehensive review of the properties of fly ash-based geopolymer with additive of nano-SiO_2. **Nanotechnology Reviews**, Berlin, vol. 11, no. 1, pp. 1478–1498, 2022.

HAN, F. *et al.* Effect of steel slag on hydration kinetics and rheological properties of alkali-activated slag materials: a comparative study with fly ash. **Materials**, Basel, vol. 17, no. 10, p. 2260, 2024.

HAN, T. *et al.* Machine learning enabled closed-form models to predict strength of alkali-activated systems. **Journal of the American Ceramic Society**, Hoboken, vol. 105, no. 6, pp. 4414–4425, 2022.

HAN, T. *et al.* On the prediction of the mechanical properties of limestone calcined clay cement: a random forest approach tailored to cement chemistry. **Minerals**, Basel, vol. 13, no. 10, p. 1261, 2023.

HEROZI, M. R. *et al.* Numerical and experimental investigation of the appropriate geometry of asphalt specimens for quality control using impact resonance tests. **Journal of Testing and Evaluation**, West Conshohocken, 2025. Available at: https://dl.astm.org/jte/article/doi/10.1520/JTE20240298/28899/Numerical-and-Experimental-Investigation-of-the. Accessed on: 5 dec. 2025.

HOAYEK, A. *et al.* Prediction of geopolymer pumpability and setting time for well zonal isolation - Using machine learning and statistical based models. **Heliyon**, Amsterdam, vol. 9, no. 7, p. e17925, 2023.

HONG, J.; CHOI, H. Monitoring hardening behavior of cementitious materials using contactless ultrasonic method. **Sensors**, Basel, vol. 21, no. 10, p. 3421, 2021.

HOYOS-MONTILLA, A. A. *et al.* Infrared spectra experimental analyses on alkali-activated fly ash-based binders. **Spectrochimica Acta Part A: Molecular and Biomolecular Spectroscopy**, Amsterdam, vol. 269, p. 120698, 2022.

HSU, C.-H. *et al.* Efficient compressive strength prediction of alkali-activated waste materials using machine learning. **Materials**, Basel, vol. 17, no. 13, p. 3141, 2024.

HUANG, Y. *et al.* Hybrid organic–inorganic blast furnace slag binders activated with alkali acetates. **ACS Omega**, Washington, vol. 9, no. 33, pp. 35888–35905, 2024.

HUANG, G. *et al.* Simultaneous utilization of mine tailings and steel slag for producing geopolymers: Alkali-hydrothermal activation, workability, strength, and hydration mechanism. **Construction and Building Materials**, Amsterdam, vol. 414, p. 135029, 2024.

HUNG, C.-C. *et al.* Delayed setting time for alkali-activated slag composites using activator containing SiO_2 and Na_2 O. **Materials Science-Poland**, Warsaw, vol. 39, no. 4, pp. 570–579, 2021.

HUO, Y. *et al.* Retarding the setting time of alkali-activated slag paste by processing the alkali activator into pills and capsules. **Structures**, Amsterdam, vol. 64, p. 106644, 2024.

JIA, D. *et al.* **Geopolymer and Geopolymer matrix composites**. Singapore: Springer, 2020. Available at: https://link.springer.com/book/10.1007/978-981-15-9536-3. Accessed on: 5 oct. 2025.

JIANG, D.; SHI, C.; ZHANG, Z. Recent progress in understanding setting and hardening of alkali-activated slag (AAS) materials. **Cement and Concrete Composites**, Amsterdam, vol. 134, p. 104795, 2022.

JOSEPH, S.; CIZER, Ö. Comparative analysis of heat release, bound water content and compressive strength of alkali-activated slag-fly ash. **Frontiers in Materials**, Lausanne, vol. 9, p. 861283, 2022.

JURADO-CONTRERAS, S. *et al.* Synthesis and characterization of alkali-activated materials containing biomass fly ash and metakaolin: effect of the soluble salt content of the residue. **Archives of Civil and Mechanical Engineering**, Amsterdam, vol. 22, no. 3, p. 121, 2022.

KAMATH, M.; PRASHANT, S.; KUMAR, M. Micro-characterisation of alkali activated paste with fly ash-GGBS-metakaolin binder system with ambient setting characteristics. **Construction and Building Materials**, Amsterdam, vol. 277, p. 122323, 2021.

KARBASSI, A. *et al.* Damage prediction for regular reinforced concrete buildings using the decision tree algorithm. **Computers & Structures**, Amsterdam, vol. 130, pp. 46–56, 2014.

KATATCHAMBO, A. Y.; BINGÖL, Ş. Comparison of regression based functions and ANN models for predicting the compressive strength of geopolymer mortars. **Scientific Reports**, London, vol. 15, no. 1, p. 11652, 2025.

KAYA, M. *et al.* Influence of micro Fe2O3 and MgO on the physical and mechanical properties of the zeolite and kaolin based geopolymer mortar. **Journal of Building Engineering**, Amsterdam, vol. 52, p. 104443, 2022.

KAZE, C. R. *et al.* Alkali-activated laterite binders: Influence of silica modulus on setting time, Rheological behaviour and strength development. **Cleaner Engineering and Technology**, Amsterdam, vol. 4, p. 100175, 2021.

KAZE, C. R. *et al.* Effect of silicate modulus on the setting, mechanical strength and microstructure of iron-rich aluminosilicate (laterite) based-geopolymer cured at room temperature. **Ceramics International**, Cham, vol. 44, no. 17, pp. 21442–21450, 2018.

KAZE, C. R. *et al.* Reaction kinetics and rheological behaviour of meta-halloysite based geopolymer cured at room temperature: Effect of thermal activation on physicochemical and microstructural properties. **Applied Clay Science**, Amsterdam, vol. 196, p. 105773, 2020.

KEPPERT, M. *et al.* Reactivity of precursors for geopolymerization studied by isothermal calorimetry. **Journal of Thermal Analysis and Calorimetry**, Budapest, vol. 149, no. 19, pp. 10619–10631, 2024.

KHAN, N. M. *et al.* Interpretable machine learning approaches to assess the compressive strength of metakaolin blended sustainable cement mortar. **Scientific Reports**, London, vol. 15, no. 1, p. 19414, 2025.

KIM, R. *et al.* Evaluation of self-healing in concrete using linear and nonlinear resonance spectroscopy. **Construction and Building Materials**, Amsterdam, vol. 335, p. 127492, 2022.

KING, I. J.; STEPHENS, R. W. B. Experimental acoustics. I. measurement of velocity of sound in terms of elastic modulus (student experiment). **Physics Education**, Bristol, vol. 10, no. 6, pp. 420–423, 1975.

KOU, Y. *et al.* Rheological properties of cemented paste backfill with alkali-activated slag. **Minerals**, Basel, vol. 10, no. 3, p. 288, 2020.

KOZHUKHOVA, N. I. *et al.* Understanding the relationship between composition and rheology in alkali-activated binders. **Journal of Physics: Conference Series**, Bristol, vol. 2124, no. 1, p. 012004, 2021.

KRIVOSHEIN, P. K. *et al.* FTIR photoacoustic and ATR spectroscopies of soils with aggregate size fractionation by dry sieving. **ACS Omega**, Washington, D.C., vol. 7, no. 2, pp. 2177–2197, 2022.

KUSUMASTUTI, E.; ARIATI, F. I.; ATMAJA, L. Synthesis of volcanic ash-based geopolymer with calcium oxide (CaO) addition for building material application. **Journal of Physics: Conference Series**, Bristol, vol. 1567, no. 2, p. 022030, 2020.

LAHLOU NOUHA *et al.* Effect of the formulation of sodium activation solutions on the setting time of metakaolin based geopolymers. **Journal of Materials Science and Engineering B**, Amsterdam, vol. 9, no. 1, 2019. Available at: http://www.davidpublisher.org/index.php/Home/Article/index?id=38765.html. Accessed on: 2 dec. 2025.

LANJEWAR, B. A. *et al.* Application of alkali-activated sustainable materials: a step towards net zero binder. **Energies**, Basel, vol. 16, no. 2, p. 969, 2023.

LEE, T.; LEE, J.; CHOI, H. Assessment of strength development at hardened stage on high-strength concrete using NDT. **Applied Sciences**, Amsterdam, vol. 10, no. 18, p. 6261, 2020.

LEONG, H. Y. *et al.* The effect of different Na2O and K2O ratios of alkali activator on compressive strength of fly ash based-geopolymer. **Construction and Building Materials**, Amsterdam, vol. 106, pp. 500–511, 2016.

LI, J. *et al.* Properties and microstructure development of alkali-activated coal bottom ash and titanium- extraction tailing slag binder. **Construction and Building Materials**, Amsterdam, vol. 403, p. 133087, 2023.

LI, Q. *et al.* Splitting tensile strength prediction of metakaolin concrete using machine learning techniques. **Scientific Reports**, London, vol. 13, no. 1, p. 20102, 2023.

LIANG, G.; YAO, W.; SHE, A. New insights into the early-age reaction kinetics of metakaolin geopolymer by 1H low-field NMR and isothermal calorimetry. **Cement and Concrete Composites**, Amsterdam, vol. 137, p. 104932, 2023.

LIMA JUNIOR, L. C. M. **Temperature-chemistry-microstructure correlations for alkali-activated binders**. 2025. 338 f. Thesis (Doctor in Civil Engineering) - Department Materials, Mechanics, Management & Design, Delft University of Technology, Delft, Netherlands, 2025.

LIN, S. *et al.* Setting time measurement of concrete mixtures through monitoring of shear-wave velocity with shear-horizontal waves. **Journal of Materials in Civil Engineering**, Reston, vol. 34, no. 9, p. 04022210, 2022.

LIU, J. *et al.* Methods to evaluate and quantify the geopolymerization reactivity of waste-derived aluminosilicate precursor in alkali-activated material: A state-of-the-art review. **Construction and Building Materials**, Amsterdam, vol. 362, p. 129784, 2023.

LIU, W. *et al.* Setting and hardening behaviour of alkali-activated landfilled fly ash-slag binder at room temperature. **Materials**, Basel, vol. 13, no. 14, p. 3130, 2020.

LÓPEZ, O. A. M.; LÓPEZ, A. M.; CROSSA, J. **Fundamentals of artificial neural networks and deep learning**. Cham: Springer International Publishing, 2022. Available at: https://doi.org/10.1007/978-3-030-89010-0_10. Accessed on: 5 oct. 2025.

LUGA, E. *et al.* Alkali-activated binders as sustainable alternatives to Portland cement and their resistance to saline water. **Materials**, Basel, vol. 17, no. 17, p. 4408, 2024.

LUO, Y. *et al.* Uncover the thermal behavior of geopolymer: insights from in-situ high temperature exposure. **Cement and Concrete Composites**, Amsterdam, vol. 164, p. 106282, 2025.

LV, Y. *et al.* Study of the mechanical properties and microstructure of alkali-activated fly ash-slag composite cementitious materials. **Polymers**, Basel, vol. 15, no. 8, p. 1903, 2023.

MA, Z. *et al.* Long-term dissolution behavior of amorphous aluminosilicate in sodium hydroxide solution for geopolymer synthesis using circulating fluidized bed combustion fly ash. **Construction and Building Materials**, Amsterdam, vol. 394, p. 132143, 2023.

MACIEL, M. H.; ROMANO, R. C. D. O.; PILEGGI, R. G. Hy_Surf model: viscoelastic evolution in Portland cement suspensions during the early-age hardening. **Cement and Concrete Research**, Amsterdam, vol. 174, p. 107342, 2023.

MAHMED, N.; ZAILAN, S. N. S.; ABDULLAH, M. M. A.-B. Influence of TiO_2 nanoparticles (wt%) onto the physical and mechanical properties of the TiO_2 -geopolymer

paste. **IOP Conference Series: Materials Science and Engineering**, Bristol, vol. 864, no. 1, p. 012177, 2020.

MALONE, C.; SUN, H.; ZHU, J. Nonlinear impact-echo test for quantitative evaluation of ASR damage in concrete. **Journal of Nondestructive Evaluation**, Cham, vol. 42, no. 4, p. 93, 2023.

MANDLER, H.; WEIGAND, B. A review and benchmark of feature importance methods for neural networks. **ACM Computing Surveys**, New York, vol. 56, no. 12, pp. 1–30, 2024.

MARVILA, M. T.; AZEVEDO, A. R. G. D.; VIEIRA, C. M. F. Reaction mechanisms of alkali-activated materials. **Revista IBRACON de Estruturas e Materiais**, São Paulo, vol. 14, no. 3, p. e14309, 2021.

MATOS, B. D. M. *et al.* Evaluation of commercially available polylactic acid (PLA) filaments for 3D printing applications. **Journal of Thermal Analysis and Calorimetry**, Budapest, vol. 137, no. 2, pp. 555–562, 2019.

MATSIMBE, J. *et al.* Fundamental machine learning algorithms and statistical models applied in strength prediction of geopolymers: a systematic review. **Discover Applied Sciences**, Cham, vol. 6, no. 10, p. 538, 2024.

MIENYE, I. D.; SWART, T. G. A comprehensive review of deep learning: architectures, recent advances, and applications. **Information**, Basel, vol. 15, no. 12, p. 755, 2024.

MIKHAILOVA, O. *et al.* In situ characterization of main reaction products in alkali-activated slag materials by Confocal Raman Microscopy. **Cement and Concrete Composites**, Amsterdam, vol. 99, pp. 32–39, 2019.

MISHRA, J. *et al.* Sustainable fly ash based geopolymer binders: a review on compressive strength and microstructure properties. **Sustainability**, Basel, vol. 14, no. 22, p. 15062, 2022.

MOHAMED, O. A. Effects of the curing regime, acid exposure, alkaline activator dosage, and precursor content on the strength development of mortar with alkali-activated slag and fly ash binder: a critical review. **Polymers**, Basel, vol. 15, no. 5, p. 1248, 2023.

MYERS, R. J. *et al.* Generalized structural description of calcium–sodium aluminosilicate hydrate gels: the cross-linked substituted tobermorite model. **Langmuir**, Washington, DC, vol. 29, no. 17, pp. 5294–5306, 2013.

NAGAJOTHI, S.; ELAVENIL, S. Parametric studies on the workability and compressive strength properties of geopolymer concrete. **Journal of the Mechanical Behavior of Materials**, Berlin, vol. 27, no. 3–4, 2018. Available at: https://www.degruyterbrill.com/document/doi/10.1515/jmbm-2018-0019/html. Accessed on: 5 oct. 2025.

NAQI, A. *et al.* Effect of solution-to-binder ratio and alkalinity on setting and early-age properties of alkali-activated slag-fly ash binders. **Materials**, Basel, vol. 16, no. 1, p. 373, 2022.

NASCIMENTO, F. R. S.; CAVALCANTI, G. D. C.; COSTA-ABREU, M. D. Gender bias detection on hate speech classification: an analysis at feature-level. **Neural Computing and Applications**, Cham, vol. 37, no. 5, pp. 3887–3905, 2025.

NASIR, N. A. M. *et al.* Performance of high-content waste ash geopolymer-based composites for sustainable construction. **Archives of Civil and Mechanical Engineering**, Amsterdam, vol. 25, no. 4, p. 228, 2025.

NAZAR, S. *et al.* Computational intelligence for modeling the rheological properties of the developed hydrated lime-based alkali-activated materials. **Materials Today Communications**, Amsterdam, vol. 41, p. 110602, 2024.

NEDUNURI, A. S. S. S.; MUHAMMAD, S. Fundamental understanding of the setting behaviour of the alkali activated binders based on ground granulated blast furnace slag and fly ash. **Construction and Building Materials**, Amsterdam, vol. 291, p. 123243, 2021.

NGO, A. Q.; NGUYEN, L. Q.; TRAN, V. Q. Developing interpretable machine learning-Shapley additive explanations model for unconfined compressive strength of cohesive soils stabilized with geopolymer. **PLOS ONE**, San Francisco, vol. 18, no. 6, p. e0286950, 2023.

NGUYEN, T. N. *et al.* Alteration in molecular structure of alkali activated slag with various water to binder ratios under accelerated carbonation. **Scientific Reports**, London, vol. 12, no. 1, p. 5524, 2022.

NGUYEN, K. T. *et al.* Analyzing the compressive strength of green fly ash based geopolymer concrete using experiment and machine learning approaches. **Construction and Building Materials**, Amsterdam, vol. 247, p. 118581, 2020.

NKWAJU, R. Y. *et al.* Effective stabilization of cadmium and copper in iron-rich laterite-based geopolymers and influence on physical properties. **Materials**, Basel, vol. 16, no. 24, p. 7605, 2023.

NODEHI, M.; TAGHVAEE, V. M. Alkali-activated materials and geopolymer: a review of common precursors and activators addressing circular economy. **Circular Economy and Sustainability**, Cham, vol. 2, no. 1, pp. 165–196, 2022.

NOFALAH, M.-H. *et al.* Effects of binder proportion and curing condition on the mechanical characteristics of volcanic ash- and slag-based geopolymer mortars; machine learning integrated experimental study. **Construction and Building Materials**, Amsterdam, vol. 395, p. 132330, 2023.

NUNES, V. A. *et al.* Influence of activation parameters on the mechanical and microstructure properties of an alkali-activated BOF steel slag. **Applied Sciences**, Amsterdam, vol. 12, no. 23, p. 12437, 2022.

OLARD, F.; DI BENEDETTO, H. General “2S2P1D” model and relation between the linear viscoelastic behaviours of bituminous binders and mixes. **Road Materials and Pavement Design**, Abingdon, vol. 4, no. 2, pp. 185–224, 2003.

PALACIOS, M. *et al.* Early reactivity of sodium silicate-activated slag pastes and its impact on rheological properties. **Cement and Concrete Research**, Amsterdam, vol. 140, p. 106302, 2021.

PARK, S. *et al.* A multi-frequency ultrasonic method for nondestructive detection of setting times and internal structure transition of building materials. **Construction and Building Materials**, Amsterdam, vol. 425, p. 136087, 2024.

PAUL, G. V.; GUNNESWARA RAO, T. D. Workability and strength characteristics of alkali-activated fly ASH/GGBS concrete activated with neutral grade Na2/SiO3 for various binder contents and the ratio of the liquid/binder. **Slovak Journal of Civil Engineering**, Bratislava, vol. 30, no. 3, pp. 53–64, 2022.

PERUŃ, G. Advances in non-destructive testing methods. **Materials**, Basel, vol. 17, no. 3, p. 554, 2024.

PHAM, T.-T. *et al.* Effects of superplasticizer and water–binder ratio on mechanical properties of one-part alkali-activated geopolymer concrete. **Buildings**, Amsterdam, vol. 13, no. 7, p. 1835, 2023.

PILARIO, K. E. *et al.* A review of kernel methods for feature extraction in nonlinear process monitoring. **Processes**, Basel, vol. 8, no. 1, p. 24, 2019.

POGGETTO, G. D.; LEONELLI, C.; SPINELLA, A. Influence of anionic silica forms in clear sodium silicate precursors on metakaolin geopolymerisation via 29Si and 27Al MAS-NMR and microstructural studies. **Journal of Materials Science**, Cham, vol. 59, no. 36, pp. 16963–16980, 2024.

POLYDOROU, T. *et al.* Development of a high strength geopolymer incorporating quarry waste diabase mud (DM) and ground granulated blast-furnace slag (GGBS). **Materials**, Basel, vol. 15, no. 17, p. 5946, 2022.

PROCHON, P.; PIOTROWSKI, T.; KĘPNIAK, M. The effects of phosphate compounds on the microstructure and mechanical properties of fly ash geopolymer mortars. **Materials**, Basel, vol. 17, no. 22, p. 5451, 2024.

PROVIS, J. L. Alkali-activated materials. **Cement and Concrete Research**, Amsterdam, vol. 114, pp. 40–48, 2018.

PROVIS, J. L.; BERNAL, S. A. Geopolymers and related alkali-activated materials. **Annual Review of Materials Research**, Palo Alto, vol. 44, no. 1, pp. 299–327, 2014.

PRUSTY, J. K.; PRADHAN, B. Effect of GGBS and chloride on compressive strength and corrosion performance of steel in fly ash-GGBS based geopolymer concrete. **Materials Today: Proceedings**, Amsterdam, vol. 32, pp. 850–855, 2020.

QADER, D. N. *et al.* A systematic review of metakaolin-based alkali-activated and geopolymer concrete: A step toward green concrete. **REVIEWS ON ADVANCED MATERIALS SCIENCE**, Berlin, vol. 64, no. 1, p. 20240076, 2025.

QIN, Y. *et al.* One-Part Alkali-Activated Materials: State of the Art and Perspectives. **Polymers**, [*s. l.*], vol. 14, no. 22, p. 5046, 2022a.

QIN, Y. *et al.* One-part alkali-activated materials: state of the art and perspectives. **Polymers**, Basel, vol. 14, no. 22, p. 5046, 2022b.

QURESHI, Y.; PAL, B.; SINGH, S. K. Influence of novel activation techniques on mechanical and microstructural characteristics of alkali activated one-part binder. **Construction and Building Materials**, Amsterdam, vol. 475, p. 141273, 2025.

RAHIMPOUR, H.; ESMAEILI, J. Characterization, mechanical strength, rheological properties and life cycle assessment of fully recycled concrete through geopolymer technology. **Scientific Reports**, London, vol. 15, no. 1, p. 9424, 2025.

RATH, B.; DEO, S.; RAMTEKKAR, G. Curing: the easiest and cheapest method to increase the durability and strength of concrete. **Facta universitatis - series: Architecture and Civil Engineering**, Niš, vol. 16, no. 3, pp. 475–487, 2018.

REINHARDT, H. W.; GROSSE, C. U. Continuous monitoring of setting and hardening of mortar and concrete. **Construction and Building Materials**, Amsterdam, vol. 18, no. 3, pp. 145–154, 2004.

REZZOUG, A.; AYED, K.; LEKLOU, N. Thermal, mechanical and microstructural properties of geopolymer mortars derived from ceramic sanitary-ware wastes: Pathway to net zero emission. **Ceramics International**, Cham, vol. 50, no. 24, pp. 55535–55545, 2024.

ROMANO, R. C. O.; CINCOTTO, M. A.; PILEGGI, R. G. Hardening phenomenon of Portland cement suspensions monitored by Vicat test, isothermal calorimetry and oscillatory rheometry. **Revista IBRACON de Estruturas e Materiais**, São Paulo, vol. 11, no. 5, pp. 949–959, 2018.

ROUYER, J.; POULESQUEN, A. Evidence of a fractal percolating network during geopolymerization. **Journal of the American Ceramic Society**, Hoboken, vol. 98, no. 5, pp. 1580–1587, 2015.

RUIZ, G. *et al.* Synthesis of a geopolymer binders using spent fluid catalytic cracking (FCC) catalyst. **IOP Conference Series: Materials Science and Engineering**, Bristol, vol. 660, no. 1, p. 012009, 2019.

RÜSCHER, C. H. *et al.* The effect of gel-type contributions in lime-sand bricks, alkali-activated slags and CEMI/CEMIII pastes: implications for next generation concretes. **Gels**, Basel, vol. 8, no. 1, p. 9, 2021.

RYU, G.-S. *et al.* A study on initial setting and modulus of elasticity of AAM mortar mixed with CSA expansive additive using ultrasonic pulse velocity. **Materials**, Basel, vol. 13, no. 19, p. 4432, 2020.

SACHET, W. H. *et al.* Experimental investigation on compressive strength enhancement of geopolymer paste fly ash/slag based cured at ambient condition. **Diyala Journal of Engineering Sciences**, Cham, vol. 13, no. 2, pp. 87–92, 2020.

SADEGHI, P. *et al.* A comprehensive evaluation of damping, vibration, and dynamic modulus in reclaimed asphalt pavement: The role of rejuvenators, polymer, temperature, and aging. **Case Studies in Construction Materials**, Amsterdam, vol. 21, p. e03366, 2024.

SCHMIDT, H.; DETHOF, F.; KESSLER, S. Automated honeycomb detection during Impact Echo inspections in concrete using AI trained by simulation data. **Research and Review**

Journal of Nondestructive Testing, New Delhi, vol. 1, no. 1, 2023. Available at: https://www.ndt.net/search/docs.php3?id=28149. Accessed on: 5 oct. 2025.

SCHONLAU, M.; ZOU, R. Y. The random forest algorithm for statistical learning. **The Stata Journal: Promoting communications on statistics and Stata**, College Station, vol. 20, no. 1, pp. 3–29, 2020.

SEGURA, I. P. *et al.* A review: alkali-activated cement and concrete production technologies available in the industry. **Heliyon**, Amsterdam, vol. 9, no. 5, p. e15718, 2023.

SHAH, S. F. A. *et al.* Compressive strength prediction of one-part alkali activated material enabled by interpretable machine learning. **Construction and Building Materials**, Amsterdam, vol. 360, p. 129534, 2022.

SHARAFATI, A.; ASADOLLAH, S. B. H. S.; AL-ANSARI, N. Application of bagging ensemble model for predicting compressive strength of hollow concrete masonry prism. **Ain Shams Engineering Journal**, Cairo, vol. 12, no. 4, pp. 3521–3530, 2021.

SHEN, Q. *et al.* Associated effects of sodium chloride and dihydrate gypsum on the mechanical performance and hydration properties of slag-based geopolymer. **Buildings**, Amsterdam, vol. 13, no. 5, p. 1285, 2023.

SHI, X. *et al.* Response surface methodology for multi-objective optimization of fly ash-GGBS based geopolymer mortar. **Construction and Building Materials**, Amsterdam, vol. 315, p. 125644, 2022.

SHILTON, R.; WANG, S.; BANTHIA, N. Use of polysaccharides as a rheology modifying admixture for alkali activated materials for 3D printing. **Construction and Building Materials**, Amsterdam, vol. 458, p. 139661, 2025.

SIDDIQUE, S. *et al.* Influence of the precursor, molarity and temperature on the rheology and structural buildup of alkali-activated materials. **Materials**, Basel, vol. 14, no. 13, p. 3590, 2021.

SIDDIQUE, S.; JANG, J. G. Mechanical properties, microstructure, and chloride content of alkali-activated fly ash paste made with sea water. **Materials**, Basel, vol. 13, no. 6, p. 1467, 2020.

SILVA, M. I. *et al.* Review of conventional and advanced non-destructive testing techniques for detection and characterization of small-scale defects. **Progress in Materials Science**, Amsterdam, vol. 138, p. 101155, 2023.

SINGH, N. B.; MIDDENDORF, B. Geopolymers as an alternative to Portland cement: An overview. **Construction and Building Materials**, Amsterdam, vol. 237, p. 117455, 2020.

SIYAL, A. A. *et al.* A comprehensive review of synthesis kinetics and formation mechanism of geopolymers. **RSC Advances**, London, vol. 14, no. 1, pp. 446–462, 2024.

SONG, X. *et al.* Sustainable improvement in the polylactic acid properties of 3D printing filaments: The role of bamboo fiber and EPOXIDIZED SOYBEAN OIL-BRANCHED CARDANOL ETHER compatibilizer. **Polymer Composites**, Hoboken, vol. 45, no. 12, pp. 11276–11288, 2024.

SONG, Y.; LANGE, D. A. Measuring dynamic Young's modulus of low-density foam concrete using resonant frequency test. **Journal of Testing and Evaluation**, West Conshohocken, vol. 50, no. 1, pp. 522–533, 2022.

SOUZA, M. L. **Rheological, microstructural, mechanical and durability properties of BSSF slag alkali-activated binders and concretes for interlocking blocks production**. 2024. 181 f. Dissertation (Master of Science in Civil Engineering) - Department of Structural Engineering and Civil Construction, Federal University of Ceará, Fortaleza, Brazil, 2024. Available at: https://repositorio.ufc.br/handle/riufc/80540. Accessed on: 5 oct. 2025.

STATKAUSKAS, M.; VAIČIUKYNIENĖ, D.; GRINYS, A. Mechanical properties of low calcium alkali activated binder system under ambient curing conditions. **Scientific Reports**, London, vol. 14, no. 1, p. 13060, 2024.

SU, M.; ZHONG, Q.; PENG, H. Regularized multivariate polynomial regression analysis of the compressive strength of slag-metakaolin geopolymer pastes based on experimental data. **Construction and Building Materials**, Amsterdam, vol. 303, p. 124529, 2021.

SUN, Y. *et al.* Rheology of alkali-activated slag pastes: New insight from microstructural investigations by cryo-SEM. **Cement and Concrete Research**, Amsterdam, vol. 157, p. 106806, 2022.

SUN, J. *et al.* Sustainable utilization of alkali-activated steel slag material: Effects of silicate modulus and GBFS on fresh, mechanical and pore structure properties. **Developments in the Built Environment**, Amsterdam, vol. 18, p. 100410, 2024.

SUN, Z.; VOLLPRACHT, A. Isothermal calorimetry and in-situ XRD study of the NaOH activated fly ash, metakaolin and slag. **Cement and Concrete Research**, Amsterdam, vol. 103, pp. 110–122, 2018.

SYARIF, I. *et al.* Application of bagging, boosting and stacking to intrusion detection. *In*: PERNER, P. (ed.). **Machine Learning and Data Mining in Pattern Recognition**. Berlin, Heidelberg: Springer Berlin Heidelberg, 2012. (Lecture Notes in Computer Science). vol. 7376, pp. 593–602. Available at: http://link.springer.com/10.1007/978-3-642-31537-4_46. Accessed on: 5 oct. 2025.

TANG, Y. X. *et al.* Artificial neural network-forecasted compression strength of alkaline-activated slag concretes. **Sustainability**, Basel, vol. 14, no. 9, p. 5214, 2022.

TEKLE, B. H.; HERTWIG, L.; HOLSCHEMACHER, K. Rheology of alkali-activated blended binder mixtures. **Materials**, Basel, vol. 14, no. 18, p. 5405, 2021.

TEKLE, B. H.; HOLSCHEMACHER, K. Alkali activated cement mixture at ambient curing: Strength, workability, and setting time. **Structural Concrete**, Hoboken, vol. 23, no. 4, pp. 2496–2509, 2022.

TEO, W. *et al.* Experimental investigation on ambient-cured one-part alkali-activated binders using combined high-calcium fly ash (HCFA) and ground granulated blast furnace slag (GGBS). **Materials**, Basel, vol. 15, no. 4, p. 1612, 2022.

TIAN, X.; XU, W. Prediction of the mechanical performance of cemented tailings backfill using ultrasonic pulse velocity measurement. **Minerals**, Basel, vol. 12, no. 8, p. 986, 2022.

TOGNONVI, T. M.; PASCUAL, A. B.; TAGNIT-HAMOU, A. Physico-chemistry of geopolymers based on recycled glass powder and metakaolin: Effect of metakaolin content. **Materials Today: Proceedings**, Amsterdam, vol. 58, pp. 1508–1514, 2022.

TOOBPENG, N.; THAVORNITI, P.; JIEMSIRILERS, S. Effect of additives on the setting time and compressive strength of activated high-calcium fly ash-based geopolymers. **Construction and Building Materials**, Amsterdam, vol. 417, p. 135035, 2024.

TRAN, K. *et al.* Kinetics of geopolymerization followed by rheology: a general model. **Soft Matter**, London, vol. 18, no. 13, pp. 2549–2557, 2022.

TRAN THI, K.-D.; LIAO, M.-C.; VO, D.-H. The characteristics of alkali-activated slag-fly ash incorporating the high volume wood bottom ash: Mechanical properties and microstructures. **Construction and Building Materials**, Amsterdam, vol. 394, p. 132240, 2023.

TRINDADE, E. *et al.* Identification of obstacles to implementing sustainability in the civil construction industry using bow-tie tool. **Buildings**, Amsterdam, vol. 10, no. 9, p. 165, 2020.

TRTNIK, G.; VALIČ, M. I.; TURK, G. Measurement of setting process of cement pastes using non-destructive ultrasonic shear wave reflection technique. **NDT & E International**, Amsterdam, vol. 56, pp. 65–75, 2013.

UKRITNUKUN, S. *et al.* Predictive model of setting times and compressive strengths for low-alkali, ambient-cured, fly ash/slag-based geopolymers. **Minerals**, Basel, vol. 10, no. 10, p. 920, 2020.

VIZUREANU, P.; BURDUHOS-NERGIS, D.-D. **Green materials obtained by geopolymerization for a sustainable future**. Millersville, United States: Materials Research Forum LLC, 2021.

VÖLKER, C. *et al.* Sequential learning to accelerate discovery of alkali-activated binders. **Journal of Materials Science**, Cham, vol. 56, no. 28, pp. 15859–15881, 2021.

WANG, Xingang *et al.* High performance C-A-S-H seeds and sulfate-rich lithium slag by nano-mechanochemical method on cement hydration: Microstructure and mechanical performance. **Advanced Powder Technology**, Amsterdam, vol. 35, no. 10, p. 104623, 2024.

WANG, Y. *et al.* Lamb waves-based computation of impact echo thickness resonant frequency: theory development and case study. **Advances in Civil Engineering**, London, vol. 2024, no. 1, p. 7811595, 2024.

WANG, M. *et al.* Mechanical performance optimization and microstructural mechanism study of alkali-activated steel slag–slag cementitious materials. **Buildings**, Amsterdam, vol. 14, no. 5, p. 1204, 2024.

WANG, Xiaoping *et al.* Study on the compressive strength and reaction mechanism of alkali-activated geopolymer materials using coal gangue and ground granulated blast furnace slag. **Materials**, Basel, vol. 17, no. 15, p. 3659, 2024.

WANG, W. *et al.* Workability, rheology, and geopolymerization of fly ash geopolymer: Role of alkali content, modulus, and water–binder ratio. **Construction and Building Materials**, Amsterdam, vol. 367, p. 130357, 2023.

WEI, J. *et al.* Higher-order multivariable polynomial regression to estimate human affective states. **Scientific Reports**, London, vol. 6, no. 1, p. 23384, 2016.

WOODMAN, R. J.; MANGONI, A. A. A comprehensive review of machine learning algorithms and their application in geriatric medicine: present and future. **Aging Clinical and Experimental Research**, Milan, vol. 35, no. 11, pp. 2363–2397, 2023.

WU, J. *et al.* Characterization of slag reprocessing tailings-based geopolymers in marine environment. **Minerals**, Basel, vol. 10, no. 9, p. 832, 2020.

XIE, T. *et al.* Mix design and mechanical properties of geopolymer and alkali activated concrete: Review of the state-of-the-art and the development of a new unified approach. **Construction and Building Materials**, Amsterdam, vol. 256, p. 119380, 2020.

XU, F. *et al.* Characterization and performance evaluation of geopolymer prepared with thermal-mechanical activated aluminum sulfate residue. **Construction and Building Materials**, Amsterdam, vol. 384, p. 131454, 2023.

XU, X. *et al.* Sustainable enhancement of fly ash-based geopolymers: Impact of Alkali thermal activation and particle size on green production. **Process Safety and Environmental Protection**, Amsterdam, vol. 191, pp. 478–489, 2024.

XU, D. *et al.* Ultrasonic monitoring of hydration behavior of cement paste doped with triethanolamine using novel piezoelectric ultrasonic transducer. **Sensors and Actuators A: Physical**, Amsterdam, vol. 366, p. 115014, 2024.

YADOLLAHI, M. M.; BENLI, A.; DEMIRBOĞA, R. The effects of silica modulus and aging on compressive strength of pumice-based geopolymer composites. **Construction and Building Materials**, Amsterdam, vol. 94, pp. 767–774, 2015.

YAN, S. *et al.* Effect of additional Al sources on early-age strength of fly ash-based geopolymer containing calcium carbide residue and Glauber's salt as activators. **Construction and Building Materials**, Amsterdam, vol. 447, p. 138158, 2024.

YANG, T. *et al.* Modification on the chloride binding capacity of alkali activated slag by applying calcium and aluminium containing phases. **Construction and Building Materials**, Amsterdam, vol. 358, p. 129427, 2022.

YANG, X.; ZHANG, Y.; LIN, C. Microstructure analysis and effects of single and mixed activators on setting time and strength of coal gangue-based geopolymers. **Gels**, Basel, vol. 8, no. 3, p. 195, 2022.

YANKWA DJOBO, J. N.; NKWAJU, R. Y. Preparation of acid aluminum phosphate solutions for metakaolin phosphate geopolymer binder. **RSC Advances**, London, vol. 11, no. 51, pp. 32258–32268, 2021.

YASEEN, N. *et al.* Concrete incorporating supplementary cementitious materials: Temporal evolution of compressive strength and environmental life cycle assessment. **Heliyon**, Amsterdam, vol. 10, no. 3, p. e25056, 2024.

YI, C.; BOLUK, Y.; BINDIGANAVILE, V. Preparation of geopolymers with nanosilica and water-in-air Pickering emulsion: mechanisms underlying its rheology, polymerization, and strength. **Langmuir**, Washington, DC, vol. 40, no. 22, pp. 11436–11449, 2024.

YIN, K. *et al.* Characterization of one-part alkali-activated slag with rice straw ash. **Construction and Building Materials**, Amsterdam, vol. 345, p. 128403, 2022.

YU, M. *et al.* Enhancing the performance of alkali-activated slag using KH-550 as a multi-functional admixture. **Case Studies in Construction Materials**, Amsterdam, vol. 21, p. e03434, 2024.

YUAN, Y. *et al.* Synthesis of geopolymer using glass fiber powder from retired wind blades: A new attempt to recycle solid waste in wind power industries. **Journal of Building Engineering**, [*s. l.*], vol. 95, p. 110130, 2024.

YUAN, Y.; WEI, W.; NI, Z. Analytical and experimental studies on an innovative steel damper reinforced polyurethane bearing for seismic isolation applications. **Engineering Structures**, Amsterdam, vol. 239, p. 112254, 2021.

YUSSLEE, E.; BESKHYROUN, S. The effect of water-to-binder ratio (W/B) on pore structure of one-part alkali activated mortar. **Heliyon**, Amsterdam, vol. 9, no. 1, p. e12983, 2023.

ZERZOURI, M. *et al.* Comparative study of the structural, microstructural, and mechanical properties of geopolymer pastes obtained from ready-to-use metakaolin–quicklime powders and classic geopolymers. **Materials**, Basel, vol. 17, no. 16, p. 4151, 2024.

ZHAN, J. *et al.* Effect of slag on the strength and shrinkage properties of metakaolin-based geopolymers. **Materials**, Basel, vol. 15, no. 8, p. 2944, 2022.

ZHANG, M. *et al.* A multiscale investigation of reaction kinetics, phase formation, and mechanical properties of metakaolin geopolymers. **Cement and Concrete Composites**, Amsterdam, vol. 78, pp. 21–32, 2017.

ZHANG, P. *et al.* A state-of-the-art review on frost resistance of fiber-reinforced geopolymer composites. **Sustainable Chemistry and Pharmacy**, Amsterdam, vol. 45, p. 102006, 2025.

ZHANG, J. *et al.* Elemental design of alkali-activated materials with solid wastes using machine learning. **Materials**, Basel, vol. 17, no. 18, p. 4573, 2024.

ZHANG, P. *et al.* Fabrication and engineering properties of concretes based on geopolymers/alkali-activated binders - A review. **Journal of Cleaner Production**, Amsterdam, vol. 258, p. 120896, 2020.

ZHANG, G. *et al.* Study on the effects and mechanisms of fly ash, silica fume, and metakaolin on the properties of slag–Yellow River sediment-based geopolymers. **Materials**, Basel, vol. 18, no. 8, p. 1845, 2025.

ZHANG, K. *et al.* Study on the influence mechanism of micro-mechanical properties of heterogeneous geopolymer gels. **Journal of Building Engineering**, Amsterdam, vol. 76, p. 107164, 2023.

ZHANG, Y.; ÇOPUROĞLU, O. The effect of slag chemistry on CO2 binding capacity of C3S-slag (-gypsum) system. **Construction and Building Materials**, Amsterdam, vol. 354, p. 129208, 2022.

ZHANG, Y.; LIU, W.; LIU, M. Setting time and mechanical properties of chemical admixtures modified FA/GGBS-based engineered geopolymer composites. **Construction and Building Materials**, Amsterdam, vol. 431, p. 136473, 2024.

ZHANG, R.; SIAS, J. E.; DAVE, E. V. Using mix design information for modelling of fundamental viscoelasticity of asphalt mixtures. **Construction and Building Materials**, Amsterdam, vol. 329, p. 127029, 2022.

ZHAO, X. *et al.* Investigation into the effect of calcium on the existence form of geopolymerized gel product of fly ash based geopolymers. **Cement and Concrete Composites**, Amsterdam, vol. 103, pp. 279–292, 2019.

ZHONG, Q. *et al.* Investigation of setting time and microstructural and mechanical properties of MK/GGBFS-blended geopolymer pastes. **Materials**, Basel, vol. 15, no. 23, p. 8431, 2022.

ZHOU, H. *et al.* Investigation on pore properties, thermal conductivity, and compressive behavior of fly ash/slag-based geopolymer foam. **International Journal of Applied Ceramic Technology**, Hoboken, vol. 20, no. 6, pp. 3517–3534, 2023.

ZOU, Y. *et al.* Evaluation of artificial intelligence methods to estimate the compressive strength of geopolymers. **Gels**, Basel, vol. 8, no. 5, p. 271, 2022.

ZRIBI, M.; BAKLOUTI, S. Investigation of phosphate based geopolymers formation mechanism. **Journal of Non-Crystalline Solids**, Amsterdam, vol. 562, p. 120777, 2021.

ZULKARNAIN, N. N. *et al.* Reducing the waiting-on-cement time of geopolymer well cement using calcium chloride ($CaCl_2$) as the accelerator: analysis of the compressive strength and acoustic impedance for well logging. **Sustainability**, Basel, vol. 13, no. 11, p. 6128, 2021.

APPENDIX A – PARAMETERS OF THE MULTIVARIATE POLYNOMIAL REGRESSION MODEL FOR INITIAL AND FINAL SETTING TIME

Parameter	Value		Parameter	Value	
	Initial ST	Final ST		Initial ST	Final ST
Intercept	183.968	291.712	$P_2O_5 \times Fe_2O_3$	-0.272	-0.740
Al_2O_3	2.059	5.353	$P_2O_5 \times S/N$	0.275	-0.201
SiO_2	0.420	-0.144	$P_2O_5 \times Temperature$	0.036	0.781
P_2O_5	0.176	0.083	$P_2O_5 \times N/B$	3.331	2.649
SO_3	1.120	3.420	$P_2O_5 \times W/B$	-1.191	-0.614
Cl	-0.883	0.076	SO_3^2	-0.783	0.214
K_2O	-2.587	-6.392	$SO_3 \times Cl$	-0.728	-0.552
CaO	-1.153	-2.684	$SO_3 \times K_2O$	0.264	-1.263
TiO_2	-0.660	1.109	$SO_3 \times CaO$	-0.719	-2.833
MnO	-0.006	-0.001	$SO_3 \times TiO_2$	-0.691	-0.239
Fe_2O_3	0.804	1.848	$SO_3 \times MnO$	-0.237	-0.718
S/N	0.172	1.425	$SO_3 \times Fe_2O_3$	0.281	1.262
Temperature	-0.374	-2.279	$SO_3 \times S/N$	-0.625	-0.276
N/B	-3.104	-1.607	$SO_3 \times Temperature$	-0.360	-1.485
W/B	2.467	-0.662	$SO_3 \times N/B$	2.381	5.561
$Al_2O_3^2$	1.330	3.743	$SO_3 \times W/B$	-0.295	-2.284
$Al_2O_3 \times SiO_2$	0.748	-0.694	Cl^2	-1.433	-4.863
$Al_2O_3 \times P_2O_5$	-0.374	-1.736	$Cl \times K_2O$	2.303	3.677
$Al_2O_3 \times SO_3$	0.182	1.959	$Cl \times CaO$	-0.447	-3.514
$Al_2O_3 \times Cl$	-1.202	-0.276	$Cl \times TiO_2$	-1.376	-4.436
$Al_2O_3 \times K_2O$	-1.212	-5.088	$Cl \times MnO$	0.188	-0.015
$Al_2O_3 \times CaO$	-0.862	-2.308	$Cl \times Fe_2O_3$	-0.015	0.429
$Al_2O_3 \times TiO_2$	-0.985	1.102	$Cl \times S/N$	-0.628	-0.926
$Al_2O_3 \times MnO$	-0.428	-1.121	$Cl \times Temperature$	0.750	1.290
$Al_2O_3 \times Fe_2O_3$	0.480	1.768	$Cl \times N/B$	1.258	2.493
$Al_2O_3 \times S/N$	-0.916	-0.879	$Cl \times W/B$	-1.115	-4.691
$Al_2O_3 \times Temperature$	-0.872	-3.320	K_2O^2	0.006	2.232
$Al_2O_3 \times N/B$	1.258	5.786	$K_2O \times CaO$	1.205	4.897
$Al_2O_3 \times W/B$	1.231	-2.824	$K_2O \times TiO_2$	2.723	3.968
SiO_2^2	-1.619	-4.572	$K_2O \times MnO$	0.538	1.329
$SiO_2 \times P_2O_5$	-0.015	0.127	$K_2O \times Fe_2O_3$	-0.154	-0.894
$SiO_2 \times SO_3$	1.051	0.711	$K_2O \times S/N$	1.102	0.872
$SiO_2 \times Cl$	1.024	3.733	$K_2O \times Temperature$	0.384	1.780
$SiO_2 \times K_2O$	-1.451	-3.314	$K_2O \times N/B$	1.845	0.725
$SiO_2 \times CaO$	0.554	3.876	$K_2O \times W/B$	-2.278	0.261
$SiO_2 \times TiO_2$	1.227	4.382	CaO^2	0.118	-0.629
$SiO_2 \times MnO$	-0.084	0.025	$CaO \times TiO_2$	-0.888	-5.235
$SiO_2 \times Fe_2O_3$	0.196	0.293	$CaO \times MnO$	0.242	0.566
$SiO_2 \times S/N$	-1.094	-2.378	$CaO \times Fe_2O_3$	-0.245	-0.529
$SiO_2 \times Temperature$	-0.708	-1.835	$CaO \times S/N$	0.691	0.198
$SiO_2 \times N/B$	-1.953	-1.767	$CaO \times Temperature$	0.914	3.073
$SiO_2 \times W/B$	1.335	2.056	$CaO \times N/B$	-1.439	-6.152
$P_2O_5^2$	0.184	0.127	$CaO \times W/B$	-0.612	0.740

$P_2O_5 \times SO_3$	-0.244	-1.195	TiO_2^2	-1.338	-4.488
$P_2O_5 \times Cl$	0.225	-0.078	$TiO_2 \times MnO$	0.141	-0.231
$P_2O_5 \times K_2O$	0.979	2.334	$TiO_2 \times Fe_2O_3$	-0.005	0.585
$P_2O_5 \times CaO$	0.135	0.855	$TiO_2 \times S/N$	-0.392	-0.109
$P_2O_5 \times TiO_2$	0.252	-0.405	$TiO_2 \times Temperature$	0.653	0.911
$TiO_2 \times W/B$	-1.301	-4.917	$TiO_2 \times N/B$	3.164	4.526
MnO^2	-0.014	0.011	$Al_2O_3 \times P_2O_5 \times SO_3$	0.303	-0.488
$MnO \times Fe_2O_3$	-0.184	-0.383	$Al_2O_3 \times P_2O_5 \times Cl$	0.218	-0.044
$MnO \times S/N$	-0.035	-0.274	$Al_2O_3 \times P_2O_5 \times K_2O$	0.463	1.884
$MnO \times Temperature$	0.079	0.475	$Al_2O_3 \times P_2O_5 \times CaO$	-0.310	0.445
$MnO \times N/B$	0.653	0.321	$Al_2O_3 \times P_2O_5 \times TiO_2$	0.374	-0.401
$MnO \times W/B$	-0.500	0.141	$Al_2O_3 \times P_2O_5 \times MnO$	0.082	0.358
$Fe_2O_3^2$	-0.211	-1.313	$Al_2O_3 \times P_2O_5 \times Fe_2O_3$	-0.122	-0.649
$Fe_2O_3 \times S/N$	0.730	1.727	$Al_2O_3 \times P_2O_5 \times S/N$	1.118	0.978
$Fe_2O_3 \times Temperature$	-0.161	-0.312	$Al_2O_3 \times P_2O_5 \times Temperature$	0.093	1.078
$Fe_2O_3 \times N/B$	1.149	1.932	$Al_2O_3 \times P_2O_5 \times N/B$	4.459	2.544
$Fe_2O_3 \times W/B$	0.140	0.856	$Al_2O_3 \times P_2O_5 \times W/B$	-1.080	-1.005
S/N^2	-1.652	-2.604	$Al_2O_3 \times SO_3^2$	1.354	3.364
$S/N \times Temperature$	-0.561	-1.353	$Al_2O_3 \times SO_3 \times Cl$	0.386	1.930
$S/N \times N/B$	-1.769	-2.041	$Al_2O_3 \times SO_3 \times K_2O$	-0.499	-2.763
$S/N \times W/B$	0.730	-0.079	$Al_2O_3 \times SO_3 \times CaO$	-1.020	-2.000
$Temperature^2$	0.071	0.948	$Al_2O_3 \times SO_3 \times TiO_2$	0.783	2.756
$Temperature \times N/B$	-1.063	-2.501	$Al_2O_3 \times SO_3 \times MnO$	-0.033	-0.411
$Temperature \times W/B$	-0.572	1.844	$Al_2O_3 \times SO_3 \times Fe_2O_3$	-0.063	-0.914
N/B^2	6.824	14.860	$Al_2O_3 \times SO_3 \times S/N$	1.101	2.182
$N/B \times W/B$	-0.726	-7.109	$Al_2O_3 \times SO_3 \times Temperature$	-0.345	-1.620
W/B^2	1.025	-0.360	$Al_2O_3 \times SO_3 \times N/B$	3.642	5.755
$Al_2O_3^3$	2.328	6.372	$Al_2O_3 \times SO_3 \times W/B$	0.536	-1.062
$Al_2O_3^2 \times SiO_2$	-0.057	-1.712	$Al_2O_3 \times Cl^2$	-0.985	-3.335
$Al_2O_3^2 \times P_2O_5$	0.377	-0.803	$Al_2O_3 \times Cl \times K_2O$	0.706	0.434
$Al_2O_3^2 \times SO_3$	1.445	4.409	$Al_2O_3 \times Cl \times CaO$	-1.256	-5.214
$Al_2O_3^2 \times Cl$	0.196	3.423	$Al_2O_3 \times Cl \times TiO_2$	-0.756	-2.690
$Al_2O_3^2 \times K_2O$	-1.117	-5.036	$Al_2O_3 \times Cl \times MnO$	0.250	0.060
$Al_2O_3^2 \times CaO$	-1.439	-2.782	$Al_2O_3 \times Cl \times Fe_2O_3$	0.246	0.545
$Al_2O_3^2 \times TiO_2$	0.632	4.209	$Al_2O_3 \times Cl \times S/N$	0.333	1.321
$Al_2O_3^2 \times MnO$	-0.273	-0.780	$Al_2O_3 \times Cl \times Temperature$	0.509	0.229
$Al_2O_3^2 \times Fe_2O_3$	0.217	0.224	$Al_2O_3 \times Cl \times N/B$	-0.053	0.664
$Al_2O_3^2 \times S/N$	0.567	2.389	$Al_2O_3 \times Cl \times W/B$	0.020	-3.278
$Al_2O_3^2 \times Temperature$	-0.949	-3.302	$Al_2O_3 \times K_2O^2$	0.548	3.208
$Al_2O_3^2 \times N/B$	5.496	9.055	$Al_2O_3 \times K_2O \times CaO$	1.115	3.609
$Al_2O_3^2 \times W/B$	1.053	-1.194	$Al_2O_3 \times K_2O \times TiO_2$	0.567	-0.416
$Al_2O_3 \times SiO_2^2$	-0.771	-4.228	$Al_2O_3 \times K_2O \times MnO$	0.255	1.056
$Al_2O_3 \times SiO_2 \times P_2O_5$	0.017	0.455	$Al_2O_3 \times K_2O \times Fe_2O_3$	-0.054	0.021
$Al_2O_3 \times SiO_2 \times SO_3$	-0.224	-0.279	$Al_2O_3 \times K_2O \times S/N$	0.447	-0.349
$Al_2O_3 \times SiO_2 \times Cl$	0.836	3.689	$Al_2O_3 \times K_2O \times Temperature$	0.379	2.323
$Al_2O_3 \times SiO_2 \times K_2O$	-0.674	-1.088	$Al_2O_3 \times K_2O \times N/B$	-0.581	-3.810
$Al_2O_3 \times SiO_2 \times CaO$	0.832	3.212	$Al_2O_3 \times K_2O \times W/B$	-1.190	1.261
$Al_2O_3 \times SiO_2 \times TiO_2$	0.746	3.341	$Al_2O_3 \times CaO^2$	0.306	-0.551

$Al_2O_3 \times SiO_2 \times MnO$	-0.153	0.145	$Al_2O_3 \times CaO \times TiO_2$	-1.500	-5.126
$Al_2O_3 \times SiO_2 \times Fe_2O_3$	0.108	0.658	$Al_2O_3 \times CaO \times MnO$	0.175	0.485
$Al_2O_3 \times SiO_2 \times S/N$	-0.879	-0.774	$Al_2O_3 \times CaO \times Fe_2O_3$	-0.074	-0.004
$Al_2O_3 \times SiO_2 \times Temperature$	-0.556	-0.815	$Al_2O_3 \times CaO \times S/N$	-0.493	-1.571
$Al_2O_3 \times SiO_2 \times N/B$	-0.011	0.583	$Al_2O_3 \times CaO \times Temperature$	0.888	2.595
$Al_2O_3 \times SiO_2 \times W/B$	0.111	2.524	$Al_2O_3 \times CaO \times N/B$	-4.410	-6.224
$Al_2O_3 \times P_2O_5^2$	0.750	1.038	$Al_2O_3 \times CaO \times W/B$	-0.557	-0.799
$Al_2O_3 \times TiO_2 \times MnO$	0.204	-0.229	$Al_2O_3 \times TiO_2^2$	-0.286	-1.400
$Al_2O_3 \times TiO_2 \times Fe_2O_3$	0.128	-0.164	$SiO_2 \times P_2O_5 \times N/B$	2.386	2.244
$Al_2O_3 \times TiO_2 \times S/N$	0.896	1.910	$SiO_2 \times P_2O_5 \times W/B$	-0.722	-1.438
$Al_2O_3 \times TiO_2 \times Temperature$	0.343	-0.330	$SiO_2 \times SO_3^2$	-0.786	-0.092
$Al_2O_3 \times TiO_2 \times N/B$	2.740	4.960	$SiO_2 \times SO_3 \times Cl$	0.135	1.547
$Al_2O_3 \times TiO_2 \times W/B$	-0.258	-4.557	$SiO_2 \times SO_3 \times K_2O$	0.022	-0.255
$Al_2O_3 \times MnO^2$	0.086	0.231	$SiO_2 \times SO_3 \times CaO$	0.268	0.627
$Al_2O_3 \times MnO \times Fe_2O_3$	-0.100	-0.380	$SiO_2 \times SO_3 \times TiO_2$	-0.017	1.323
$Al_2O_3 \times MnO \times S/N$	0.193	0.164	$SiO_2 \times SO_3 \times MnO$	-0.213	-0.152
$Al_2O_3 \times MnO \times Temperature$	0.182	0.693	$SiO_2 \times SO_3 \times Fe_2O_3$	-0.119	-0.103
$Al_2O_3 \times MnO \times N/B$	-0.268	-1.193	$SiO_2 \times SO_3 \times S/N$	-0.092	0.503
$Al_2O_3 \times MnO \times W/B$	-0.264	0.594	$SiO_2 \times SO_3 \times Temperature$	-0.290	-0.235
$Al_2O_3 \times Fe_2O_3^2$	-0.139	-0.365	$SiO_2 \times SO_3 \times N/B$	1.129	2.205
$Al_2O_3 \times Fe_2O_3 \times S/N$	0.343	0.146	$SiO_2 \times SO_3 \times W/B$	-0.500	1.439
$Al_2O_3 \times Fe_2O_3 \times Temperature$	-0.128	-0.334	$SiO_2 \times Cl^2$	-0.028	0.116
$Al_2O_3 \times Fe_2O_3 \times N/B$	1.240	0.452	$SiO_2 \times Cl \times K_2O$	-0.281	-1.306
$Al_2O_3 \times Fe_2O_3 \times W/B$	-0.020	0.481	$SiO_2 \times Cl \times CaO$	-1.031	-3.614
$Al_2O_3 \times S/N^2$	0.864	0.783	$SiO_2 \times Cl \times TiO_2$	0.052	0.167
$Al_2O_3 \times S/N \times Temperature$	-0.288	-0.884	$SiO_2 \times Cl \times MnO$	-0.216	-0.775
$Al_2O_3 \times S/N \times N/B$	1.172	1.107	$SiO_2 \times Cl \times Fe_2O_3$	-0.074	-0.261
$Al_2O_3 \times S/N \times W/B$	0.039	-0.579	$SiO_2 \times Cl \times S/N$	1.127	2.584
$Al_2O_3 \times Temperature^2$	0.347	1.601	$SiO_2 \times Cl \times Temperature$	-0.347	-1.114
$Al_2O_3 \times Temperature \times N/B$	-2.304	-4.641	$SiO_2 \times Cl \times N/B$	2.845	4.140
$Al_2O_3 \times Temperature \times W/B$	-0.433	1.887	$SiO_2 \times Cl \times W/B$	-0.283	-0.413
$Al_2O_3 \times N/B^2$	6.806	12.792	$SiO_2 \times K_2O^2$	0.806	1.031
$Al_2O_3 \times N/B \times W/B$	-2.198	-8.757	$SiO_2 \times K_2O \times CaO$	0.054	-0.296
$Al_2O_3 \times W/B^2$	1.616	0.375	$SiO_2 \times K_2O \times TiO_2$	-0.137	-0.968
SiO_2^3	-1.734	-4.092	$SiO_2 \times K_2O \times MnO$	0.306	0.685
$SiO_2^2 \times P_2O_5$	0.702	1.760	$SiO_2 \times K_2O \times Fe_2O_3$	0.219	0.774
$SiO_2^2 \times SO_3$	0.408	-1.230	$SiO_2 \times K_2O \times S/N$	-0.075	-0.264
$SiO_2^2 \times Cl$	0.805	1.769	$SiO_2 \times K_2O \times Temperature$	0.461	0.946
$SiO_2^2 \times K_2O$	-0.155	0.594	$SiO_2 \times K_2O \times N/B$	-0.886	-0.933
$SiO_2^2 \times CaO$	1.117	4.240	$SiO_2 \times K_2O \times W/B$	-0.398	-2.111
$SiO_2^2 \times TiO_2$	0.933	1.885	$SiO_2 \times CaO^2$	-1.393	-4.466
$SiO_2^2 \times MnO$	0.340	0.953	$SiO_2 \times CaO \times TiO_2$	-0.958	-3.251
$SiO_2^2 \times Fe_2O_3$	0.415	1.457	$SiO_2 \times CaO \times MnO$	-0.122	-0.802
$SiO_2^2 \times S/N$	-1.628	-3.248	$SiO_2 \times CaO \times Fe_2O_3$	-0.013	-0.230
$SiO_2^2 \times Temperature$	0.132	0.311	$SiO_2 \times CaO \times S/N$	1.087	0.944
$SiO_2^2 \times N/B$	-2.879	-3.246	$SiO_2 \times CaO \times Temperature$	0.117	-0.273
$SiO_2^2 \times W/B$	0.313	0.128	$SiO_2 \times CaO \times N/B$	1.315	1.944
$SiO_2 \times P_2O_5^2$	0.224	0.075	$SiO_2 \times CaO \times W/B$	0.133	-2.572

$SiO_2 \times P_2O_5 \times SO_3$	-0.255	-0.193	$SiO_2 \times TiO_2^2$	0.151	0.284
$SiO_2 \times P_2O_5 \times Cl$	-0.462	-1.428	$SiO_2 \times TiO_2 \times MnO$	-0.257	-0.913
$SiO_2 \times P_2O_5 \times K_2O$	0.552	1.215	$SiO_2 \times TiO_2 \times Fe_2O_3$	-0.230	-0.838
$SiO_2 \times P_2O_5 \times CaO$	-0.428	-1.563	$SiO_2 \times TiO_2 \times S/N$	1.522	3.028
$SiO_2 \times P_2O_5 \times TiO_2$	-0.454	-1.622	$SiO_2 \times TiO_2 \times Temperature$	-0.338	-0.930
$SiO_2 \times P_2O_5 \times MnO$	0.009	-0.031	$SiO_2 \times TiO_2 \times N/B$	4.313	6.139
$SiO_2 \times P_2O_5 \times Fe_2O_3$	-0.032	-0.134	$SiO_2 \times TiO_2 \times W/B$	-0.733	-0.762
$SiO_2 \times P_2O_5 \times S/N$	0.664	1.101	$SiO_2 \times MnO^2$	0.015	-0.006
$SiO_2 \times P_2O_5 \times Temperature$	0.184	0.631	$SiO_2 \times MnO \times Fe_2O_3$	-0.036	-0.074
$P_2O_5 \times MnO$	-0.058	-0.012	$SiO_2 \times MnO \times S/N$	0.228	0.481

APPENDIX B – PARAMETERS OF THE MULTIVARIATE POLYNOMIAL REGRESSION MODEL FOR COMPRESSIVE STRENGTH

Parameter	Value	Parameter	Value
Intercept	-5.211E+11	$SO_3 \times Fe_2O_3$	1.142E+10
Al_2O_3	7.728E+10	$SO_3 \times S/N$	-4.548E+00
SiO_2	2.796E+11	$SO_3 \times Temperature$	2.805E+09
P_2O_5	-1.505E+11	$SO_3 \times N/B$	4.744E-01
SO_3	1.838E+11	$SO_3 \times W/B$	9.793E+00
Cl	-2.518E+11	Cl^2	3.359E+12
K_2O	2.693E+11	$Cl \times K_2O$	4.677E+11
CaO	-3.765E+11	$Cl \times CaO$	-1.299E+12
TiO_2	-8.061E+11	$Cl \times TiO_2$	-2.582E+12
MnO	9.095E+09	$Cl \times MnO$	4.214E+11
Fe_2O_3	7.909E+10	$Cl \times Fe_2O_3$	5.526E+11
S/N	3.968E+00	$Cl \times S/N$	5.480E+00
Temperature	5.567E+10	$Cl \times Temperature$	1.499E+11
N/B	2.142E+00	$Cl \times N/B$	-1.877E+01
W/B	-4.788E+00	$Cl \times W/B$	1.889E+01
$Al_2O_3^2$	-5.654E+10	K_2O^2	7.480E+09
$Al_2O_3 \times SiO_2$	-1.553E+10	$K_2O \times CaO$	2.869E+09
$Al_2O_3 \times P_2O_5$	5.720E+10	$K_2O \times TiO_2$	-8.124E+10
$Al_2O_3 \times SO_3$	9.901E+10	$K_2O \times MnO$	1.706E+11
$Al_2O_3 \times Cl$	5.983E+11	$K_2O \times Fe_2O_3$	-2.601E+10
$Al_2O_3 \times K_2O$	-2.554E+09	$K_2O \times S/N$	-6.955E+00
$Al_2O_3 \times CaO$	-6.697E+10	$K_2O \times Temperature$	7.457E+09
$Al_2O_3 \times TiO_2$	4.904E+10	$K_2O \times N/B$	-5.975E+00
$Al_2O_3 \times MnO$	-4.332E+11	$K_2O \times W/B$	9.602E+00
$Al_2O_3 \times Fe_2O_3$	-2.940E+10	CaO^2	3.032E+10
$Al_2O_3 \times S/N$	-8.617E+00	$CaO \times TiO_2$	1.409E+11
$Al_2O_3 \times Temperature$	4.214E+10	$CaO \times MnO$	-3.817E+11
$Al_2O_3 \times N/B$	-1.219E+00	$CaO \times Fe_2O_3$	1.167E+11
$Al_2O_3 \times W/B$	6.434E+00	$CaO \times S/N$	-1.430E+01
SiO_2^2	-1.163E+10	$CaO \times Temperature$	1.474E+10
$SiO_2 \times P_2O_5$	6.955E+10	$CaO \times N/B$	-3.724E+00
$SiO_2 \times SO_3$	-2.449E+10	$CaO \times W/B$	7.921E+00
$SiO_2 \times Cl$	8.632E+11	TiO_2^2	9.839E+09
$SiO_2 \times K_2O$	1.474E+10	$TiO_2 \times MnO$	-1.927E+11
$SiO_2 \times CaO$	6.541E+10	$TiO_2 \times Fe_2O_3$	8.631E+10
$SiO_2 \times TiO_2$	3.539E+11	$TiO_2 \times S/N$	-8.701E+00
$SiO_2 \times MnO$	-5.332E+11	$TiO_2 \times Temperature$	-9.048E+09
$SiO_2 \times Fe_2O_3$	6.770E+10	$TiO_2 \times N/B$	1.079E+01
$SiO_2 \times S/N$	-7.369E+00	$TiO_2 \times W/B$	-4.220E+00
$SiO_2 \times Temperature$	-7.115E+09	MnO^2	-1.882E+11
$SiO_2 \times N/B$	-1.349E+01	$MnO \times Fe_2O_3$	-3.486E+11
$SiO_2 \times W/B$	3.400E+01	$MnO \times S/N$	-3.601E+00
$P_2O_5^2$	-6.601E+10	$MnO \times Temperature$	-1.220E+10
$P_2O_5 \times SO_3$	-4.400E+10	$MnO \times N/B$	-1.144E+01

$P_2O_5 \times Cl$	-4.421E+11	MnO × W/B	4.453E+01
$P_2O_5 \times K_2O$	1.803E+11	$Fe_2O_3^2$	1.337E+11
$P_2O_5 \times CaO$	1.422E+11	$Fe_2O_3 \times S/N$	-2.208E+00
$P_2O_5 \times TiO_2$	1.640E+11	$Fe_2O_3 \times$ Temperature	-1.492E+10
$P_2O_5 \times MnO$	2.730E+11	$Fe_2O_3 \times N/B$	-4.395E+00
$P_2O_5 \times Fe_2O_3$	1.409E+09	$Fe_2O_3 \times W/B$	5.331E+00
$P_2O_5 \times S/N$	-3.328E+00	S/N^2	-2.789E+00
$P_2O_5 \times$ Temperature	4.977E+10	S/N × Temperature	-2.115E+00
$P_2O_5 \times N/B$	-1.536E+01	S/N × N/B	-1.529E+00
$P_2O_5 \times W/B$	4.561E+00	S/N × W/B	3.395E-03
SO_3^2	-6.847E+09	Temperature²	-1.105E+01
$SO_3 \times Cl$	3.357E+11	Temperature × N/B	5.450E+00
$SO_3 \times K_2O$	3.447E+10	Temperature × W/B	5.858E+00
$SO_3 \times CaO$	6.064E+10	N/B^2	-3.932E+00
$SO_3 \times TiO_2$	3.824E+10	N/B × W/B	-7.725E-01
$SO_3 \times MnO$	1.601E+11	W/B^2	3.310E+00